

AD-A125 513

REMOTE SENSING OF SURFACE PROPAGATION PARAMETERS:
APPLICATION OF IMAGERY. (U) ATMOSPHERIC AND
ENVIRONMENTAL RESEARCH INC CAMBRIDGE MA R G ISAACS

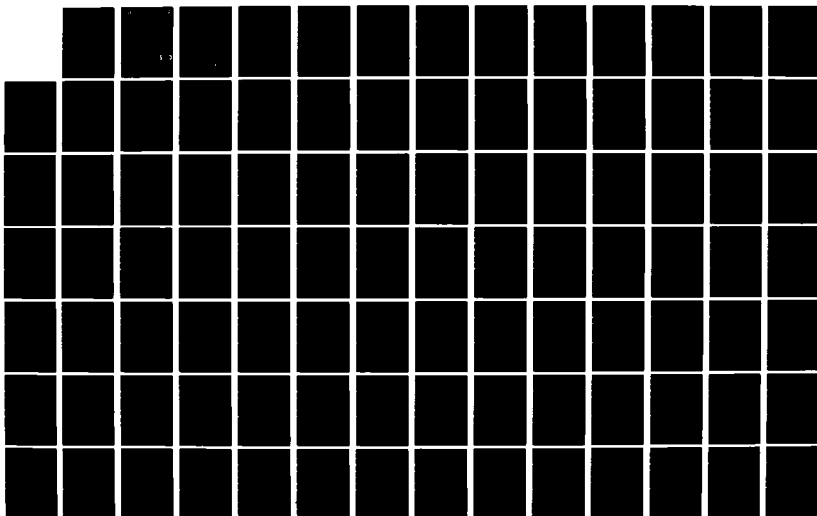
1/3

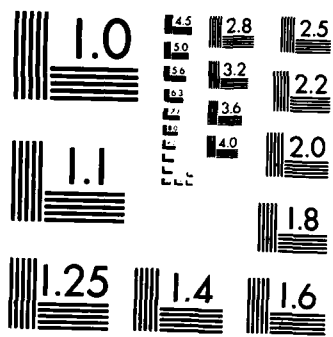
UNCLASSIFIED

31 OCT 82 N88014-88-C-0262

F/G 12/1

NL





MICROCOPY RESOLUTION TEST CHART
NATIONAL BUREAU OF STANDARDS-1963-A

AER

②

AD A 1 255 13

REMOTE SENSING OF SURFACE
PROPAGATION PARAMETERS:
APPLICATION OF IMAGERY
SIMULATION MODEL RESULTS

DTIC FILE COPY

DTIC
ELECTE
MAR 10 1983
S **D**
B

DISTRIBUTION STATEMENT A
Approved for public release
Distribution Unlimited

ATMOSPHERIC & ENVIRONMENTAL RESEARCH, INC.
Cambridge, Massachusetts

83 03 10 052

REMOTE SENSING OF SURFACE
PROPAGATION PARAMETERS:
APPLICATION OF IMAGERY
SIMULATION MODEL RESULTS

Prepared by:

Ronald G. Isaacs
Atmospheric and Environmental Research, Inc.
840 Memorial Drive
Cambridge, Massachusetts 02139

Contract No. N00014-80-C-0262

Final Report
1 October, 1980 - 31 October 1982

Prepared for:

Office of Naval Research
Arlington, Virginia 22217

DTIC
ELECTE
MAR 10 1983
S D
B

DISTRIBUTION STATEMENT A

Approved for public release;
Distribution Unlimited

REPORT DOCUMENTATION PAGE		READ INSTRUCTIONS BEFORE COMPLETING FORM								
1. REPORT NUMBER	2. GOVT ACCESSION NO. AD-A125 513	3. RECIPIENT'S CATALOG NUMBER								
4. TITLE (and Subtitle) Remote Sensing of Surface Propagation Parameters: Application of Imagery Simulation Model Results		5. TYPE OF REPORT & PERIOD COVERED FINAL REPORT 1 October 1980-31 October 1982								
7. AUTHOR(s) Ronald G. Isaacs		6. PERFORMING ORG. REPORT NUMBER								
9. PERFORMING ORGANIZATION NAME AND ADDRESS Atmospheric and Environmental Research, Inc. 840 Memorial Drive Cambridge, MA 02139		8. CONTRACT OR GRANT NUMBER(s) N00014-80-C-0262								
11. CONTROLLING OFFICE NAME AND ADDRESS Procuring Contracting Officer Office of Naval Research, Dept. of the Navy 800 N. Quincy St., Arlington, VA 22217		10. PROGRAM ELEMENT, PROJECT, TASK AREA & WORK UNIT NUMBERS								
14. MONITORING AGENCY NAME & ADDRESS (if different from Controlling Office) DCASMA 666 Summer Street Boston, MA 02210		12. REPORT DATE 31 October 1982								
		13. NUMBER OF PAGES 248								
		15. SECURITY CLASS. (of this report)								
		15a. DECLASSIFICATION/DOWNGRADING SCHEDULE								
16. DISTRIBUTION STATEMENT (of this Report)										
<div style="border: 1px solid black; padding: 5px; width: fit-content; margin: 0 auto;"> <p>DISTRIBUTION STATEMENT A</p> <p>Approved for public release; Distribution Unlimited</p> </div>										
17. DISTRIBUTION STATEMENT (of the abstract entered in Block 20, if different from Report)										
18. SUPPLEMENTARY NOTES										
19. KEY WORDS (Continue on reverse side if necessary and identify by block number)										
<table style="width: 100%; border: none;"> <tr> <td style="width: 50%;">Remote Sensing</td> <td style="width: 50%;">Radiative Transfer</td> </tr> <tr> <td>Aerosols</td> <td>Optical Range</td> </tr> <tr> <td>Optical Depth</td> <td>Sunglint</td> </tr> <tr> <td>Satellite Imagery</td> <td>Optical Properties</td> </tr> </table>			Remote Sensing	Radiative Transfer	Aerosols	Optical Range	Optical Depth	Sunglint	Satellite Imagery	Optical Properties
Remote Sensing	Radiative Transfer									
Aerosols	Optical Range									
Optical Depth	Sunglint									
Satellite Imagery	Optical Properties									
20. ABSTRACT (Continue on reverse side if necessary and identify by block number)										
<p>A mathematical model is described and documented which simulates the sensitivity of satellite incident visible and near infrared radiances (0.4-1.1μm wavelength spectral interval) to variations in the meteorological variables (such as relative humidity and wind speed) characterizing the environment near the ocean surface. Potential applications include support of meteorological analysis of DMSP visible imagery and operational satellite-based retrieval of the aerosol contribution to optical range degradation.</p>										

Attributes of the model include: (a) calculation of solar/satellite sub-point and scan line pixel location based on nominal DMSP orbital characteristics (b) choice of aerosol optical properties from among tropospheric, maritime, rural and urban models, (c) surface reflectivity based on statistics of wind-driven, rough ocean, and (d) approximate radiative transfer calculation of satellite incident radiances. The theoretical basis of each model subcomponent is fully discussed.

A variety of supporting calculations are provided including radiance simulations in sunglint regions, DMSP imagery simulation, and comparison of simulated DMSP radiances to hardcopy imagery. The model is applied to evaluate theoretical DMSP radiance/aerosol optical depth relationships for a variety of meteorological conditions. Additionally, a prototype multispectral range retrieval algorithm is proposed to utilize the aerosol optical depth information available as a result of the previous calculations.

The model is implemented in the form of a user-oriented, computationally efficient computer algorithm for a desk-top mini-computer. Documentation, listings, and sample test runs are provided.

TABLE OF CONTENTS

DEDICATION

EXECUTIVE SUMMARY

1. INTRODUCTION

1.1 Overview

1.2 Study Objectives

1.3 Report Summary

2. REVIEW OF PREVIOUS WORK

2.1 Simulation Model Development

2.2 Model Results

2.3 Model Applications

3. MODEL VALIDATION STUDIES

3.1 MAGAT Data

3.2 Comparison Results

3.2.1 Ladder Profile 5

3.2.2 Ladder Profile 14

3.2.3 Ladder Profile 23

3.2.4 Ladder Profile 24

3.3 Discussion

4. CONTINENTAL AEROSOL MODELS

4.1 Non-Maritime Origin Aerosols

4.2 Rural Aerosol Model

4.3 Urban Aerosol Model

4.4 Aerosol Model Intercomparisons



Accession For	
NTIS GRA&I	<input checked="" type="checkbox"/>
DTIC TAB	<input type="checkbox"/>
Unannounced	<input type="checkbox"/>
Justification	
PER LETTER	
By _____	
Distribution/ _____	
Availability Codes	
Dist	Avail and/or Special
A	

5. SUN/SENSOR GEOMETRY FOR DATA SIMULATION APPLICATIONS
 - 5.1 Satellite Subtrack Position
 - 5.2 Sensor Scan Line Position
 - 5.3 Pixel-Related Sun/Sensor Geometry
6. RADIATIVE TRANSFER MODELING
 - 6.1 Technique Selection Criteria
 - 6.2 Analytical Approaches
 - 6.3 Adopted Approach
 - 6.4 Theory
 - 6.4.1 Phase function parameterization
 - 6.4.2 Flux parameterization
 - 6.5 Comparison to Exact Results
 - 6.5.1 Isotropic scattering
 - 6.5.2 Rayleigh scattering
 - 6.5.3 Aerosol scattering
 - 6.5.3.1 Optically thin case
 - 6.5.3.2 Optically thick case
 - 6.5.3.3 Comparison to look-up table results
 - 6.6 DMSP Bandpass Weighted Radiances
7. REFLECTION FROM THE OCEAN SURFACE
 - 7.1 Sunlint
 - 7.2 Surface Modeling
 - 7.3 Wind Driven, Rough Ocean Surface Reflection Geometry
 - 7.4 Effective Fresnel Reflectivity Formulation

- 7.5 Incorporation Within the Radiance Simulation
- 7.6 Radiance Simulations in Sunlint Regions
- 7.7 Data Intercomparison Case Study
- 7.8 DMSP Imagery Simulation
- 8. DMSP RADIANCE/OPTICAL DEPTH RELATIONSHIPS
 - 8.1 Radiance Spectra
 - 8.2 Bandpass Weighting and Linear Relationships
 - 8.3 Discussion of Radiance/Optical Depth Relationships
- 9. MULTISPECTRAL RANGE RETRIEVAL
 - 9.1 Rationale
 - 9.2 Aerosol Contribution
 - 9.3 Non-Aerosol Contribution
 - 9.3.1 Rayleigh scattering
 - 9.3.2 Molecular line absorption
 - 9.3.3 Continuum absorption
 - 9.4 Multispectral Range Retrieval Results
- 10. SUMMARY, CONCLUSIONS AND RECOMMENDATIONS
 - 10.1 Report Summary
 - 10.2 Conclusions
 - 10.3 Recommendations
- 11. ACKNOWLEDGEMENTS
- 12. REFERENCES

APPENDIX A: DERIVATION OF APPROXIMATE ANALYTICAL
SOLUTION TO RADIATIVE TRANSFER EQUATION

APPENDIX B: PROGRAM DESCRIPTION

B.1 Technical Approach

B.2 Program Attributes

B.3 Program Listings

B.4 Sample Calculation

DEDICATION

This report is dedicated to the memory of Robert E. Specht.

EXECUTIVE SUMMARY

This report describes model development and application activities undertaken in the investigation of the sensitivity of remotely sensed radiances in the DMSP VHR/LF spectral region (0.4 to 1.1 μ m) to near surface meteorological parameters such as relative humidity, wind speed, and aerosol characteristics including mixing height and number density. A research grade computer code developed in an earlier study (Isaacs, 1980) to simulate DMSP visible and near infrared radiances has been upgraded and augmented with additional capabilities desirable in imagery analysis for tactical purposes including: (a) treatment of continental (i.e., urban and rural) aerosol size distribution and composition models, (b) data simulation calculations based on realistic sun/sensor geometries, and (c) approximate ocean surface reflection modeling for potential sunglint regions. Additionally, the approximate, analytical radiative transfer submodel incorporated into the code is fully described and the results of comparisons with accurate numerical treatments are provided for a variety of scattering situations. Comprehensive program documentation is included consisting of listings of the algorithm, sample output, and operating instructions for implementation on a desk top minicomputer.

A variety of simulation studies employing the algorithm are discussed illustrating the effect of relative humidity and mixing height on radiances in non sunglint situations

for both rural and urban aerosol models as compared to the maritime models previously examined (i.e. in Isaacs, 1980). Radiance calculations in sunglint regions using the maritime aerosol model illustrate the effect of relative humidity, wind speed, and aerosol scale height on the intensity gradient observed along simulated sensor scan lines in the vicinity of the primary specular point. Additionally, the model is exercised to simulate a swath of DMSP imagery for illustrative purposes. Results of these simulations confirm the behavior generally observed in relevant imagery for corresponding meteorological analysis case studies as previously reported (cf. Fett and Mitchell, 1973).

Comparison of model predicted values to measured data are presented in two contexts: (a) multiwavelength aerosol extinction coefficient profiles calculated from field measured size distributions are compared to model predicted values based on measured relative humidity profiles as the required meteorological input, and (b) model calculated radiances along a simulated scan line in sunglint are compared to data points obtained from sensometry for the corresponding hardcopy imagery.

In addition to these imagery simulation exercises potentially related to meteorological analyses, application of the algorithm to the inference of surface propagation parameters is explored. Utilizing the model's capability to provide simulated radiances for specified meteorology and choice of aerosol, DMSP radiance/aerosol optical depth

relationships are computed. Results provide a theoretical fit of radiance to aerosol optical depth for maritime, rural, and urban aerosols and relative humidities of 50 through 95%. These may potentially be applied to the retrieval of aerosol optical depth (at visible wavelengths) from appropriately calibrated DMSP radiances.

Since surface propagation parameters are desired at other than visible wavelengths, a prototype algorithm is devised to infer optical range multispectrally using the DMSP radiance/optical depth relationships described above to provide the aerosol contribution to extinction.

The following conclusions and observations are based on the work summarized above:

- Although limited in scope, the validation effort associated with the MAGAT data set indicates that the AFGL maritime aerosol model performs relatively well where expected.
- A variety of comparisons performed between the model adopted approximate radiative transfer scheme and accurate numerical treatments for a range of optical depths, angular scattering functions, and observer/sun orientations leads to the conclusion that simulated radiances are accurate to within 10% overall. This level of accuracy is consistent with the accuracy of input data and the intended purpose of the model, i.e. the simulation of meteorological influences in

the imagery. The results of specific sensitivity tests conclude that adoption of simple analytical phase function representations and the hybrid modified δ -Eddington flux parameterization are appropriate choices.

- The wind-driven, rough ocean surface reflection model implemented within the radiance simulation code provides a good representation of the sun-glint phenomenon as compared to accurate numerical treatments, simulated radiance comparisons to hardcopy imagery, and qualitative observations.
- Model simulations in sun-glint regions suggest a decrease in radiance in the vicinity of the primary specular point due to increases in aerosol optical depth (related to increased relative humidity or scale height). Away from the primary sun-glint region, radiances increase with increasing optical depth as predicted in previous studies.
- A comparison of the optical properties of the maritime and recently implemented rural and urban models suggests that some care must be taken in the interpretation of meteorological influences on individual air masses. For example, the maritime aerosol coarse mode is much more hygroscopic than the others, while the carbon

component of the urban aerosol is critical in determining its radiative properties.

- As a consequence of the above, each aerosol composition model and relative humidity range exhibit unique radiance/optical depth relationships. While those for maritime and rural aerosols are close enough to permit a single linear predictor equation to be used operationally, those for the urban aerosol introduce a potential ambiguity. It appears that it may be important to know whether the air mass aerosol under investigation has any carbon component present (anthropogenic or natural). This may be important in the vicinity of inland seas, coastal regions, or open ocean in situations of long range transport. A parameter which may potentially be retrievable in this regard is the single scattering albedo (Kaufman and Joseph, 1982).
- A sample multispectral range retrieval exercise illustrates both the dominance of aerosol extinction in constraining range at visible wavelengths and the complementary significance of non-aerosol extinction contributions in the infrared. With respect to the latter, calculated aerosol extinction accounts for less than 7% of the total at 10.6 μ m, while that for water vapor continuum absorption is 75%. While visible radiance data may

be useful in predicting visible range, it must be augmented by absolute humidity data from other sources to evaluate IR range.

1. INTRODUCTION

1.1 Overview

This report describes the results of applied research efforts conducted at Atmospheric and Environmental Research, Inc. (AER) in support of the Naval Environmental Prediction Research Facility (NEPRF) during the period 1 October 1980 to 30 September 1982. In a previous study sponsored by NEPRF, AER investigators undertook a study of the influence of meteorological variables and optical propagation parameters on remotely sensed data in the visible (0.4-0.7 μ m) and near infrared (0.7-1.1 μ m) spectral regions such as that potentially available from the DMSP sun synchronous polar orbiting satellite sensor platforms. In the course of that effort (Isaacs, 1980) a computationally efficient model was developed to simulate the sensitivity of wavelength dependent, satellite incident radiances to variations in characteristic meteorological variables such as relative humidity, wind speed, mixing height, and aerosol number density and size range. The model is based in part on extant propagation codes commonly applied within the DOD community to evaluate point-to-point optical transmission and, in that context, provides an extension of these codes to simulate satellite-based observations. The model developed may therefore provide an informative link between concurrent in situ and remotely sensed data bases.

Although simulation results presented provided insights into a variety of imagery analysis questions, a number of limitations to the model were identified. The objective of the work reported here was to supplement and extend the theoretical studies previously performed and provide the foundation for an operationally useful analysis tool by validating elements of the model.

1.2 Study Objectives

The objectives of this study included: (a) validation of model and submodel elements through comparison of model predicted results based on in situ meteorological input data and field measured quantities where possible, (b) incorporation of non-maritime aerosol optical properties models to facilitate treatment of coastal regions and areas over the open ocean subject to continental aerosol sources, (c) implementation of the simulation algorithm in a format more consistent with the operational analysis of imagery, (d) extension of the domain of applicable cases to include those in potential sunglint areas, (e) application of the model to the retrieval of surface propagation parameters particularly aerosol contributions to range degradation, and (f) provision for program documentation and description.

1.3 Report Summary

This document is organized into ten sections. Section 2 briefly reviews work previously completed. Section 3

discusses model validation studies based on comparison of measured and model predicted aerosol extinction. Section 4 describes the incorporation of continental (i.e., urban and rural) aerosol optical properties submodels within the simulation code. Section 5 catalogs the equations used in the model to provide the necessary sun/sensor geometry for the simulation of real data. Section 6 discusses the radiative transfer theory implemented within the model. Section 7 documents the treatment of ocean surface reflection in potential sunglint regions. Section 8 provides theoretical DMSP radiance/aerosol optical depth relationships calculated by the model which may be used to infer the aerosol contribution to range degradation. Section 9 proposes an algorithm for multispectral range retrieval based on the availability of satellite visible radiance data (using the results of Section 8). Finally, Section 10 summarizes relevant conclusions and recommendations.

Two supporting appendices are included. Appendix A includes a derivation of the radiative transfer solutions used to calculate radiance and Appendix B incorporates a program description and basic users' guide into the report.

2. REVIEW OF PREVIOUS WORK

2.1 Simulation Model Development

Mathematical models to simulate satellite based data sets have been applied extensively in the recent past both a priori to investigate the optimum configuration of proposed sensor systems for observing specific phenomena or parameters and after system deployment as tools to aid in the analysis and reduction of resultant real data. A significant amount of input data describing the composition and optical properties of the atmosphere-surface system is required to successfully implement these models. Meteorological imaging sensors (as contrasted with sounders) are generally designed to sense near surface phenomena and, therefore, simulation of such "window region" data requires input of meteorologically dependent optical properties of the lower atmosphere. A number of previous studies concerning, for example, the near infrared properties of clouds, precipitation monitoring, and remote sensing of surface properties (Isaacs et al., 1974; Gaut et al., 1975; Isaacs and Chang, 1975) employed standard optical propagation models linked with radiative transfer theory to provide such simulations.

Studies of so-called anomalous gray shade patterns (see Fett and Mitchell, 1977), identifiable in wide band (0.4-1.1 μm) DMSP VHR and LF imagery suggested the role of low level haze and moisture as one potential cause, highlighting the

role of meteorological variables such as relative humidity in determining remotely sensed imagery data. In a subsequent study undertaken to investigate the relative wavelength dependent effects of atmospheric particulates and water vapor content in these gray shade phenomena (Barnes et al., 1979), a simulation model was employed using optical properties based on LOWTRAN 2 (Selby and McClatchey, 1972) and a radiative transfer code. Results suggested the significant role of atmospheric aerosol content in backscattering solar radiation. A related first order analysis (Fett and Isaacs, 1979) emphasized the role of particulates and their characteristic scattering properties especially in the near infrared spectral region. Because of the limiting assumptions adopted in these studies, a more comprehensive modeling program was initiated.

The technical approach adopted consisted of simulating the sensitivity of satellite incident visible and near IR radiances to variations in near surface ambient meteorological variables by modeling the physical mechanisms linking the meteorologically-dependent optical properties of the lower atmosphere to the transfer of incident solar radiation due to reflection and scattering from the atmosphere-ocean system. Mechanisms simulated included: (1) the change in aerosol size distribution and complex index of refraction due to variations in relative humidity, (2) enhanced aerosol coarse mode loading due to wind speed dependent sea spray, (3) variations in aerosol optical properties due to the preceding effects, (4) relative humidity dependent variations in non-

aerosol atmospheric transmission due to molecular absorption by water vapor, and (5) radiative transfer including multiple scattering, scattering anisotropy, and surface reflection. With the objective of providing an economical tool to aid in the analysis of DMSP imagery, the modeling level-of-effort devoted to each mechanism's submodel was kept as simple as possible.

As a result of this work (Isaacs, 1980), a model to relate simulated satellite radiances (in the wavelength region 0.4-1.1 μm) to variations in meteorological variables such as relative humidity, wind speed, aerosol number density/visual range, and aerosol scale height was developed and implemented. This model was exercised to provide a theoretical sensitivity analysis of wavelength-dependent and DMSP bandpass weighted radiances to the above cited meteorological variables.

2.2 Model Results

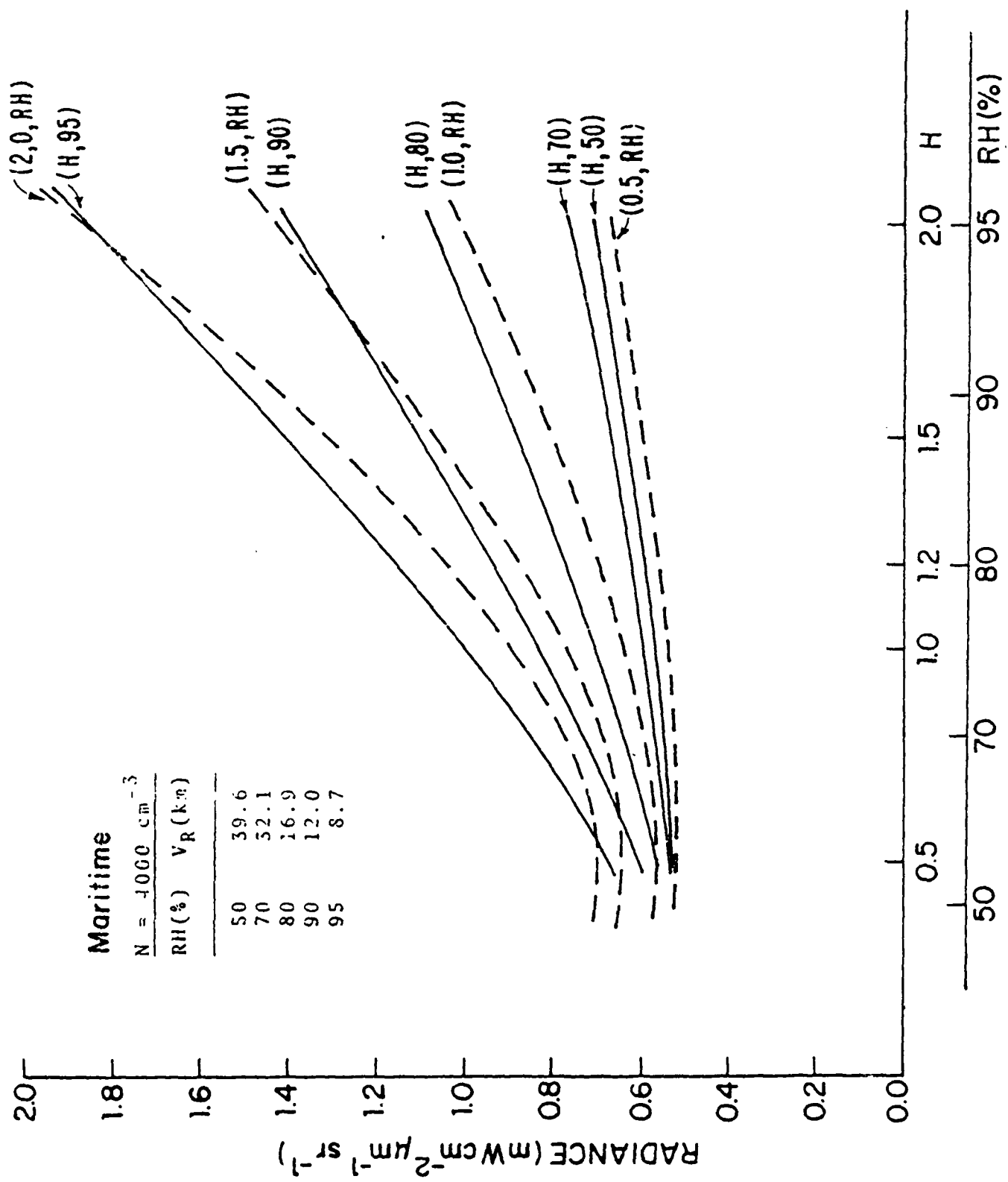
By consolidating individual model simulations of DMSP bandpass weighted radiances for each of the two maritime aerosol models adopted, nomograms of radiance, $\bar{I}(\text{DMSP})$, vs. relevant meteorological variables were prepared. These are illustrated in Figures 2-1 and 2-2 for the maritime and hybrid aerosol models, respectively. As illustrated in the sensitivity analysis results, DMSP radiances are dependent on a number of meteorologically based variables. Theoretically, a single DMSP radiance data point can be expected to provide one piece of information in the inverse applica-

tion. Conceptually, if DMSP radiances were strongly associated with the variation of one meteorological variable and only weakly dependent on the others, it would be possible to obtain information about the controlling independent variable. The results indicate, however, that both relative humidity and aerosol scale height are of equal importance within the context of the maritime aerosol model (Figure 2-1). Therefore, either variable cannot be uniquely determined from DMSP data alone. The situation is similar for the wind speed dependent hybrid model (Figure 2-2) although in this case wind speed effects are apparently of second order with respect to relative humidity and scale height dependence.

2.3 Model Applications

As written, the simulation model was applicable to the following cases:

- . regions characterized by maritime aerosol models (chemical composition, number size distribution, and aerosol growth laws),
- . regions remote from sunglint (i.e., the surface is treated as a Lambert reflector and no treatment of surface reflectance on wind speed dependent surface slope geometry is included),
- . the spectral region extending from 0.4 μ m in the visible to 1.1 μ m in the near infrared, i.e. that of the DMSP primary sensor.



Maritime

$N = 1000 \text{ cm}^{-3}$

RH(%)	V_R (km)
50	39.6
70	52.1
80	16.9
90	12.0
95	8.7

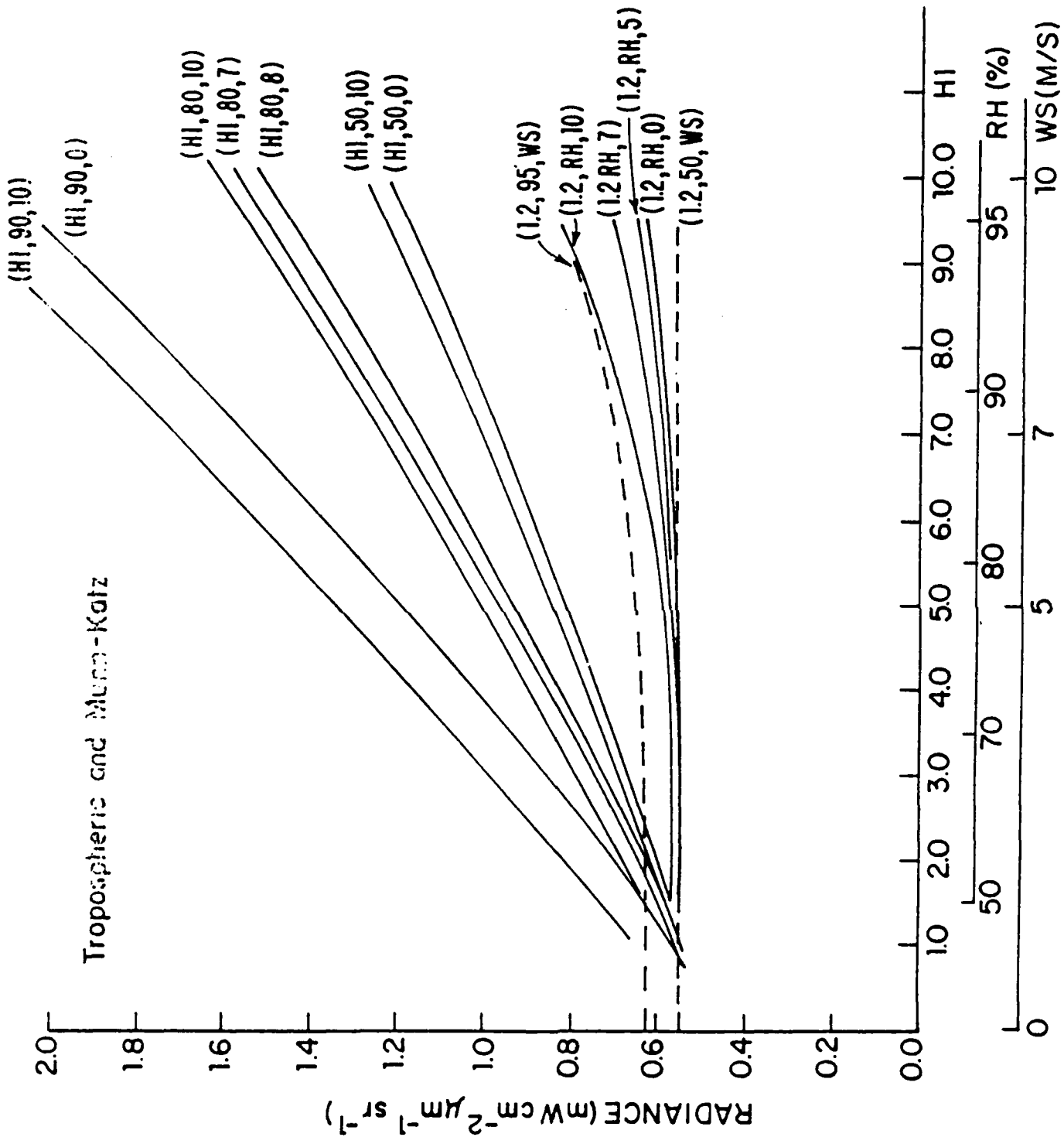


Figure 2-2. DNISP Bandpass-Weighted Radiances (Hybrid Model)

3. MODEL VALIDATION STUDIES

3.1 MAGAT Data

Data from the Monterey Aerosol Generation and Atmospheric Turbulence (MAGAT) experiment conducted in the vicinity of Monterey Bay in May 1980 were employed in support of the evaluation and validation of the aerosol optical properties submodel of the simulation model. Seven (7) sets of MAGAT data were supplied by the Naval Environmental Prediction Research Facility consisting of: (1) wavelength-dependent (.49, .53, .63, .83, 1.03 μm) aerosol extinction (km^{-1}) calculated from Knollenberg spectrometer size spectra measurements made during aircraft ladder profile (LP) flights on 1, 4 and 7 May 1980, (2) coincident temperature and dew point temperature, (3) water vapor mixing ratio, and (4) location of each ladder profile. Data received for analysis are summarized in Table 3-1. Subsequent to receipt of the aerosol optical data, a variety of corresponding DMSP LF (visible and near IR) and thermal imagery was obtained in hardcopy (i.e., photographic print) format. Due to our inability to extract correlative quantitative radiance data from the photographic print imagery, validation exercises focused on the aerosol extinction data.

In order to manipulate the aerosol optical data (which were received in tabular form), data files were established for each data subset. The object of the validation exercise was: (1) to use the aerosol optical properties submodel of

Identification (LP = Ladder Profile)	Date	Data Times		Altitude Range (ft)	Comments
		Begin	End		
(1) LP 5*	05/01/80	175430	184900	10-6000	light winds, haze 3.4-5.5 kft
(2) LP 6	05/01/80	190350	194355	10-4000	haze 3.4-5.5 kft, cumulus below 3.0 kft
(3) LP 14*	05/04/80	102417	104740	10-1500	light winds, haze 0.6-1.4 kft, stratus parallel to shore
(4) LP 15	05/04/80	111000	113215	10-2000	hazy stratus 0.7-1.2 kft
(5) LP 16	05/04/80	120115	130350	10-2000	scattered puffy clouds, top 1.5 kft
(6) LP 23*	05/07/80	104300	112430	10-4000	cloud 1.1-1.4 kft
(7) LP 24*	05/07/80	185800	194100	10-4000	weak inversion 4.4 kft, stratus 1.3-1.5 kft, upper haze layer above 4.2 kft

*Data set used in validation analysis.

Table 3-1 Summary of MAGAT Data

the simulation algorithm to predict wavelength dependent extinction properties of the atmosphere given the measured in situ meteorological variables (e.g., wind speed, relative humidity) as model input, and (2) to compare the predicted aerosol extinction to that actually measured.[†] To accomplish these steps, software was written to: (1) read in each MAGAT data set, (2) evaluate the required relative humidity profile from temperature and dew point data, (3) evaluate corresponding model aerosol extinction profiles at the required wavelengths and relative humidities for tropospheric, maritime, rural, and urban aerosol models, and (4) provide plots comparing measured and modeled aerosol optical extinction. To accomplish the comparison step, model number densities were normalized to yield measured extinction at 0.53 μm . Normalization of overall results was necessary since no data were available to select appropriate total aerosol number density values for each data set. Thus, comparison results provide only relative wavelength consistency of measured to modeled results.

3.2 Comparison Results

Of the seven data sets received, four were selected for in-depth analysis. These are indicated by an asterisk in Table 3-1 and generally consist of those ladder profiles not contaminated by the presence of excessive clouds. For each

[†] The measured extinction was actually calculated from size distribution measurements using Mie theory (A. Goroch, personal communication).

data set results are presented in this section consisting of: (a) profiles of the measured extinction data at each of the five available wavelengths (0.49, 0.53, 0.63, 0.83 and 1.03 μm), (b) a corresponding profile of relative humidity calculated from the temperature and dew point data supplied, (c) comparison of model predicted extinction profiles at selected wavelengths for each of the four available aerosol models (tropospheric, rural, urban, and maritime) based on the measured relative humidity profile as model input[†] and normalizing results to the data at 0.53 μm , and (d) comparison of the wavelength dependence of modeled and measured extinction at selected pressure levels.

3.2.1 Ladder Profile 5 (LP 5)

Extinction profile data for LP 5 on 5 May 1980 are illustrated in Figure 3-1 (note: pressure profile coordinates (mb) with surface toward top of plot). The corresponding relative humidity profile is shown in Figure 3-2. The comparison of measured (crosses) to simulated extinction is given in Figure 3-3 for wavelengths of: (a) 0.49, (b) 0.63, (c) 0.83, and (d) 1.03 μm . The general slope of the vertical extinction profile is reproduced by all four available aerosol models. At the longer wavelengths (0.83 μm - Figure 3-3c; 1.03 μm - Figure 3-3d), extinction is overestimated by the

[†] Light winds (i.e., $<5 \text{ ms}^{-1}$) were reported for the data sets used in the analysis (A. Goroch, personal communication) and therefore, 0 ms^{-1} was used as coarse model input when required.

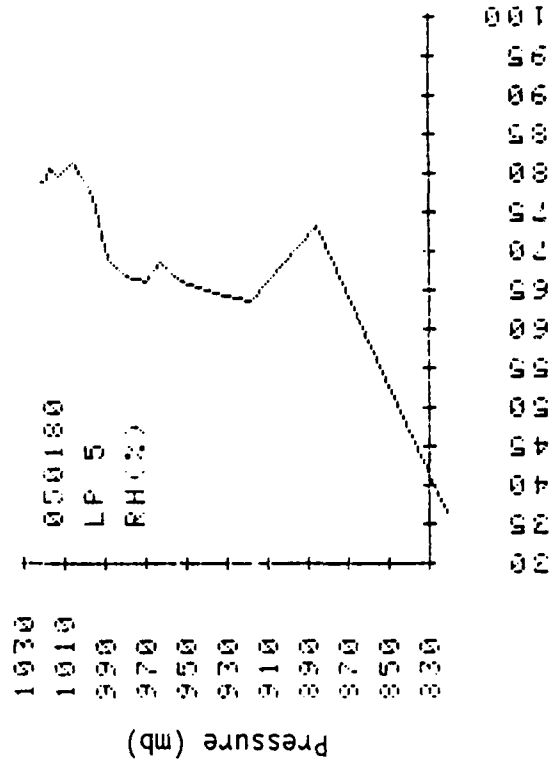


Figure 3-1. Extinction coefficient (km^{-1}) data for ladder profile #5 on 050180. Wavelengths: (a) $0.49\mu\text{m}$, (b) $0.53\mu\text{m}$, (c) $0.63\mu\text{m}$, (d) $0.83\mu\text{m}$, and (e) $1.03\mu\text{m}$.

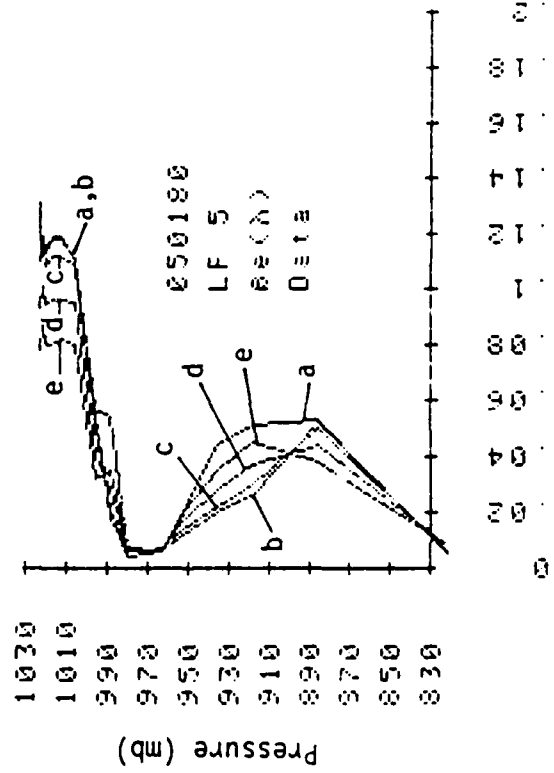


Figure 3-2. Relative humidity (%) profile for ladder profile #5 on 050180.

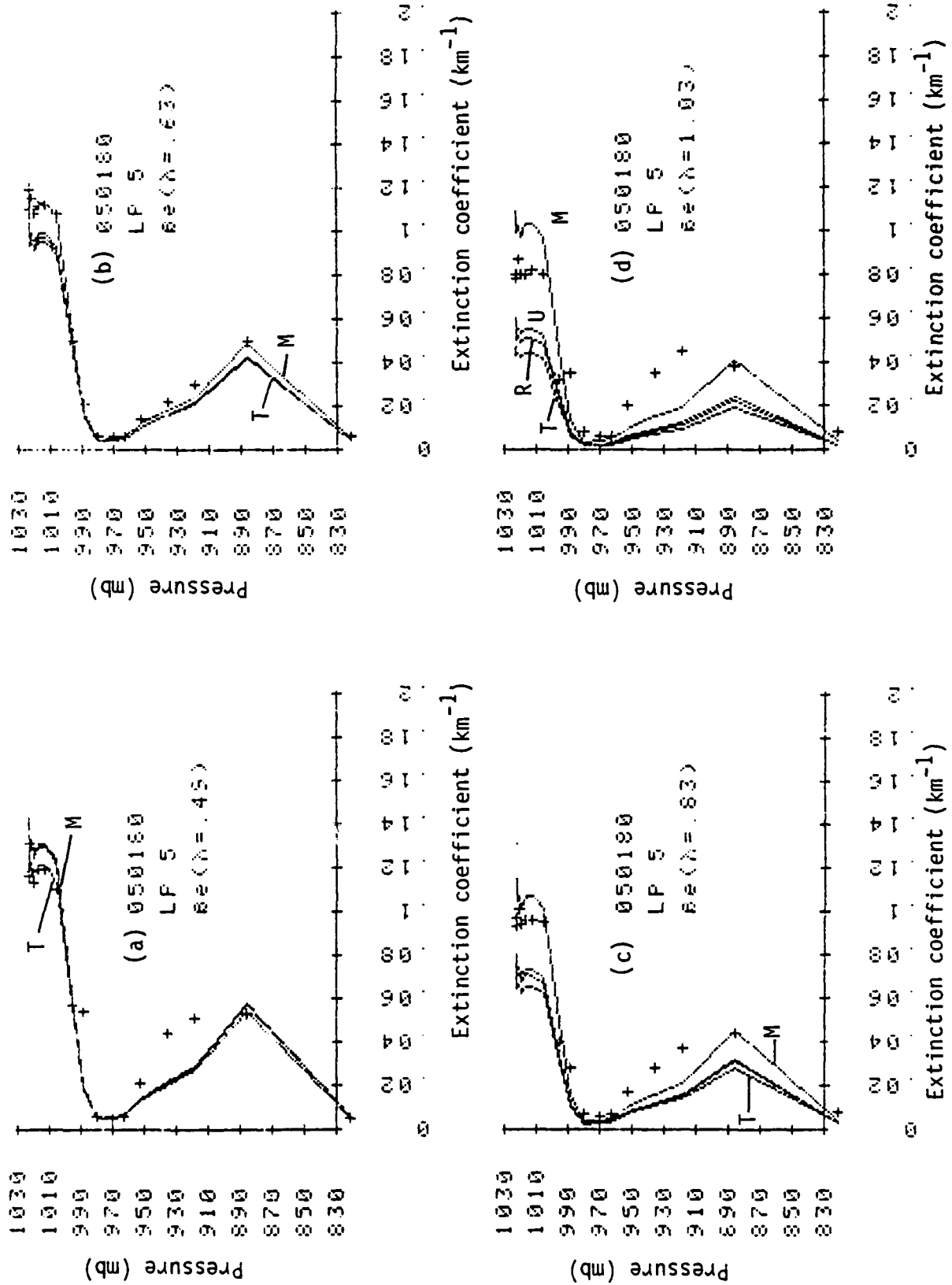
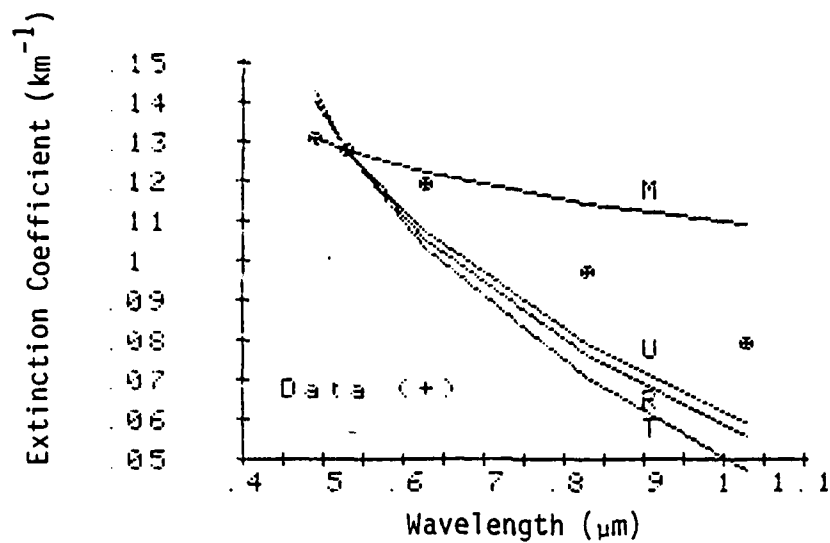


Figure 3-3. Comparison of model predicted extinction coefficient profiles to data(+) at wavelength of: (a) 0.49 μm , (b) 0.63, (c) 0.83, and (d) 1.03 μm (normalized at 0.53 μm).

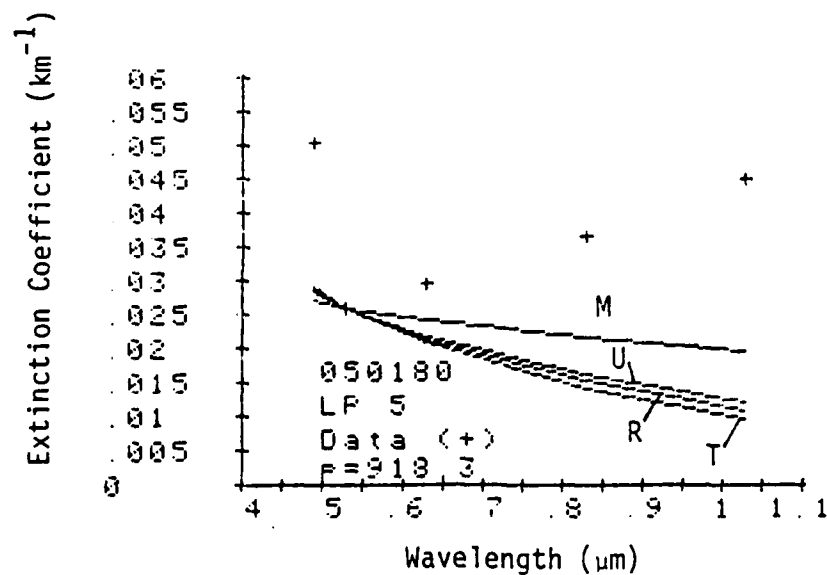
maritime model in the layer near the surface ($p > 990$ mb) while it is underestimated by the other models. Note that this layer is a region of higher relative humidity. Selecting a pressure level within this region and examining the wavelength dependence of the modeled extinction results in Figure 3-4a. Here extinction data are selected at $p = 1023$ mb near the surface where the relative humidity is about 80%. At shorter wavelengths ($< 0.7 \mu\text{m}$), the maritime model does relatively well in predicting extinction wavelength dependence. In the near IR, however, extinction apparently decreases with wavelength faster than the maritime model permits. The wavelength dependence at these longer wavelengths is closer to that at the urban and rural models which have much smaller coarse mode number densities. As Figure 3-4b indicates, it is difficult to connect some of the predicted extinction curves with the measured data. These data are at $p = 918$ mb which is probably within a haze layer perceived by the surface observer.

3.2.2 Ladder Profile 14 (LP 14)

A less complicated situation is illustrated by the data from LP 14 collected on 4 May 1980. Figures 3-5 and 3-6 illustrate the extinction profile data and calculated relative humidity profiles, respectively, for a haze layer extending from about 600 to 1400 ft. in altitude (~ 970 -1010 mb). The relative humidity in this layer is between 80 and 85%. If model predicted extinction profiles are compared to the data

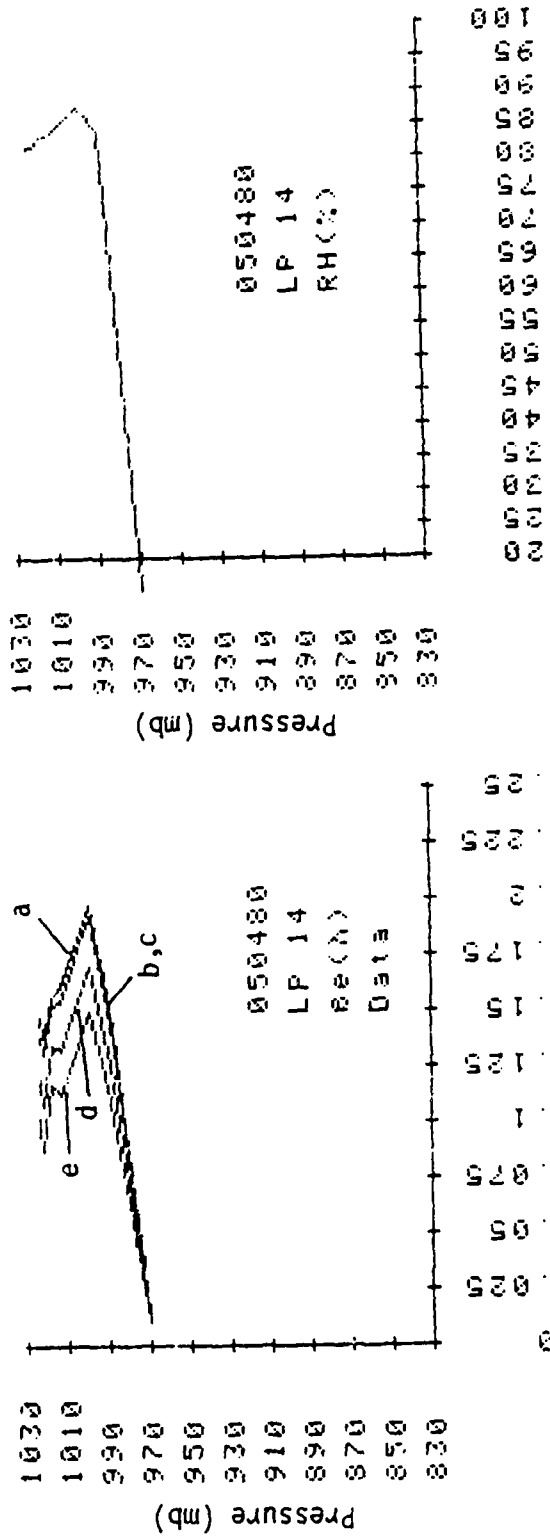


(a) Pressure = 1023 mb, Relative Humidity = 78.7%



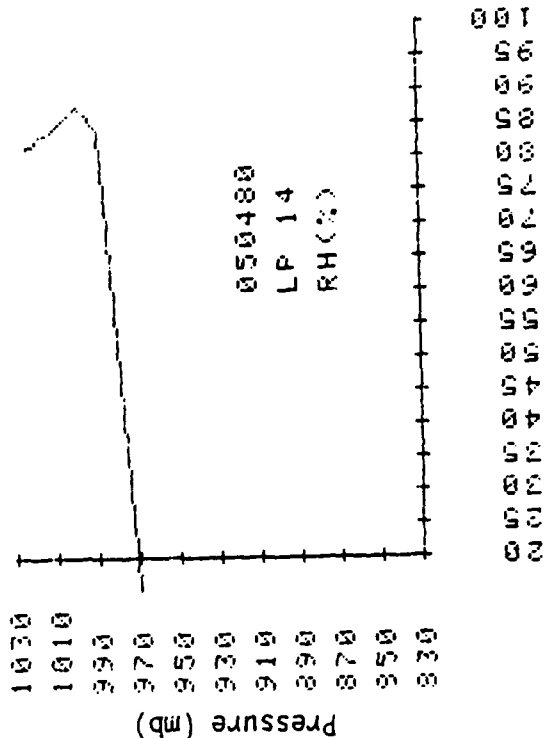
(b) Pressure = 918.3 mb, Relative Humidity = 63.5%

Figure 3-4. Comparison of model predicted extinction coefficients and data (+) at (a) 1023 mb and (b) 918.3 mb pressure levels for: maritime (M), urban (U), rural (R), and tropospheric (T) aerosol models (normalized at $0.53\mu\text{m}$)



Extinction coefficient (km^{-1})

Figure 3-5. Extinction coefficient (km^{-1}) data for ladder profile #14 on 050480. Wavelengths: (a) $0.49\mu\text{m}$, (b) $0.53\mu\text{m}$, (c) $0.63\mu\text{m}$, (d) $0.83\mu\text{m}$, and (e) $1.03\mu\text{m}$.



Relative Humidity (%)

Figure 3-6. Relative humidity (%) profile for ladder profile #14 on 050480.

at wavelengths of 0.83 (Figure 3-7a) and 1.03 μm (Figure 3-7b), the urban, tropospheric, and rural models all underestimate extinction, while the maritime model performs rather well particularly at the lower relative humidities (from 970-990 mb). Examining the comparison from near the bottom of the perceived haze layer (at $p = 1013$ mb) in Figure 3-8, it may be noted that the wavelength dependence of the data and that of the maritime model are more consistent than for the previous data set.

3.2.3 Ladder Profile 23 (LP 23)

The data from LP 23 gathered on 7 May 1980 are interesting due to the presence of a cloud between 1100 and 1400 ft. (approximated 970-980 mb). The transition from clear to cloudy can be seen both in the extinction profile data in Figure 3-9 and the relative humidity profile in Figure 3-10. Note the scale change in Figure 3-9 at 990 mb where extinction changes by an order of magnitude. These data provide an excellent test of the model's ability to treat relative humidity dependent aerosol growth by comparison in the high relative humidity region below the cloud ($p > 990$ mb) and the low relative humidity region above the cloud ($p < 990$ mb). Such a comparison is illustrated in Figure 3-11 for extinction data at 1.03 μm (again note the scale change at 990 mb). The maritime model appears to reproduce the data well above 990 mb, while it overestimates the data near the surface. The other models all underestimate the measured extinction.

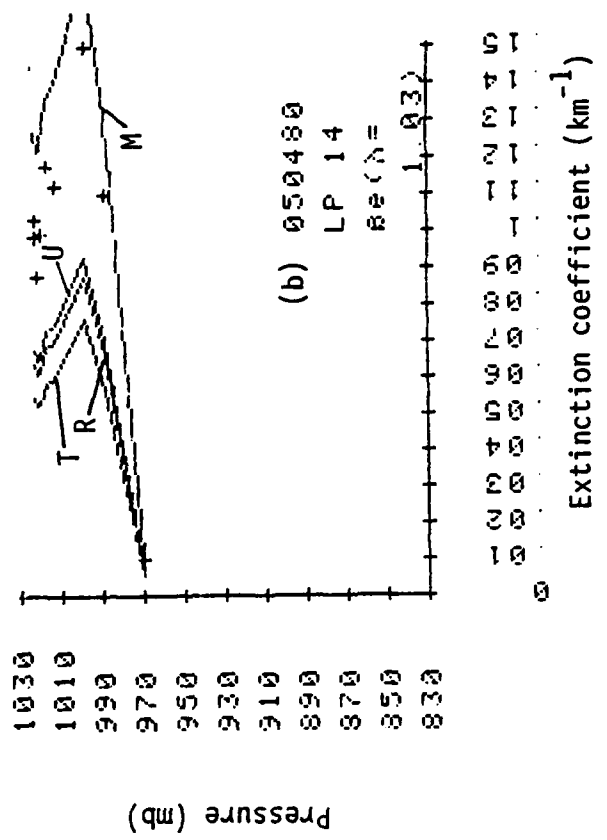
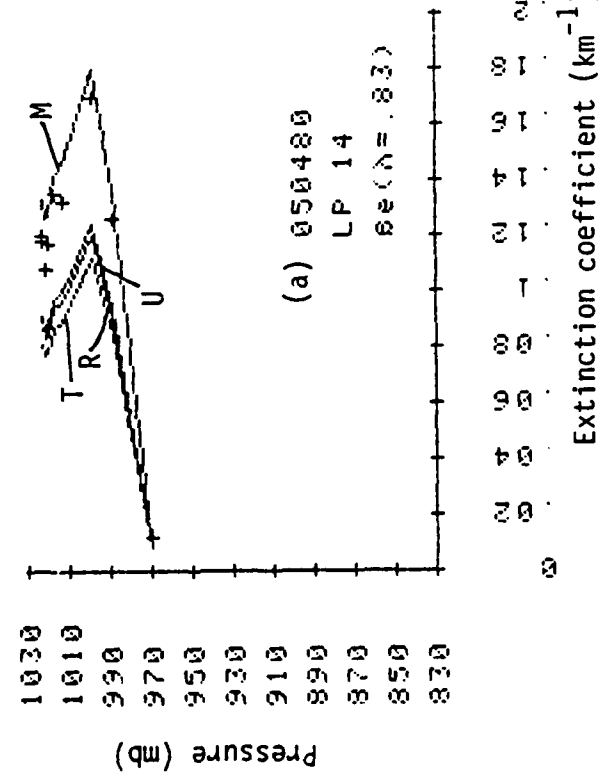


Figure 3-7. Comparison of model predicted extinction coefficient profiles to data(+) at wavelengths of: (a) 0.83 μm and (b) 1.03 μm (normalized at 0.53 μm).

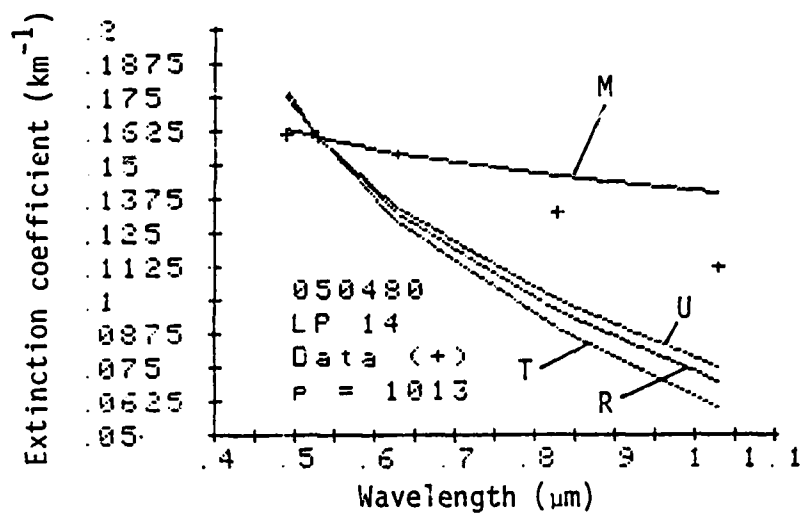


Figure 3-8. Comparison of model predicted extinction coefficient and data(+) at the 1013 mb pressure level for: maritime (M), urban (U), rural (R), and tropospheric (T) aerosol models (normalized at 0.53μm).

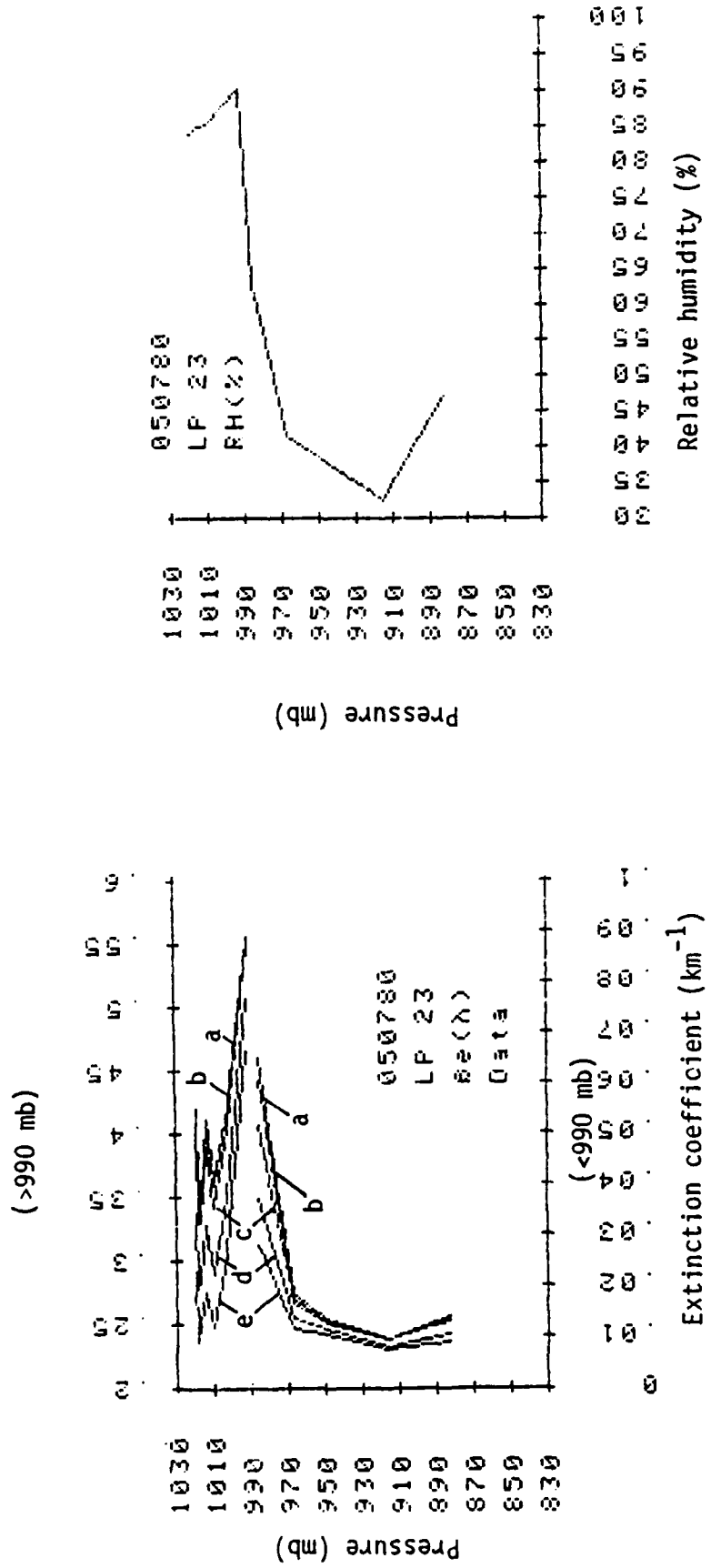


Figure 3-9. Extinction coefficient (km^{-1}) data for ladder profile #23 on 050780. Wavelengths: (a) 0.49 m, (b) 0.53 m, (c) 0.63 m, (d) 0.83 m, and (e) 1.03 m (note scale change at 990 mb).

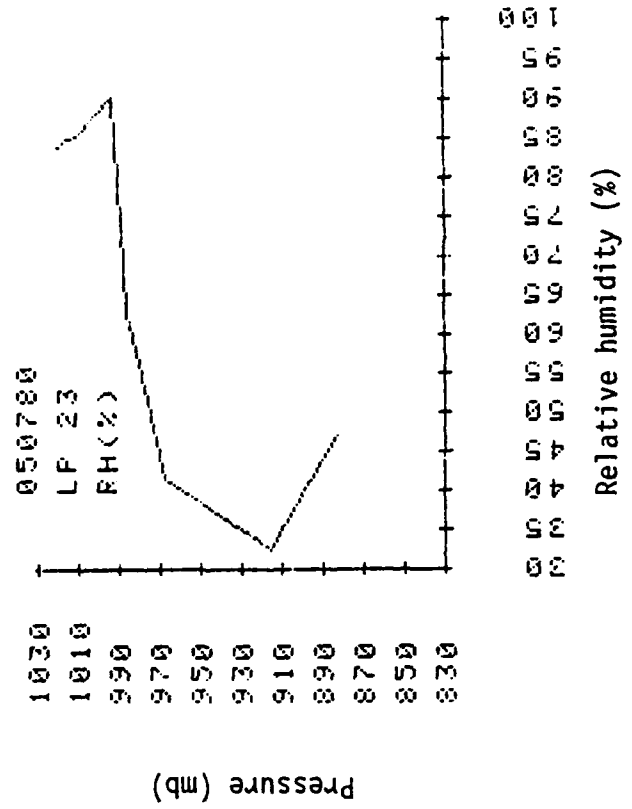


Figure 3-10. Relative humidity (%) profile for ladder profile #23 on 050780.

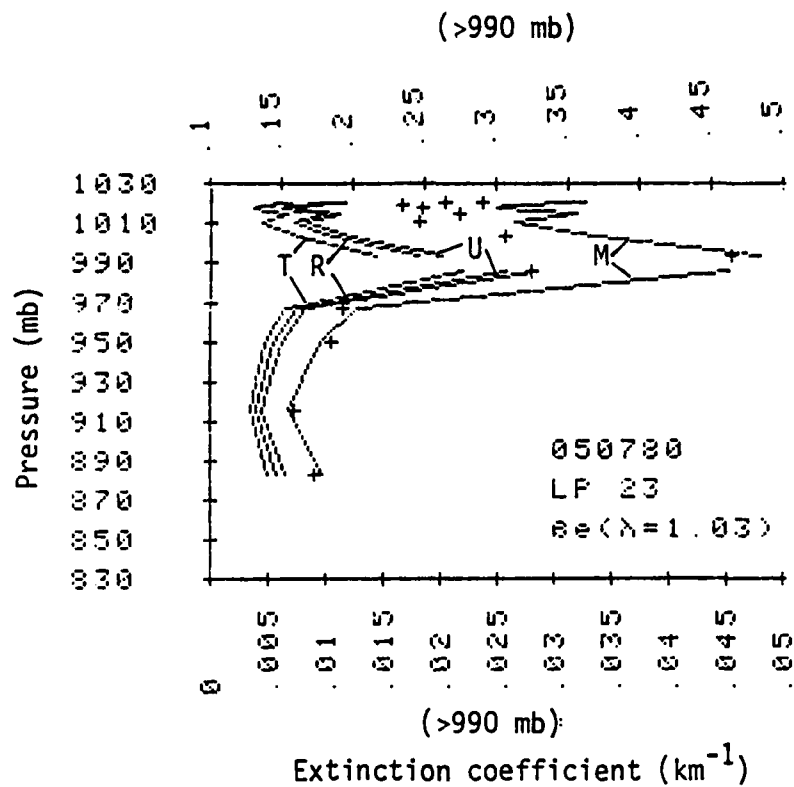
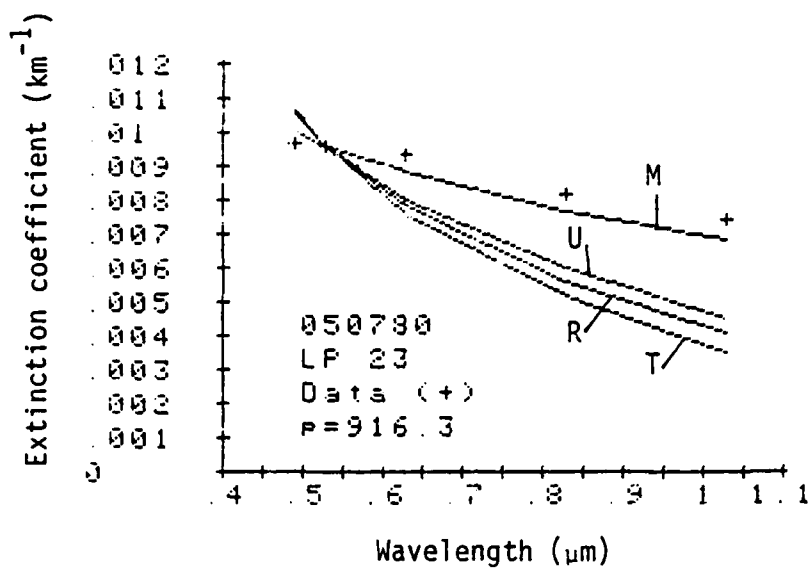


Figure 3-11. Comparison of model predicted extinction coefficient profiles with data(+) at wavelength of $1.03\mu\text{m}$ for: maritime (M), urban (U), rural (R), and tropospheric (T) aerosol models (note scale change at 990mb).

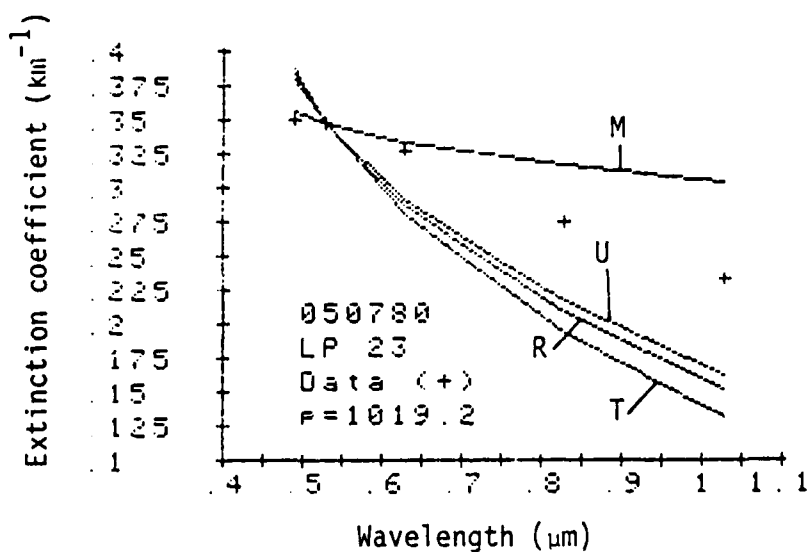
In Figure 3-12 data is compared to the modeled extinction coefficients at one altitude within the low relative humidity region (at $p = 916$ mb, $RH = 33\%$, Figure 3-12a) and one within the high relative humidity region (at $p = 1019$ mb, $RH = 84\%$, Figure 3-12b). The comparison at high relative humidity is like that observed in previous cases. Within the dry layer aloft, the maritime model and data are quite consistent.

3.2.4 Ladder Profile 24 (LP 24)

A final example which also illustrates the effect of cloud is the LP 24 from 7 May 1980. As the extinction coefficient data indicate (Figure 3-13), there is a cloud between about 1200 and 1500 ft. (960-990 mb). In this region, cloud extinction coefficients are uniformly greater than 1.0 km^{-1} and, hence, are off scale in Figure 3-13. Corresponding to this stratus cloud is a region of enhanced relative humidity (Figure 3-14). Near the base of the cloud, the relative humidity approaches saturation. This can be seen in Figure 3-15 where the relative humidity profile is reproduced for a pressure scale expanded in the region below the cloud deck (i.e., $p > 980$ mb). The modeled extinction at $1.03 \mu\text{m}$ wavelength significantly underestimates the data in this region, except for the maritime model which again characteristically overestimates (Figure 3-16). In the drier region above the cloud ($p < 960$ mb), the maritime model fits the data well (Figure 3-17). This behavior is further supported by a comparison of wavelength fitting



(a) Pressure = 916.3 mb, Relative Humidity = 32.5%



(b) Pressure = 1019.2mb, Relative Humidity = 83.9%

Figure 3-12. Comparison of model predicted extinction coefficient and data(+) at: (a) 916mb and (b) 1019.2mb pressure levels for: maritime (M), urban (U), rural (R) and tropospheric (T) aerosol models (normalized at $0.53\mu\text{m}$).

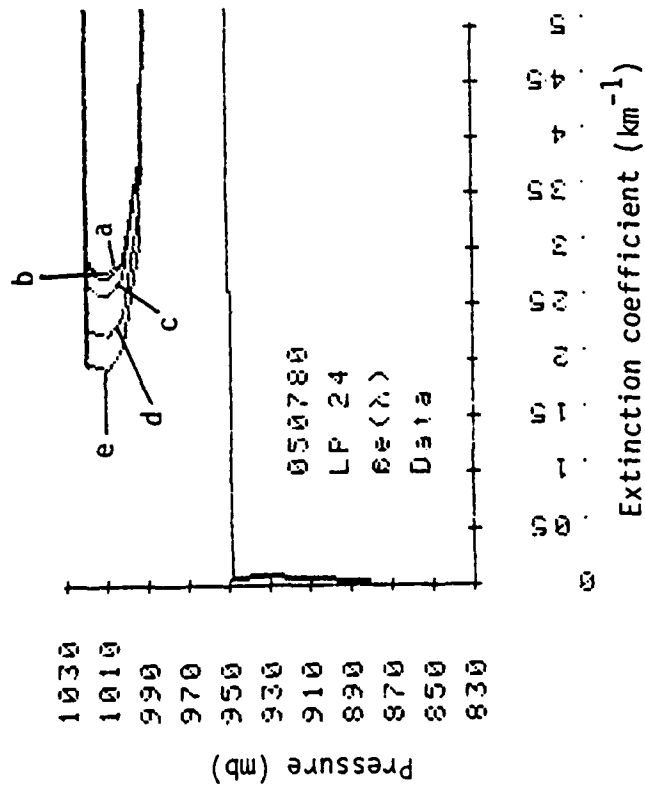


Figure 3-13. Extinction coefficient (km^{-1}) data for ladder profile #24 on 050780. Wavelengths: (a) $0.49\mu\text{m}$, (b) $0.53\mu\text{m}$, (c) $0.63\mu\text{m}$, (d) $0.83\mu\text{m}$, and (e) $1.03\mu\text{m}$

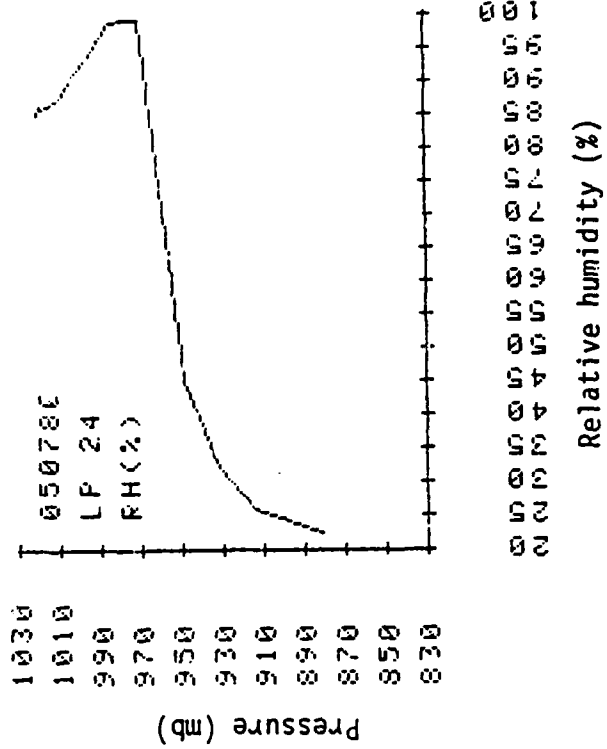


Figure 3-14. Relative humidity (%) profile for ladder profile #24 on 050780.

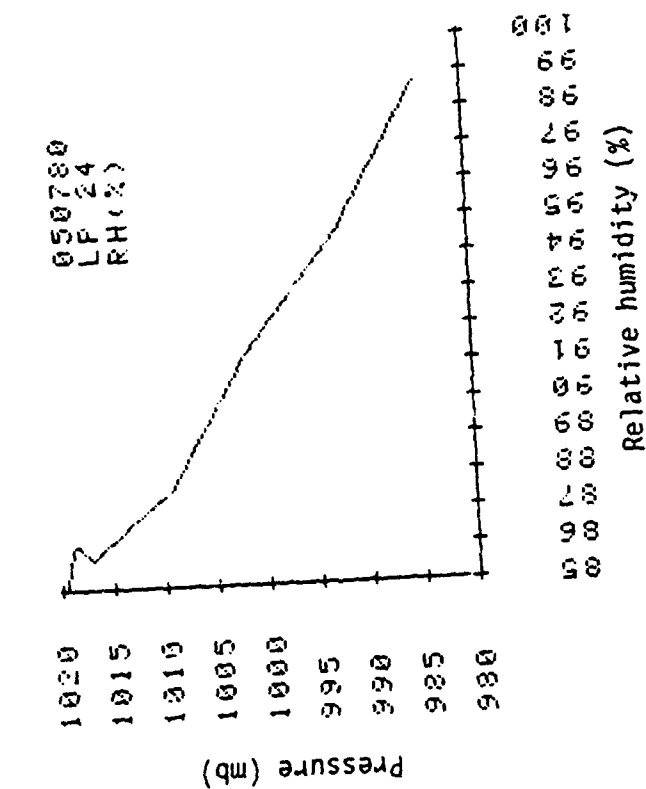


Figure 3-15. Relative humidity (%) profile for ladder profile #24 on 050780. (Expanded scale, high humidity region.)

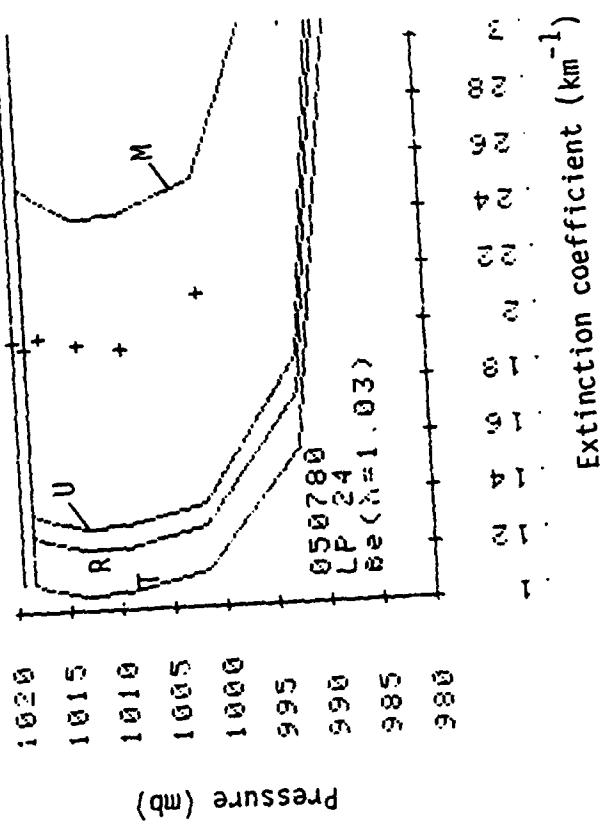


Figure 3-16. Comparison of model predicted extinction coefficient profiles to data(+) at wavelength of 1.03 μm . (High relative humidity region; normalized at 0.53 μm .)

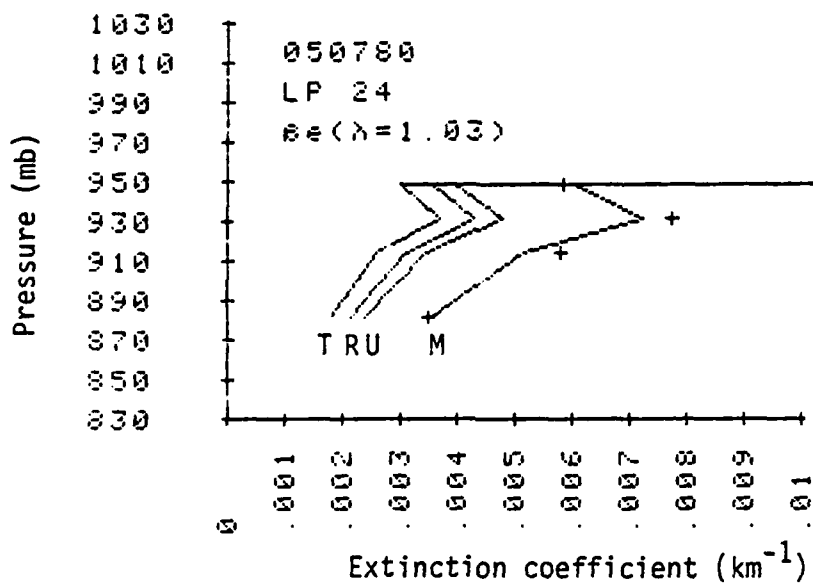
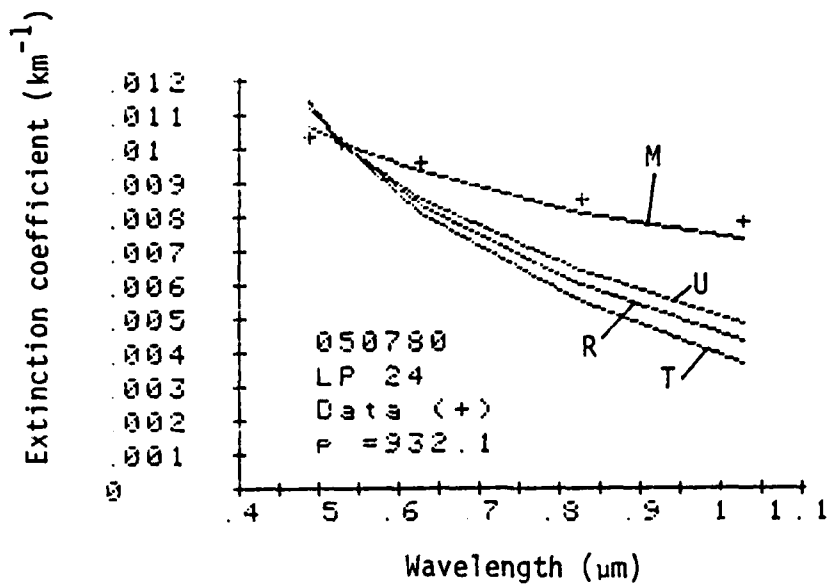
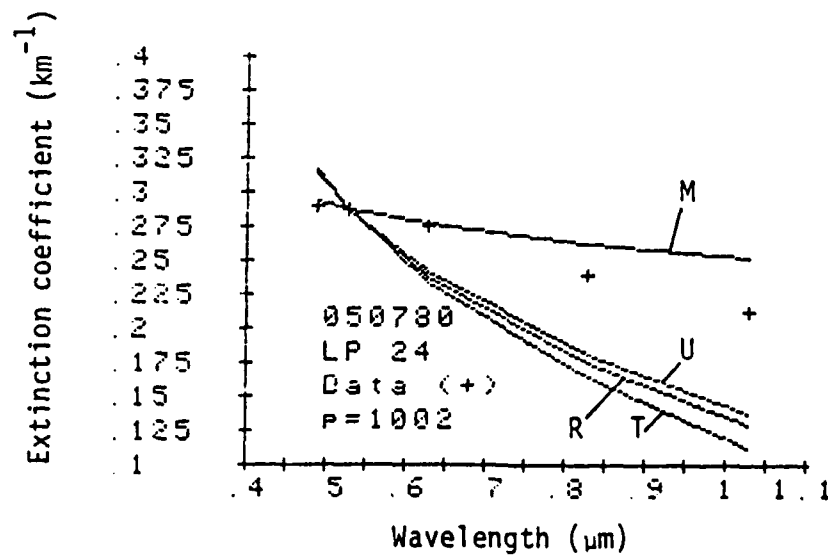


Figure 3-17. Comparison of model predicted extinction coefficient profiles to data(+) at wavelength of $1.03\mu m$. (Low relative humidity region, $RH < 45\%$, normalized at 0.53 m.)



(a) Pressure = 932.1mb, Relative Humidity = 32.1%



(b) Pressure = 1002mb, Relative Humidity = 91.3%

Figure 3-18. Comparison of model predicted extinction coefficient and data(+) at: (a) 932.1mb and (b) 1002mb pressure levels for: maritime (M), urban (U), rural (R), and tropospheric (T) aerosol models (normalized at 0.53 μ m).

in the low RH region above the cloud at $p = 932$ mb and $RH = 32\%$ (Figure 3-18a) to that in the high RH region below the cloud at $p = 1002$ mb and $RH = 91\%$ (Figure 3-18b).

3.3 Discussion

Prediction of wavelength dependent aerosol optical properties (including extinction) based on meteorological input data is the kernel of existing optical propagation and transmission algorithms. Furthermore, as illustrated in Figure 2-1 (and of particular relevance to the current study), it is a key step in the approach to simulating remotely sensed radiances from meteorological input parameters. For this reason, the comparisons of measured and model predicted aerosol extinction discussed above provide valuable insight into the simulation problem.

Based on the relatively small sample of comparisons presented, it is gratifying to see that the maritime aerosol model performs relatively well where expected. It is clear that for the MAGAT data sets examined predictions based on the rural, tropospheric, and urban models are not consistent with the measured extinction in wavelength dependence. This is almost certainly due to their lack of appropriate oceanic origin coarse mode particles.

It is noteworthy, however, that the maritime model also exhibits deficiencies which are manifested in overestimation of extinction at longer wavelengths (as contrasted with underestimation by the other models) particularly at high relative

humidity (e.g., greater than 80%). This may be attributable to either too many particles in the oceanic origin coarse mode or to too large a relative humidity dependent aerosol growth factor (see Figure 4-2b) assumed in the model.

4. CONTINENTAL AEROSOL MODELS

4.1 Non-Maritime Origin Aerosols

While investigating the effect of low level maritime haze in DMSP visible imagery, two oceanic origin aerosol size models were treated: (a) the relative humidity dependent maritime model of Shettle and Fenn (1979), and (b) a hybrid model consisting of a fine mode identical to that of Shettle and Fenn's (1979) tropospheric model and a wind speed dependent, sea spray origin coarse mode adopted from the Munn-Katz model (cf. Wells et al., 1977). The physical, chemical, and optical properties of these aerosol models are described in Sections 4 and 5 of Isaacs (1980) and are implemented within the computer code described in Section 7 of this report.

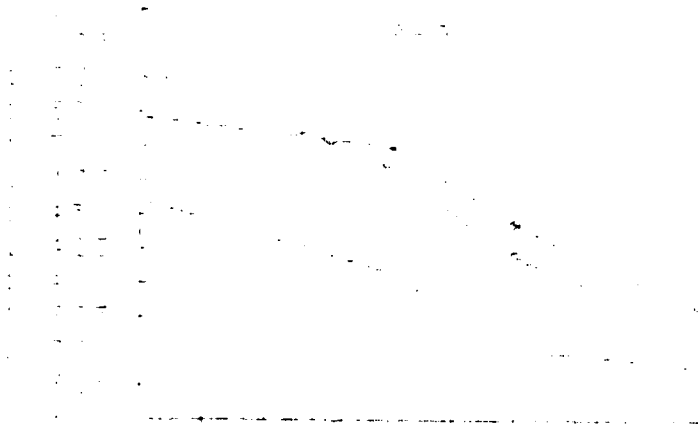
It is notable that regions over the open ocean are often under the influence of air masses of continental origin. This is particularly true of coastal regions. A variety of examples is presented in Fett and Mitchell (1979) illustrating the effect of continental origin dust, smoke, and other atmospheric pollutants on DMSP VHR imagery. These include, for example, scirocco conditions in North Africa and Santa Ana outflows over the Los Angeles bight. Other fugitive dust conditions over the open oceans have been documented (cf., Fraser, 1976; Duce et al., 1980). Recognizing that analysis of imagery in coastal regions is often required in support of tactical naval operations, it seems appropriate to include the capability to treat such continental origin aerosols within the

simulation model. For this purpose, the domain of applicable situations was extended by introducing relative humidity dependent aerosol optical data into the simulation algorithm for both rural and urban aerosol models. The rural and urban aerosol models differ fundamentally from the maritime model both in chemical composition and size distribution: for example, the composition dependent complex index of refraction of each model is quite distinct (see Figure 4-1). In the following sections, the specific optical data implemented for each aerosol model and relevant simulation results based on them are presented. Details of the physical and chemical basis of these models are described in Shettle and Fenn (1979). A review of the theory relating physical aerosol models and their respective optical properties is given in Isaacs (1980).

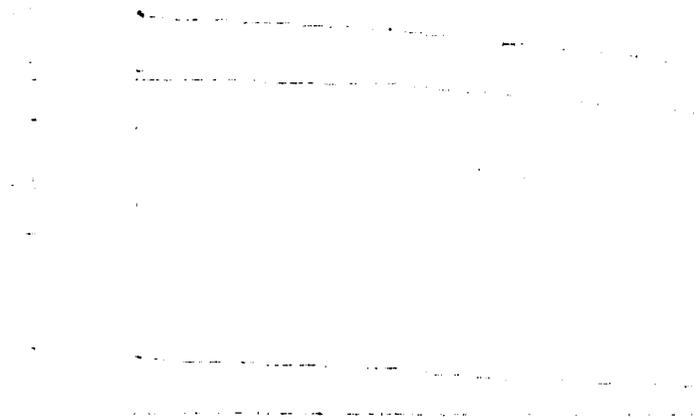
4.2 Rural Aerosol Model

The rural aerosol model adopted from Shettle and Fenn (1979) is described as applicable to situations not directly influenced by urban and/or industrial aerosol sources. Its chemical composition includes both water soluble salts and dust-like components in a bimodal, log normal size distribution. The size distribution is illustrated in Figure 4-2 with relative humidity dependent mode radii in fine and coarse modes given by the growth factors illustrated in Figures 4-3a and 4-3b, respectively.

The relevant wavelength-dependent aerosol optical properties based on the rural model and normalized to a total number density of $1.5 \times 10^4 \text{ cm}^{-3}$ which are incorporated within the simulation model are the: (a) extinction coefficient



(a) Real part of the complex index of refraction vs. relative humidity.



(b) Imaginary part of the complex index of refraction vs. relative humidity.

Figure 4-1. Dependence of the complex index of refraction of maritime (-), urban (o), and rural (+) aerosol models on relative humidity.

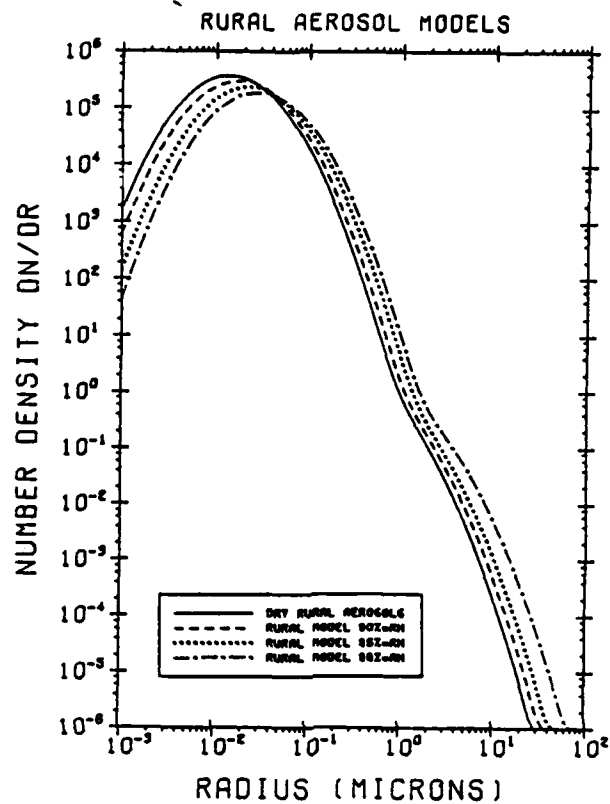
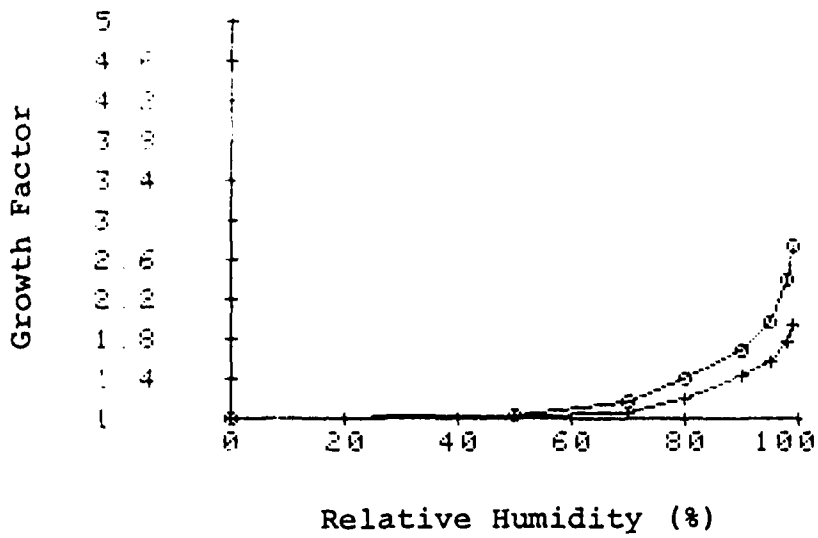
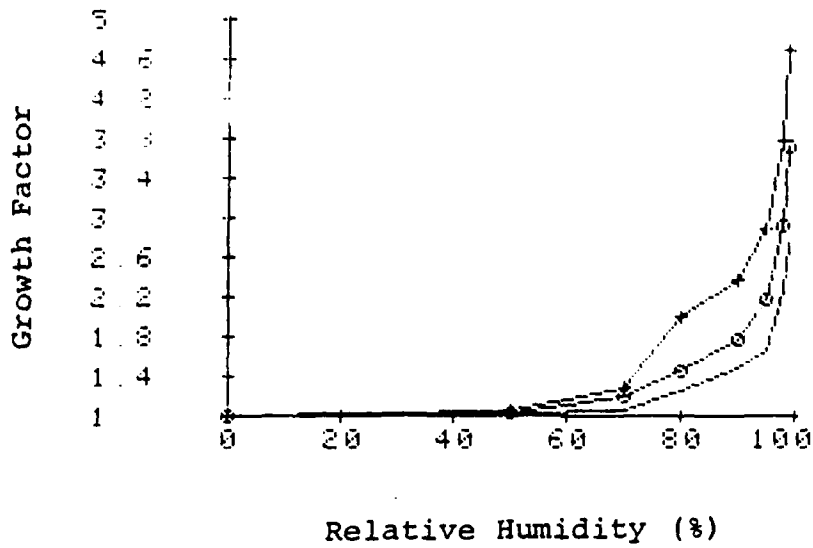


Figure 4-2. Aerosol number distribution ($\text{cm}^{-3} \mu\text{m}^{-1}$) for rural model as a function of relative humidity with $N = 1.5 \times 10^4 \text{ cm}^{-3}$ (from Shettle and Fenn, 1979).



(a) Fine mode growth factors for rural (+) and urban (o) models.



(b) Coarse mode growth factors for rural (-), urban (o), and maritime (+) models.

Figure 4-3. Aerosol model relative humidity growth factors (Shettle and Fenn, 1979).

and (c) phase function asymmetry parameter (Figure 4-4c). These are given as functions of relative humidity for discrete values of 0, 50, 70, 80, 90, 95, 98 and 99%. Employing the simulation model, sensitivity analyses were conducted in analogy to those performed for the oceanic aerosol models in Isaacs (1980).

Figures 4-5a through 4-5d illustrate the wavelength-dependent radiance spectra for relative humidities between 50 and 95% assuming aerosol scale heights of (a) 0.5, (b) 1.0, (c) 1.5, and (d) 2.0 km, respectively. The sun/sensor geometry corresponds to a nadir viewing sensor ($\mu = 1.0$) and a solar zenith angle cosine of $\mu_0 = 0.5$ as in the previous sensitivity studies. The results are qualitatively similar to those obtained for the maritime aerosol model although on closer inspection it is noted (see Figures 4-6a and b) for a given scale height, sensor incident radiances for the rural model (particularly in the near IR spectral region) are much less sensitive to relative humidity. This is primarily due to the larger coarse mode relative humidity growth factor of the maritime model compared to that of the rural model (see Figure 4-3b).

4.3 Urban Aerosol Model

The urban aerosol model considers the modification of aerosol optical properties when combustion products from various anthropogenic and perhaps natural sources introduce soot-like aerosol components.

Figure 4-4a.
 Extinction coefficient
 (km^{-1}) - Rural model
 (from Shettle and
 Fenn, 1979)

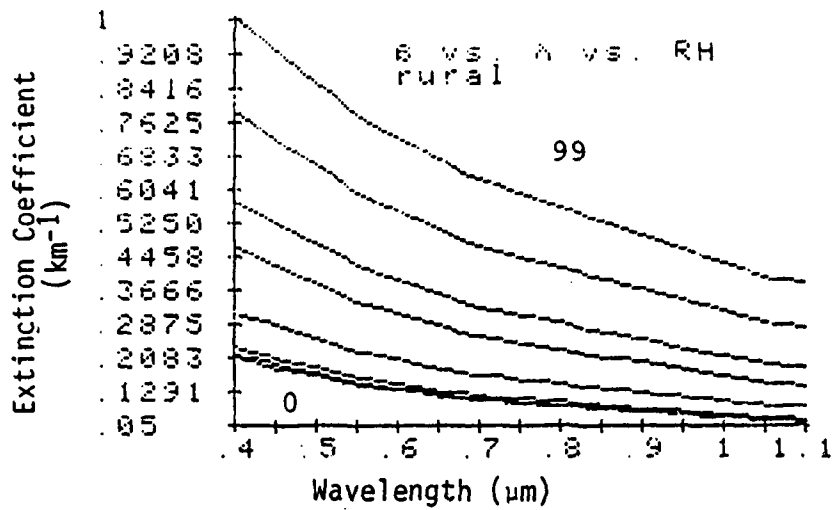


Figure 4-4b.
 Single Scattering
 Albedo - Rural model
 (from Shettle and
 Fenn, 1979)

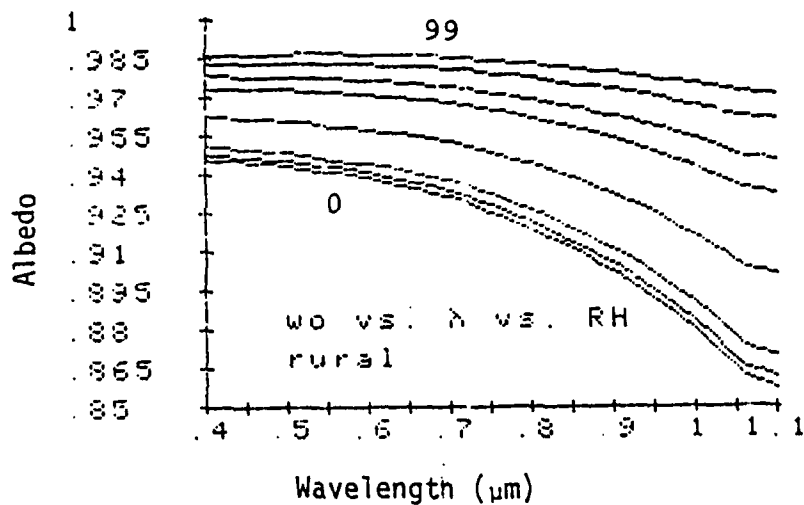
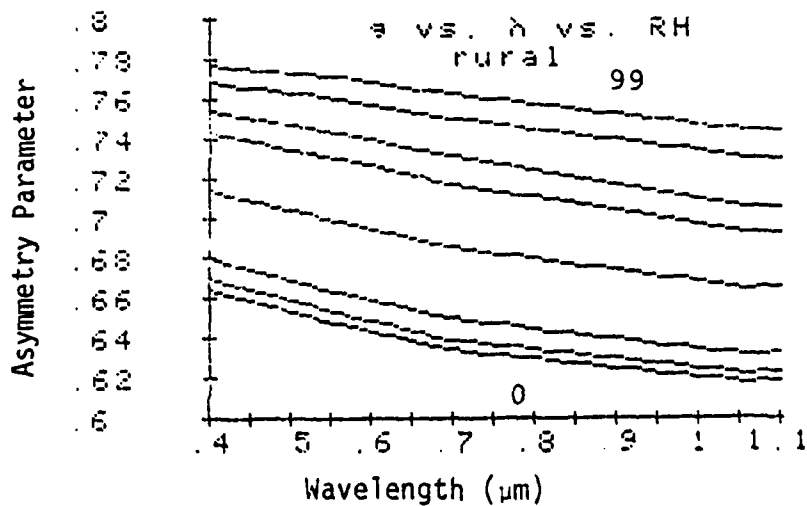


Figure 4-4c.
 Asymmetry Parameter -
 Rural model (from
 Shettle and Fenn,
 1979)



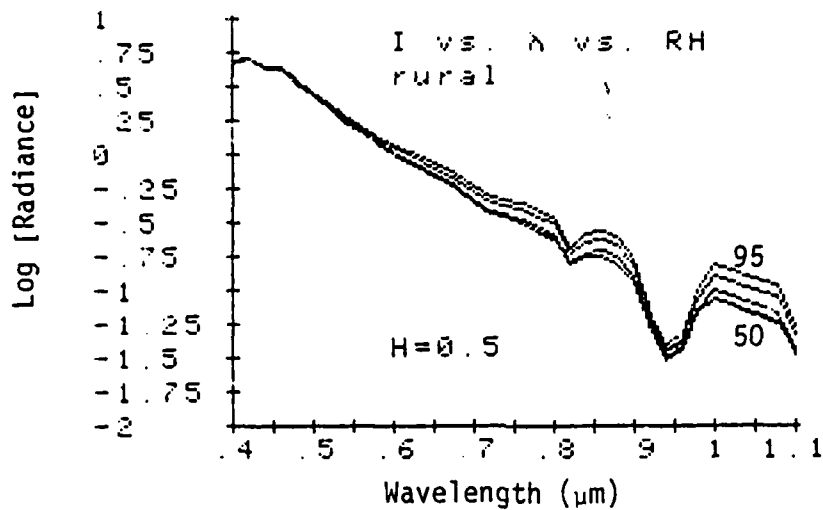


Figure 4-5a. Dependence on Relative Humidity (Rural Model, H = 0.5)

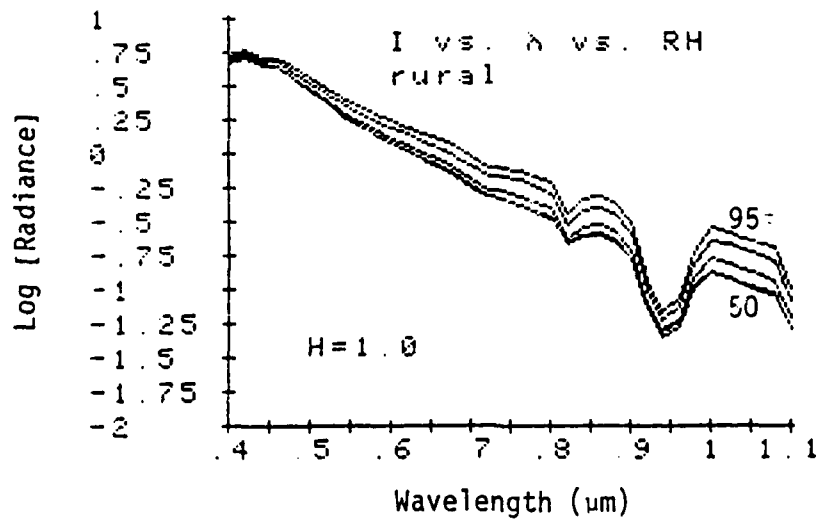


Figure 4-5b. Dependence on Relative Humidity (Rural Model, H = 1.0)

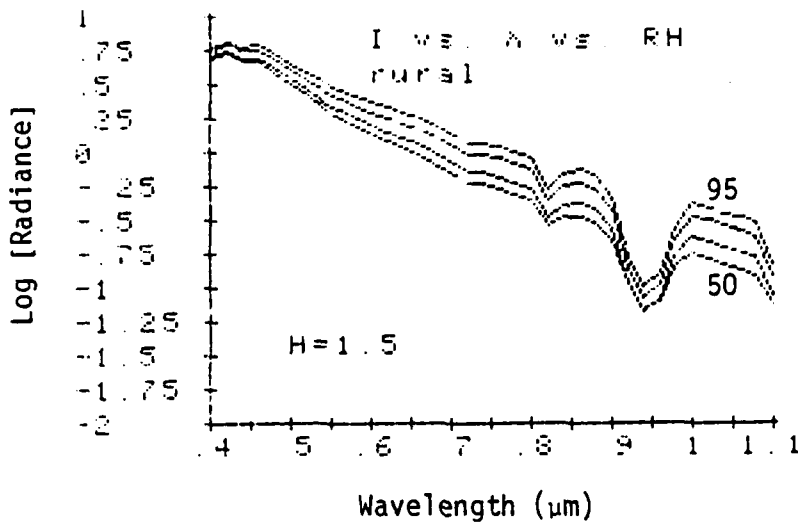


Figure 4-5c. Dependence on Relative Humidity
(Rural Model, H = 1.5)

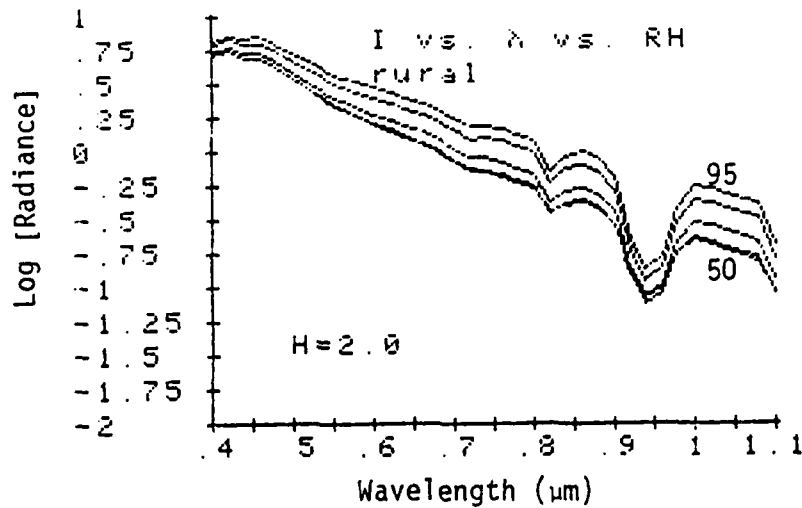


Figure 4-5d. Dependence on Relative Humidity
(Rural Model, H = 2.0)

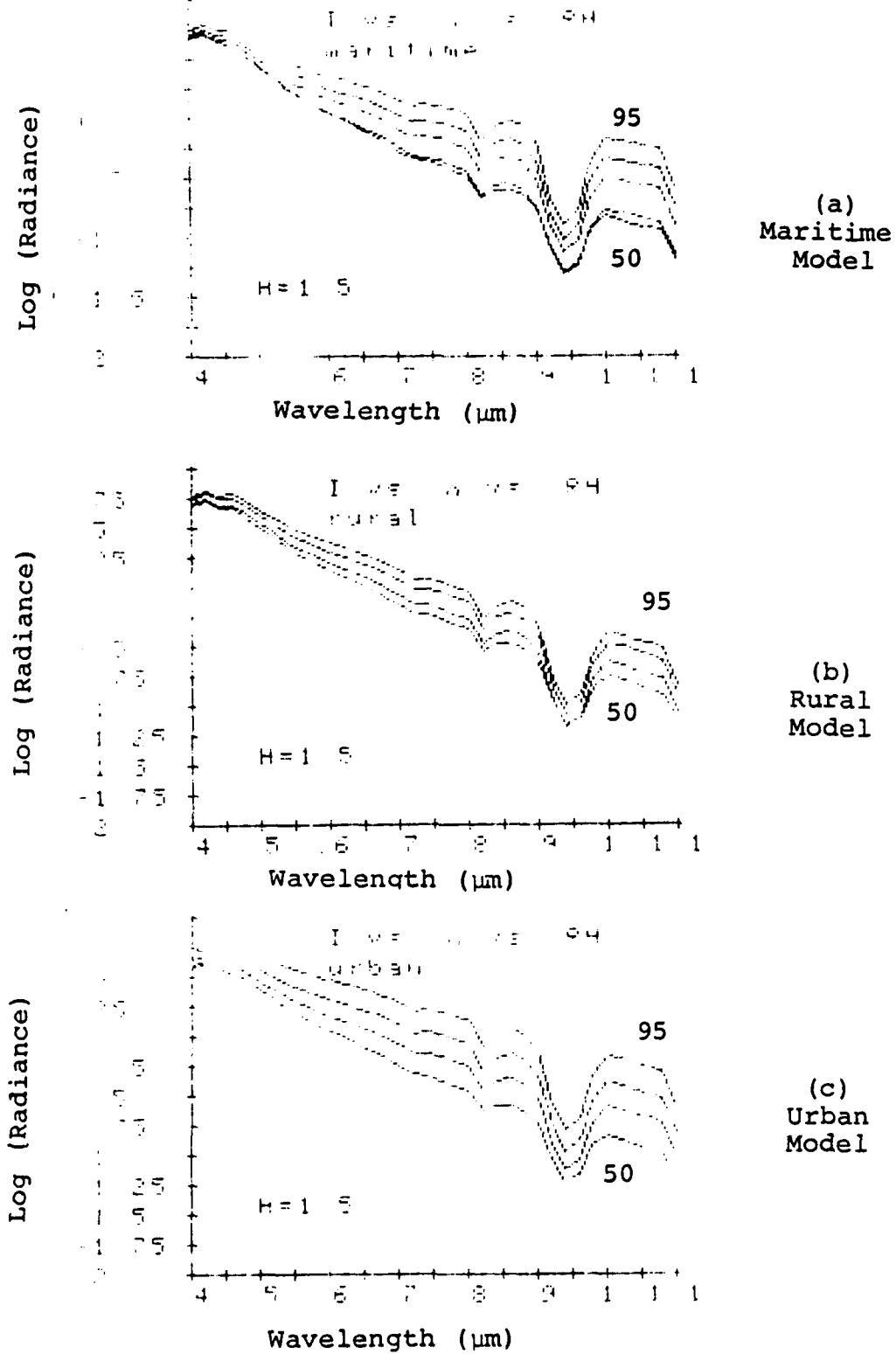


Figure 4-6. Comparison of radiance spectra for (a) maritime, (b) rural, and (c) urban aerosol models as functions of relative humidity (50 to 95%) for $H = 1.5$ km, $\mu = 1.0$, and $\mu_0 = 0.5$.

Its size distribution is assumed identical to that of the rural model, however, the total number density is $2.0 \times 10^4 \text{ cm}^{-3}$ (one third higher than that of the rural model and five times higher than the maritime model). But for the number density difference, the distinguishing characteristic of the urban model is chemical, i.e., the presence of carbon. Notably, recent studies suggest that soot-like aerosol components are quite pervasive in the atmosphere (cf. Rosen et al., 1981) and thus, the optical properties of the urban aerosol model may be appropriate over regions hitherto assumed remote from urban influence.

As a consequence of its soot component, two important effects are noted. As indicated in Figure 4-3, the relative humidity growth factor for both the fine (Figure 4-3a) and coarse (Figure 4-3b) modes are distinct from the other models considered. This is due to the dependence of aerosol growth on chemical composition. Secondly, carbon is quite absorbing (Bergstrom, 1973). This can be seen by examining the extinction coefficient and single scattering albedo at low relative humidities in Figures 4-7a and 4-7b, respectively. (The implemented optical properties of the urban model are given in Figures 4-7a,b,c, respectively.) Such high absorption suggests a potential adverse impact on optical transmission.

The sensitivity analyses performed on scale height and relative humidity for a nadir viewing sensor ($\mu = 1.0$) and solar zenith angle cosine of ($\mu_0 = 0.5$) are illustrated in Figure 4-3 for scale heights of: (a) 0.5, (b) 1.0, (c) 1.5,

Figure 4-7a.
 Extinction coefficient
 (km^{-1}) - Urban model
 (from Shettle and
 Fenn, 1979)

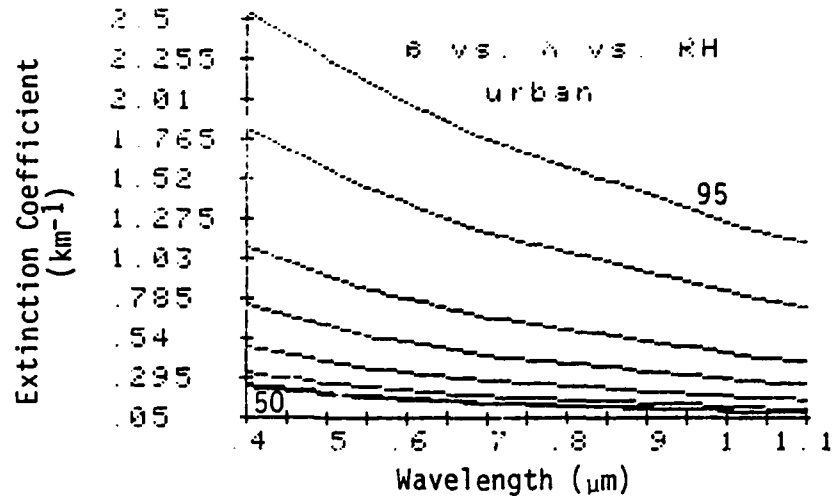


Figure 4-7b.
 Single scattering
 albedo - Urban model
 (from Shettle and
 Fenn, 1979)

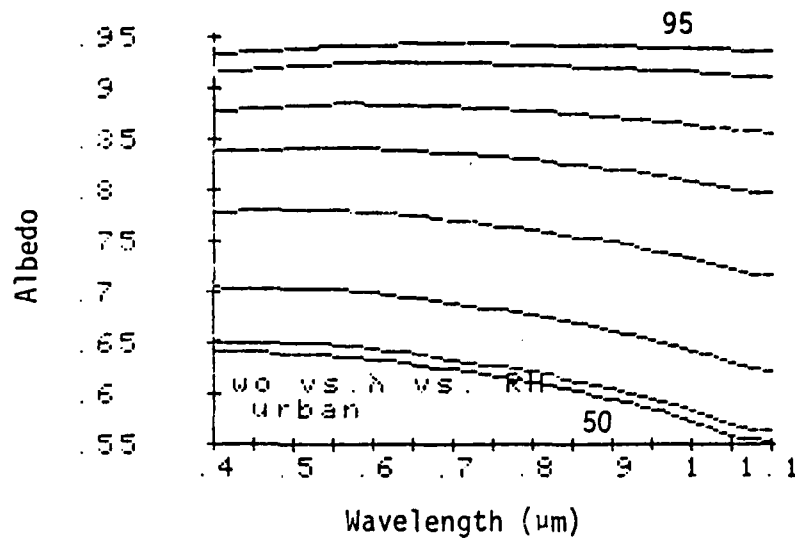
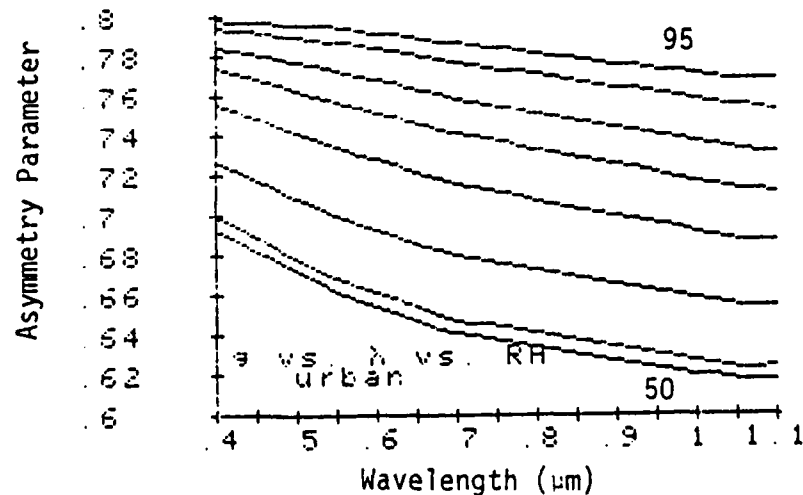


Figure 4-7c.
 Asymmetry parameter
 Urban model (from
 Shettle and Fenn,
 1979)



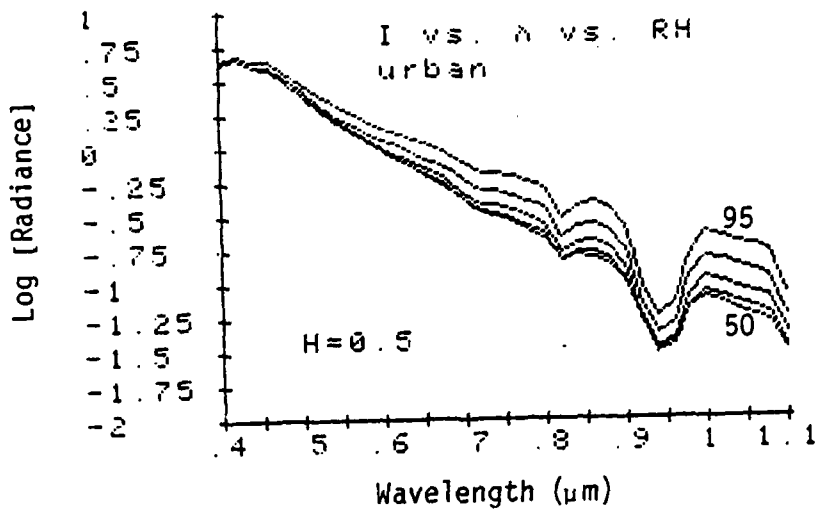


Figure 4-8a. Dependence on Relative Humidity (Urban Model, H = 0.5)

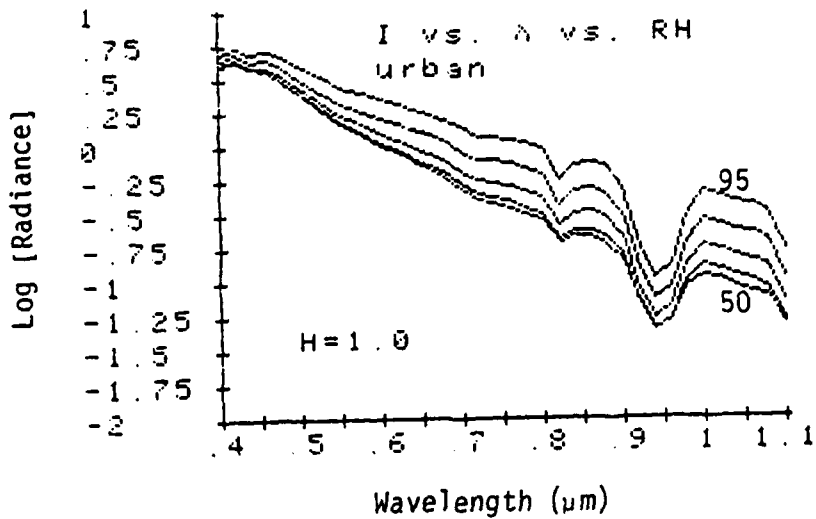


Figure 4-8b. Dependence on Relative Humidity (Urban Model, H = 1.0)

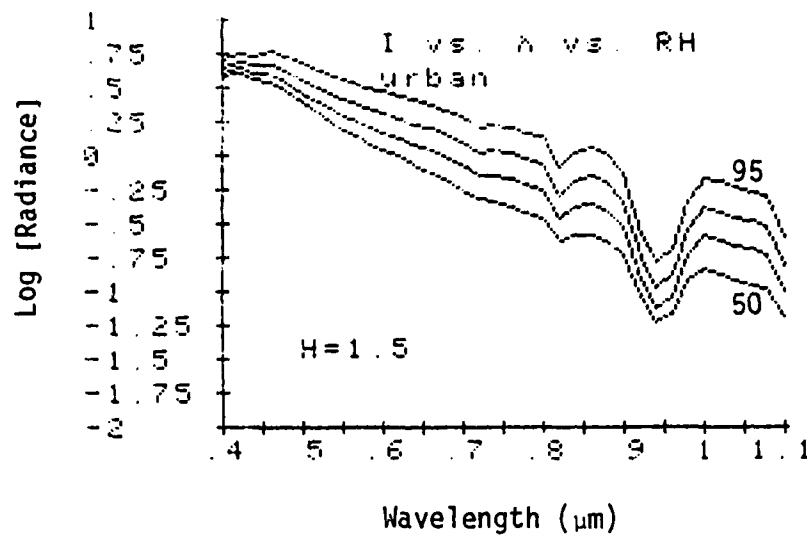


Figure 4-8c. Dependence on Relative Humidity (Urban Model, H = 1.5)

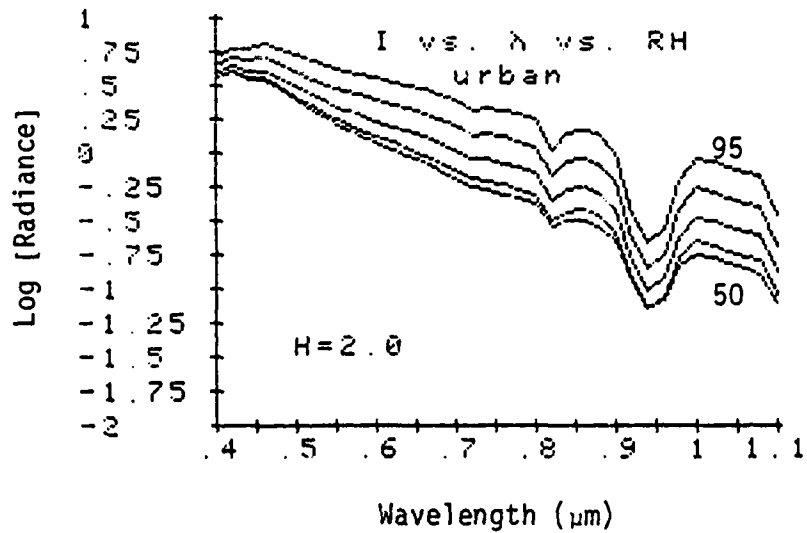


Figure 4-8d. Dependence on Relative Humidity (Urban Model, H = 2.0)

and (d) 2.0 km, respectively. Results show wavelength dependent radiance spectra for relative humidities of 50, 70, 80, 90 and 95%. Qualitatively, they are not remarkably different from those for the maritime and rural models. Inspection of Figure 4-6, however, suggests a few notable distinctions. The relative humidity dependence of the urban aerosol fine and coarse model growth factors is somewhat higher than that of the rural model although it is not as large as that of the maritime model (see Figures 4-3a,b). Nevertheless, in the resultant radiance calculation, it is apparent that radiance spectra sensitivity to increases in relative humidity given the urban aerosol (Figure 4-6c) are much closer to those of the maritime aerosol (Figure 4-6a) than are those for the rural aerosol model (Figure 4-6b). This is true both in the visible and near IR regions. As a consequence of the presence of absorbing carbon, however, radiance spectrum levels in the visible at low relative humidities (i.e., 50%) are appreciably lower when backscattered from the urban atmosphere. At higher relative humidities, single scattering albedos increase due to the additional water volume of the aerosol and the effect is not as drastic. It can be seen, however, in Figure 4-9 which directly compares radiance spectra for the four adopted aerosol models.

4.4 Aerosol Model Intercomparisons.

The distinct wavelength and relative humidity dependent optical properties of the hybrid, maritime, rural and urban

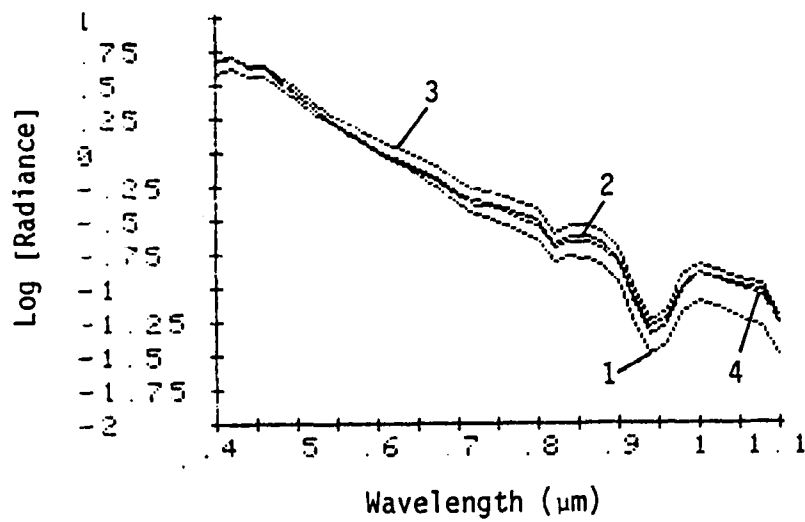


Figure 4-9. Simulated Radiances for: (1) hybrid, (2) maritime, (3) rural, and (4) urban₁ aerosol models. [RH = 50%, WS = 5 ms⁻¹, H1 = 1.2, H2 = 0.8, μ = 1.0, μ₀ = 0.5, Δφ = 0]

aerosol models are manifested in their respective radiance spectra signatures when viewed over the ocean surface. In the previous comparisons, the degree of sensitivity to increases in relative humidity has been noted. This section compares the wavelength dependence of the various aerosol models discussed above. Radiance spectra are presented for a relative humidity of 50% and fixed scale height of 1.2 km for the fine mode of the hybrid model and both modes of other models. For the hybrid model a scale height of 0.8 km is assumed for the coarse mode and a wind speed of 5 ms^{-1} is used to evaluate the loading in this size range. Table 4-1 presents the number densities and corresponding visual ranges represented by each curve in Figure 4-9.

A number of observations can be made based on this aerosol model intercomparison. Given the variety of aerosol chemical and size distribution models and the range of number densities and visual ranges indicated, the radiance spectra in Figure 4-9 are remarkably similar. Although it might be expected that at a given wavelength the radiance would be proportional to loading (i.e., total number density), this is not so for a variety of reasons. In the visible, for example, although the urban model has the largest particle density, its radiance is lowest of the four models due to absorption. The highest radiance is from backscattering from the model with the next largest loading, the rural model. In the near IR, the number of larger particles (i.e., in the coarse mode) determines to a great extent the backscattered radiance. As

Model	Total Number Density (cm^{-3})	Visual Range (km)
hybrid	5.0×10^3	59.4
maritime	4.0×10^3	39.6
rural	1.5×10^4	23.9
urban	2.0×10^4	19.9

Table 4-1. Number densities (cm^{-3}) and visual ranges corresponding to aerosol models (1-4) in Figure 4-8.

Figure 4-9 indicates, the hybrid model is predicted to have the smallest number of coarse mode particles which is, in fact, the case. As the discussion suggests, much information concerning the properties of the ambient aerosol is potentially available in the wavelength dependent radiance spectra. This additional information content is essentially destroyed when integrated by a broad band sensor such as DMSP.

•
P
P
•
P
•
•
•
•

5. SUN/SENSOR GEOMETRY FOR DATA SIMULATION APPLICATIONS

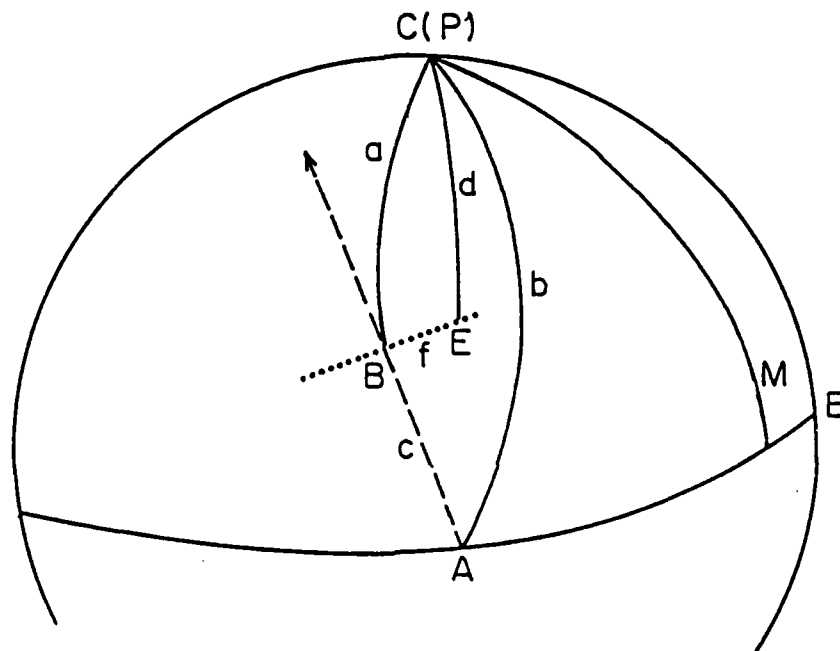
Previous sensitivity analyses results based on the simulation model were evaluated for a fixed generic sun/sensor geometry (cf. Isaacs, 1980). For the purpose of providing an applications oriented analysis tool, however, the present study focuses on program modifications which directly model the sun/sensor geometry characteristic of specific polar-orbiting satellite platforms (such as DMSP). Thus given basic information regarding the orbital parameters of the satellite and the desired time (since the imagery is annotated in GMT time), a method is sought to both locate (i.e. latitude/longitude) specific surface elements (pixels) along the sensor scan line perpendicular to the satellite subpoint track and to provide information regarding the solar and sensor positions relative to each of the individual pixels. These relative solar and sensor positions are then used as the basis of the radiative transfer calculations to follow.

The problem is simplified considerably if the satellite subtrack is assumed to be a great circle. In this case concepts from spherical trigonometry may be applied to both subtrack and scan line location calculations. As discussed in Tsui and Fett (1980), who used the same approach in locating the primary specular point (PSP), the magnitude of the errors introduced by adopting this assumption should be acceptable

for practical purposes, especially in light of other sources of error. The calculation may be divided into three fundamental steps: (1) location of the satellite subtrack position for a given time, (2) specification of the sensor scan line pixels (with arbitrary density along the scan line) corresponding to that time, and (3) calculation (for each pixel) of the spherical coordinates (relative to a fixed coordinate system) determining the local sun and sensor positions. These calculations are discussed in the following sections with reference to Figure 5-1 which illustrates the satellite subtrack (AB) and sensor scan line (BE) geometry for a generic polar orbiting satellite with ascending node A. Indicated are the positions of the pole, C(P), equator (E), and prime meridian (M).

5.1 Satellite Subtrack Position

Assuming the satellite subtrack (SST) in Figure 5-1 (arc AB) to be a great circle, the position in latitude (θ_s) and longitude (ϕ_s) of point B at time t_1 can be calculated given the time, t_0 , and longitude, ϕ_0 , of the ascending node (crossing of the equator, point A) provided an orbital period, p , and inclination of the orbit to the equatorial plane, ϵ , are assumed. For DMSP, a nominal circular orbit (although rarely achieved in practice) would be characterized by a period of 101.35m (or 1.6982h), an orbital inclination



--- Satellite Subpoint Track
 Sensor Scan Line

Figure 5-1. Scan line generation geometry based on nominal satellite parameters.

of 98.7° (making it sun synchronous), and an altitude of 833km.

Referring to the figure, the length of side C (in degrees) will be:

$$C = 360(t_1 - t_0)/p \quad (5-1)$$

The angle at A is determined by the orbital inclination or

$$A = \epsilon - 90 = 8.7^\circ \quad (5-2)$$

The arc length (in degrees) from point A (on the equator) to the pole C(p) is side b, clearly:

$$b = 90^\circ \quad (5-3)$$

The latitude of the subsatellite point at t_1 will be given by side a:

$$\theta_s = 90 - a \quad (5-4)$$

while the longitude will depend on the angle at point C(p) or:

$$\phi_s = \phi_0 + C + (t_1 - t_0)15 \quad (5-5)$$

(The final term above accounts for the earth's rotation at a rate of $15^\circ h^{-1}$ during the time interval from t_0 to t_1). Solution for the unknown quantities (a and C, above) is based on Napier's analogies for a spherical triangle (Selby, 1967; p. 223):

$$a = 2 \tan^{-1} [h(b,c,B,C)] \quad (5-6)$$

$$C = \tan^{-1} [f(b,c,A)] - \tan^{-1} [g(b,c,A)] \quad (5-7)$$

where:

$$B = \tan^{-1} [f(b,c,A)] + \tan^{-1} [g(b,c,A)] \quad (5-8)$$

and the functions f , g , and h are given by:

$$f(b,c,A) = \tan \frac{1}{2} (B+C) = \cos \frac{1}{2} (b-c) \sec \frac{1}{2} (b+c) \cot \frac{1}{2} A \quad (5-9)$$

$$g(b,c,A) = \tan \frac{1}{2} (B-C) = \sin \frac{1}{2} (b-c) \csc \frac{1}{2} (b+c) \cot \frac{1}{2} A \quad (5-10)$$

$$h(b,c,B,C) = \tan \frac{1}{2} a = \tan \frac{1}{2} (b-c) \sin \frac{1}{2} (B+C) \csc \frac{1}{2} (B-C) \quad (5-11)$$

Upon substitution of the known quantities c (5-1), A (5-2), and b (5-3) into (5-8) through (5-11), the unknowns a (5-6) and C (5-7) can be evaluated. Equations (5-4) and (5-5) then yield the desired satellite subtrack point latitude and longitude, respectively. Sample satellite subpoint track latitude/longitude calculated as a function of time using the procedure described above are presented in Table 5-1.

5.2 Sensor Scan Line Position

Applying similar considerations, the location of specific surface elements along a sensor scan line can be evaluated.

Table 5-1

SATELLITE SUBPOINT TRACK LATITUDE AND LONGITUDE
FOR DMSP SATELLITE IMAGE FOR 22 AUGUST 1978

Input Data: $\phi_0 = 113.5W$
 $t_0 = 18.92$ GMT

Time	Latitude/Longitude	Time	Latitude/Longitude
185827	10.3/115.8	190427	31.3/121.1
185927	13.8/116.6	190527	34.8/122.1
190027	17.3/117.5	190627	38.3/123.2
190127	20.8/118.3	190727	41.8/124.3
190227	24.3/119.2	190827	45.3/125.6
190327	27.8/120.1	190927	48.7/127.0

Table 5-2

SCANLINE PIXEL LOCATIONS CORRESPONDING TO
SUBTRACK POINT AT 185827 GMT

Pixel	Latitude/Longitude	Pixel	Latitude/Longitude
1	10.3/115.8	11	11.2/109.1
2	10.4/115.2	12	11.3/108.5
3	10.5/114.5	13	11.4/107.8
4	10.6/113.8	14	11.5/107.1
5	10.7/113.2	15	11.6/106.4
6	10.8/112.5	16	11.6/105.8
7	10.9/111.8	17	11.7/105.1
8	11.0/111.1	18	11.8/104.4
9	11.1/110.5	19	11.9/103.7
10	11.1/109.8	20	11.9/103.1
		21	12.0/102.4

It is assumed that the location and time (θ_s, ϕ_s, t_s) of the subtrack point (B in Figure 5-1) associated with the desired sensor scan line are known based on the procedure described in the previous section and that the scan line including point B (i.e. arc BE) is also a great circle perpendicular to the subpoint track. Considering spherical triangle BEC(P), the length of side A (deg) from (5-4) is:

$$a = 90 - \theta_s \quad (5-12)$$

The angle at B is determined by the orbital inclination and thus from the figure:

$$B = 81.3^\circ \quad (5-13)$$

The length of the scan line (in degrees), side f, is determined from the length of the scan from subpoint to horizon (1479km) and the earth's radius, R_E (6370km):

$$\begin{aligned} f &= 360(1479)/2\pi(6370) \\ &= 13.303^\circ \end{aligned} \quad (5-14)$$

The i th surface element pixel is chosen such that the length of the arc from the subpoint B to the pixel is given by:

$$f_i \text{ (deg)} = \frac{(i-1)}{n} 13.303 \quad (5-15)$$

for $i = 1$ to $n+1$. Thus, the first pixel ($i = 1$) corresponds to the subtrack point (B) and the last pixel ($n+1$) corresponds to the point on the easterly horizon (E). The

latitude of the i th pixel along the scan line will be:

$$\theta_i (\text{deg}) = 90 - d_i \quad (5-16)$$

and the corresponding longitude will be:

$$\phi_i (\text{deg}) = \phi_s - C_i \quad (5-17)$$

Again using Napier's analogies to solve:

$$d_i = 2 \tan^{-1} [h(a, f_i, E, C_i)] \quad (5-18)$$

$$C_i = \tan^{-1} [f(a, f_i, B)] - \tan^{-1} [g(a, f_i, B)] \quad (5-19)$$

where:

$$E_i = \tan^{-1} [f(a, f_i, B)] + \tan^{-1} [g(a, f_i, B)] \quad (5-20)$$

and the functions f , g , and h are given by:

$$\begin{aligned} f(a, f_i, B) &= \tan \frac{1}{2} (E_i + C_i) \\ &= \cos \frac{1}{2} (a - f_i) \sec \frac{1}{2} (a + f_i) \cot \frac{1}{2} B \end{aligned} \quad (5-21)$$

$$\begin{aligned} g(a, f_i, B) &= \tan \frac{1}{2} (E_i - C_i) \\ &= \sin \frac{1}{2} (a - f_i) \csc \frac{1}{2} (a + f_i) \cot \frac{1}{2} B \end{aligned} \quad (5-22)$$

$$\begin{aligned} h(a, f_i, E_i, C_i) &= \tan \frac{1}{2} d \\ &= \tan \frac{1}{2} (a - f_i) \sin \frac{1}{2} (E_i + C_i) \csc \frac{1}{2} (E_i - C_i) \end{aligned} \quad (5-23)$$

Substitution of (5-18) through (5-23) into (5-16) and (5-17) yield pixel latitude and longitude. Calculations for the scan line beginning at the subtrack point corresponding

to 185827 GMT in Table 5-1 and considering 21 equally spaced pixels are given in Table 5-2.

5.3 Pixel-related Sun/Sensor Geometry

Evaluation of pixel location (θ_i, ϕ_i) using the procedures outlined in the previous sections provides the necessary data to calculate the solar zenith angle, θ_o^i , sensor zenith angle, θ_R^i , and azimuth angle difference, $\Delta\phi_i$, relative to each pixel location. These sun/sensor geometric parameters are required as input to the radiative transfer calculation performed in the simulation and additionally specify the sun and sensor position vectors (\hat{s} , \hat{o} , respectively; see Figure 7-1, Section 7.3) used in the surface reflection model.

The solar zenith angle at the i th pixel, θ_o^i , and its associated zenith angle cosine, $\mu_o^i = \cos\theta_o^i$ are given by:

$$\theta_o^i = \cos^{-1}[\mu_o^i] = 90 - \sin^{-1}[\sin\theta_i \sin\delta + \cos\theta_i \cos\delta \cos\eta_i] \quad (5-24)$$

where δ is the solar declination angle and η_i is the hour angle (deg) given approximately by the difference between the pixel longitude (ϕ_i) and the longitude (ϕ_{SSP}) of the subsolar point (SSP), i.e.:[†]

$$\eta_i = \phi_i - \phi_{SSP} \quad (5-25)$$

[†]For morning satellites, η_i will generally be positive; that is the scan line pixels will be at earlier solar times than the SSP.

The solar declination angle, δ , is a function of the date (zero at the equinoxes and $\pm 23^\circ 27'$ at the solstices) and may be obtained from a solar ephemeris. It is given approximately by the equation:

$$\delta(d) = \sin^{-1}\{.3978 \sin[.9863(d-80)]\} \quad (5-26)$$

where d is the Julian day of the year (i.e. January 1 is 001 and December 31 is 365).

The solar azimuth angle, α_i (the azimuth of the sun measured clockwise from north, see Figure 7-1), at pixel location (θ_i, ϕ_i) is given by:

$$\begin{aligned} \alpha_i &= \cos^{-1}(1-2q_5) && \text{for } \eta_i > 0 \quad (\text{morning}) \\ &360 - \cos^{-1}(1-2q_5) && \eta_i < 0 \quad (\text{afternoon}) \end{aligned} \quad (5-27)$$

where:

$$q_5 = \frac{\sin(q_4 - q_2) \sin(q_4 - q_1)}{\sin q_2 \sin q_1}$$

$$q_4 = (q_1 + q_2 + q_3)/2$$

and: $q_1 = 90 - \theta_i$

$$q_2 = \theta_o$$

$$q_3 = 90 - \delta$$

Since the sensor azimuth looking eastward is fixed at 261.3° , the azimuth angle difference is:

$$\Delta\phi_i = 261.3 - \alpha_i \quad (5-28)$$

The satellite zenith angle at the i th pixel, θ_R^i , and its associated zenith angle cosine, $\mu^i = \cos\theta_R^i$ are given by:

$$\theta_R^i = \cos^{-1}\mu^i = \tan^{-1}\left[\frac{(i-1)}{n} 1479/833\right] \quad (5-29)$$

for $i = 1, 2, 3, \dots, (n+1)$ pixels and assuming a sensor altitude of 833km for a nominal circular orbit.

6. RADIATIVE TRANSFER

6.1 Technique Selection Criteria

Radiative transfer theory provides a mathematical description of the interaction between incident solar radiation and the relevant optically active constituents of the atmosphere including both ambient gases and aerosols. The interaction mechanisms treated by radiative transfer theory have been alluded to in the preceding discussions of atmospheric optical properties and include molecular (Rayleigh) scattering, gaseous absorption, and aerosol absorption and scattering. In the context of the present radiance simulation model, the radiative transfer sub-package facilitates a quantitative link between the meteorologically dependent optical properties of the atmosphere (especially aerosol content) and sensor incident backscattered solar radiation. For this purpose, it is minimally required that the radiative transfer treatment which is implemented is capable of handling: (a) multiple scattering, (b) the inherent anisotropic (i.e. highly directional) scattering characteristic of aerosols, (c) reflection of radiation at the atmosphere-ocean interface, and (d) the azimuthal dependence given by the sun/sensor/geometry.

The general attributes cited above require a solution to the radiative transfer equation (RTE) for a multiple scattering atmosphere (cf. Chandrasekhar, 1950; Goody, 1964; Liou, 1980). An extensive hierarchy of potential computational methods exists to treat the RTE ranging from simple,

single scattering analyses (such as that in Fett and Isaacs, 1979) to a variety of highly numerical computational algorithms (Hansen and Travis, 1974; Lenoble, 1977). Numerical solutions generally provide high accuracies (less than 1% difference between competing state-of-the-art methods for identical input data) at the expense of considerable computer resources. Highly accurate modeled radiances are useful, of course, only when the accuracies of input atmospheric optical data are consistently high. In general, the tradeoff analysis is between desired accuracy and computational efficiency (Filmore and Karp, 1980).

A variety of analytical solutions to the RTE are available for simulation model implementation which require very little computational effort. However, their use does incur a penalty in the form of associated errors and uncertainties (Isaacs and Özkaynak, 1980). Often, application of these methods is precluded by their low levels of achievable accuracy.

Implementation of radiative transfer theory within larger operational models introduces severe constraints on the available computational level of effort. For this reason investigators have increasingly relied on approximate, analytical solutions to the RTE to provide tractable simulation algorithms (Kaufman, 1979, 1981; Hering, 1981; Isaacs, 1981).

In selecting an appropriate approach in this investigation, criteria have included: (a) ability to satisfactorily treat mechanisms cited above, (b) maximization of the number

of sensitivity analyses which could be undertaken, (c) optimization of available computer resources, and (d) consistency of approach accuracies with those in other components of the simulation model (such as in specifying the physical aerosol models).

An additional consideration in the context of the current study was the possible application of the radiance simulation model discussed here to the operational analysis of DMSP imagery for the purpose of inferring surface propagation properties. For this reason an algorithm implementable on a desk top type computer was desired. These considerations led to selection of an approximate, analytical solution to the RTE.

In the following sections the adopted radiative transfer formulation is discussed and accuracies are assessed by comparison with highly accurate numerical methods. These comparisons are performed for a representative set of cases including: (a) variations in aerosol optical depth representative of optically thin ($\tau = 0.1$) and optically thick ($\tau = 1.0$) situations, (b) isotropic, Rayleigh, and aerosol (i.e., anisotropic) scattering (c) conservative (i.e. non-absorbing, $\omega_0 = 1.0$) and absorbing aerosols ($\omega_0 \neq 1.0$) and (d) differing geometries (variations in observer and solar orientations).

6.2 Analytical Approaches

From a practical perspective, the essential difference between numerical and analytical approaches is that the latter require very little computational effort and hence a significant amount of computer time may be saved if they are implemented. Analytical approaches are defined as those which are implementable using only simple algebraic equations with specifiable parameters. There are no recurrent or iterative calculations and no convergence criteria. Unfortunately, exact analytical treatments are available only for a few cases which are not immediately applicable to geophysical remote sensing problems. They are of interest mathematically, however, to compare with corresponding cases of more computationally complex numerical techniques. These cases include, for the most part, approaches based on Chandrasekhar's H functions for semi-infinite atmospheres ($\tau = \infty$) and X and Y functions for finite atmospheres (Chandrasekhar, 1960). For the former set of problems solutions are available for isotropic (Stibbs and Weir, 1959; Abhyankar and Fymat, 1971), Rayleigh (Chandrasekhar, 1960; Lenoble, 1970) and various anisotropic phase functions (Chandrasekhar, 1960; Sobolev, 1956; Kolesov, 1972). For finite atmospheres, solutions are available only for isotropic (Carlstedt and Mullikan, 1966) and Rayleigh scattering (Sekera and Kahle, 1966).

For remote sensing problems relevant to radiative transfer in the atmosphere-ocean system, methods are required

which treat a finite atmosphere (i.e., the total optical depth is not infinite) with scattering properties which are anisotropic in order to simulate aerosol scattering. Although exact analytical treatments are not available in such cases, a variety of approximate analytical methods with quantifiable accuracy may be employed. The utility of approximate analytical treatments lies in their extreme computational efficiency while retaining treatment of the salient physical mechanisms of radiative transfer involved.

Approximate analytical methods include those based on taking the first few tractable orders of more extensive numerical treatments and those formulated specifically as approximate treatments. Examples falling into the first category include first (Deirmendjian, 1969) and second (Hovenier, 1971) order of scattering treatments explicitly formulated from successive order of scattering approaches (Irvine, 1965; Nagel et al., 1978), analytic two and four stream (Liou, 1974) approximations based on discrete ordinate methods (Liou, 1973), and the two-step function approach (Burke and Sze, 1977) derived from more general variational methods (Sze, 1976). Treatments explicitly formulated as approximate approaches include hybrid methods evaluating single scattering exactly and approximating multiply scattered terms (Bergstrom et al., 1980; Hering, 1981) and various general finite stream methods (Meador and Weaver, 1981) when applied as suggested by the work of Kaufman (1979).

The inherent degree of accuracy associated with a specific approximate analytical treatment varies considerably with the relevant optical propagation parameters involved. Thus a domain of applicability must be ascertained. Expected errors may be quantified by examining standard cases and comparing accuracies either with available exact solutions or with numerical solutions of specified precision. For example, Table 6-1 lists percentage error for a comparison between upward and downward radiances derived from single scattering vs. multiple scattering (Coulson et al., 1960) treatments in a Rayleigh atmosphere with the sun at zenith ($\mu_0 = 1.0$) and zero surface albedo ($A_L = 0.0$).[†] Results are presented for various observer zenith angles (μ) and total atmospheric optical depths (τ^*). Note that even for this fundamental approximate analytical approach, errors are highly dependent on atmospheric optical depth, emphasizing the need to quantify the behavior of such treatments a priori.

6.3 Adopted Approach

The approximate solution to the radiative transfer equation adopted in the current radiance simulation model is based on that suggested by Kaufman (1979) and employed in a variety of remote sensing contexts (Kaufman, 1981, 1982;

[†]These parameters are defined in §6.4.

μ	Upward Radiance			Downward Radiance		
	τ^*			τ^*		
	0.10	0.25	0.50	0.10	0.25	0.50
1.00	13.2	24.6	37.1	12.3	24.7	37.9
0.72	13.8	25.6	39.3	13.4	26.1	40.3
0.52	14.3	26.9	40.8	13.9	27.2	42.3
0.28	14.7	27.8	41.9	14.6	28.5	44.6
0.10	14.8	27.6	40.2	14.9	29.3	46.1

Table 6-1. Percent error: single scattering vs. multiple scattering with Rayleigh phase function ($\mu_0 = 1.0$, $A_L = 0.0$).

Kaufman and Joseph, 1982; Mekler and Kaufman, 1980, 1982). The approximate solution for the radiance is an extension of existing methods for flux calculation (Meador and Weaver, 1980) based on the assumption that the diffuse incident flux may be used instead of the actual directionally dependent radiance in the calculation of the scattered radiance contribution. Originally formulated using the two stream (Coakley and Chylek, 1975; Acquista et al., 1981) flux parameterization, the method is generally applicable to any two parameter flux parameterization including the Eddington, δ -Eddington, and others discussed in Meador and Weaver (1981). The accuracy of derived radiances is, of course, dependent in turn on the accuracy of the flux parameterization used. By employing calculated backscatter fractions (Wiscombe and Grams, 1976) for general aerosol-phase functions in the analysis, the general scattering anisotropy of the real atmosphere-ocean system may be calculated.

6.4 Theory

In order to simulate the upward radiance at the top of the atmosphere by a meteorological satellite viewing the atmosphere-ocean system, it is necessary to solve the RTE for a plane-parallel, multiple scattering atmosphere of the form (Chandrasekhar, 1960):

$$\mu \frac{\partial I}{\partial \tau} (\tau, \mu, \phi) = I(\tau, \mu, \phi) - \omega_0 J(\tau, \mu, \phi) \quad (6-1)$$

where:

$$J(\tau, \mu, \phi) = \frac{F}{4} P(\theta_0) e^{-\tau/\mu_0} + \frac{1}{4\pi} \int_0^{2\pi+1} \int_{-1}^1 P(\theta) I(\tau, \mu', \phi') d\mu' d\phi' \quad (6-2)$$

Expression (6-2) is the scattering source function with terms on the right-hand side corresponding to single scattered and multiply scattered (i.e., the integral over angles) radiances, respectively. The following definitions apply:

- $I(\tau, \mu, \phi)$ = radiance ($\text{mW cm}^{-2} \mu\text{m}^{-1} \text{sr}^{-1}$)
- $J(\tau, \mu, \phi)$ = source function due to scattering by atmosphere
- τ, τ^* = optical depth, total optical depth $\int_z^\infty \beta(z) dz$
- $\beta(z)$ = total extinction coefficient (km^{-1}) at height z (km)
 - = $\beta_R^S + \beta_g^a + \beta_A^S + \beta_A^a$
- β_R^S = Rayleigh scattering coefficient (km^{-1})
- β_g^a = molecular absorption coefficient (km^{-1})
- $\beta_A^{S,a}$ = aerosol scattering, absorption coefficients (km^{-1})
- ω_0 = single scattering albedo
 - = $(\beta_R^S + \beta_A^S) / \beta$
- $P(\theta)$ = angular scattering (phase) function
 - = $[\beta_R^S P_R(\theta) + \beta_A^S P_A(\theta)] / \beta$
- $P_R(\theta)$ = Rayleigh phase function
- $P_A(\theta)$ = aerosol phase function
- πF = incident solar irradiance (see Figure 6-1)

All of the above are wavelength dependent optical properties of the atmosphere. The sun-sensor geometry is defined by the angles:

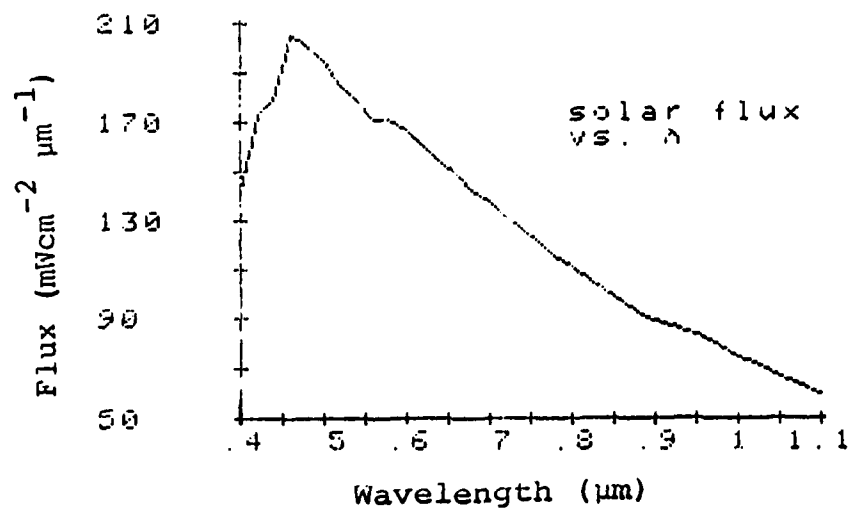


Figure 6-1. Incident Solar Irradiance

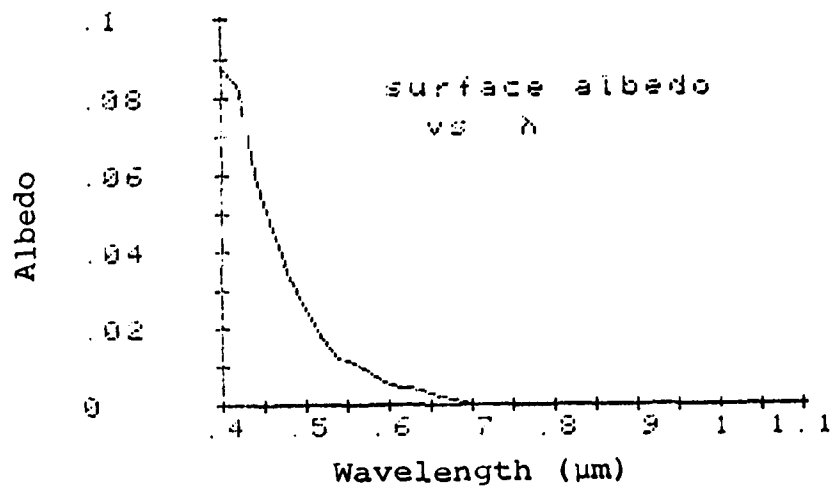


Figure 6-2. Ocean Surface Albedo (Ramsey, 1968)

$$\begin{aligned}
\mu &= \cos\theta \quad (\theta \text{ is the sensor zenith angle}) \\
\mu_0 &= \cos\theta_0 \quad (\theta_0 \text{ is the sun zenith angle}) \\
\phi &= \text{azimuth angle difference between sensor and sun} \\
\theta &= \text{scattering angle for incident direction } \mu \text{ and} \\
&\quad \text{scattered direction } \mu' \text{ with azimuth angle} \\
&\quad \text{difference } \phi \\
&= \mu\mu' + (1-\mu^2)^{\frac{1}{2}} (1-\mu'^2)^{\frac{1}{2}} \cos\phi
\end{aligned}$$

Analytical radiance solutions to (6-1, 6-2) are obtained as described above by assuming that the angular dependent intensity factor in the integral sum of the source function may be taken as isotropic (i.e., independent of angle) to first order (see Appendix A, A.1). This approximates the multiply scattered field. A quantity independent of angle related to radiance is flux (or irradiance) is defined as:

$$\begin{aligned}
F(\tau) &= \int_0^{2\pi+1} \int_{-1}^{-1} I(\tau, \mu', \phi') \mu' d\mu' d\phi' & (6-3) \\
&= \pi I(\tau)
\end{aligned}$$

The last step follows by assuming radiance is independent of angle. The result above (6-3) is substituted back into (6-1, 6-2) [cf. A.8] to relate radiance to flux. Thus by solving the resulting coupled differential equations (A.9, A.10), radiance solutions are obtained dependent on the fluxes. The boundary conditions required for solution at the surface ($\tau = \tau^*$) and top of the atmosphere ($\tau = 0$) are imposed on the fluxes:

$$\begin{aligned}
F^-(\tau = 0) &= 0 \\
F^+(\tau = \tau^*) &= A_L [\pi F \mu_0 e^{-\tau^*/\mu_0} + F^-(\tau = \tau^*)]. & (6-4)
\end{aligned}$$

and state that there is no diffuse irradiance from space at the top boundary and that the upward irradiance at the surface is equal to the product of a constant, A_L (wavelength-dependent), and the downward irradiance due to the direct solar beam and the multiply scattered radiance.[†]

Here A_L is the wavelength-dependent Lambert surface albedo from Ramsey (1968) [as given in Curran (1972)].[†] Ocean surface albedo as a function of wavelength is illustrated in Figure 6-2.

Solutions to (6-1, 6-2) for upward radiance are obtained of the form:

$$I(\tau, \mu, \phi) = D_1 e^{\tau/\mu} + \frac{U_1 e^{k\tau}}{1-\mu k} + \frac{U_2 e^{-k\tau}}{1+\mu k} + \frac{U_3 e^{-\tau/\mu_0}}{1+\mu/\mu_0} \quad (6-5)$$

where:

$$D_1 = \left[\frac{F^+(\tau^*)}{\pi} - \frac{U_1 e^{k\tau^*}}{1-\mu k} - \frac{U_2 e^{-k\tau^*}}{1+\mu k} - \frac{U_3 e^{-\tau^*/\mu_0}}{1+\mu/\mu_0} \right] e^{-\tau^*/\mu} \quad (6-6)$$

$$U_1 = \frac{A\omega_0}{\pi} \left[1-\beta(\mu) + \frac{\beta(\mu)}{\gamma_2} (\gamma_1-k) \right] \quad (6-7)$$

$$U_2 = \frac{B\omega_0}{\pi} \left[1-\beta(\mu) + \frac{\beta(\mu)}{\gamma_2} (\gamma_1+k) \right] \quad (6-8)$$

$$U_3 = \frac{C\omega_0}{\pi} \left[1-\beta(\mu) \right] + \frac{\omega_0}{\pi} \frac{\beta(\mu)}{\gamma_2} Y + \frac{F}{4} P(\mu, -\mu_0; \phi, \phi_0) \quad (6-9)$$

[†] Discussion of the specular (non-Lambert) surface reflectance due to sunglint is deferred until Section 7.

$$Y = C \left(\gamma_1 + \frac{1}{\mu_0} \right) - \pi F \omega_0 \beta(\mu_0) \quad (6-10)$$

$$k = (\gamma_1^2 - \gamma_2^2)^{1/2} \quad (6-11)$$

$$\beta(\mu) = \frac{1}{4\pi\omega_0} \int_0^1 \int_0^{2\pi} P(\mu, \mu'; \phi, \phi') d\mu' d\phi' \quad (6-12)$$

Values of A, B, C and the upward flux at the surface, $F^+(\tau^*)$ are given by expressions in Appendix A (A.15, 16, 17, and 11a, respectively). The backscatter fractions, $\beta(\mu)$, defined in (6-12) above (see also A.4, 5, 6) are obtained from results of Wiscombe and Grams (1976) and are dependent on the phase function asymmetry parameter defined as Joseph et al. (1976):

$$g = \frac{1}{2} \int_{-1}^{+1} \mu P(\mu) d\mu \quad (6-13)$$

Figure 6-3 illustrates the dependence of $\beta(\mu)$ and β' on g as used in the radiance simulation model. The correct choice of asymmetry parameter used in the evaluation of $\beta(\mu)$ is that obtained using the effective phase function (see 6-14) in the definition of g (6-13) above. Generally β' varies from 0.5 for isotropic or Rayleigh scattering ($g = 0$) to 0.0 for total forward scattering ($g = 1.0$) [i.e., there is no backscatter]. The range of $\beta(\mu)$ values is similar, however, the rate of change in the domain $0.0 \leq g \leq 1.0$ is dependent on the specific value of $\mu (= \cos\theta)$ chosen.

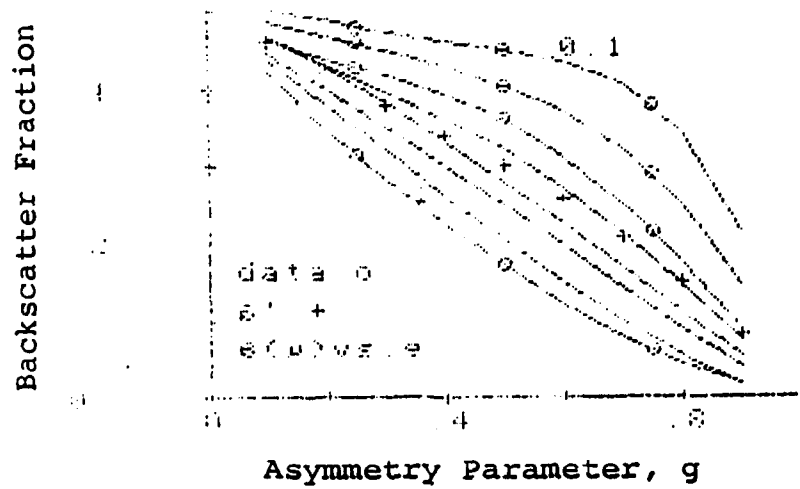


Figure 6-3. Backscatter Fractions as a Function of Asymmetry Parameter (Wiscombe and Grams, 1976)

6.4.1 Phase function parameterization

The phase function $P(\theta)$ defined above appears explicitly in the solution (see 6-9) where it determines primary scattering. As noted immediately above, the backscatter fractions $\beta(\mu)$, β' are also dependent on the phase function. The appropriate phase function above is the effective phase function at a given wavelength weighted for Rayleigh scattering and aerosol scattering contributions. For a one layer model this is given by:

$$P_{\text{eff}}(\theta) = [\tau_R^S P_R(\theta) + \tau_A^S P_A(\theta)]/\tau^* \quad (6-14)$$

where:

$$\tau_R^S = \beta_R^S H_R \quad (6-15)$$

$$\tau_A^S = \beta_A^S H_A \quad (6-16)$$

$$P_R(\theta) = \frac{3}{4} (1 + \cos^2 \theta) \quad (6-17)$$

and H_R , H_A are molecular and aerosol scale heights, respectively. Figure 6-4 illustrates the variation of the effective, weighted phase function at $0.55\mu\text{m}$ wavelength (where $\tau_R^S = 0.1$) with increasing aerosol optical depth. The aerosol phase function $P_A(\theta)$ is the Shettle and Fenn (1979) maritime aerosol model at 70% relative humidity. A question naturally arises concerning the degree of accuracy required in specifying the aerosol phase function in order to provide useful radiance simulations. Two alternatives were investigated: (a) exact phase function digitized at θ increments

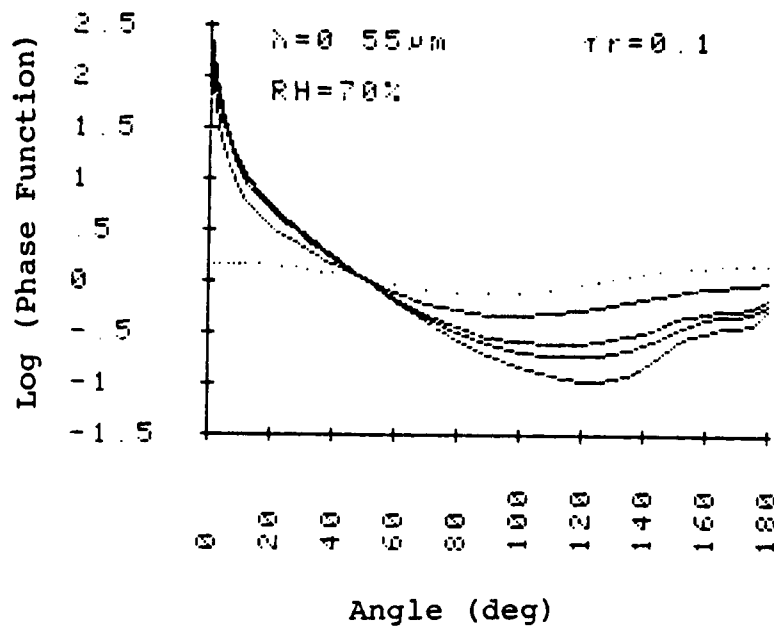


Figure 6-4. Change of weighted atmospheric phase function at $0.55 \mu\text{m}$ wavelength with increasing aerosol optical depth. Illustrated are Rayleigh phase function (.....) $\tau_r: 0.1$, $\tau_a = 0.0$ and curves for $\tau_a = 0.1, 0.5, 1.0$, and 5.0 (in descending magnitude order at 120°).

sufficiently dense to characterize the shape and (b) the analytical Henyey-Greenstein (1941) phase function (H-G) given by

$$P(\theta, g) = (1-g^2)/(1 + g^2 - 2g \cos\theta)^{3/2} \quad (6-18)$$

Figure 6-5 illustrates a comparison between exact and H-G phase functions for the Shettle and Fenn (1979) maritime aerosol at relative humidities of 70% and 80% within the DMSP spectral interval; (a) $\lambda = 0.55\mu\text{m}$, (b) $\lambda = 0.69\mu\text{m}$, and (c) $\lambda = 1.06\mu\text{m}$. In the context of model parameterization it is noted that the apparent dependence on relative humidity is greater than that on wavelength. This is illustrated by Figures 6-6 and 6-7. Figures 6-6a and b illustrate the exact maritime phase functions at relative humidities of 70% and 80%, respectively. All three wavelengths are plotted in each and it is obviously difficult to distinguish three distinct curves. (There are certainly differences in the forward ($\theta = 0^\circ$) and backscatter ($\theta = 180^\circ$) directions which may be important in some cases.) In contrast, Figure 6-7 illustrates the exact phase functions at $0.55\mu\text{m}$ wavelength for 70% and 80%. Considerable difference is noted especially at intermediate scattering angles. The conclusion (which may also be apparent from the respective g factors provided in Figure 6-5) is that for a given relative humidity/aerosol model, one phase function may suffice for all wavelengths within the chosen spectral interval.

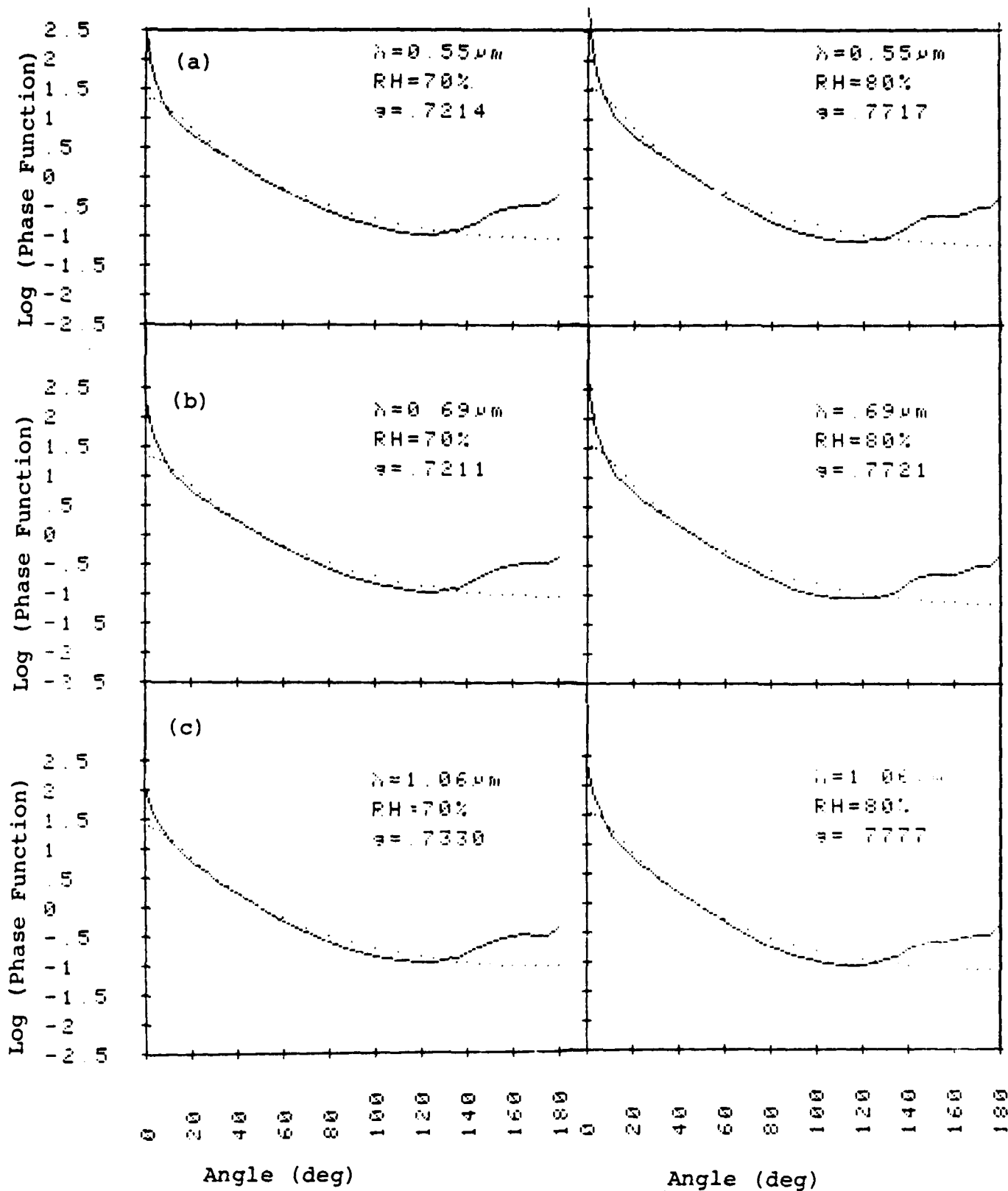


Figure 6-5. Comparison of exact (-) and approximate H-G(...) phase functions for maritime aerosol at wavelengths of: (a) $0.55 \mu\text{m}$, (b) $0.69 \mu\text{m}$, and (c) $1.06 \mu\text{m}$ and relative humidities of 70% and 80%.

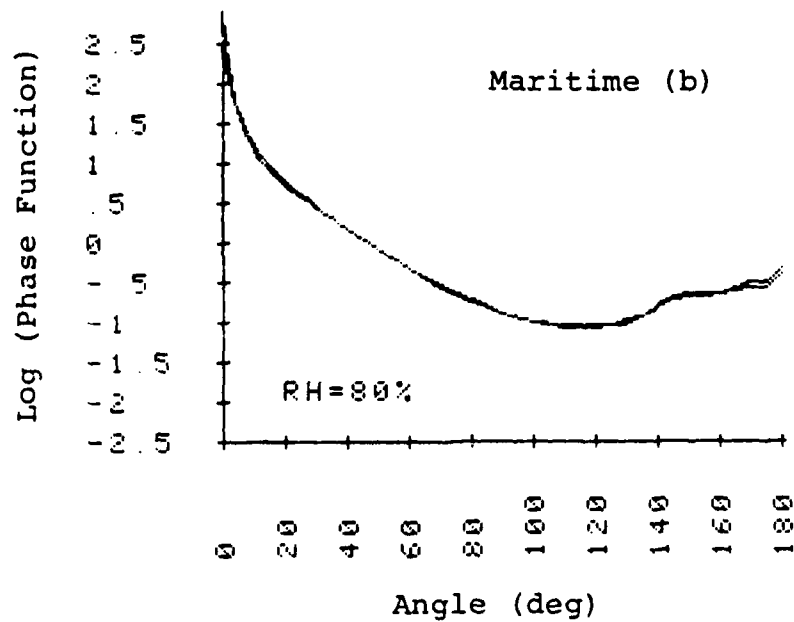
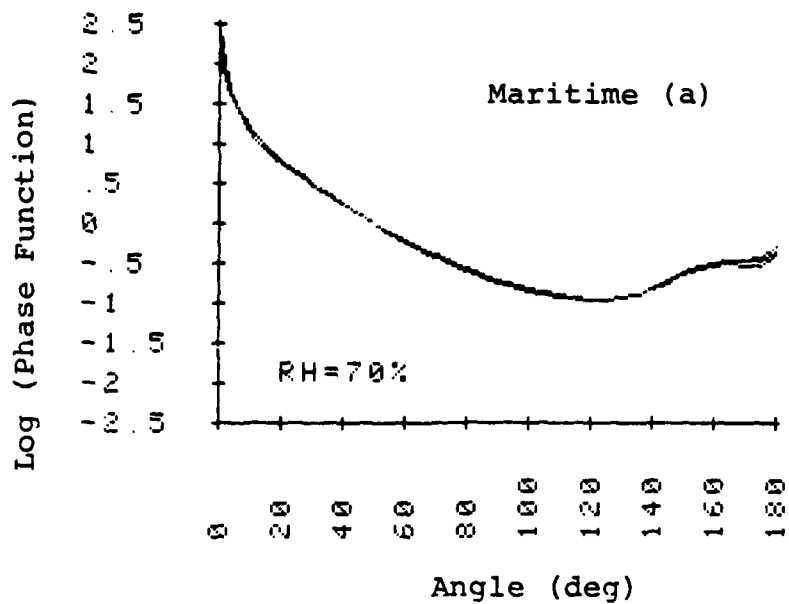


Figure 6-6. Maritime aerosol phase function for relative humidities of: (a) 70% and (b) 80%. Plotted are values at wavelengths of 0.55, 0.68, 1.06 μ m.

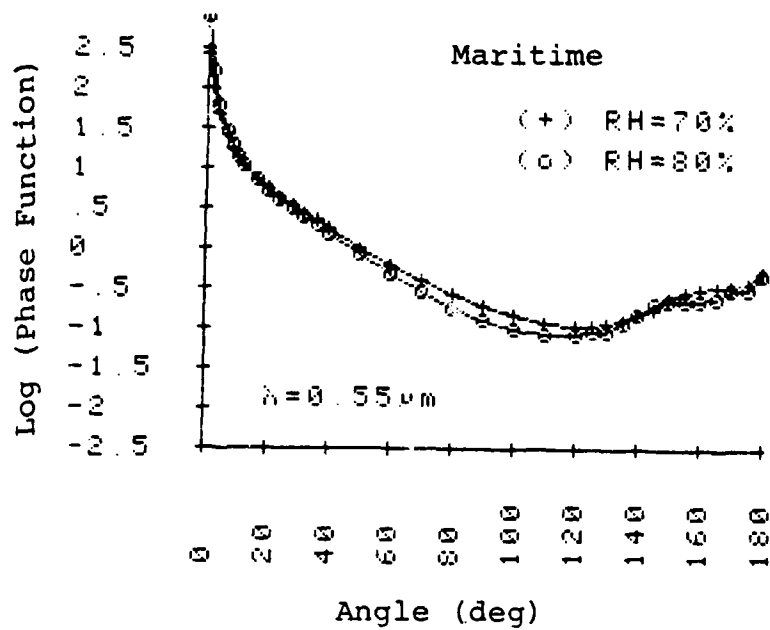


Figure 6-7. Maritime aerosol phase function at wavelength of $0.55\mu\text{m}$ for relative humidities of: 70% (+) and 80% (o).

AD-A125 513

REMOTE SENSING OF SURFACE PROPAGATION PARAMETERS:
APPLICATION OF IMAGERY. (U) ATMOSPHERIC AND
ENVIRONMENTAL RESEARCH INC CAMBRIDGE MA R G ISAACS

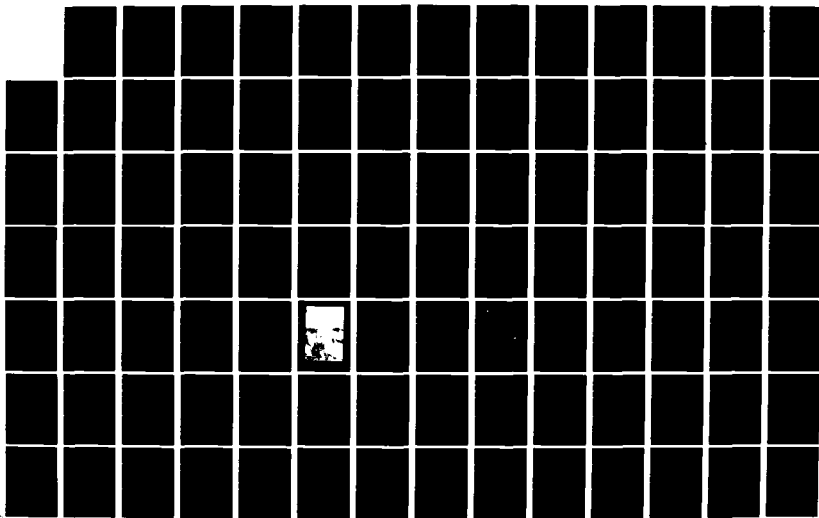
2/3

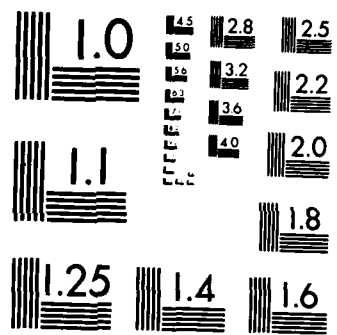
UNCLASSIFIED

31 OCT 82 N00014-80-C-0262

F/G 12/1

NL





MICROCOPY RESOLUTION TEST CHART
NATIONAL BUREAU OF STANDARDS-1963-A

It is also apparent from Figure 6-5 that the analytical H-G parameterization does not reproduce the exact phase function in the forward and backscatter directions although it does well in the approximate range from $40^\circ \leq \theta \leq 140^\circ$. One possible remedy (Hering, 1981) is adoption of a two term H-G phase function (TTHG) (Irvine, 1968) given by the linear combination of single term H-G phase functions (STHG):

$$P(\theta, g_1, g_2, c) = c P_{H-G}(\theta, g_1) + (1-c) P_{H-G}(\theta, g_2) \quad (6-19)$$

Figure 6-8 compares: (a) an exact continental aerosol scattering function (from Selby and McClatchey, 1972), (b) a suggested TTHG phase function (Hering, 1981) with $g_1 = .714$, $g_2 = -.613$, and $c = .963$, (c) the corresponding STHG [i.e., overall g factor same as (c) above $g = cg_1 + (1-c)g_2 = .664$] and (d) a STHG used in Liou (1973) to characterize aerosol scattering with $g = 0.62$. The TTHG phase function (b) does a much better job at providing the overall shape of a typical exact phase function than does either of the STHG parameterizations. In order to investigate the impact of the phase function parameterization on simulation of upward radiances using the approximate stream method (SA) described above, calculations were performed for a range of optical depths (0.125 to 1.0) and sensor zenith angles from 0 to 75° for an overhead sun ($\mu_0 = 1.0$) using both the STHG (curve d, Figure 6-8) and TTHG (curve b, Figure 6-8). For optical depth 0.125 a single scattering (SS) calculation was done using the TTHG phase function

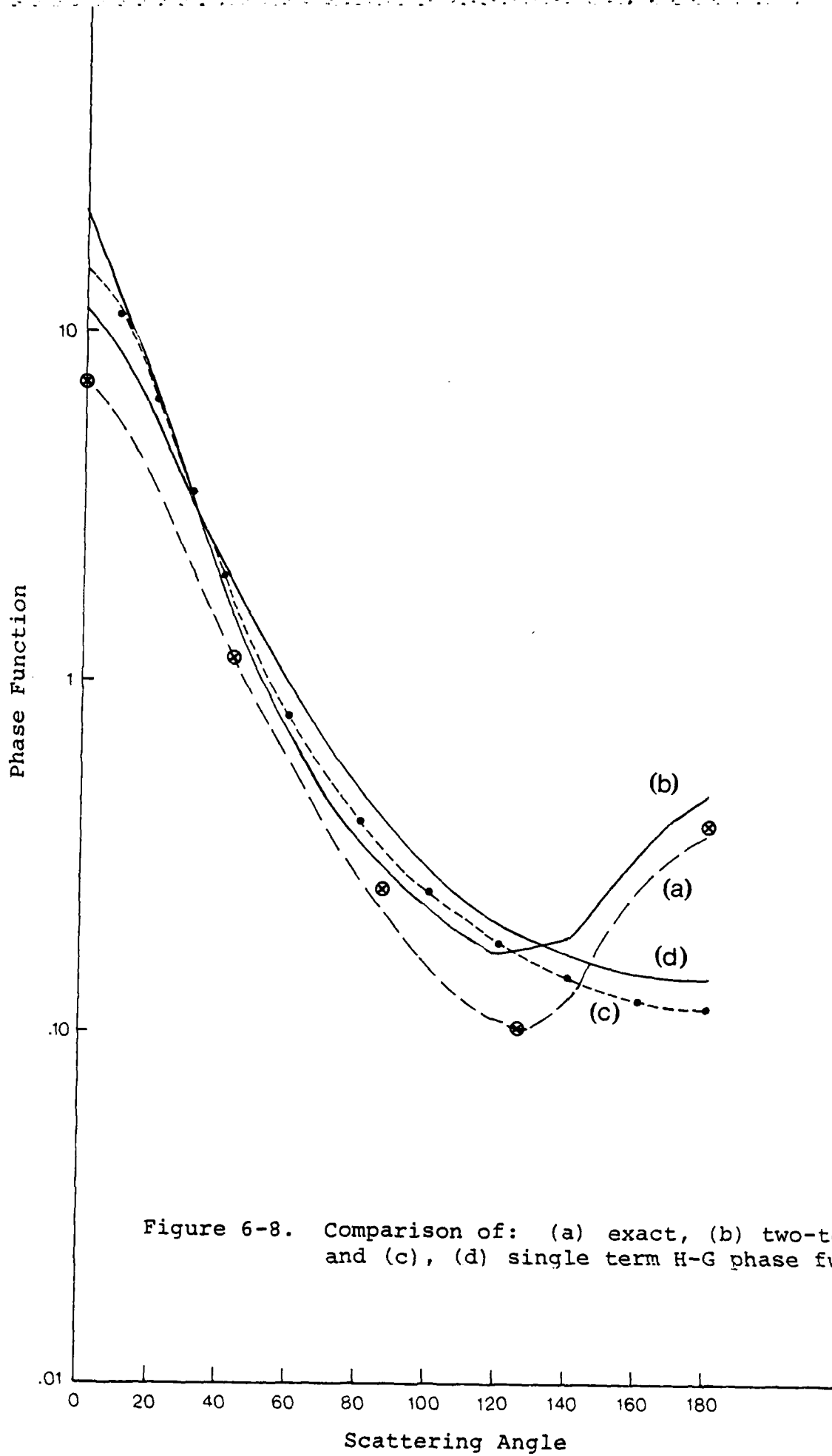
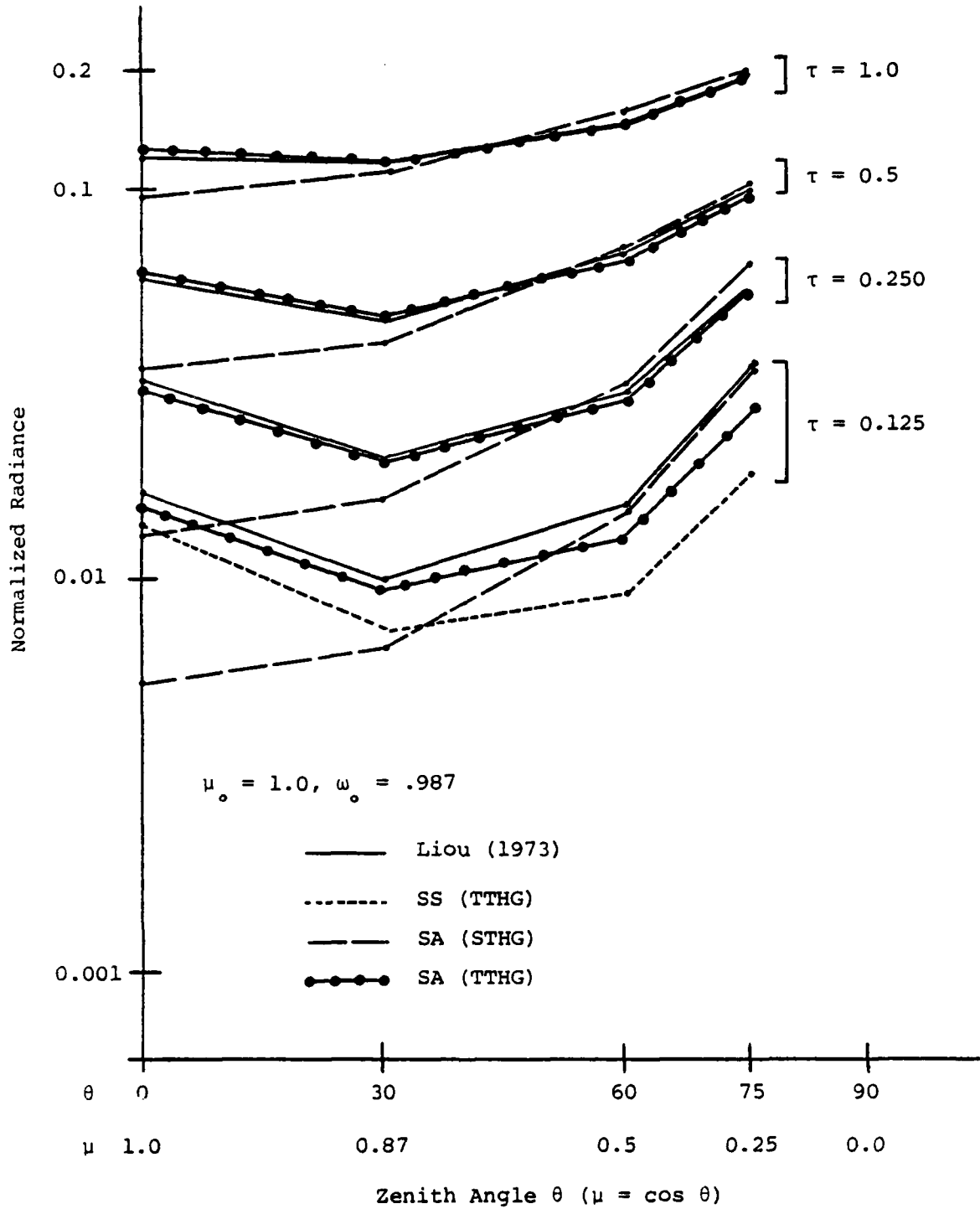


Figure 6-8. Comparison of: (a) exact, (b) two-term, and (c), (d) single term H-G phase functions

(single scattering would not be appropriate for larger optical depths). The single scattering albedo, ω_0 , for these calculations was 0.987. Results are illustrated in Figure 6-8. The single scattering result uniformly underestimates the exact radiance due to the neglect of multiply scattered contributions. The best fit overall (i.e., for all τ and θ) is obtained using the TTHG. The STHG particularly underestimates backscattering (in this case, the vicinity of $\mu = 1.0$) due to its failure to provide the backscatter lobe of the exact phase function (see Figure 6-8). For scattering angles in the vicinity of 120° (zenith angles of 60°) both STHG and TTHG provide similar results. This is as expected since the two parameterizations cross over near this angle. Coincidentally a nadir viewing, sun synchronous (morning or afternoon) satellite sensor will have a scattering geometry with backscatter angle in this vicinity. Figure 6-10 compares simulated wavelength dependent DMSP radiances using exact and STHG (denoted P and HG, respectively) phase functions assuming the 70% maritime model. The scattering geometry corresponds to about 110° backscatter. Note that the radiance spectra and bandpass weighted DMSP radiances are virtually identical. As illustrated here (and also in Hering, 1981) the TTHG gives a better overall fit to the angular scattering function and resultant radiances. However, for the purpose of DMSP simulation within the present context a STHG approach may be adequate.

Figure 6-9

Comparison of Stream Approx. Intensities Using
Single (STHG) and Two Term (TTHG) Henyey-Greenstein
Phase Functions



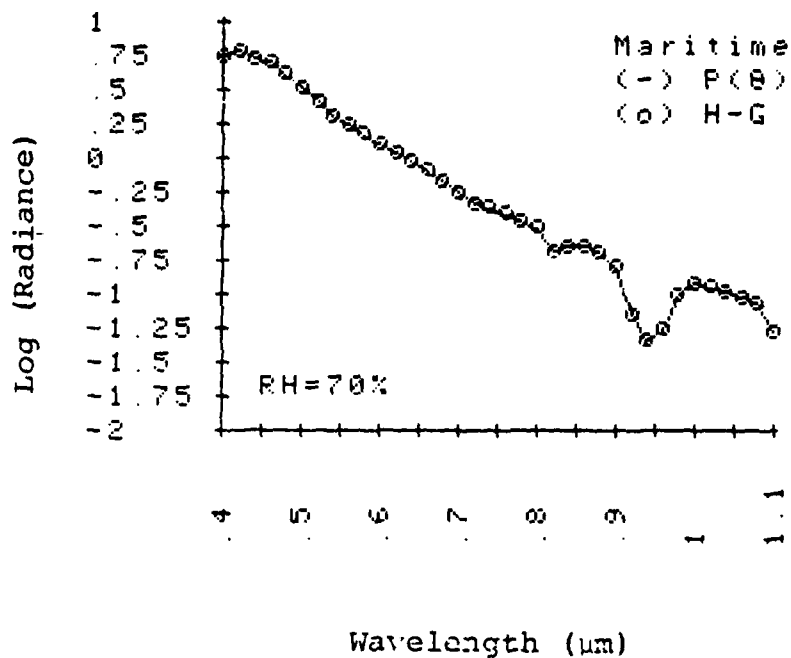


Figure 6-10. Comparison of wavelength dependent radiances calculated using the complete phase function $P(\theta)$ and the corresponding approximate H-G phase function for the maritime aerosol model at 70% relative humidity. Corresponding simulated DMSP radiances are 0.6985 and $0.7054 \text{ mW cm}^{-2} \mu\text{m}^{-1} \text{ sr}^{-1}$, respectively.

6.4.2 Flux Parameterization

As noted previously, any two parameter flux parameterization may be utilized in the evaluation of the radiances using (6-5, 6-12). The specific parameterization used enters the analysis through the values γ_1 and γ_2 in the expressions cited above. Table 6-2 from Meador and Weaver (1980) presents two of the possible choices. As noted the Appendix is based on the hemisphere constant (HC) parameterization which was used by Kaufman in his original paper (1979). Since the validity of the radiance approximation depends on the degree to which fluxes are accurately calculated, various applicable flux parameterizations described in Meador and Weaver (1980) were tested in comparison to accurate numerical calculations. Table 6-3 compares reflection (R) and transmission (T) functions:

$$R = F^+(\tau = 0) / \mu_0 \pi F \quad (6-20)$$

$$T = e^{-\tau^* / \mu_0} + F^-(\tau = \tau^*) / \mu_0 \pi F \quad (6-21)$$

from accurate discrete ordinate method (E) calculations (Liou, 1973) to analytic flux parameterizations including: Liou's (1974) two stream (TS), the hemisphere constant (HC) approach of Coakley and Chylek (1975) and the hybrid modified Eddington-delta function (HM δ E) (Meador and Weaver, 1980) (see Table 6-2). Calculations assume $g = 0.75$, $\mu = 1.0$ and total optical depths of 0.25 and 1.0, single scatter albedos of 0.8 and 1.0, and solar zenith angle

<u>Method</u>	γ_1	γ_2	<u>Reference</u>
Hemispheric Constant (HC)	$2[1-\omega_0(1-\beta)]$	$2\omega_0\beta$	Coakley and Chylek (1975)
Hybrid Modified Eddington-delta Function (HMδE)	$\frac{\{7-3g^2-\omega_0(4+3g)+\omega_0g^2(4\beta_0+3g)\}}{4[1-g^2(1-\mu_0)]}$		Meador and Weaver (1980)
		$\frac{-\{1-g^2-\omega_0(4-3g)-\omega_0g^2(4\beta_0+3g-4)\}}{4[1-g^2(1-\mu_0)]}$	

Table 6-2. Coefficients γ_1 and γ_2 determining two stream flux parameterization (from Meador and Weaver, 1980).

cosines of 0.1, 0.5, and 0.9. The R and T functions determine the upward and total downward fluxes given by a particular flux calculation. Examining the values in Table 6-3 the following conclusions are drawn: (1) the TS parameterization is the least reliable sometimes predicting negative values for the smaller optical depth, (2) the HC approach is more accurate for the smaller optical depth (it is formulated to have the correct limit for small optical depths) than either of the others, however, it is less accurate by far than the HM δ E for the larger optical depth, and (3) overall the HM δ E gives the best representation for the domain illustrated. Based on these conclusions the hybrid modified Eddington delta function flux parameterization of Meador and Weaver (1980) [see Table 6-2] was adopted for the overall radiance simulation model. In particular some inaccuracies may be expected for small optical depth situations, however, these cases correspond to high visual ranges. Since from a practical perspective it is probably more important to have higher operational accuracy for low visual range (i.e., higher optical depth) cases this seems an appropriate choice. Future refinements may include an option to switch to the HC parameterization for increased accuracy at small optical depths.

6.5 Comparison to Exact Results

The approximate solution to the RTE described above based on Kaufman (1979) was compared to a variety of exact treatments.

		R			T			
τ	ω_0	μ_0			μ_0			
		0.1	0.5	0.9	0.1	0.5	0.9	
0.25	1.0	0.41610	0.07179	0.02250	0.5839	0.9282	0.9775	E
		0.41433	0.07635	0.01294	0.5887	0.9237	0.0129	TS
		0.37221	0.0681	0.0255	0.6102	0.9279	0.9721	HC
		0.38574	0.0634	0.0198	0.6141	0.9365	0.9802	HM δ E
	0.8	0.28961	0.04855	0.01547	.4302	.8476	.9266	E
		0.31802	0.05739	-.01125	.4657	.8498	.9540	TS
		.28416	0.04976	0.017861	.4800	.8530	.9210	HC
		.28567	0.046186	0.01421	.4739	.8588	.9298	HM δ E
1.0	1.0	0.58148	0.24048	0.09672	0.5839	0.7595	0.9033	E
		0.51962	0.22559	0.02389	0.4822	0.7744	0.9761	TS
		0.51753	0.2392	0.1381	0.4648	0.7575	0.8567	HC
		0.5746	0.2026	0.0848	0.4250	0.7971	0.9150	HM δ E
	0.8	0.35487	0.12342	0.04929	.2055	.5161	.7177	E
		0.37519	0.14279	-.00064	.2902	.5527	.7633	TS
		0.36987	.14511	.07754	.2695	.5280	.6739	HC
		0.36111	.11606	.04726	.21540	.56020	.7321	HM δ E

Table 6-3. Comparison of two stream (TS), hemisphere constant (HC), and hybrid modified Eddington delta function (HM δ E) flux parameterizations to exact (E) discrete ordinate method calculations (from Liou, 1973).

6.5.1 Isotropic scattering

Isotropic scattering is defined by the angular scattering function:

$$P(\theta) = \omega_0 \quad (6-22)$$

i.e., there is no angular dependence. While this is not applicable to the realistic atmosphere exact results exist for comparison. Table 6-4 summarizes a comparison between the two-stream model and exact results for isotropic scattering obtainable using Chandrasekhar's X and Y function tabulated in Carlstedt and Mullikin (1966). These calculations were done using the HC flux parameterization and assume $\omega_0 = 0.5$, $\mu_0 = 1.0$. It is particularly notable that errors are less than 5% over much of this domain, and particularly for emergent intensities with zenith angles approaching unity ($\mu \rightarrow 1.0$). This geometry simulates a nadir-pointing satellite.

6.5.2 Rayleigh Scattering

Analogous results for Rayleigh scattering are provided in Table 6-5. Rayleigh scattering characterizes the pure molecular atmosphere without aerosols. In this case, the solar zenith angle is fixed at 57° and the observer zenith at 13.5° to simulate a satellite field of view for a polar-orbiting sensor. Percent errors are given, comparing two-stream results to the exact calculation of Rayleigh scattering by Coulson et al. (1960) for a variety of optical depths,

	Upward Radiance			Downward Radiance		
	τ^*			τ^*		
	0.4	1.0	3.5	0.4	1.0	3.5
μ						
0.2	-14.6	2.7	2.7	4.8	1.8	2.5
0.6	-24.8	-4.6	1.8	5.0	2.6	.2
0.9	- 3.0	.1	1.4	4.9	2.7	- .3

Table 6-4. Percent error: Two-stream approximation vs. exact result for isotropic scattering evaluated from Chandrasekhar's X and Y functions. ($\omega_0 = 0.5$, $\mu_0 = 1.0$)

τ^*	$A_L =$	Upward Radiance			Downward Radiance		
		ϕ			ϕ		
		30°	90°	150°	30°	90°	150°
.05	0.0	-10	-5	-1	4	4	3
	0.25	- 1	0	0	3	3	2
.10	0.0	6	-2	1	6	5	4
	0.25	- 1	-1	0	5	4	3
.25	0.0	- 2	2	5	9	7	6
	0.25	- 1	0	2	7	6	4
.50	0.0	0	4	8	10	7	4
	0.25	- 1	2	4	8	6	4

Table 6-5. Percent error: Two-stream approximation vs. exact result for Rayleigh scattering. ($\mu = .98$, $\mu_0 = .60$)

surface albedos of 0.0 and 0.25, and azimuth distances of 30°, 90°, and 150°. A comparison of these results to the single scattering approximation results in Table 6-1, indicates that a much higher degree of accuracy is achievable using the two-stream approach. Further examples are provided in Isaacs (1981).

6.5.3 Aerosol Scattering

The most stringent test of an approximate multiple-scattering radiative transfer model is highly anisotropic aerosol scattering. Using the hemispherical constant flux parameterization Kaufman (1979) has estimated the error for a nadir viewing satellite to be a few percent. Calculations based on the implementation of the approach described above have achieved errors between 5% and 16% in radiance for typical cases.

6.5.3.1 Optically thin case

Table 6-6 summarizes a comparison between exact Gauss-Seidel (Dave and Gazdag, 1970) calculations and the adopted approach for an optically thin ($\tau^* = .11026$) situation taken from Dave (1972). The effective phase function is illustrated in Figure 6-11 along with the H-G parameterization used in the approximate calculation ($g = .6862$). Two values of the surface albedo (0.0, 0.4) were investigated. Comparisons of exact and approximate radiances are illustrated in Figures 6-12, 13, and 14. Upward radiance errors

			$F^+(0)$	$F^-(\tau^*)$	$F^+(\tau^*)$	
(a)	$r =$	0.0	.1391	.1496	-	Gauss-Seidel ¹
	$\tau^* =$.11026	.1466	.1569	-	Hemi-const ²
	$\mu_0 =$	0.5	.1463	.1571	-	H-Mod- δ -Edd ³
	$\omega_0 =$.979				
(b)	$r =$	0.4	.6683	.1984	.5811	Gauss-Seidel
	$\tau^* =$.11026	.6779	.2112	.5885	Hemi-const
	$\mu_0 =$	0.5	.6860	.1978	.5831	H-Mod- δ -Edd
	$\omega_0 =$.979				

¹Dave (1972)

²Kaufman (1979)

³Meador and Weaver (1980)

Table 6-6. Comparison of upward and downward diffuse fluxes $F^+(0)$, $F^-(\tau^*)$ and upward total flux $F^+(\tau^*)$ for various parameterizations.

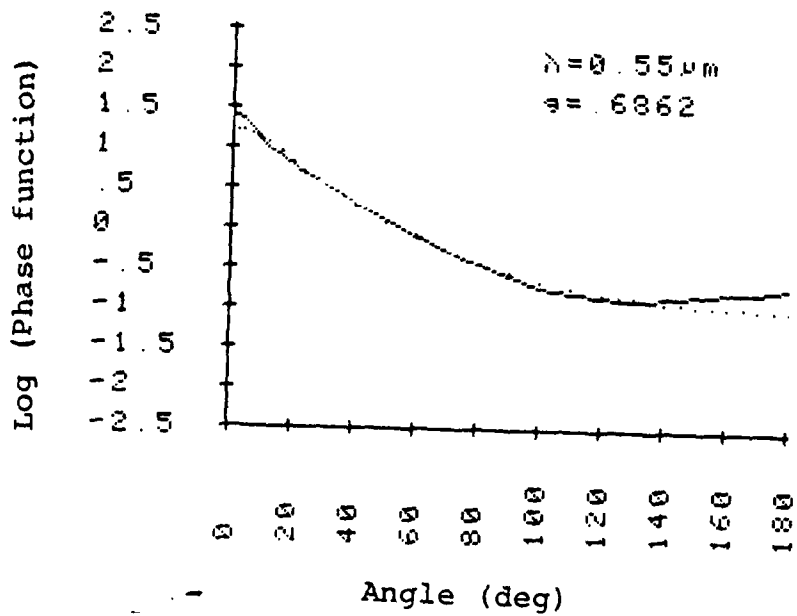


Figure 6-11. Comparison of exact Junge aerosol phase function and analytical approximation.

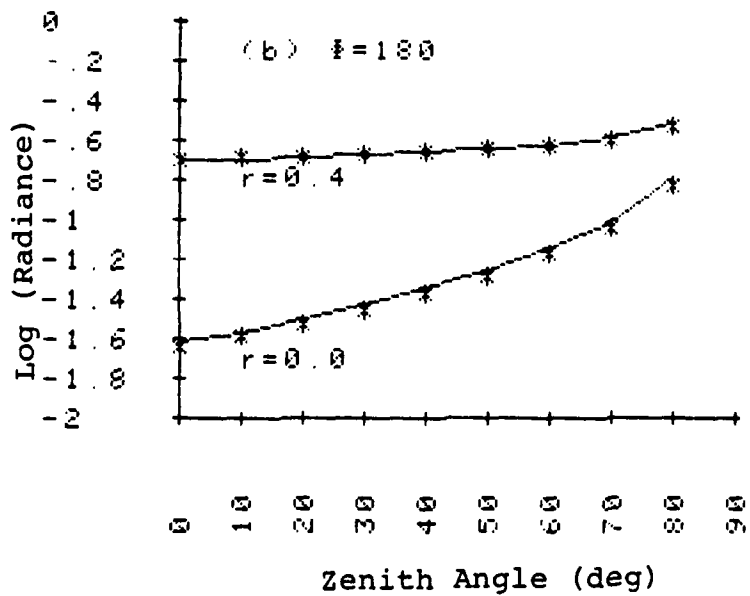
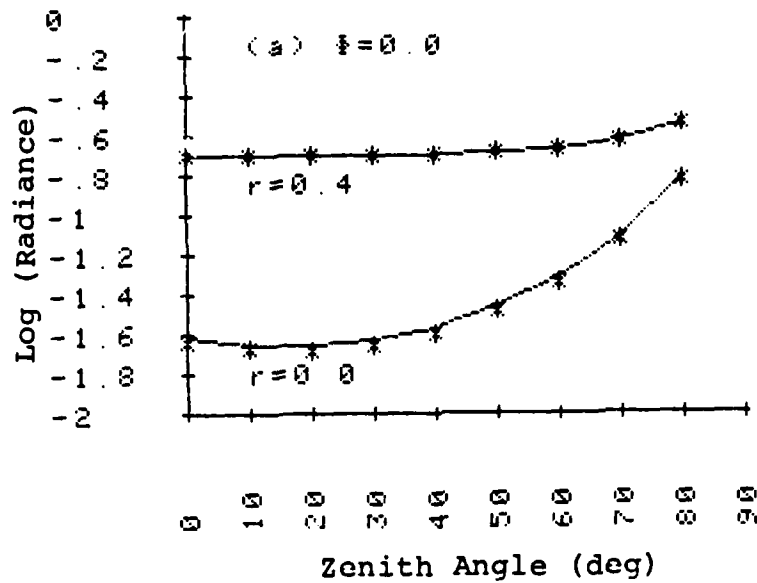


Figure 6-12. Comparison of exact (-) and approximate (*) upward radiances for two surface reflectances for azimuth angles of: (a) 0° and (b) 180° .

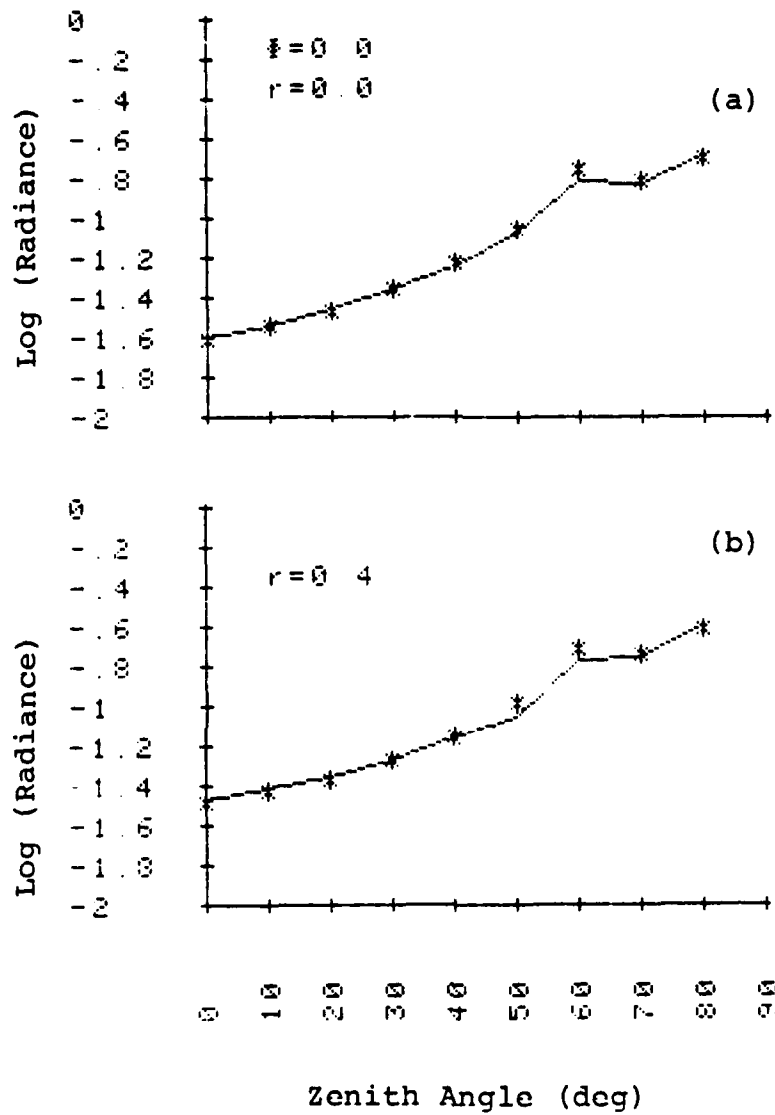


Figure 6-13. Comparison of exact (-) and approximate (*) downward radiances for surface reflectances of: (a) 0.0 and (b) 0.4 in solar direction ($\phi = 0.0^\circ$).

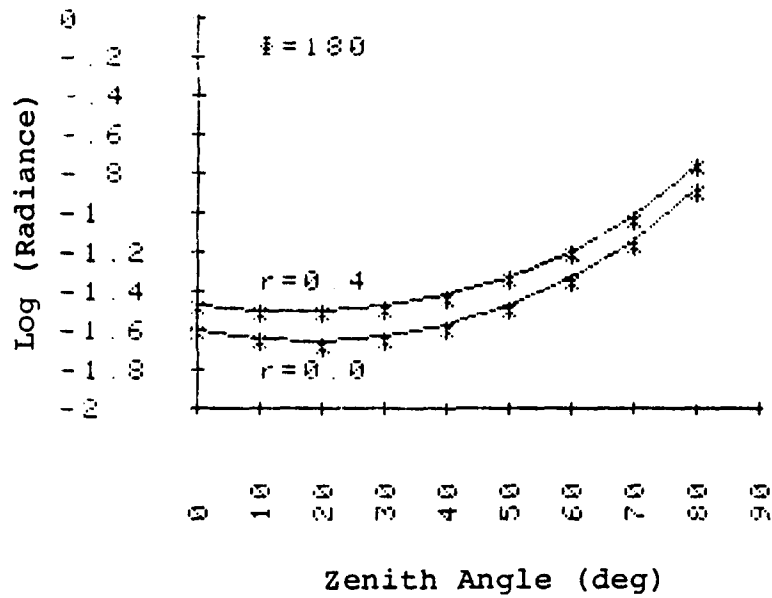


Figure 6-14. Comparison of exact (-) and approximate (*) downward radiances for surface reflectances of 0.0 and 0.4 in antisolar direction ($\phi = 180^\circ$).

(Figure 6-12) for zero surface albedo ($r = 0.0$) and nadir viewing (zenith angle of 0°) are about 5%. This level of error is consistent with Rayleigh scattering results (Table 6-5) since in backscatter the Rayleigh phase function dominates for low aerosol loading (see Figure 6-4). Error is minimal for the larger surface albedo since reflected radiance is significant. Maximum errors (20%) are evident in the forward scattering direction (Figure 6-13, $\theta = 60^\circ$).

6.5.3.2 Optically thick cases

Comparisons for three optical depth unity cases from Lenoble (1977) are summarized in Table 6-7. Flux parameterization results are compared with exact spherical harmonic results. The superiority of the HM δ E approach for larger optical depths is confirmed for cases 1 and 2 representing overhead sun. For case 3 ($\mu_0 = 0.5$), results are somewhat ambiguous. The exact phase function and its HG counterpart are illustrated in Figure 6-15. Figures 6-16 and 6-17 illustrate radiance comparisons with the exact calculations for three approximate approaches: (a) HM δ E flux parameterization, exact phase function; (b) HC flux parameterization, HG phase function; and (c) HC flux parameterization, exact phase function. For cases 1 and 2 (Figure 6-16), the first of these approaches does best overall. When the sun is not at zenith (case 3, Figure 6-17) this approach is superior only for nadir viewing. Illustrated are cases for azimuth angles of 0, 90, and

	F^+ (o)	F^- (τ^*)	
(a) Case 1			
$\tau^* = 1.0$.1736	1.8124	Spherical Harmonics ¹
$\mu_o = 1.0$.3279	1.6580	Hemi-const ²
$\omega_o = 1.0$.1615	1.8240	H-Mod- δ -Edd ³
(b) Case 2			
$\tau^* = 1.0$.1236	1.5155	Spherical Harmonics
$\mu_o = 1.0$.2362	1.3470	Hemi-const
$\omega_o = 0.9$.1202	1.5324	H-Mod- δ -Edd
(c) Case 3			
$\tau^* = 1.0$.2255	.8032	Spherical Harmonics
$\mu_o = 0.5$.2403	.8327	Hemi-const
$\omega_o = 0.9$.1962	.8803	H-Mod- δ -Edd

¹Lenoble (1977)

²Kaufman (1979)

³Meador and Weaver (1980)

Table 6-7. Comparison of upward and downward diffuse fluxes for Haze L cases using various parameterizations.

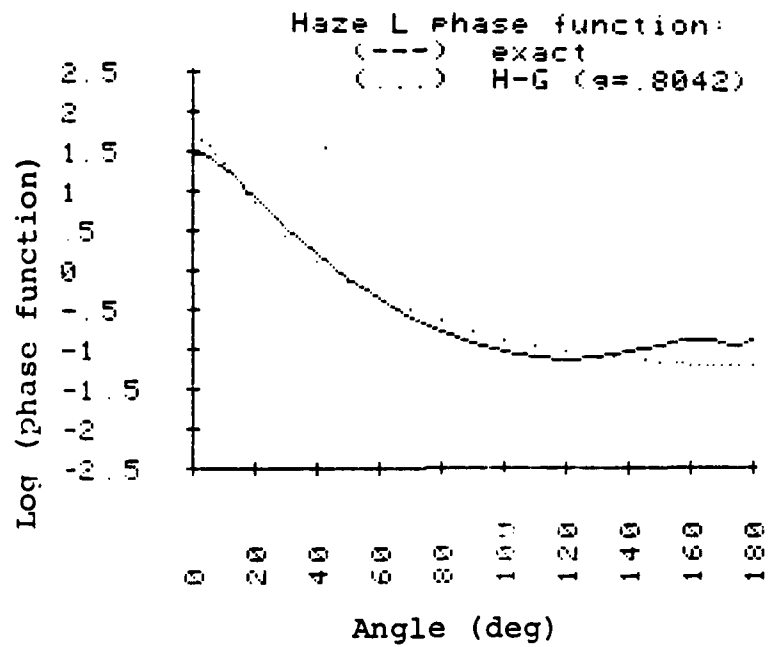


Figure 6-15. Comparison of exact haze L phase function and analytical approximation.

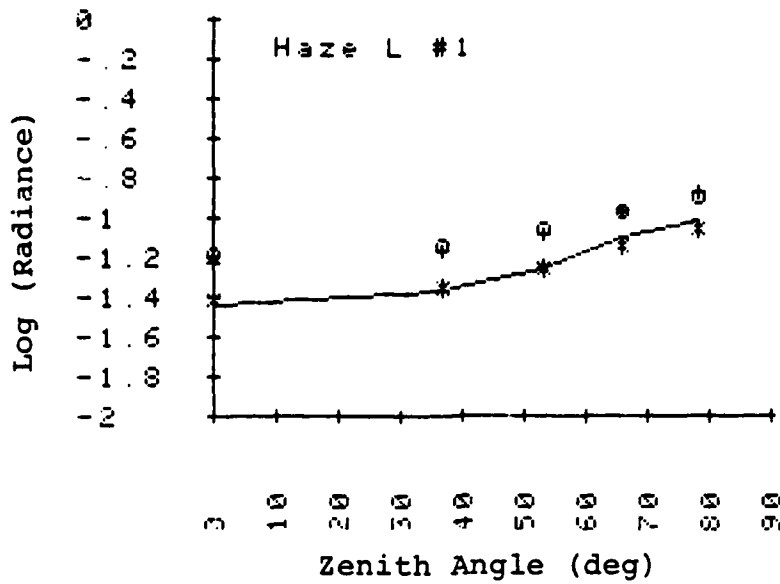


Figure 6-16. Comparison of Methods for Case 1.

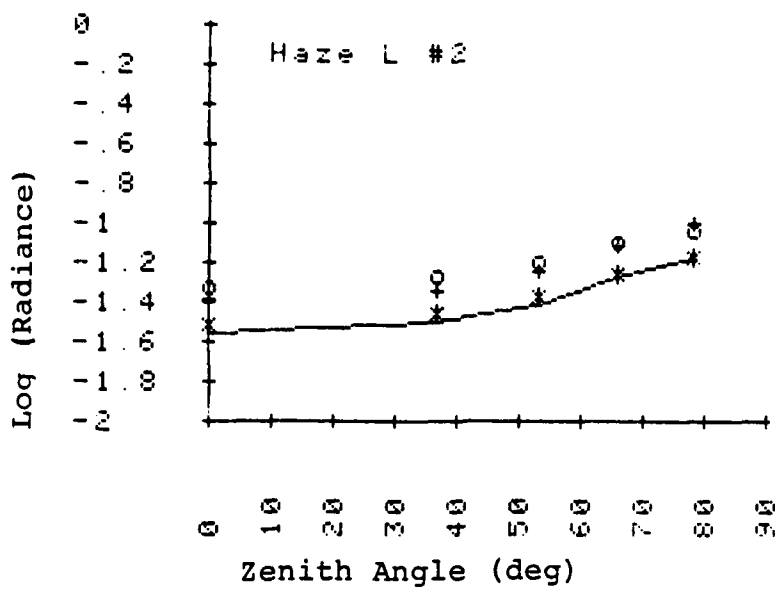
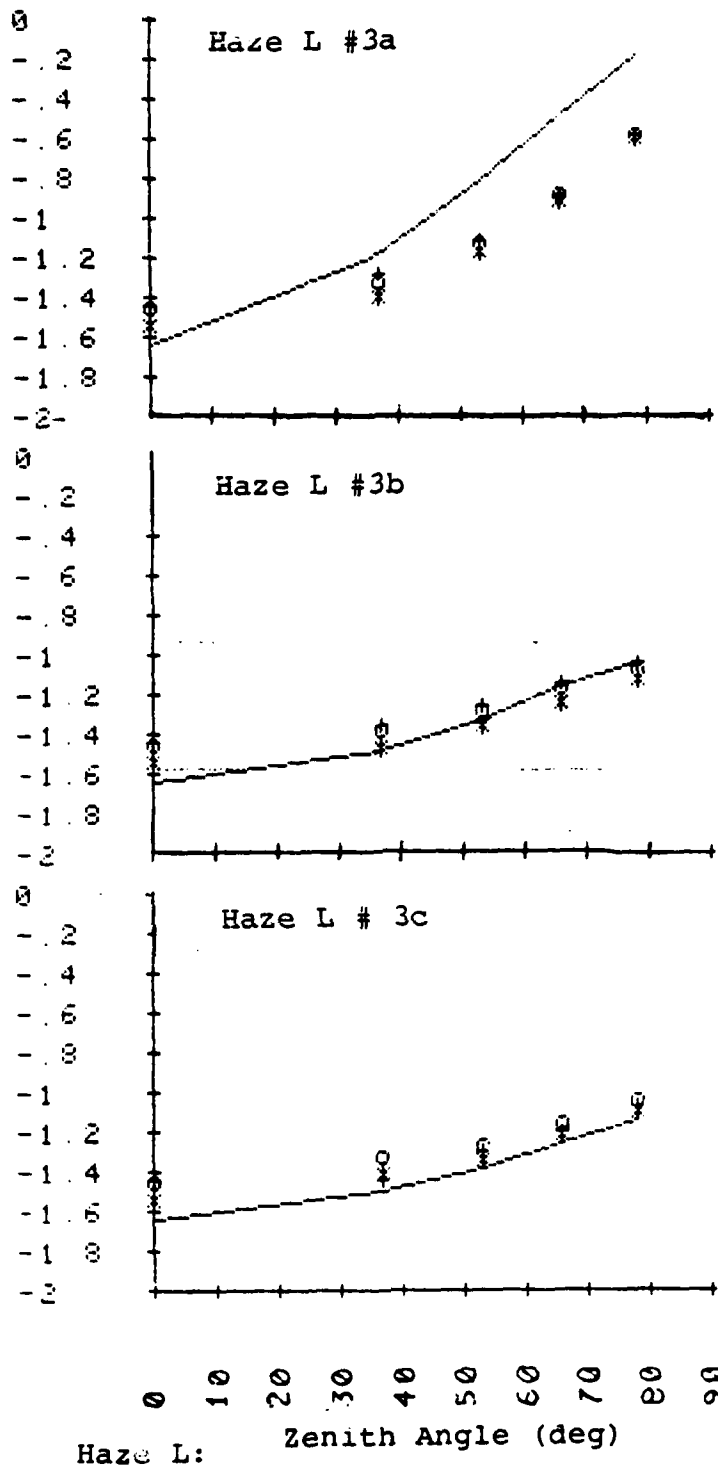


Figure 6-16. Comparison of Methods for Case 2.

Legend:

- (---) Exact calculation, Spherical harmonics [Lenoble, 1977] Approximation, [Kaufman, 1977] :
- (*) Modified δ -Eddington, exact phase function
- (+) Hemisphere const. H-G phase function
- (o) Hemisphere const. exact phase function



Case #1 $\gamma=1, \omega_0=1, \omega_1=1$
 #2 $\gamma=1, \omega_0=.9, \omega_1=1$
 #3 $\gamma=1, \omega_0=.9, \omega_1=.5$
 a $\phi=0$
 b $\phi=90$
 c $\phi=180$

Figure 6-17. Comparison of Methods for Cases 3a, b, c.

180° (3a, 3b, 3c, respectively). The accuracies for nadir viewing for cases 1, 2, and 3 are 12, 16, and 27%, respectively.

6.5.3.3 Comparison to Look-up Table Results

Griggs (1975, 1978a,b, 1979a,b) has performed extensive multiwavelength calculations based on the highly accurate Dave (1972) radiative transfer code to relate aerosol loading to remotely sensed radiances for a variety of sensors. A look-up table was formulated (Griggs, 1978b) to provide radiance values given the following input: (1) sensor zenith angle, (2) azimuth angle difference, (3) sun zenith angle, and (4) aerosol loading factor. This latter value is related to the aerosol optical depth through the aerosol model properties (Griggs, 1978a). Assuming the aerosol model illustrated in Figure 6-11, surface albedo, $A_L = 0.015$, and single scattering albedo, $\omega_0 = 1.0$, approximate radiances were evaluated (using the HM&E flux parameterization). A nadir viewing sensor ($\mu = 1.0$) was chosen and calculations were performed for aerosol loading factors of $N = 1, 2, 4, 6, 8, 10$ corresponding to $0.65\mu\text{m}$ aerosol optical depths of (Elterman, 1970):

$$\tau_A(0.65) = 0.2318N \quad (6-23)$$

The required Rayleigh optical depth of $\tau_R = .05$ was chosen. Radiance ($\text{mW cm}^{-2} \text{sr}^{-1} \mu\text{m}^{-1}$) results for exact (E) and approximate (A) radiances (assuming an incident irradiance of $150 \text{ mW cm}^{-2} \mu\text{m}^{-1}$ at $0.65\mu\text{m}$) and percent error (Δ) figures

are provided in Table 6-8 for a variety of solar zenith angles. The exact results are apparently reproduced to within 10% given that the assumed input variables are appropriate.

6.6 DMSP Bandpass Weighted Radiances

The solution to equation (6-1, 6-2) for each set of meteorological variables investigated provides a wavelength-dependent intensity spectrum, $I(\lambda)$. The intensity measured by the DMSP sensor at the satellite, \bar{I} (DMSP), however, is given by weighting these monochromatic intensities by the DMSP spectral bandpass function given in Figure 6-18 according to:

$$\bar{I} \text{ (DMSP)} = \frac{\int_{\Delta\lambda} \phi(\lambda) I(\lambda) d\lambda}{\int_{\Delta\lambda} \phi(\lambda) d\lambda} \quad (6-24)$$

where ϕ is the sensor response function over wavelength interval $\Delta\lambda$ (0.4-1.1 μm for DMSP VHR, LF).

Aerosol Loading

	N = 1.0		N = 2.0		N = 4.0		N = 6.0		N = 8.0		N = 10.0		
	E	A	E	A	E	A	E	A	E	A	E	A	
θ_0	-												
42	1.88	1.71	2.56	2.39	4.12	4.03	5.79	5.79	7.45	7.51	9.04	9.13	R
	9.0		6.6		2.2		0		1.0		1.0		Δ
48	1.76	1.61	2.44	2.29	3.96	3.90	5.54	5.59	7.08	7.20	8.52	8.70	R
	8.5		6.7		1.5		1.0		1.7		2.1		Δ
54	1.64	1.51	2.31	2.19	3.78	3.72	5.24	5.28	6.61	6.75	7.87	8.10	R
	7.9		5.2		1.6		1.0		2.1		2.9		Δ
60	1.53	1.41	2.19	2.10	3.55	3.48	4.84	4.87	6.00	6.16	7.03	7.32	R
	7.8		4.1		2.0		1.0		2.7		4.1		Δ
66	1.40	1.31	2.03	1.93	3.23	3.18	4.27	4.35	5.17	5.41	5.95	6.36	R
	6.4		4.9		1.6		1.9		4.6		6.9		Δ
72	1.26	1.17	1.80	1.70	2.73	2.67	3.46	3.54	4.07	4.34	4.60	5.04	R
	7.1		5.6		2.2		2.3		6.6		9.6		Δ
78	1.06	0.97	1.45	1.33	2.01	1.93	2.41	2.49	2.74	3.00	3.04	3.45	R
	8.5		8.3		4.0		3.3		9.5		13.5		Δ
84	0.69	0.61	0.84	0.72	1.01	0.97	1.15	1.22	1.28	1.45	1.39	1.65	R
	13.1		14.3		4.0		6.1		13.3		18.7		Δ

Table 6-8. Comparison of approximate (A) and exact (E) radiances (R) in $\text{mW cm}^{-2} \text{sr}^{-1} \mu\text{m}^{-1}$ and resulting percentage errors (Δ) in %. Exact results from Griggs (1978b).

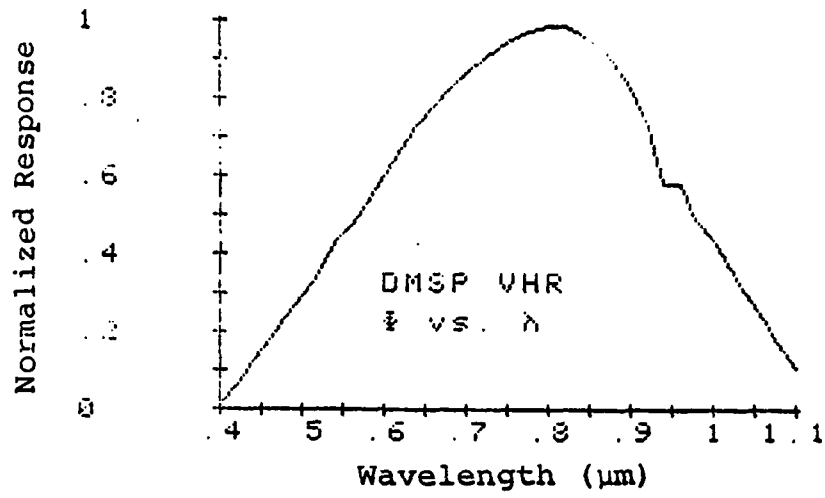


Figure 6-18. DMSP Spectral Bandpass
(Fett and Mitchell, 1977)

7. REFLECTION FROM THE OCEAN SURFACE

7.1 Sunglint

Satellite-borne visible imaging radiometers receive reflected solar radiation from the earth's surface. Due to the particular constraints imposed by their intrinsic observing geometries, such sensors see a relatively narrow solid angle field of view. In order to interpret these measurements, therefore, some understanding of the directional reflectance properties of the surface is required (Tanre et al., 1979). For many natural surfaces, it is often possible to assume that to a first approximation radiation is reflected uniformly in all directions (or isotropically). This Lambertian reflection is particularly useful for a variety of land surfaces although exceptions may be noted (cf. Eaton and Dirmhim, 1979). The most notable natural, non-Lambertian surfaces are bodies of water. Under appropriately calm conditions, water surfaces (including for example, oceans, lakes, rivers, swamps, etc.) obey Fresnel's reflection laws and produce mirror-like images of the sun for properly oriented sensors. As discussed in Fett and Mitchell (1977), for example, such sunglint (or "sun-glitter") is regularly observed in the visible imagery obtained from both geostationary and polar orbiting satellites. Since the surfaces of natural bodies of water, however, are usually rippled and roughened due to wind stress and other factors,

a perfectly specular reflection is rarely observed. Rather, the sunglint pattern is modified by the existing meteorological conditions affecting the surface and some directional reflectance intermediate between the Lambertian and specular is often evidenced. The size, shape, and intensity of the resultant sunglint pattern thus depends on a variety of factors including (Fett and Mitchell, 1979): (1) sun-sensor geometry, (2) characteristics of the image forming system, (3) sea state (i.e. wind speed) and (4) the low level distribution of atmospheric aerosols and moisture. A number of investigators have exploited this environmental modification of surface reflection properties in order to aid in the inference of surface wind conditions (McClain and Strong, 1979; Wylie et al., 1981), wind speed and direction (Kornfield, 1974), and surface ridge lines (Anderson, 1974). Additional meteorological analyses potentially available from sunglint region data for solar orbiting satellites are discussed in Fett and Mitchell (1977).

In this section, a simplified approach is described to incorporate sunglint phenomenon within the context of the current DMSP imagery simulation model. Due to the approximate nature of the radiance calculation discussed in Section 6, it is not possible to treat such effects in a vigorous manner. The methodology adopted, however, provides an excellent qualitative description based on comparison with numerical results and should provide practical guidance for imagery analysis purposes.

7.2 Surface Modeling

As discussed above, static representations of wavelength-dependent ocean surface reflectances based on simple Lambertian treatments are not necessarily appropriate due to the dynamic response of the ocean surface to meteorological forcing by wind/wave interaction. Three distinct considerations may be cited as necessary for physically realistic simulation of the reflection of radiation from the ocean surface: (1) geometric aspects for calm sea conditions obtainable from Fresnel's Laws, (2) modifications due to wind induced, time-dependent wave slope geometries, and (3) incorporation of the reflected radiation within the adopted radiative transfer algorithm.

In the basic calm state, the sea surface may be treated as a fundamental dielectric medium according to the classical Fresnel relations (Towne, 1967). For given geometries between the direction of propagation and the normal to the interface these relationships provide the reflection and transmission coefficients for an incident plane wave of arbitrary polarization and thus the required explicit bidirectional dependence of surface reflectance. This reflectance is fully specular, however. The distinction between Lambert and specular surface reflection properties may be clarified by defining the bidirectional reflection distribution function, $f_r(\mu, \phi; \mu', \phi')$. The reflected solar radiance, I_r , in direction (μ', ϕ') from a surface with reflectance characterized by f_r is:

$$I_r(\mu', \phi') = \int_0^{2\pi} \int_0^1 \mu f_r(\mu, \phi; \mu', \phi') I(\mu, \phi) d\mu d\phi \quad (7-1)$$

where the radiance directed toward the surface is:

$$I(\mu, \phi) = \frac{F_0}{\mu} \delta(\mu - \mu_0) \delta(\phi) \quad (7-2)$$

and the surface incident solar flux is:

$$F_0 = \mu_0 \pi F e^{-\tau^*/\mu_0} \quad (7-3)$$

For a Lambert surface, f_r is isotropic (independent of angle), thus:

$$f_r^L(\mu, \phi; \mu', \phi') = \frac{A_L}{\pi} \quad A_L \equiv \text{albedo} \quad (7-4)$$

Substituting into Equation (7-1) above and integrating yields the relationship

$$I_r(\mu, \phi) = A_L F_0 / \pi \quad (7-5)$$

or the ratio of reflected flux (πI_r) to incident flux (F_0) is the albedo, A_L . Except for the diffuse (or multiply scattered) term (i.e. F^-) neglected in the definition of $I(\mu, \phi)$ above, this is the boundary condition used in the analysis of non-sunglint regions (see Isaacs, 1980, Equation 38):

$$F^+(\tau = \tau^*) = A_L [\pi F \mu_0 e^{-\tau^*/\mu_0} + F^-(\tau = \tau^*)] \quad (7-6)$$

For a specular surface, the bidirectional reflection distribution function is:

$$f_r^F(\mu, \phi; \mu', \phi') = \frac{\rho(\mu)}{\mu} \delta(\mu - \mu') \delta(\phi' - \phi + \pi) \quad (7-7)$$

where $\rho(\mu)$ is the Fresnel reflectivity for incidence angle, $\cos^{-1}\mu$. Substitution into (6-1) above yields a reflected radiance of:

$$I_r(\mu, \phi) = \begin{cases} \rho(\mu_0) F_0 / \mu_0 & \text{for } (\mu, \phi) = (\mu_0, \phi_0 + \pi) \\ 0 & \text{for (other } \mu, \phi) \end{cases} \quad (7-8)$$

Thus there is a mirror (or specular) reflection at observation angle $\cos^{-1}\mu = \cos^{-1}\mu_0$ and looking toward the sun. This occurs in satellite imagery at the primary specular point (PSP) which falls between the satellite subpoint and the solar subpoint. Methods for locating the PSP are described in Fett and Mitchell (1979) and Tsui and Fett (1980).

The nature of the problem changes considerably for wind-ruffled seas (cf. Burt, 1954). In this case, wind/wave interactions produce a sea surface slope distribution which may be characterized explicitly (Cox and Munk, 1954) or spectrally (Pierson and Moskowitz, 1964; Pierson and Stacy, 1973). The resultant wave slope geometry modifies in a statistical sense the relationship between the direction of incident radiation and the normal to the time-averaged calm surface. Examination of relevant imagery for these cases indicates a sun-glint region rather than a specular point and the surface reflectivity may best be characterized as intermediate between Lambert and specular. One potential approach to

treating the reflected radiance using Equation (7-1) is to define an effective bidirectional distribution function, f_r^E which is a linear combination of Lambert and specular functions) i.e.:

$$f_r^E = \alpha f_r^L + (1-\alpha) f_r^E \quad (7-9)$$

where α is some constant.

An alternative approach consists of: (1) determining the surface orientation (i.e., crosswind and upwind slopes) necessary to produce a specular reflection or glint given the sun/sensor geometry, (2) evaluating the angle of incidence for this surface orientation in the required rotated (from a calm sea) system, (3) calculating the Fresnel reflectivity for this angle of incidence using the optical properties of sea water, and (4) finding the probability of this surface orientation for the given wind conditions based on the Cox-Munk sea slope probability distribution function (PDF). The effective specular reflectivity is then defined as the product of the computed Fresnel reflectance for the given geometry and the probability of the required sea surface orientation for the given wind condition. A variety of investigators have used variations of this approach to incorporate the effects of reflection from the rough ocean surface (Mullamaa, 1964; Raschke, 1972; Fowler et al., 1977; Takashima and Takayama, 1981; Ahmad and Fraser, 1982).

The formulation used in this work is based on identical physical principles but is much more heuristic in implementation providing, however, an analytical result. Details of

the approach and relevant results are included in the following sections.

7.3 Wind Driven, Rough Ocean Surface Reflection Geometry

As previously discussed (Section 5), the location of particular satellite radiometer resolution elements (pixels) on the earth's surface (i.e., along the satellite subtrack and associated scan lines) is fixed by spacecraft orbital parameters. Consequently, the geometric orientation of sensor/surface pixel/sun is predictable from spacecraft and solar ephemeris data. For a hypothetical calm sea, only specific points along the orbit will allow for specular reflection. For a wind driven, rough ocean surface, however, it is apparent that orientations are probable which permit reflection of specular "glints" to the sensor. This requires that the surface is oriented such that: (1) the normal to the surface is coplanar with both the sun and sensor position vectors (i.e. in the principal plane) and (2) the normal bisects the angle formed by the intersection of these position vectors. Given the sun/sensor position vectors relative to a calm ocean surface, it is possible to evaluate the surface orientation fulfilling these requirements and characterizing this orientation by the surface slopes in two chosen orthogonal planes (which depend on the local surface normal). In practice these are chosen in the upwind and crosswind directions. Evaluation of the probability of such a surface orientation is based on available empirically derived wave

slope statistics defined in terms of surface slope components chosen (arbitrarily) in crosswind and upwind directions. The geometry of the wind driven, rough ocean surface is illustrated in Figure 7-1. The parameters defining the sun/pixel/sensor geometry are listed in Table 7-1 with accompanying explanation. Supplementary discussions of the rough ocean reflection geometry may be found in Takashima and Takayama (1981) and Ahmad and Fraser (1982).

A surface capable of producing a specular return to the sensor will have a surface normal (in the rotated or primed coordinate system):

$$\hat{n}' = (\cos \epsilon / 2, \sin \epsilon / 2, 0) \quad (7-10)$$

where the angle ϵ is that between sun and sensor position vectors or:

$$\epsilon = \cos^{-1}(\hat{o} \cdot \hat{s}) \quad (7-11)$$

The coordinates of \hat{n}' in the fixed (unprimed) $(\hat{x}, \hat{y}, \hat{z})$ system (required to evaluate the surface slope components) are obtained by transforming from primed to unprimed systems employing the transpose of transformation matrix \underline{M} , i.e.:

$$\hat{n} = \underline{M}^T \hat{n}' \quad (7-12)$$

The elements of the matrix, \underline{M} , are given by the components of the defined coordinate systems or:

$$M_{ij} = \hat{e}_j \cdot \hat{e}'_i \quad (7-13)$$

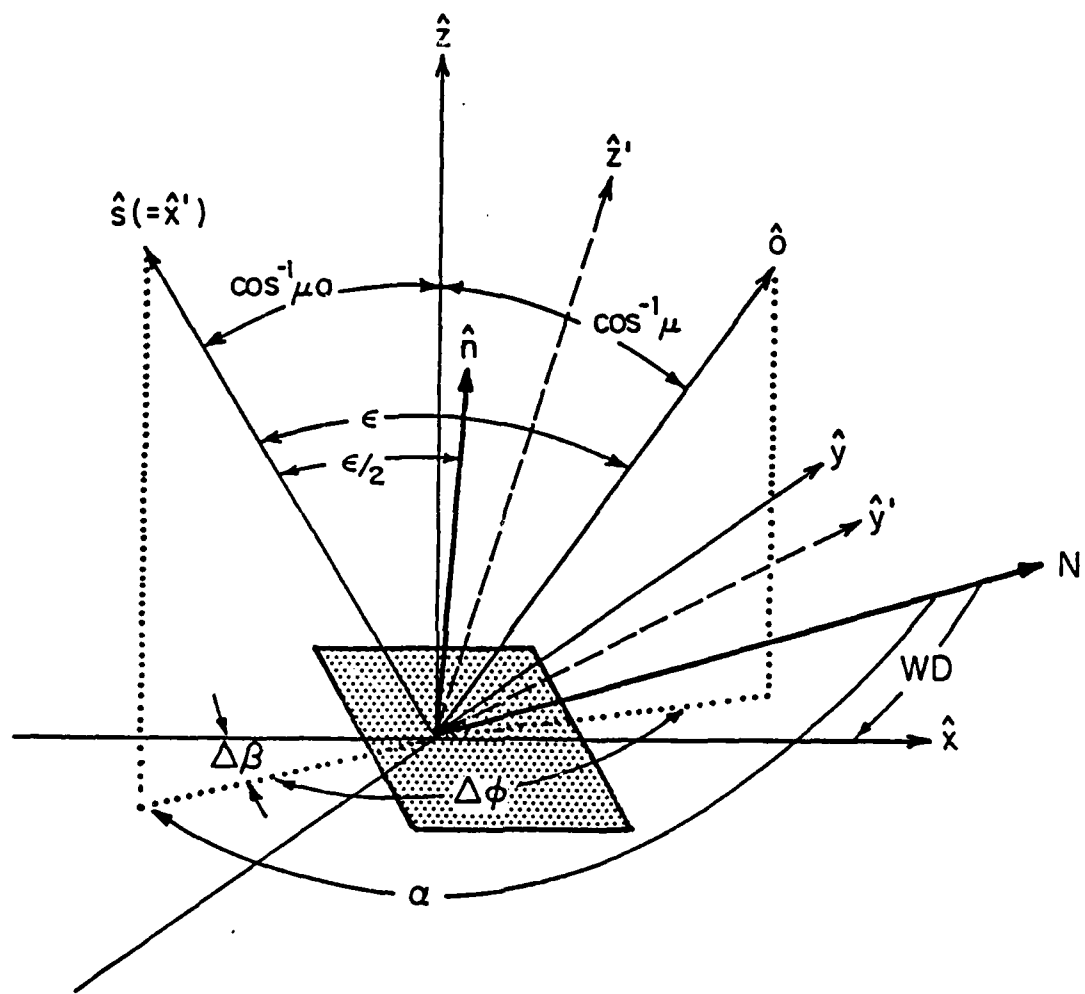


Figure 7-1. Wind driven, rough ocean surface reflection geometry.

\hat{s}	Solar unit position vector with respect to pixel
\hat{o}	Sensor unit position vector with respect to pixel
$(\hat{x}, \hat{y}, \hat{z})$	Cartesian coordinate system with respect to calm ocean surface with origin at pixel, \hat{x} oriented along direction of prevailing wind, and \hat{z} in direction of local zenith
μ_o	Solar zenith angle cosine with respect to \hat{z}
μ	Sensor zenith angle cosine with respect to \hat{z}
WD	Azimuth of wind direction measured clockwise from north
α	Azimuth of solar position vector measured clockwise from north
ϕ	Azimuth angle difference between solar and sensor position vectors
$(\hat{x}', \hat{y}', \hat{z}')$	Rotated Cartesian coordinate system on sloping ocean surface with origin at pixel, \hat{x}' in direction of \hat{s} , and \hat{z}' in direction of $(\hat{s} \times \hat{o})$
ϵ	Angle in $(\hat{s} \times \hat{o})$ plane between \hat{s} and \hat{o} ($\epsilon/2$ is the angle of incidence)
\hat{n}	Unit normal to surface in $(\hat{x}, \hat{y}, \hat{z})$ system
\hat{n}'	Unit normal to surface in $(\hat{x}', \hat{y}', \hat{z}')$ system
$\Delta\beta$	Azimuth angle difference from specular direction

Table 7-1. Sun/Pixel/Sensor Geometric Factors Defined in Figure 7-1

where: \hat{e}_j ($j = 1, 2, 3$) are vectors $\hat{x}, \hat{y}, \hat{z}$

and \hat{e}'_i ($i = 1, 2, 3$) are vectors $\hat{x}', \hat{y}', \hat{z}'$.

The rotated (primed) coordinate system is simply defined in terms of the unit position vectors \hat{s} and \hat{o} , i.e.:

$$\hat{x}' = \hat{s}, \quad \hat{z}' = \hat{s} \times \hat{o}, \quad \hat{y}' = \hat{z}' \times \hat{x}' \quad (7-14)$$

where from spherical geometry:

$$s = \begin{bmatrix} (1-\mu_0^2)^{\frac{1}{2}} \cos(180 + \Delta\beta) \\ (1-\mu_0^2)^{\frac{1}{2}} \sin(180 + \Delta\beta) \\ \mu_0 \end{bmatrix} \quad (7-15)$$

and:

$$\hat{o} = \begin{bmatrix} (1-\mu^2)^{\frac{1}{2}} \cos(180 + \Delta\beta + \Delta\phi) \\ (1-\mu^2)^{\frac{1}{2}} \sin(180 + \Delta\beta + \Delta\phi) \\ \mu \end{bmatrix} \quad (7-16)$$

Considering a sea surface height distribution $\xi(x, y)$ given by:

$$z = \xi(x, y) \quad (7-17)$$

or

$$f(x, y, z) = z - \xi(x, y) = 0,$$

the normal to the surface will be defined by the gradient function:

$$\bar{N} = \left(-\frac{\delta \xi}{\delta x}, -\frac{\delta \xi}{\delta y}, 1 \right) \quad (7-18)$$

The required surface slopes in upwind (i.e. \hat{x}) and crosswind directions then are:

$$z_u = \frac{-\delta\xi}{\delta x}, \quad z_c = \frac{-\delta\xi}{\delta y} \quad (7-19)$$

Based on the above definition of the surface normal:

$$z_u = -n_1/n_3; \quad z_c = -n_2/n_3 \quad (7-20)$$

where n_i are the components of the unit surface normal with respect to the fixed coordinate system.

Using Equations (7-10) through (7-20) the ocean surface slope components (z_u, z_c) and the angle of incidence (i.e. $\epsilon/2$) can be calculated given the sun and sensor position vectors (\hat{s}, \hat{o}).

7.4 Effective Fresnel Reflectivity Formulation

As a consequence of the relationships derived in the previous section, sea surface slope components in the upwind and crosswind directions (z_u and z_c , respectively) required to produce a specular glint can be evaluated based on satellite and sun ephemeris data. Assuming such a surface orientation, the magnitude of the ratio of reflected radiance to the incident solar radiance with incidence angle, $\epsilon/2$, is (Towne, 1967; Kraus, 1972):

$$\rho(\epsilon/2) = \frac{1}{2} \left\{ \left[\frac{\sin^2(\epsilon/2 - \kappa)}{\sin^2(\epsilon/2 + \kappa)} \right] + \left[\frac{\tan^2(\epsilon/2 - \kappa)}{\tan^2(\epsilon/2 + \kappa)} \right] \right\} \quad (7-21)$$

where

$$\kappa = \sin^{-1} \left[\frac{n_a}{n_s} \sin(\epsilon/2) \right] \quad (7-22)$$

and the indices of refraction for air and sea water are:

$$n_a = 1.000 \quad (7-23)$$

$$n_s = 1.338$$

The first term in (7-21) is the Fresnel reflectivity coefficient for the vertically polarized radiance, I_v , while the second is that for the horizontally polarized radiance, I_h . The polarization (P) is defined as their difference divided by their sum. The mean reflectivity is identical to Equation (7-21) above. These values are illustrated for an air/sea water interface as a function of incidence angle ($\theta_i = \epsilon/2$) in Figures 7-2 (a,b,c,d). The observed increase in mean reflectivity for low solar elevation angles, for example, is easily explained in terms of simple arguments based on Fresnel's relations (cf. Figure 7-2d).

Given that the surface orientation is characterized by slopes (z_u, z_c) and using Equation (7-21) to evaluate the Fresnel reflectivity, a relationship such as (7-8) may be used to calculate the reflected radiation. However, as discussed above, the probability of such a surface orientation is dependent on surface environmental conditions such as wind speed and thus, the frequency of occurrence of such an orientation given the wind conditions is sought. By coordinating aerial photographs with surface wind measurements Cox and Munk (1954) developed statistics about surface reflection derived from observed sunlint and hence inferred

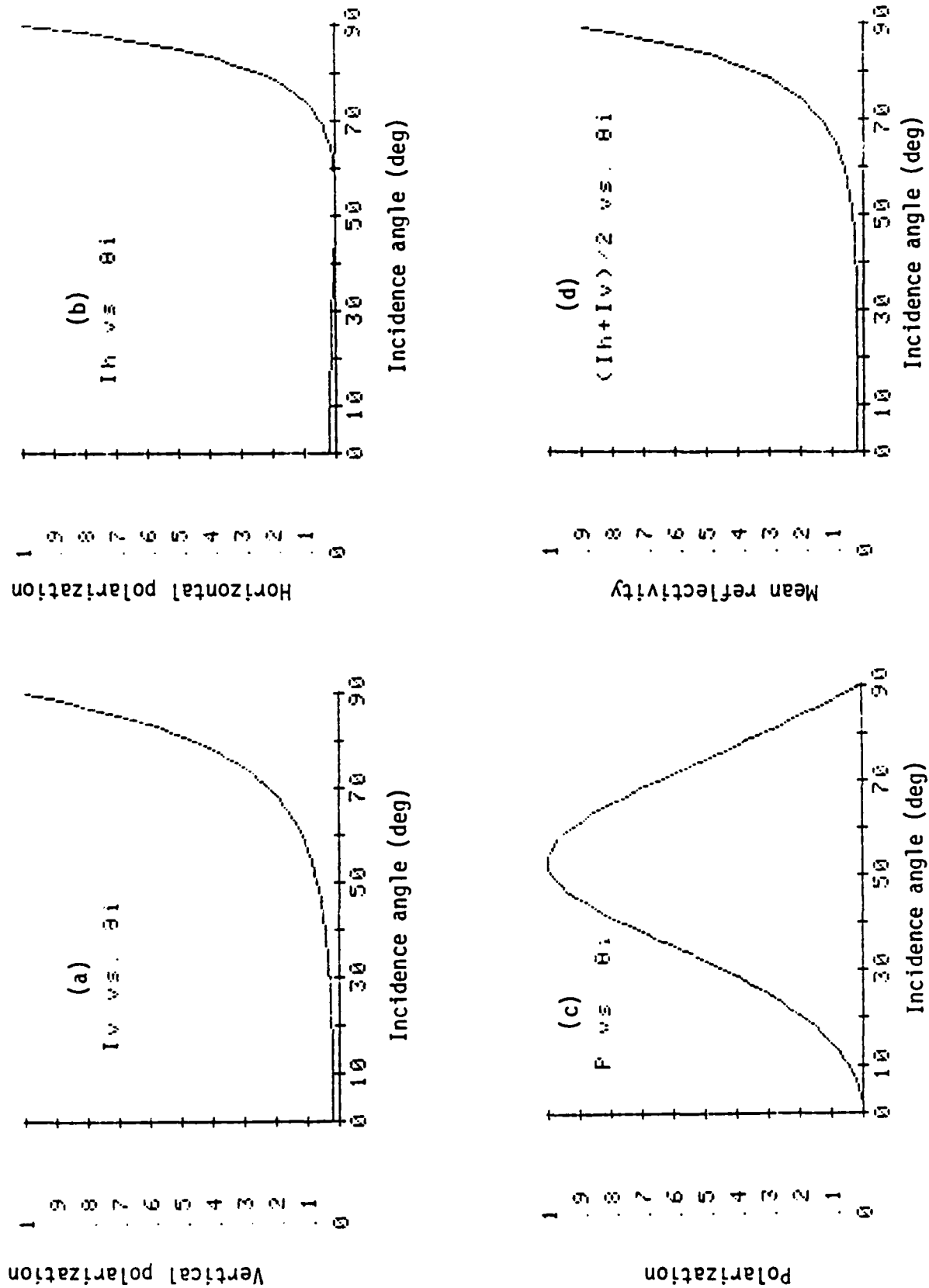


Figure 7-2. Calm ocean surface reflectivities based on Fresnel formulae for air/sea water interface: (a) vertical polarization, (b) horizontal polarization, (c) degree of polarization, and (d) mean reflectivity.

the probability density distribution function (PDF) for surface slopes (z_u, z_c) with wind speed w (ms^{-1}):

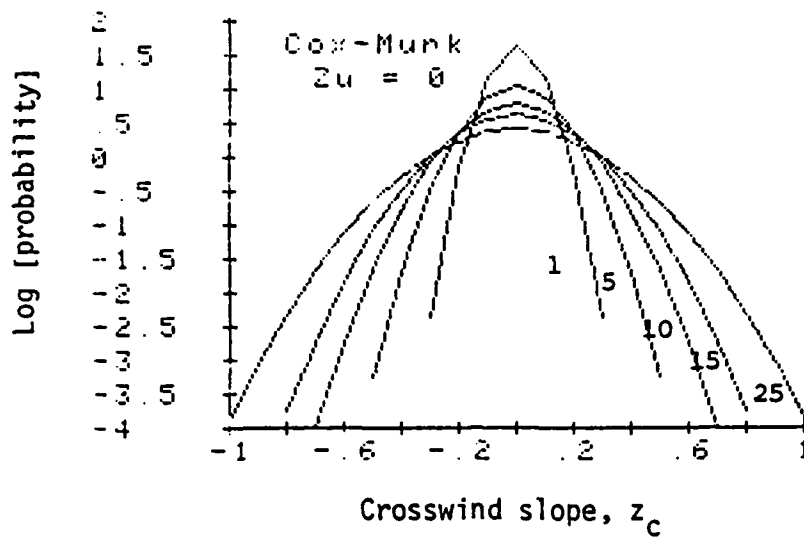
$$p(z_u, z_c) = \frac{1}{2\pi\sigma_u\sigma_c} \exp\left[-\frac{1}{2} \left\{ \left(\frac{z_c}{\sigma_c}\right)^2 + \left(\frac{z_u}{\sigma_u}\right)^2 \right\}\right] \quad (7-24)$$

where the variances in the crosswind and upwind directions, respectively, are (Guinn et al., 1979):

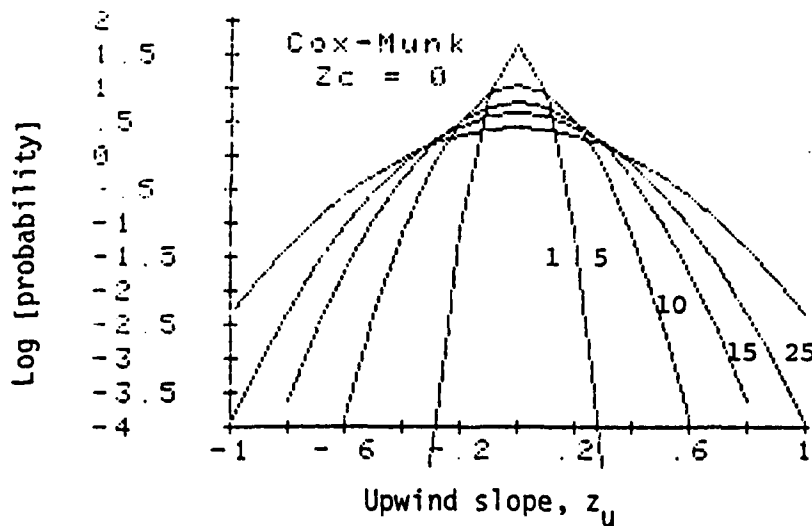
$$\begin{aligned} \sigma_c^2 &= .003 + .00192w \\ \sigma_u^2 &= .00316w \end{aligned} \quad (7-25)$$

Figure 7-3 (a,b), respectively, illustrate the variation of the crosswind and upwind probability density distribution functions for various wind speeds assuming zero slope in the orthogonal direction. As might be expected, there is a higher probability of non zero surface slopes with increasing wind speeds and, conversely, a higher probability of near zero surface slopes for lower wind speeds. When the slope in the orthogonal direction is already non zero (cf. Figure 7-4 (a,b) when it is 0.5), the PDF is predisposed to higher wind speeds and the behavior near zero slopes illustrated in Figure 7-3 is not observed.

It is important to note that the surface slope orientation statistics given by Equations (7-24, 7-25) represent a time averaged picture of the actual instantaneously changing surface slope orientation and are somewhat simplified. For example, it can be shown that the true sea height and its derivatives cannot be truly Gaussian (for a discussion, see

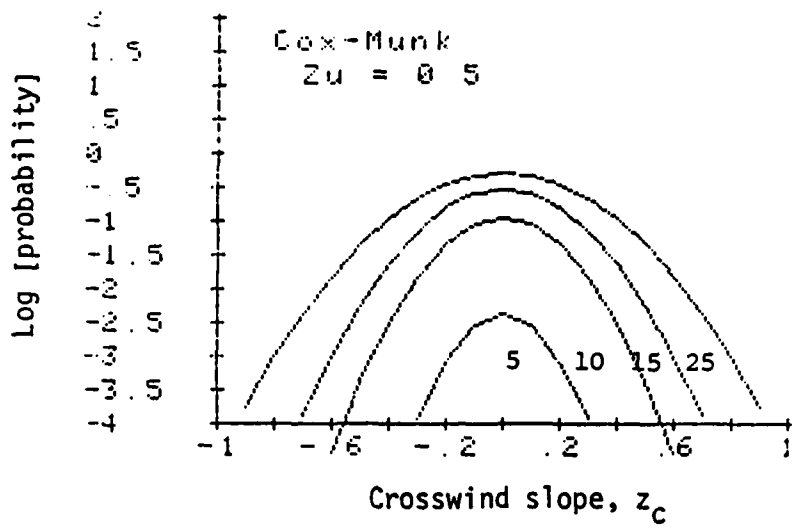


(a) Crosswind probability density distribution ($z_u = 0$).

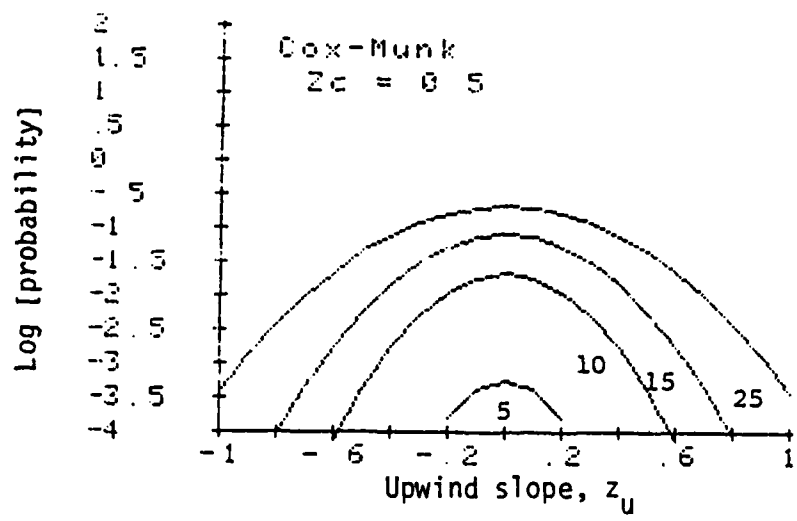


(b) Upwind probability density distribution ($z_c = 0$)

Figure 7-3. Sea surface slope probability density function (PDF) according to Cox and Munk (1954) in: (a) crosswind and (b) upwind directions.



(a) Crosswind probability density distribution ($z_u = 0.5$)



(b) Upwind probability density distribution ($z_c = 0.5$)

Figure 7-4. Sea surface slope probability density function (PDF) according to Cox and Munk (1954) in: (a) crosswind and (b) upwind directions.

Barrick, 1972). This may be remedied by adopting a product function $Gr(a,b)$ to modify the distribution in (7-24) above where $Gr(a,b)$ is the sum of products of Hermite polynomials, the Gram-Charlier sum (Guinn et al., 1979). The difference is very slight, however, and for most analytical purposes, the Gaussian is entirely adequate (see MacKay, 1959).

Given the Fresnel reflectivity (7-21) and the probability distribution function (7-24), an effective Fresnel reflectivity, R_f , is defined proportional to the product of the Fresnel reflectivity for a given surface orientation and the probability of occurrence of that orientation [as characterized by its surface slope components, (z_u, z_c)] dependent upon the surface wind speed through the Cox-Munk statistics, i.e.:

$$R_f \propto \rho(\epsilon/2) p(z_c, z_u) \quad (7-26)$$

Thus in the absence of an atmosphere, the reflected radiance, I_{ref} , above a rough ocean surface due to incident irradiance πF is (Mullamaa, 1964):

$$I_{ref} = \frac{\pi F \rho(\epsilon/2) p(z_c, z_u)}{4\mu(\hat{n} \cdot \hat{z})^4} \quad (7-27)$$

The effective Fresnel reflectivity defined above is used in this work to evaluate surface reflected contributions to the radiance in potential sunglint regions. The behavior of this function is illustrated in Figures 7-5 and 7-6 for a hypothetical sun at a zenith angle at 45° . For strict

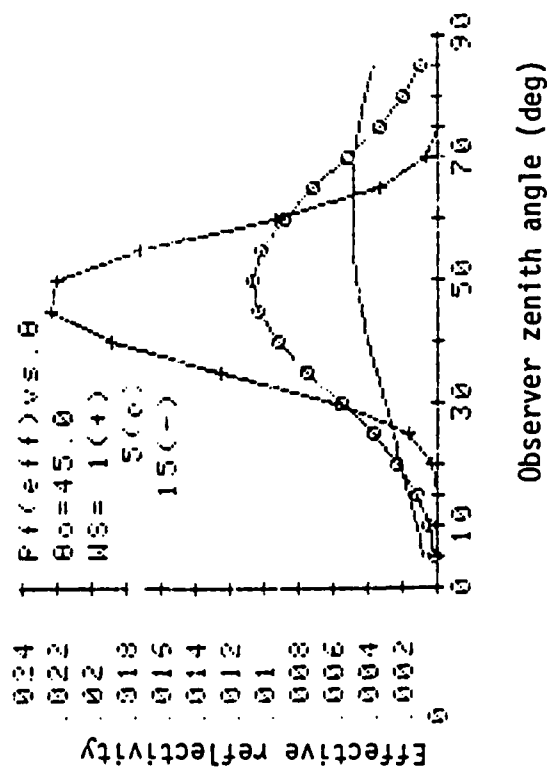


Figure 7-5. Dependence of effective reflectivity on observer zenith angle ($\Delta\phi = 180^\circ$) with sun at 45° from zenith for wind speeds of 1(+), 5(0), and 15(-) ms^{-1} .

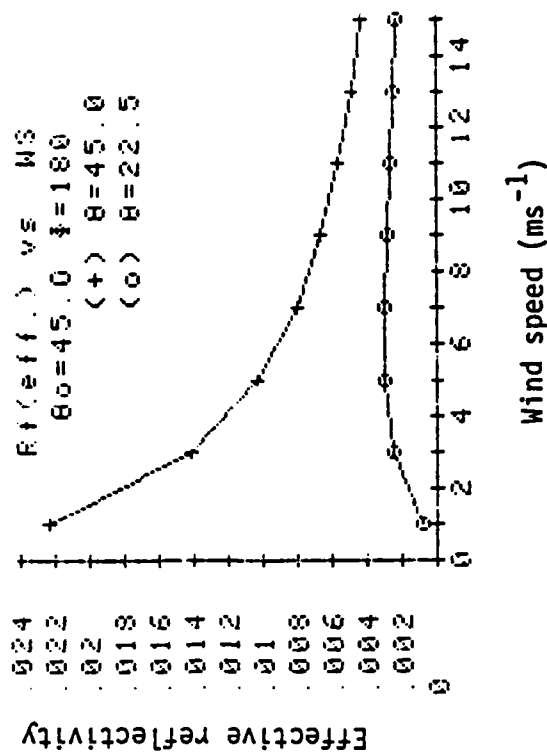


Figure 7-6. Dependence of effective reflectivity on wind speed at primary specular point (+) and in potential sunlint region (0) with sun at 45° from zenith and $\Delta\phi = 180^\circ$.

specular reflection (Equation (7-7)), the predicted mean reflectivity (Equation (7-21)) at the mirror angle (45°) is 0.0285. Figure 7-5 shows the wind speed dependent Gaussian spreading of the reflectivity due to the Cox and Munk PDF about the calm sea primary specular point (PSP) at 45° zenith angle. As wind speed increases and the sea roughens (for example at 15ms^{-1}), the angular dependence of reflection becomes less specular and more Lambertian. Figure 7-6 contrasts the dependence of the effective reflectivity on wind speed at the predicted PSP and away from the PSP but in a region of potential sunlint (here chosen at $\theta = 22.5^\circ$). Away from the PSP reflectivity actually increases with wind speed, while at the PSP rougher seas decrease predicted return from the surface. The behavior of the effective reflectivity defined above is qualitatively consistent with that based on examination of actual imagery (cf. Fett and Mitchell, 1977). In order to provide an example of the variation of surface reflectivity along an actual DMSP visible scan line, a case used by Tsui and Fett (1980) in their discussion of the primary specular point is adopted for analysis. The required input parameters characterizing the example are given in Table 7-2. These data are used in calculating solar and sensor position vectors for each of eleven surface pixels using the methodology described in Section 5. The specific scan line chosen on this revolution is that located at 185827 GMT which appears to contain the approximate position of the primary specular

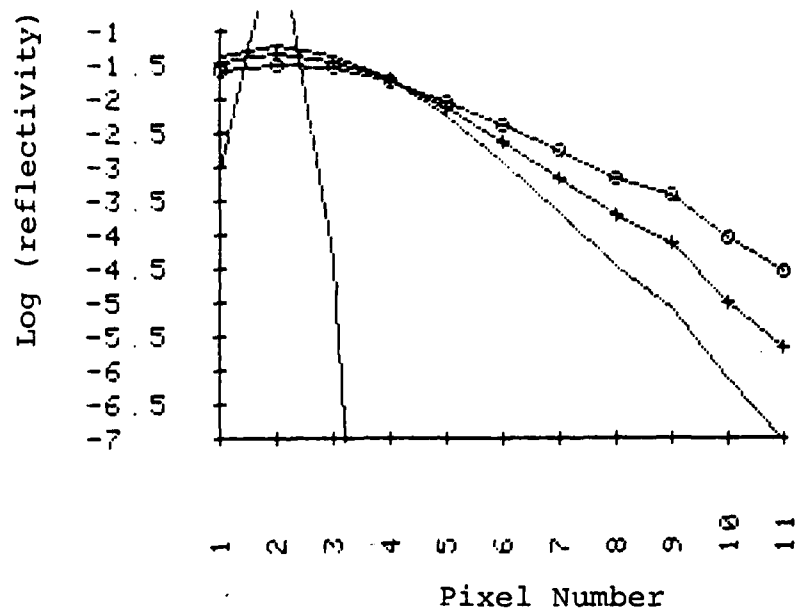
point at (10.7N, 113.9W). Results are shown in Figure 7-7(a) and (b) illustrating the dependence on wind speed and wind direction, respectively.

Table 7-2

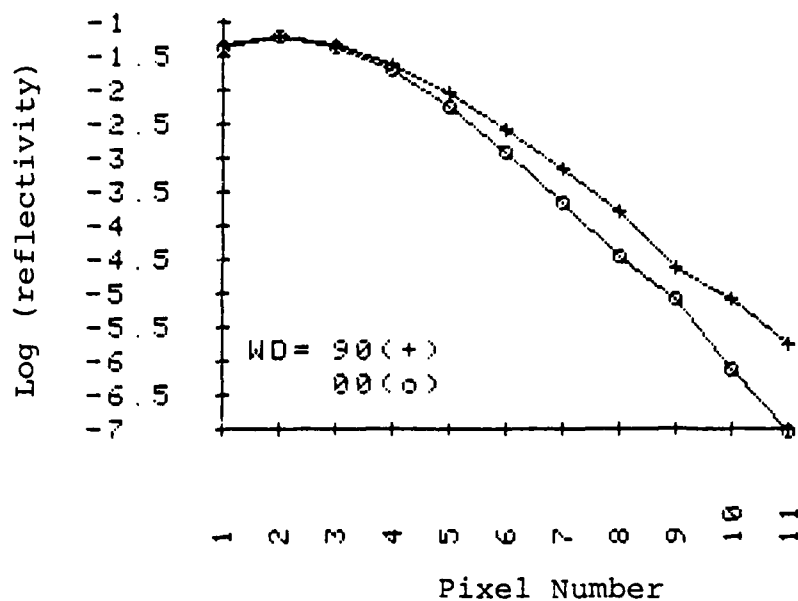
Input Background Parameters for
Surface Reflectivity Calculation

Solar Declination Angle (22 Aug 78)	12.0°
Longitude of Ascending Node	113.5°W
Time of Ascending Node	18:55:31 GMT
Satellite Orbital Inclination	98.7°
Satellite Altitude	833 km
Earth Radius	6370 km
Desired Scan Line	18:58:27 GMT

Figures 7-8 and 7-9 illustrate the application of (7-27) to the evaluation of reflected radiance above the rough ocean surface in the absence of an atmosphere (cf. Mullamaa, 1964). Assuming π units of incident flux and a solar zenith angle of 58.7°, Figure 7-8 shows the variation of the shape of the sunglint region in the principal plane ($\Delta\phi = 180^\circ$) with zenith angle (or equivalently sensor nadir angle). As wind speed increases the glint region spreads over a much broader area as the radiances near the PSP (say 60°) decrease and



(a) Wind speed dependence with wind direction of 000° for 0(|), 5(--), 7(+), and 10 ms⁻¹ (o).



(b) Wind direction dependence with wind speed of 5 ms⁻¹.

Figure 7-7. Variation of effective reflectivity along simulated scan line at 185827 GMT for assumed satellite background parameters (LN=113.5W, TN=18:55:31, SD=12.0°) illustrating dependence on: (a) wind speed and (b) wind direction.

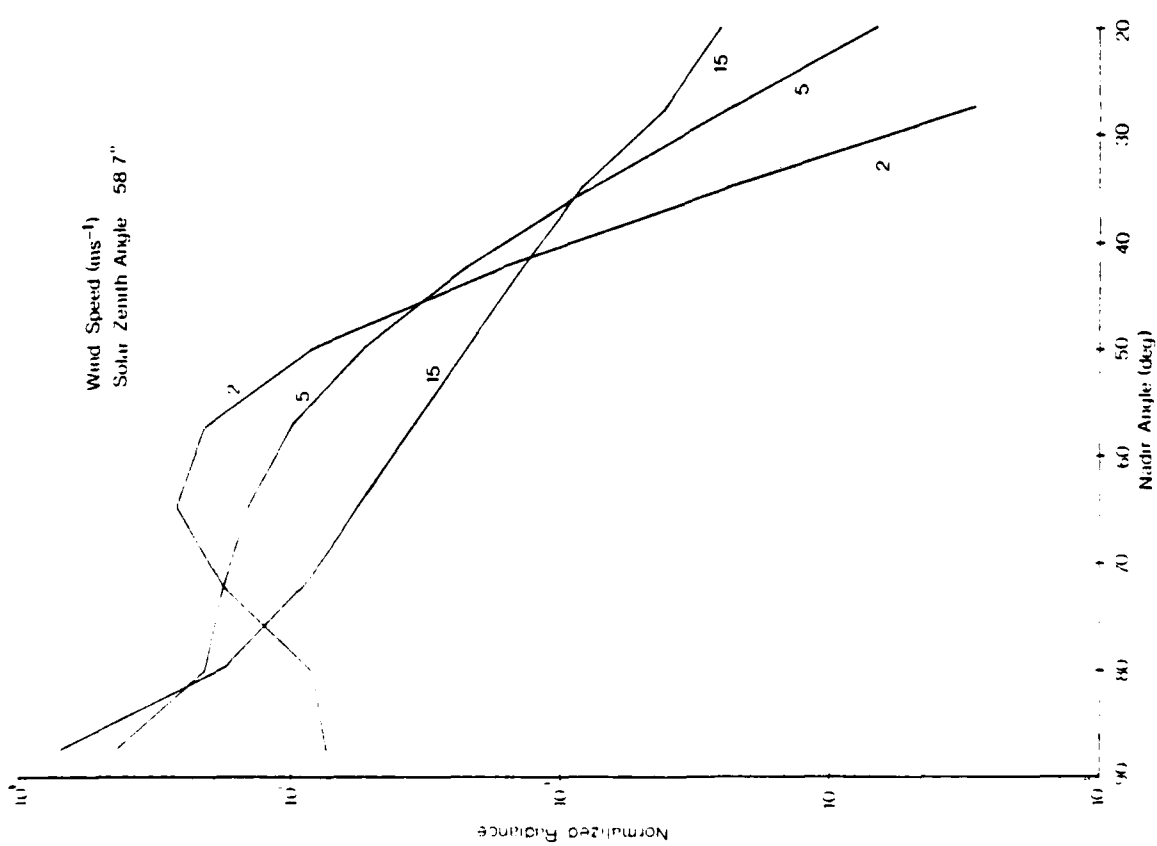


Figure 7-8. Variation of Reflected Radiance (assuming an incident irradiance of π) with zenith angle and wind speed in the principal plane (no atmosphere).

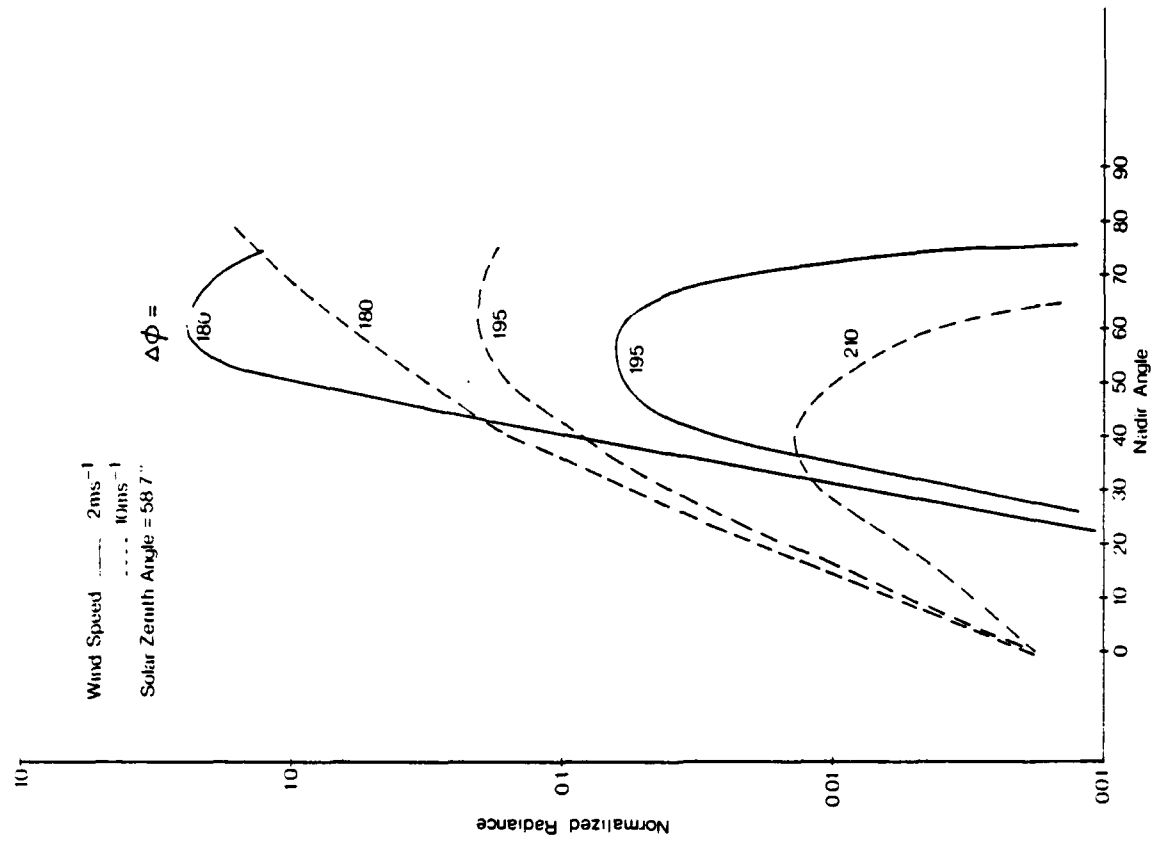


Figure 7-9. Variation of Reflected Radiance (assuming an incident irradiance of π) with wind speed and azimuth angle about the primary specular point ($\theta=58.7^\circ$, $\Delta\phi=180^\circ$).

those away from the PSP (say 30°) increase. Similar variations are notable in azimuth angle from Figure 7-9 where the spread of surface reflected energy from the vicinity of the PSP ($\Delta\phi = 180^\circ$, $\theta \approx 60^\circ$) is illustrated for the wind speed transition from 2 ms^{-1} to 10 ms^{-1} .

7.5 Incorporation Within the Radiance Simulation

In the presence of an atmosphere, incorporation of the rough ocean surface reflectance model within the radiance simulation requires some formal coupling with the radiative transfer treatment. Unfortunately, the stream approximation approach to the solution of the radiative transfer equation described in Section 6 is not ideally suited to the treatment of specular reflection. This is a consequence of the boundary condition on fluxes at the surface given by Equation (7-6). Since reflected intensities for a Lambert (i.e. non-specular) surface are independent of direction, the flux boundary condition is sufficient. For the specular case, however, reflected intensities are a strong function of direction (7-8, 7-9) and a rigorous boundary condition on the intensities should be used in the radiative transfer solution (Raschke, 1972; Plass et al., 1975; Guinn et al., 1979; Ahmad and Fraser, 1981). For example, for a surface with general bi-directional reflection distribution function, f_r , the upward radiance at the surface $I^+(\tau^*, \mu, \phi)$ is related to the downward radiance $I^-(\tau^*, \mu, \phi)$ in the direction (μ, ϕ) by:

$$\begin{aligned}
I^+(\tau^*, \mu, \phi) &= f_r(\mu, \phi; \mu_0, \phi_0) \mu_0 \pi F e^{-\tau^*/\mu_0} \\
&+ \int_0^2 \int_0^1 f_r(\mu, \phi; \mu', \phi') \mu' I^-(\tau^*, \mu', \phi') d\mu' d\phi' \quad (7-26)
\end{aligned}$$

Within the context of the stream approximation this is not possible. One suggested approach is to treat the specular reflection of the direct solar beam and Lambert reflectance of the multiply scattered field independently. Thus, for specular cases, an appropriate radiative transfer boundary condition may be formulated in analogy to (7-6) above as (Kerschgens et al., 1978):

$$F^+(\tau = \tau^*) = A_F [\pi F \mu_0] e^{-\tau^*/\mu_0} + A_L F^-(\tau = \tau^*) \quad (7-27)$$

where A_L is the wavelength dependent Lambert surface reflectance and A_F is the specular reflectance of the direct solar beam determined by Fresnel's formulae.

The approach adopted in the current radiance simulation model is based on further simplification of an approximate method for treating non-Lambertian surfaces suggested by Kaufman and Joseph (1982). The satellite incident radiance in sunglint regions, I_r , is approximated as the sum of two contributions: (a) radiance due to the specular reflection of the direct solar beam by the wind-roughened ocean surface, I_s , and (b) radiance due to back scattering by the atmosphere, I_A , i.e.:

$$I_r = I_s(R_f) + I_A(A_L) \quad (7-28)$$

The former term is evaluated based on the effective Fresnel reflectivity defined earlier, while the latter term depends on the usual Lambert surface albedo. In the immediate vicinity of the PSP for near calm conditions the contribution from (a) above clearly dominates that from (b). In regions remote from sunglint, the converse condition holds. In an atmosphere of total optical depth τ^* , the surface reflected direct solar term is:

$$I_s(R_f) = \pi F R_f \exp(-\tau^*/\mu_0) \exp(-\tau^*/\mu) \quad (7-29)$$

where πF is the wavelength dependent incident solar radiation, R_f is the effective Fresnel reflectivity (7-26) and the exponentials are attenuation factors for air masses of μ_0^{-1} , μ^{-1} in the solar and sensor directions, respectively. The atmospheric term is evaluated as described in Section 6.

This approximation essentially decouples the surface reflected radiance from that due to atmospheric scattering, an approach often used in the formulation of remote sensing problems over land (cf. Fraser and Curran, 1976). It also ignores the relation of diffuse and specularly reflected components available from (7-1), i.e.:

$$A_L = \frac{1}{\pi} \int_0^{2\pi} \int_0^1 R_f \mu d\mu d\phi \quad (7-30)$$

However, as a practical matter, comparison of a variety of results based on (7-28) with accurate numerical treatments (such as Plass et al., 1975; Ahmad and Fraser, 1982) indicate that this approach provides a quite reasonable simulation of the qualitative behavior of the sunglint phenomenon. For example, Figure 7-10 is a comparison of results using (7-28) to a numerical solution (Ahmad and Fraser, 1982) for wind speeds of 5.15 and 10.30 ms^{-1} and two solar zenith angles: (a) 20° and (b) 57° . Radiances are shown in the principal plane for a variety of sensor zenith angles extending from directions away from sunglint ($\phi = 180$) to those in the vicinity of the primary specular points ($\phi = 0$; $\theta = 20^\circ$, 57° , respectively). Note that the shape of the sunglint region ($\phi = 0$) and its variation with wind speed, solar position, and sensor zenith angle are simulated quite well by the approximation. Magnitudes of the radiances away from the respective primary specular points and particularly in the anti-solar direction ($\phi = 180^\circ$) underestimate the accurate calculations due to the particular treatment of the atmospheric scattered contribution used in the approximation results illustrated (a zero Lambert surface albedo was used).

7.6 Radiance Simulations in Sunglint Regions

Incorporating the surface reflection submodel within the overall simulation algorithm provides the capability to model radiances in sunglint regions. As an example, the sensitivity of simulated radiance to variations in relative

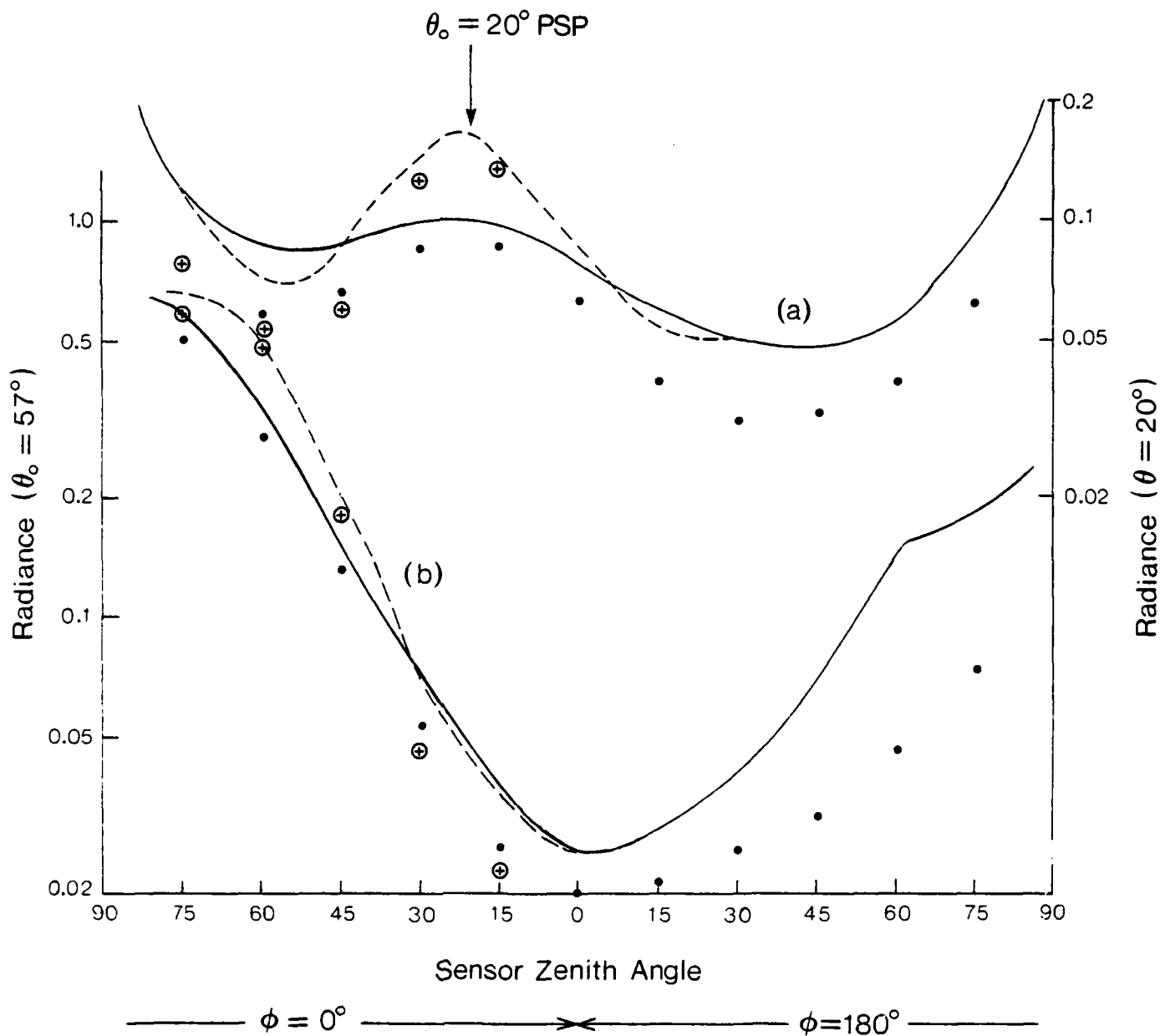


Figure 7-10. Comparison of Radiance Results from Numerical Simulation of Ahmad and Fraser (1982) to Approximate Results Summing Surface Specular Reflected and Atmospheric Scattered Contributions Only. [Exact: 5.15 ms^{-1} (---), 10.3 ms^{-1} (—); Approximate: 5.15 ms^{-1} (\oplus), 10.3 ms^{-1} (\bullet)]. Solar Zenith Angles of (a) 20° and (b) 57° .

humidity and wind speed are illustrated in Figures 7-11 and 7-12, respectively. These calculations are based on the same input data and hence scan line surface reflectivity calculation provided in Figure 7-7. Figure 7-11 illustrates the predicted effect of an increase in relative humidity from 50% to 95% in the vicinity of the primary specular point[†] (pixel number 2 in Figure 7-7) assuming a wind speed of 5.0 ms⁻¹ and a maritime aerosol model with a 0.4 km scale height. Radiances decrease by about 15% as relative humidity increases within the indicated range. Previous simulations for non-sun glint conditions (Isaacs, 1980) predicted increased radiances with increased relative humidity (see Figure 2-1) primarily due to enhanced aerosol backscattering. While scattered contributions are also enhanced in the present situation, the gross effect is determined by a decrease in the magnitude of the surface reflected solar radiation due to extinction of the solar beam both prior to and subsequent to surface reflection.

The sensitivity of simulated radiances to variations in wind speed along the chosen scan line is illustrated in Figure 7-12. The base case is a relative humidity of 50% and a maritime aerosol model with scale height of 1.2 km. Pixel 2 is closest to the PSP while pixels 1 and 3 are on either side (pixel 1 is on the subsatellite track). At low

[†]The location calculated for this pixel assuming nominal satellite orbital parameters is 10.5°N latitude, 114.5°W longitude.

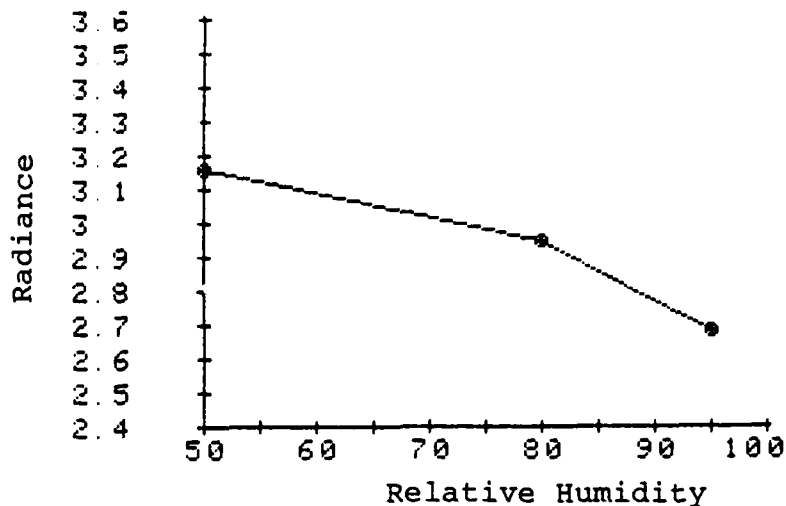


Figure 7-11. Dependence of simulated DMSP radiance (mW cm⁻² μm⁻¹ sr⁻¹) in vicinity of primary specular point on relative humidity. (Maritime aerosol model, H=0.4 km, ws=5.0 ms⁻¹)

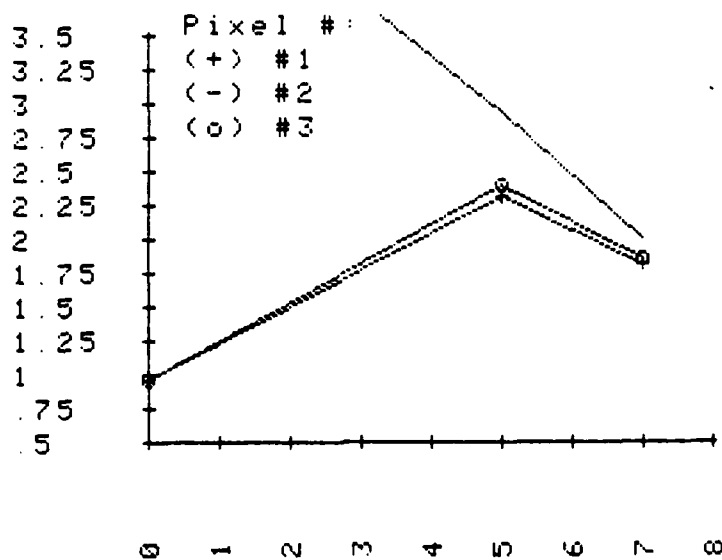


Figure 7-12. Dependence of simulated DMSP radiance on wind speed in the vicinity of the primary specular point (Pixel #2) on scan line at 185830 GMT.

wind speeds, the radiance returned to the sensor is quite specular. As wind speed increases, however, the pixels along the scan line become almost indistinguishable due to the surface roughness. Note that the radiances from pixels neighboring the PSP actually increase somewhat as their probability of returning sunglint to the sensor and, hence, effective reflectivities increase with increasing wind speed.

In each of the cases described above, the aerosol scale height has remained constant while either wind speed or relative humidity have been varied. In the example to follow the modifying effect of increased aerosol loading in a sunglint region is investigated.[†] The case examined is for a maritime aerosol with relative humidity of 50%. The scan line chosen is at 15:06:10 GMT on 7/27/75 for an ascending pass with ascending node of 94.0° West longitude at 15:00:08 GMT. The solar declination angle for this date is 19.2°. Figures 7-13 and 7-14 illustrate the effect of increasing aerosol scale height on the scan line sunglint pattern assuming surface wind speeds of 1.5 and 5.0 ms⁻¹, respectively. As the scale height increases the dominant effect is a radiance decrease near the primary specular point (located near pixel number 6). There is an accompanying slight increase for pixels remote from the glint region (numbers 1-2, 10-11). Thus, the aerosol layer acts to smooth out the radiance gradient due to surface reflection.

[†] This case is the subject of Section 7.7.

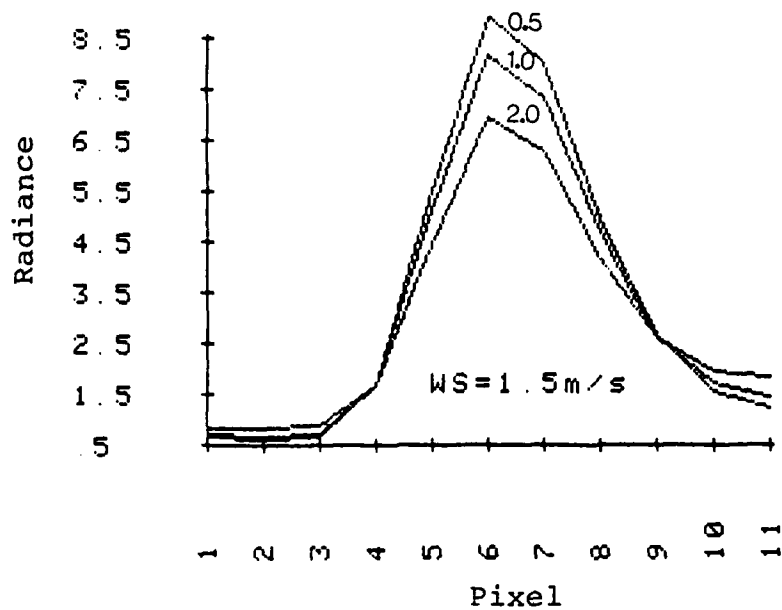


Figure 7-13. Dependence of radiance on aerosol scale height in sunglint area. (Maritime aerosol, RH = 50%, WS = 1.5 ms⁻¹, AN = 94°, TN = 15008, GMT = 150610, SD = 19.2°.)

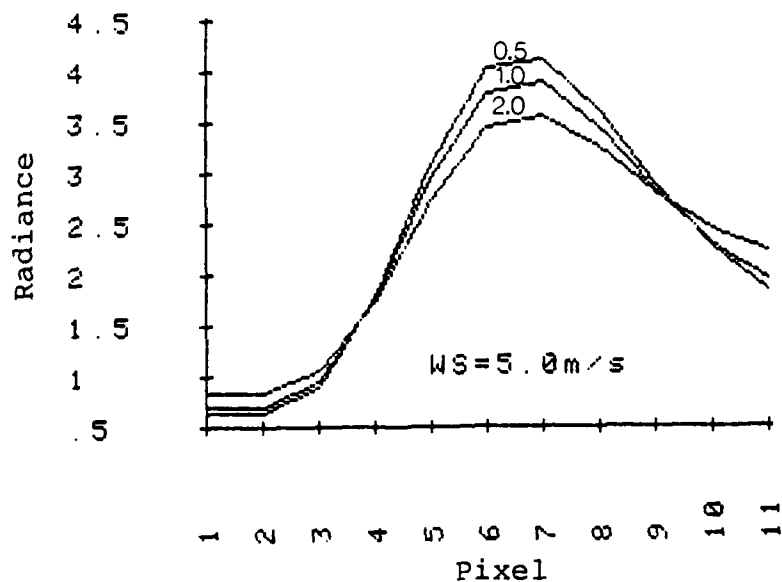


Figure 7-14. Dependence of radiance on aerosol scale height in sunglint area. (Maritime aerosol, RH = 50%, WS = 5 ms⁻¹, AN = 94°, TN = 150008, GMT = 150610, SD = 19.2°.)

7.7 Data Intercomparison Case Study

Hardcopy imagery illustrating the typical sunlint pattern observed in DMSP visible data was obtained[†] for the purpose of conducting a validation of the modeling methodology described in previous sections. The data utilized was for a morning ascending revolution of FTV 7529 on 27 July 1975 located over the Gulf of Mexico with ascending node at 94.0° West longitude at 15:00:08 GMT. The imagery is illustrated in Figure 7-15.

The simulation model was exercised for a scan line chosen at 150610 GMT in a relatively cloud free area of the Gulf of Mexico in the vicinity of the primary specular point (located at 18.7°N, 92.3°W). Concurrent meteorological data used as input for the simulation indicated variable surface winds of between 0 and 5.0 ms⁻¹, relative humidities of 90-95%, and surface visual ranges of 90-100 km. The surface visual range and relative humidity values were jointly used in conjunction with the maritime aerosol model to derive an appropriate scale height value (0.08 km). Results for the surface effective reflectivity and scan line radiance vs. pixel number are shown in Figures 7-16a and b, respectively.

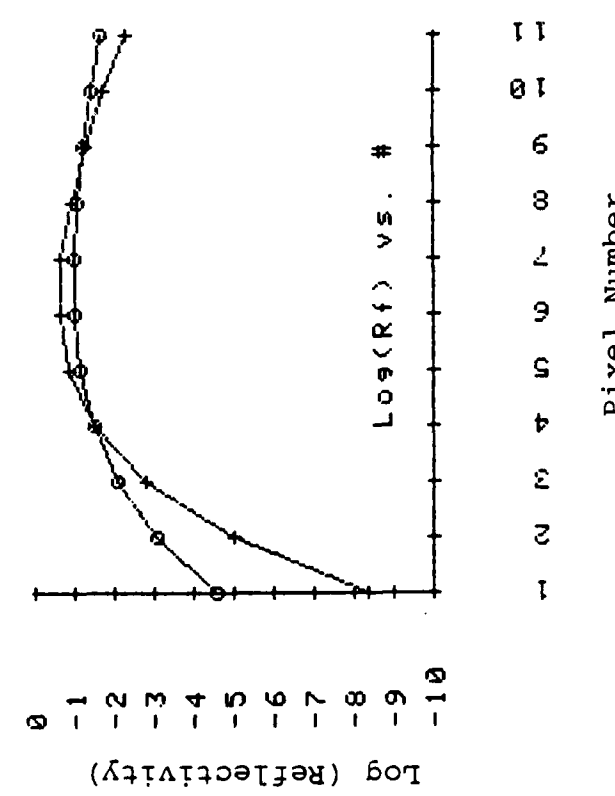
In order to accomplish a comparison with the hardcopy imagery, film transmission density was read directly from the data using a 30µm square sampler along the 150610 GMT scan line. Readings were taken every 5mm for eventual

[†]R. Fett, NEPRF.

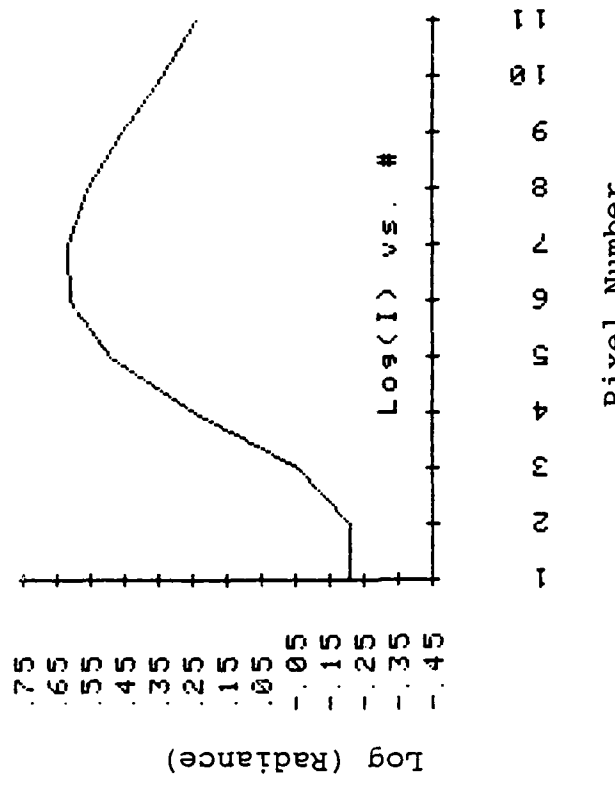


115:14:10
115:13:10
115:12:10
115:11:10
115:10:10
115:09:10
115:08:10
115:06:10
115:05:10
115:04:10

Figure 7-15. DMSP VHR imagery for 27 July 1975 (FTV 7529, ascending REV 0060)



(a) Effective reflectivity for wind speeds of 1.5 ms⁻¹ (+) and 5 ms⁻¹ (o).



(b) Radiance along scale line with wind speed 5 ms⁻¹ and relatively humidity of 95% for maritime (-) aerosol models.

Figure 7-16. Model simulation of sunglint phenomenon in vicinity of primary specular point based on data for FTV 7529 on 27 July 1975 at 150610 GMT (AN = 94°, TN = 150008, SD = 19.2°).

alignment with simulated pixels. Using the gray shade scale provided on the imagery, density readings were expressed in terms of one of the 64 available gray shades. These in turn were converted back to digital word inputs by reversing the contrast enhancement process using the appropriate (in this case MOD1-Low) mapping curve digitized from Fett and Mitchell (1977) (see Figure 7-17). In this manner, the film density trace was converted to values roughly proportional to the original radiance values used to construct the image matrix. Since these values are relative, it is not possible to assign them absolute radiance values. Instead it was decided to calibrate the data using the model simulated result at pixel number 6 for scaling, since the model performs best close to the predicted PSP. The result of this comparison is shown in Figure 7-18. Considering the assumptions adopted in the analysis and the difficulty in treating surface features and cloud elements readily apparent in the imagery, the performance of the simulation is reasonable.

7.8 DMSP Imagery Simulation

By simulating scan lines (as in Section 6.5) in an appropriate successive manner, segments of DMSP imagery may be simulated. In order to demonstrate this capability, six sample cases (see Table 7-3) of input meteorological data (consisting of wind speed, relative humidity, and scale height) were used to simulate portions of DMSP imagery

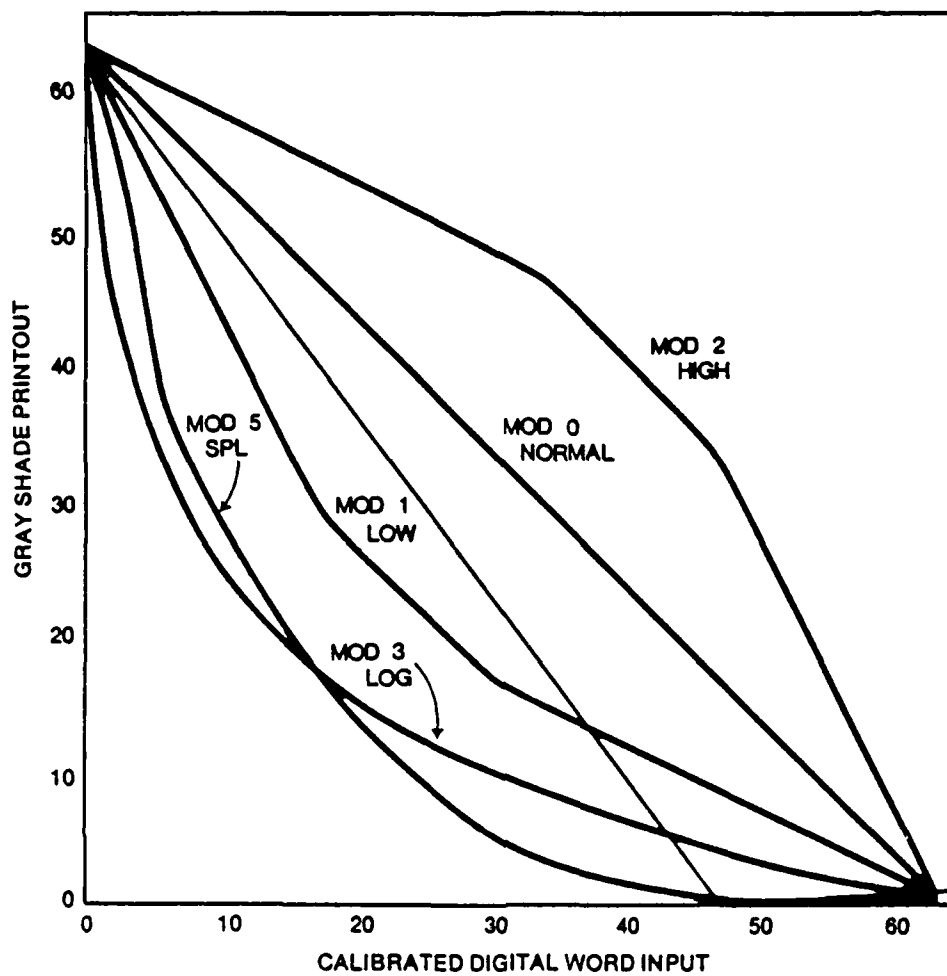


Figure 7-17. DMSP enhancement mode mapping curves (from Fett and Mitchell, 1977).

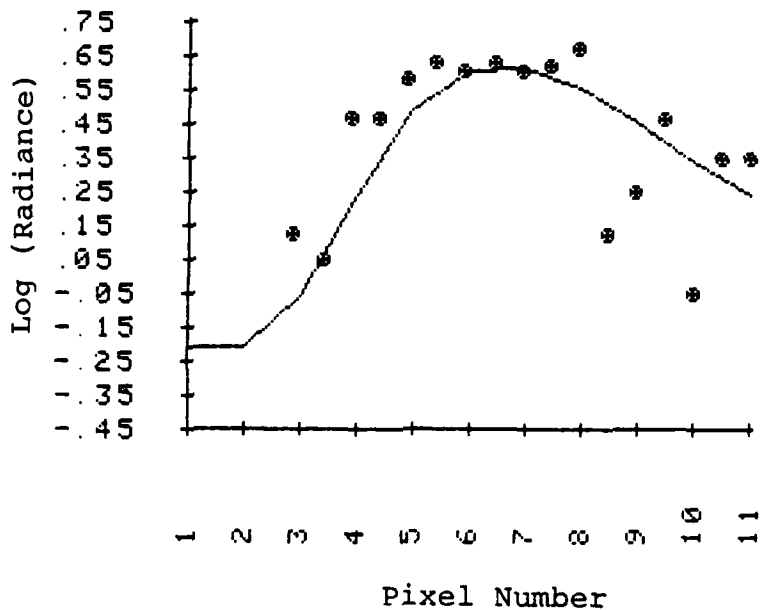


Figure 7-18. Comparison of model simulated radiance (-) and data (⊙) obtained from sensometry of corresponding hard copy imagery in the vicinity of sunlint. (FTV 7529, 7/27/75, 150610 GMT, AN = 94°, TN = 150008, SD = 19.2°, MOD1-LOW).

corresponding to the satellite parameters given in Table 7-2. The maritime aerosol model was employed in these calculations. Results for these imagery simulation cases contoured in radiance units of $\text{mWcm}^{-2} \mu\text{m}^{-1} \text{sr}^{-1}$ are illustrated in Figures 7-19 (a-f).

Table 7-3
DMSP Imagery Radiance Simulation Cases

Case #	Wind Speed (WS) ms^{-1}	Relative Humidity (%)	Scale Height (km)	Figure #
1	0.0	50	1.2	7-19a
2	5.0	50	1.2	7-19b
3	10.0	50	1.2	7-19c
4	5.0	50	0.4	7-19d
5	5.0	80	0.4	7-19e
6	5.0	90	0.4	7-19f

The ordinate corresponds to the subsatellite track and is divided into five segments hatch-marked at 30 second intervals commencing at 185730 GMT. The corresponding abscissa represents the eastward scan portion for this morning satellite and is divided into ten equal segments (i.e. eleven pixels) using (5-29) (e.g., the odd pixels in Table 5-2). Each figure thus simulates 24 minutes of imagery data assuming uniform meteorology within the field of view. (This restriction is easily removed.) Cases are selected to provide a representative variation of near surface meteorology with a calm sea base case (Table 7-3, case 1), cases 1-3 illustrating the effect of a wind speed increase, cases

4-6 that of an increase in relative humidity, and a comparison of cases 2 and 4 the effect of a decrease in aerosol scale height.

For the calm sea (case 1, Figure 7-19a), a bright specular point (at asterisk) appears at the approximate position of the PSP. Away from the PSP, radiance levels are determined by aerosol backscatter and Lambert surface reflectance. The gradual increase in radiance from the subsatellite track to the eastern edge of the data is attributable to atmospheric scattering effects. As wind speed increases (Figures 7-19b, c) and the sea surface roughens, the intensity of the PSP decreases drastically as radiance levels increase for the pixels in the immediate vicinity. The decrease of radiance at the PSP and the distance from the PSP of pixels with increased radiance levels are proportional to wind speed. At a wind speed of 10 ms^{-1} (Figure 7-19c), the radiance field is remarkably uniform differing from maximum to minimum by less than a factor of 2. (This factor is unity for a Lambert surface.)

Cases 4, 5, and 6 (Figures 7-19d, e, f, respectively) illustrate the effect of an increase in relative humidity for fixed surface wind speed and aerosol scale height. In general, as relative humidity increases, radiances in the sunlint region decrease due to increases in the attenuation factors of the dominant surface reflected direct term (see 7-29). Away from the sunlint region, increases in relative humidity increase simulated radiance due to enhanced aerosol

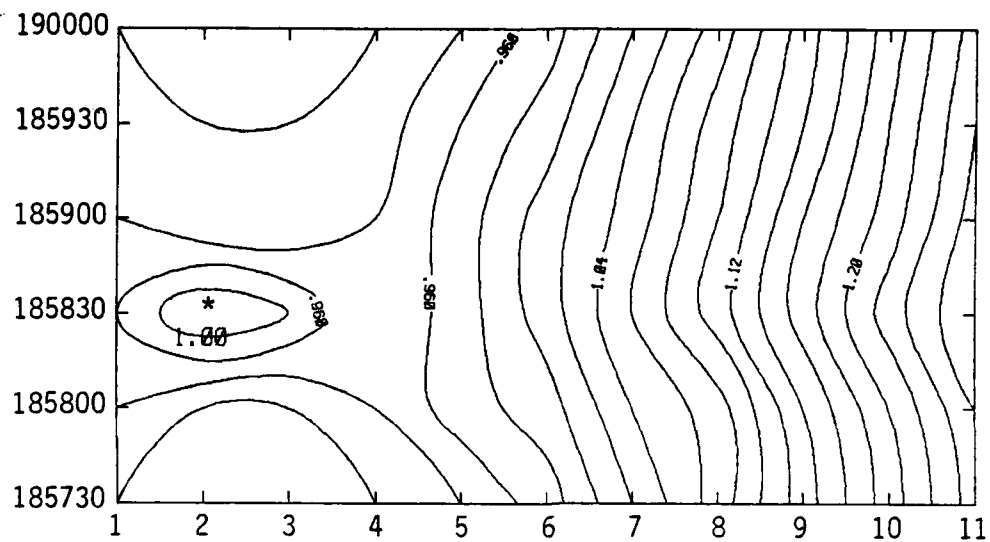


Figure 7-19a. Simulated DMSP radiances, case 1:
 $WS = 0.0 \text{ ms}^{-1}$, $RH = 50\%$, $H = 1.2 \text{ km}$.

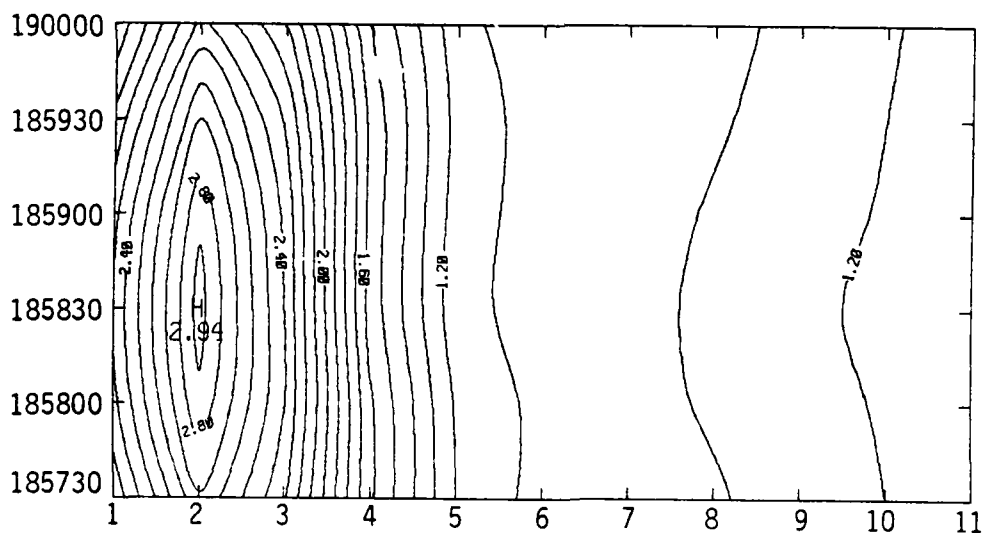


Figure 7-19b. Simulated DMSP radiances, case 2:
 $WS = 5.0 \text{ ms}^{-1}$, $RH = 50\%$, $H = 1.2 \text{ km}$.

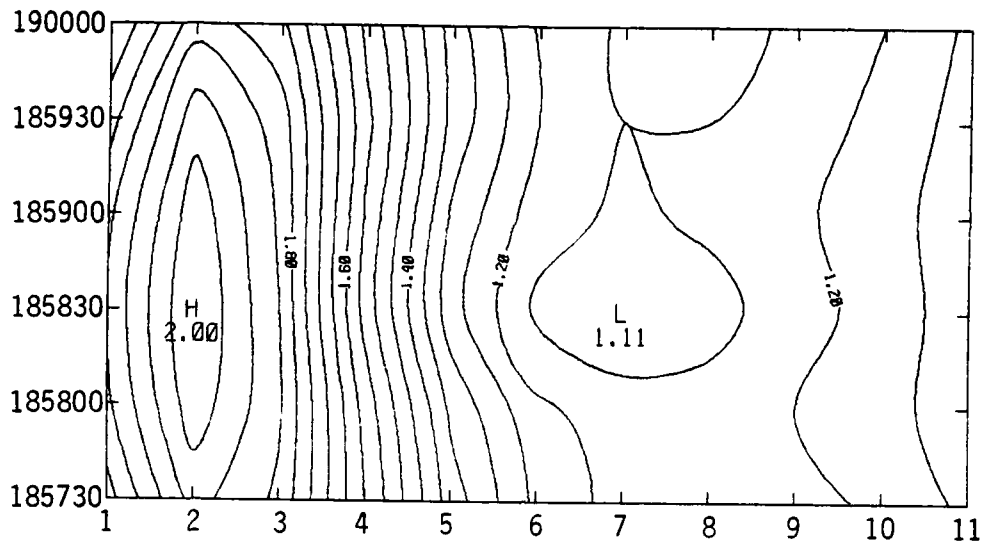


Figure 7-19c. Simulated DMSP radiances, case 3:
 $WS = 10.0 \text{ ms}^{-1}$, $RH = 50\%$, $H = 1.2 \text{ km}$.

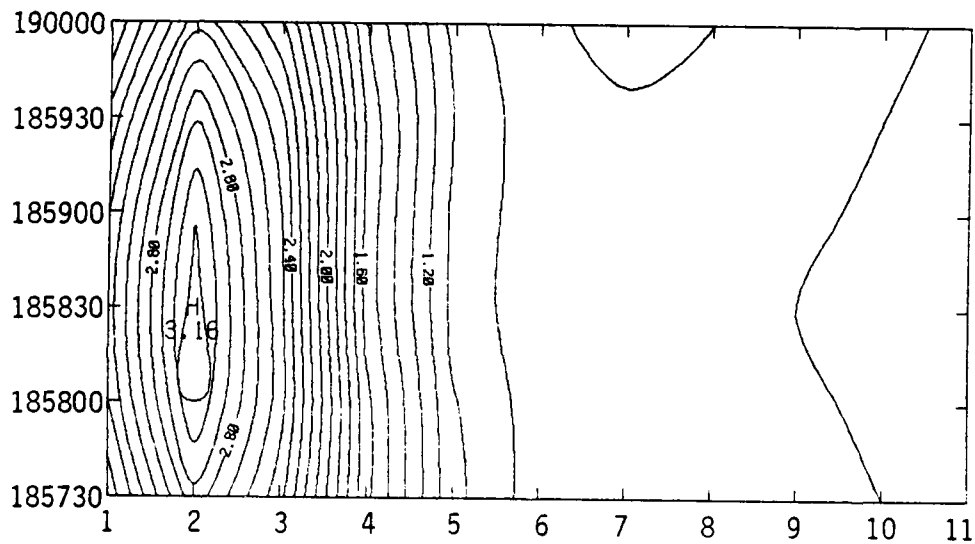


Figure 7-19d. Simulated DMSP radiances, case 4:
 $WS = 5.0 \text{ ms}^{-1}$, $RH = 50\%$, $H = 0.4 \text{ km}$.

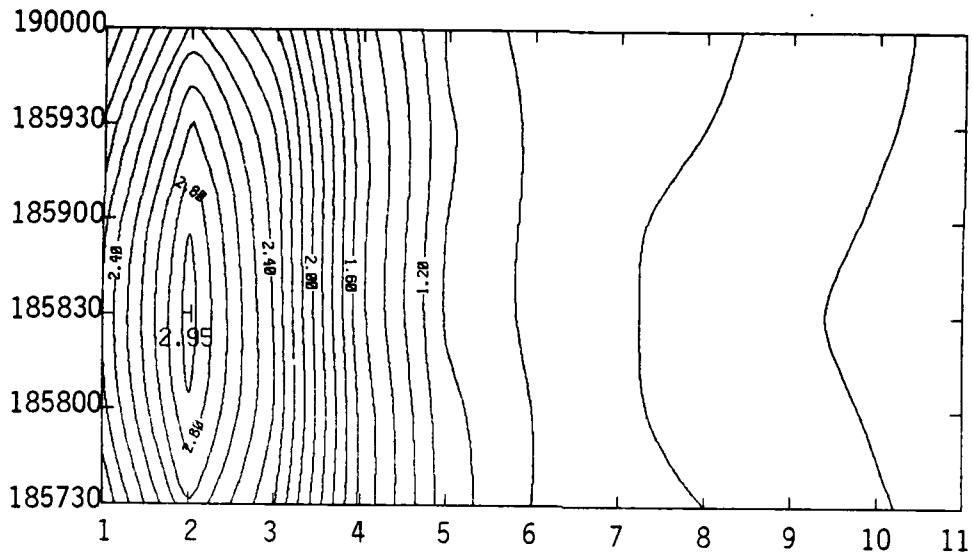


Figure 7-19e. Simulated DMSP radiances, case 5:
 $WS = 5 \text{ ms}^{-1}$, $RH = 80\%$, $H = 0.4 \text{ km}$.

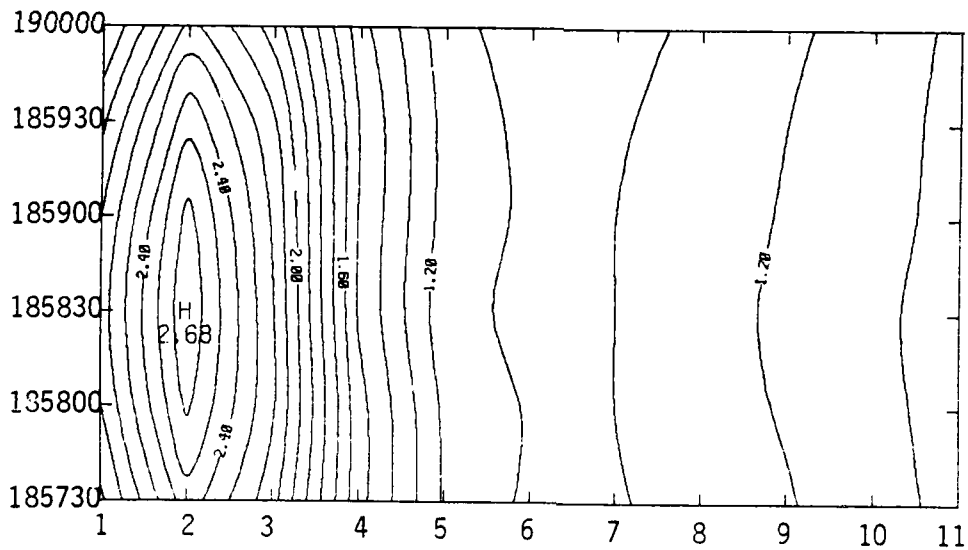


Figure 7-19f. Simulated DMSP radiances, case 6:
 $WS = 5 \text{ ms}^{-1}$, $RH = 90\%$, $H = 0.4 \text{ km}$.

backscatter. Thus increasing wind speed and relative humidity have similar impacts on the appearance of the sunlint region.

Additional ambiguity is introduced by the effect of aerosol scale height variations. Careful comparison of cases 2 (Figure 7-19b) and 4 (Figure 7-19d) illustrates that scale height increases likewise decrease the glint region radiances while increasing those in regions remote from the glint region. These calculations are summarized in Figure 7-20 where a representative scan line ($t = 185830$ GMT) of radiances is plotted for each case.

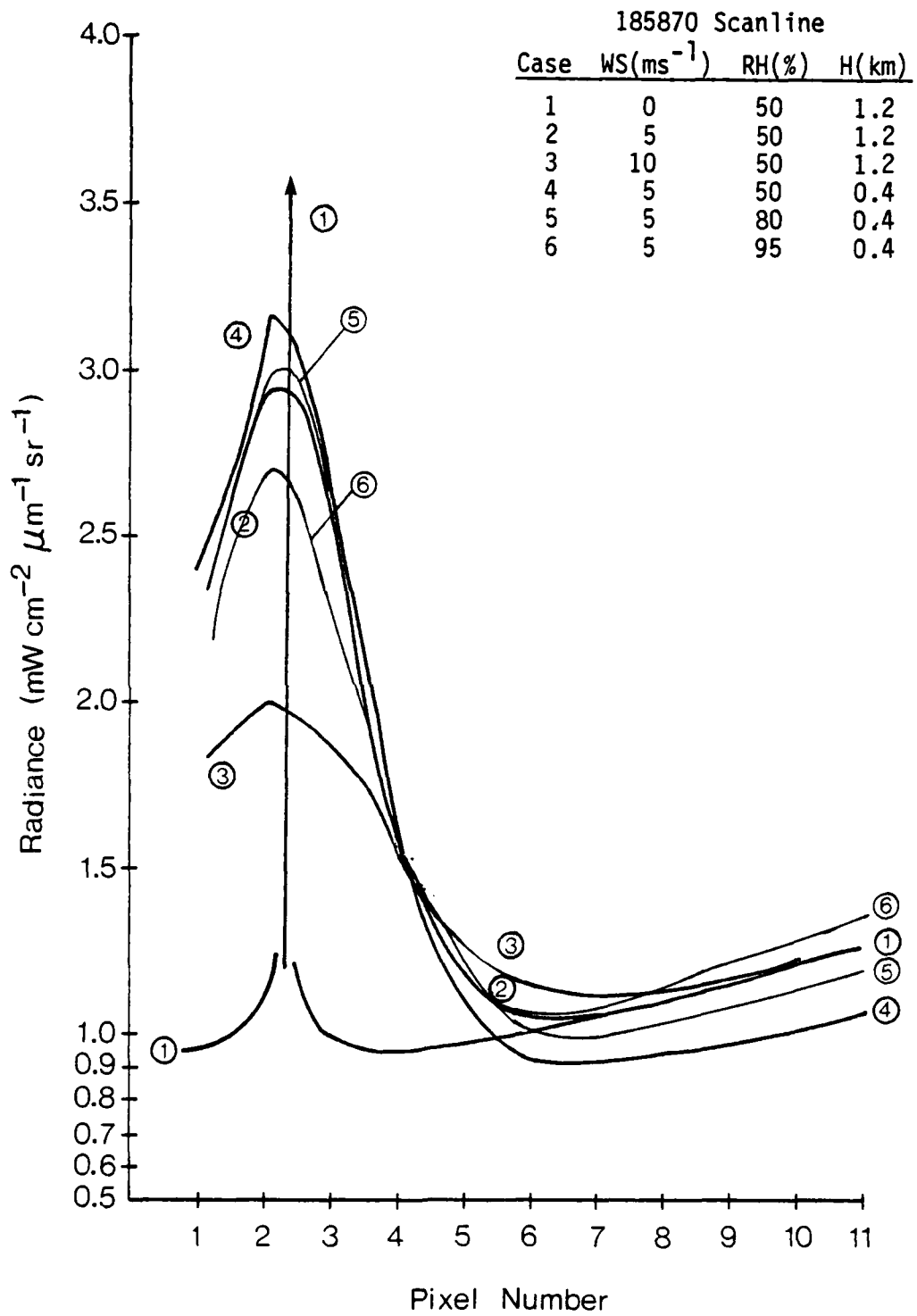


Figure 7-20. Radiance Simulation Scan Lines (see text).

8. DMSP RADIANCE/OPTICAL DEPTH RELATIONSHIPS

A necessary first step in the inference of surface range from satellite data is the retrieval of vertical aerosol optical depth from measured satellite incident radiances (Goroch, 1982). The meteorologically dependent radiance simulation model described here evaluates aerosol optical depth as an intermediate step and, therefore, radiance/aerosol optical depth relationships are provided as an adjunct calculation. Additionally, the capability exists to explore both the meteorological and aerosol model dependence of these relationships. Finally, radiance results may be bandpass weighted for the DMSP sensor (or other sensors in the 0.4 to 1.1 μ m spectral region).

In this section DMSP-bandpass weighted radiance/optical depth relationships are evaluated using the overall simulation algorithm. The methodology employed is based on first calculating wavelength dependent upward radiance spectra for maritime, rural, and urban aerosol models for relative humidity values of 50, 70, 80, 90 and 95%. For each input relative humidity, aerosol optical depth is parameterized by aerosol layer depth increases in increments of 0.5 km from 0.0 to 2.0 km. For a given aerosol layer depth, H_i , the aerosol optical depth at a chosen wavelength, λ is:

$$\tau_A(\lambda, H_i) = H_i \beta_A^e(\lambda, RH) \quad (8-1)$$

where $\beta_A^e(\lambda, RH)$ is the aerosol extinction coefficient corresponding to the appropriate choice of model and relative humidity. (Extinction coefficients are obtained from the tabulations in Shettle and Fenn, 1979).

The radiance spectra are bandpass-weighted according to (6-24) to provide DMSP simulated radiances. Finally, the bandpass-weighted radiances are plotted against the optical depths given by (8-1). For applications oriented purposes, linear regressions are provided based on the derived radiance/optical depth relationships. Calculations are performed for a nadir viewing sensor and solar zenith angle of 50° . The optical depth is evaluated at $0.55\mu\text{m}$ for direct comparison to visual range as required. Optical depths at other wavelengths are available by reference to the aerosol model and employing (8-1) above.

8.1 Radiance Spectra

Figures 8-1, 8-2, and 8-3 illustrate wavelength dependent, simulated upward radiance spectra for relative humidities of (a) 50, (b) 70, (c) 80, (d) 90, and (e) 95%, for the maritime, rural, and urban aerosol models, respectively. Each plot consists of five curves corresponding to aerosol layer depths of 0.0, 0.5, 1.0, 1.5, and 2.0 km (e.g., lowest radiance, $H = 0.0$; highest radiance, $H = 2.0$). These results provide the capability to evaluate radiance/optical depth relationships at discrete wavelengths or for narrow bands within the DMSP $0.4\text{-}1.1\mu\text{m}$ spectral interval corresponding to other sensors.

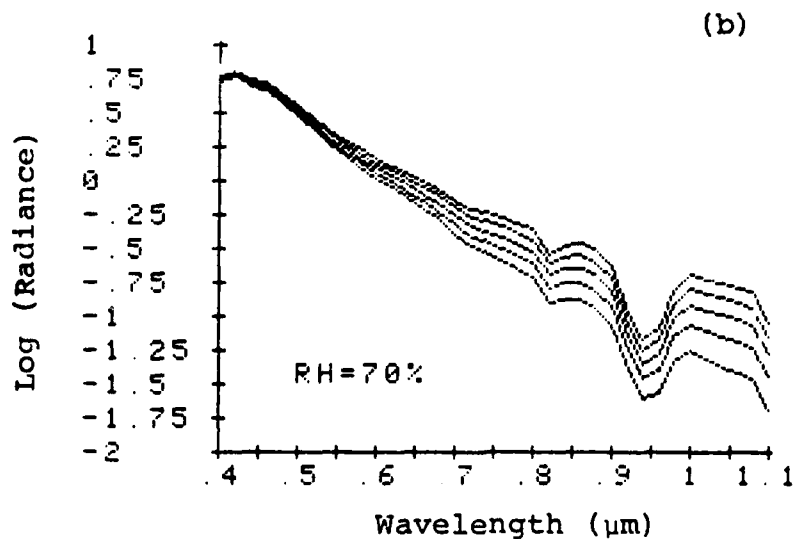
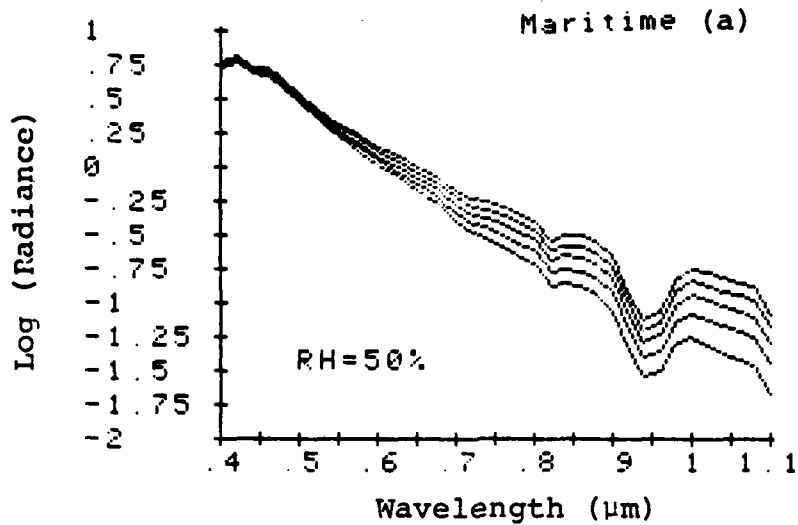


Figure 8-1. Wavelength-dependent radiances for maritime aerosol and relative humidities of: (a) 50%, (b) 70%, (c) 80%, (d) 90%, and (e) 95%. Each plot consists of five curves corresponding to aerosol layer depths of 0.0, 0.5, 1.0, 1.5, and 2.0 km, respectively.

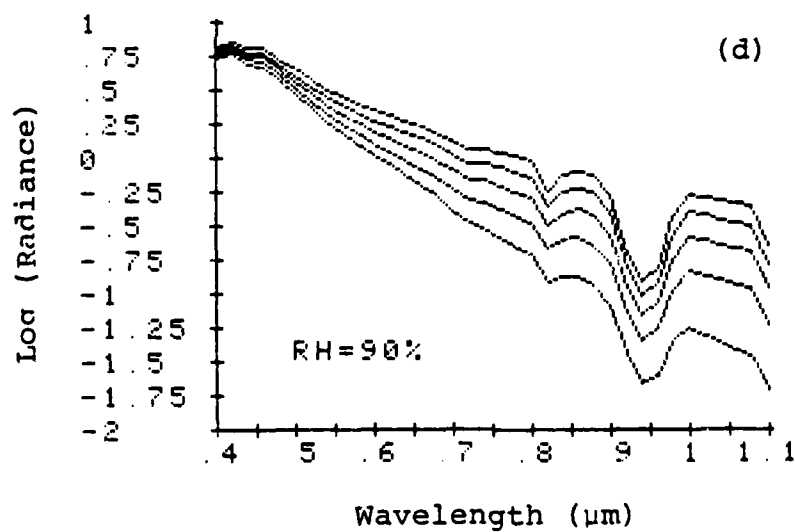
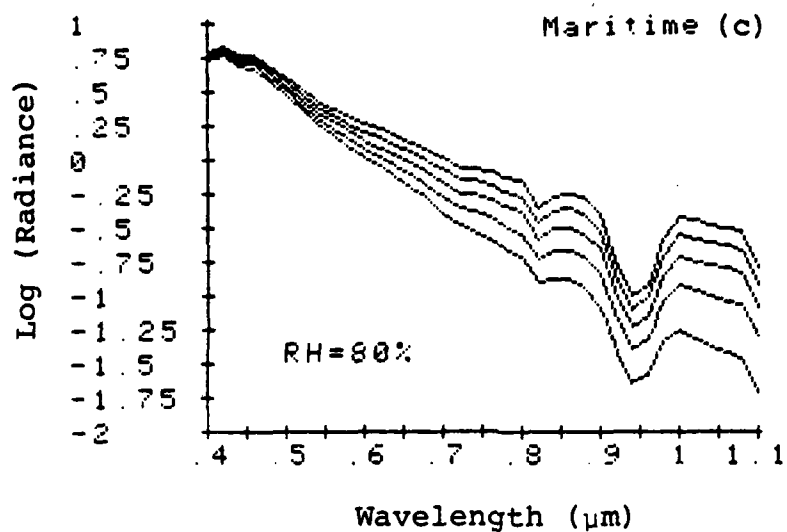


Figure 8-1. (continued)

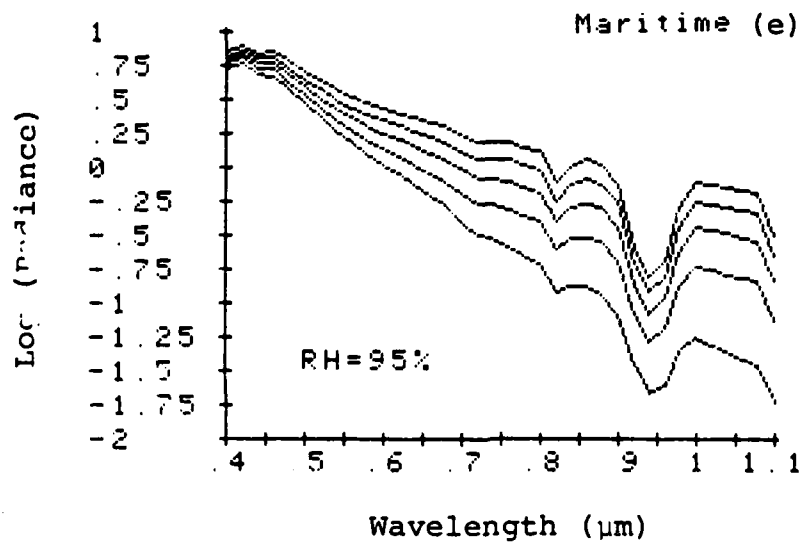


Figure 8-1. (continued)

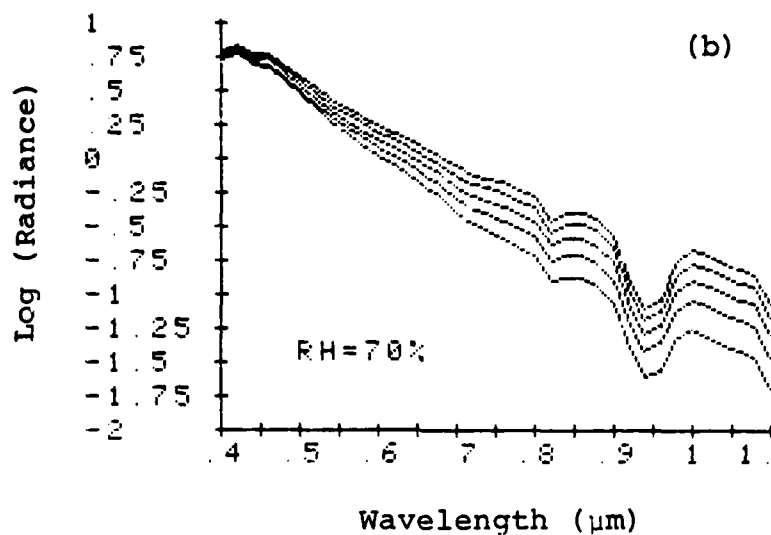
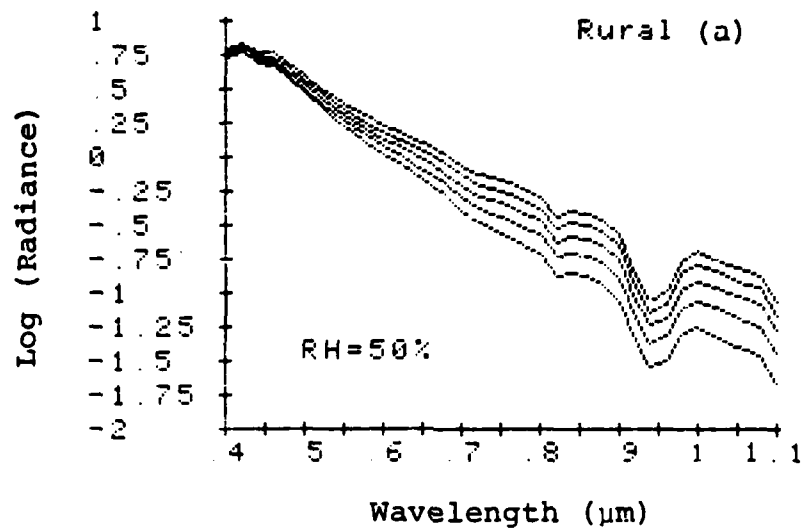


Figure 8-2. Wavelength-dependent radiances for rural aerosol and relative humidities of: (a) 50%, (b) 70%, (c) 90%, (d) 90%, and (e) 95%. Each plot consists of five curves corresponding to aerosol layer depths of 0.0, 0.5, 1.0, 1.5, and 2.0 km, respectively.

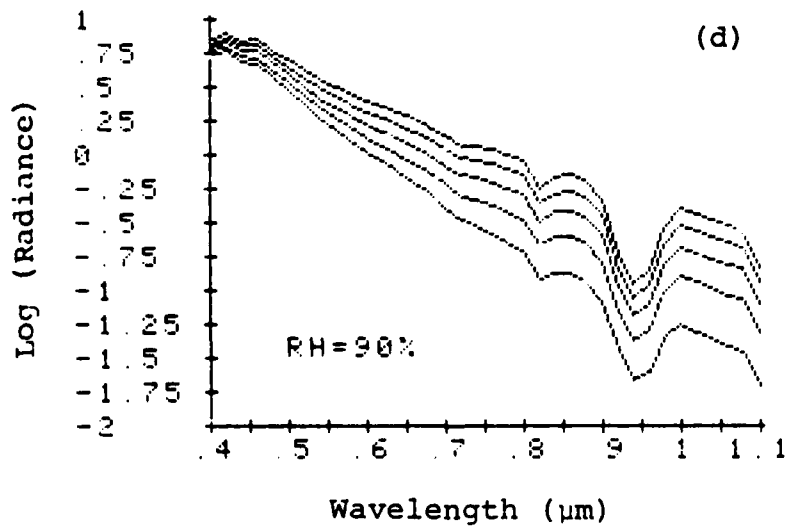
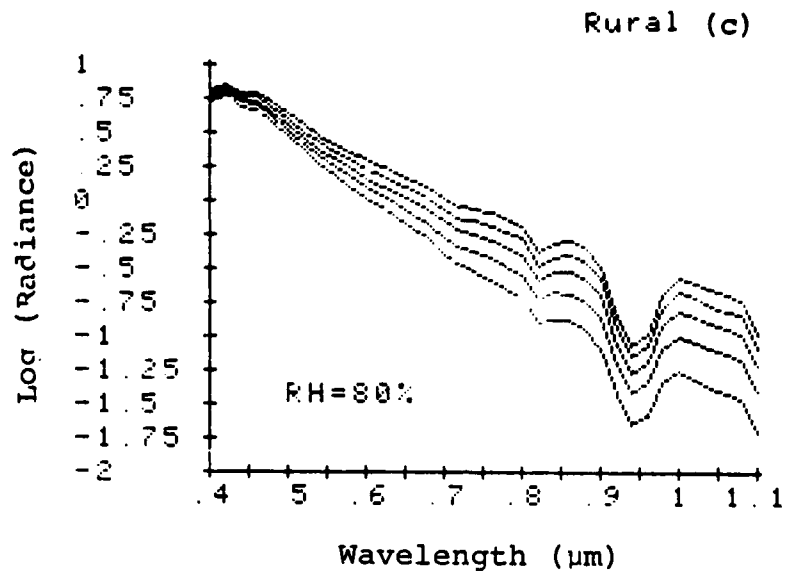


Figure 8-2. (continued)

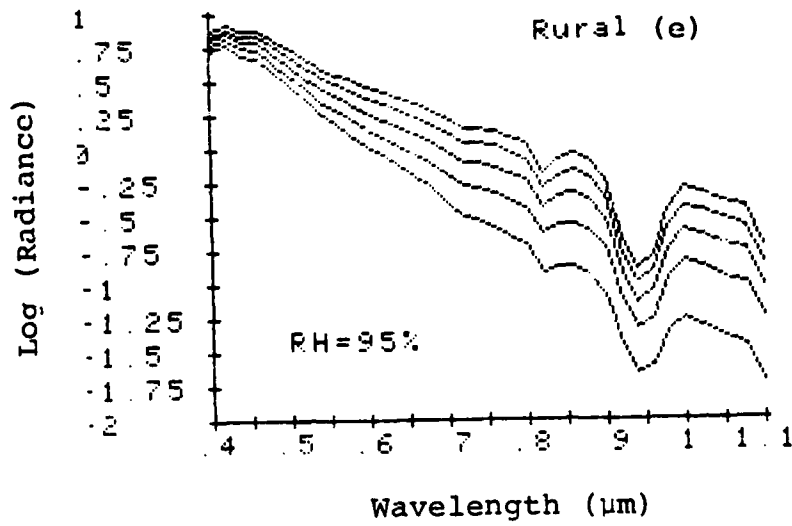


Figure 8-2. (continued)

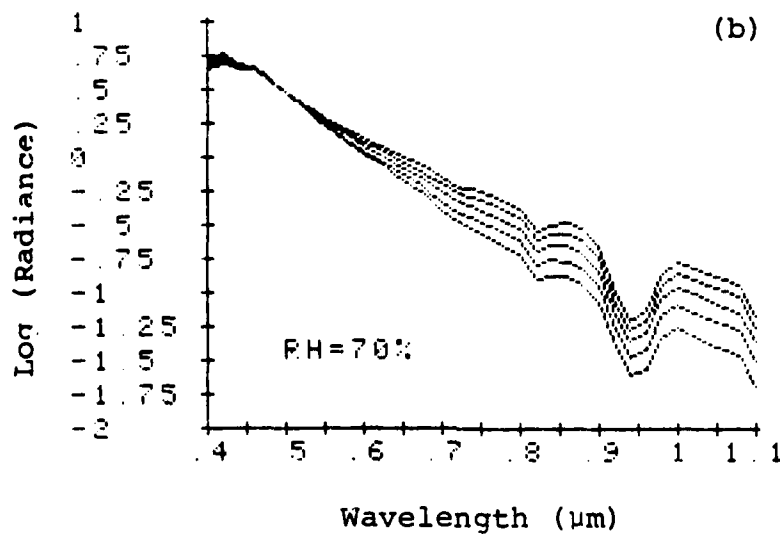
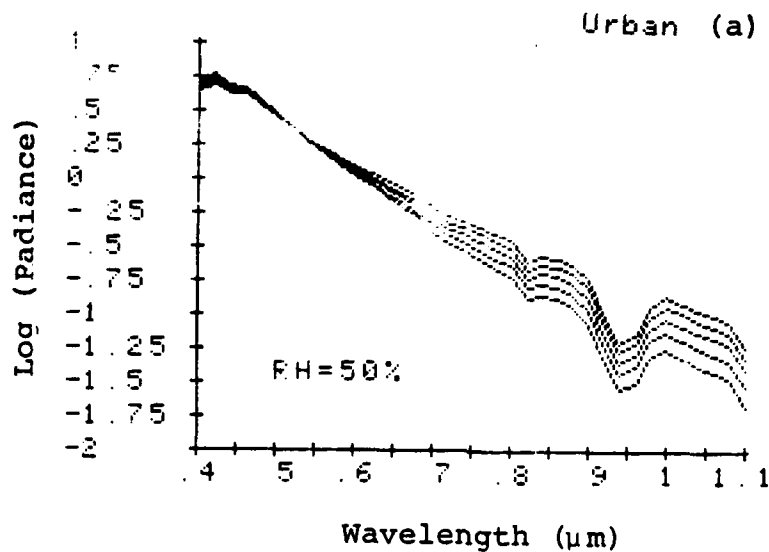


Figure 8-3. Wavelength-dependent radiances for urban aerosol and relative humidities of: (a) 50%, (b) 70%, (c) 80%, (d) 90%, and (e) 95%. Each plot consists of five curves corresponding to aerosol layer depths of 0.0, 0.5, 1.0, 1.5, and 2.0 km, respectively.

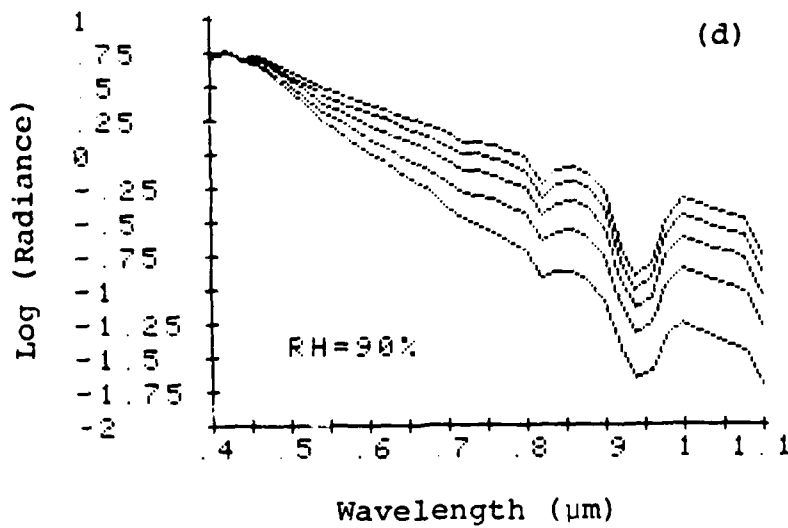
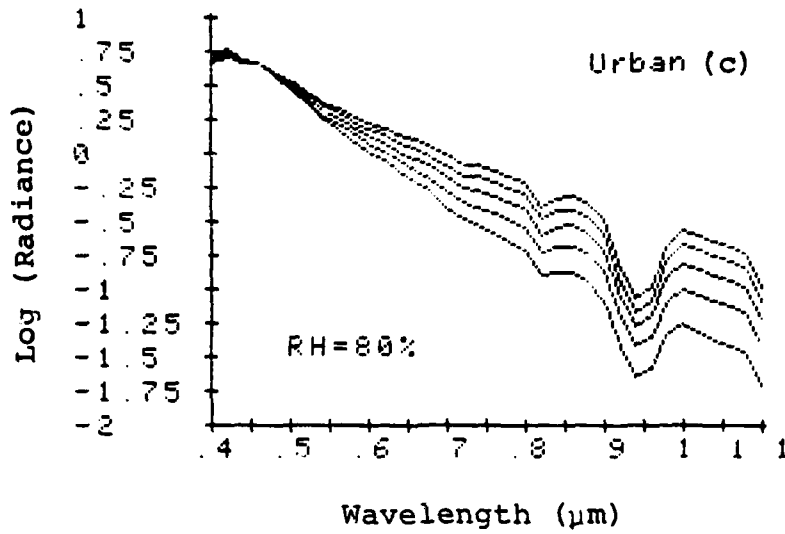


Figure 8-3. (continued)

Urban (e)

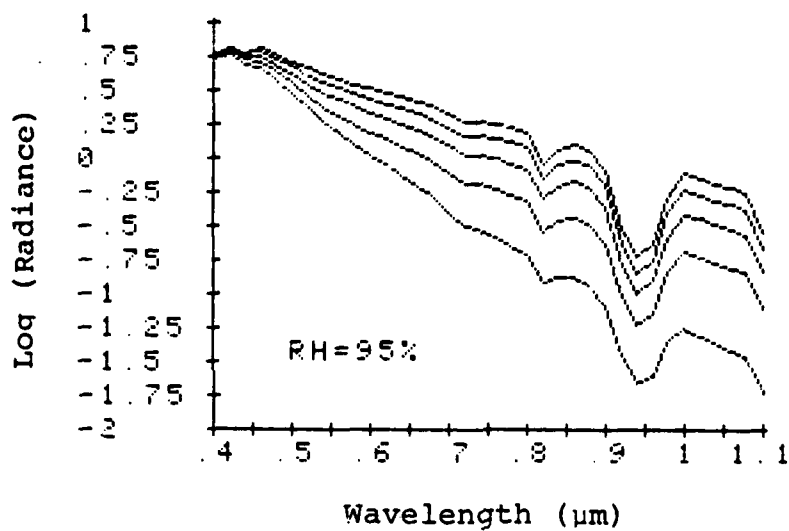


Figure 8-3. (continued)

8.2 Bandpass Weighting and Linear Relationships

For each aerosol model, relative humidity, and aerosol layer depth, the radiance spectra presented in Section 8.1 are DMSP bandpass-weighted using (6-24) and aerosol optical depths are calculated at $0.55\mu\text{m}$. Tables 8-1, 8-2, and 8-3 give these values for the maritime, rural, and urban models, respectively. (The total optical depth τ includes a Rayleigh optical depth contribution of .096 at $0.55\mu\text{m}$.) Radiances are in engineering units of $(\text{mW cm}^{-2} \mu\text{m}^{-1} \text{sr}^{-1})$.

Simulated DMSP radiance vs. τ values tabulated here are plotted for each relative humidity in Figures 8-4, 8-5, and 8-6 for the three aerosol models. For applications purposes, linear regressions are provided for each curve in Tables 8-4, 8-5, 8-6, for maritime, rural, and urban models, respectively and for all relative humidities taken together.

8.3 Discussion of Radiance/Optical Depth Relationships

The DMSP radiance/optical depth relationships illustrated in Figures 8-4, 8-5, and 8-6 are remarkably linear regardless of aerosol model and relative humidity. This is especially apparent from the r^2 values for individual relative humidity curves given in Tables 8-4 through 8-6. This linear behavior relating aerosol optical depth and sensed radiance is consistent with theoretical calculations and experimental verification performed for a variety of visible sensors including Landsat, GOES, and NOAA-5 (Griggs, 1979; Norton et al., 1980). Figure 8-8, for example, illustrates the dependence of radiance

RH	50%		70%		80%		90%		95%	
	τ	I	τ	I	τ	I	τ	I	τ	I
0.0	.0960	.575	.0960	.574	.096	.573	.096	.573	.096	.573
0.5	.1394	.630	.151	.634	.2058	.683	.2533	.728	.3147	.788
1.0	.1829	.688	.2059	.699	.3156	.810	.4106	.915	.5333	1.058
1.5	.2263	.749	.2609	.769	.4253	.952	.5679	1.129	.7520	1.371
2.0	.2697	.814	.3158	.844	.5351	1.108	.7252	1.363	.9706	1.713

Table 8-1. Simulated DMSP radiances, I ($\text{mWcm}^{-2}\mu\text{m}^{-1}\text{sr}^{-1}$), assuming a uniform maritime aerosol layer of depth H (km) and indicated relative humidity (RH). In each column, τ is the total optical depth at $0.55 \mu\text{m}$ wavelength.

RH	50%		70%		80%		90%		95%	
	τ	I	τ	I	τ	I	τ	I	τ	I
0.0	.096	.5752	.096	.5738	.096	.5730	.096	.5728	.096	.5726
0.5	.1717	.6631	.1776	.6660	.2083	.6919	.2665	.7459	.3096	.7876
1.0	.2474	.7585	.2592	.7665	.3205	.8254	.4369	.9492	.5231	1.0469
1.5	.3231	.8607	.3408	.8748	.4328	.9716	.6074	1.1758	.7367	1.3377
2.0	.3988	.9686	.4224	.9892	.5450	1.1274	.7778	1.418	.9502	1.6479

Table 8-2. Simulated DMSP radiances, I ($\text{mWcm}^{-2} \mu\text{m}^{-1} \text{sr}^{-1}$), assuming a uniform rural aerosol layer of depth H (km) and indicated relative humidity (RH). In each column, τ is the total optical depth at $0.55 \mu\text{m}$ wavelength.

RH	50%		70%		80%		90%		95%		
	H	τ	H	τ	H	τ	H	τ	H	τ	
0.0		.096	.5751	.096	.5737	.096	.5729	.096	.5728	.096	.5728
0.5		.1884	.6015	.2149	.6167	.2761	.6612	.3742	.7420	.5189	.8744
1.0		.2808	.6316	.3337	.6654	.4562	.7625	.6523	.9408	.9417	1.2351
1.5		.3732	.6645	.4526	.7179	.6363	.8696	.9305	1.1470	1.3646	1.5948
2.0		.4656	.6989	.5714	.7718	.8164	.9770	1.2086	1.3463	1.7874	1.9252

Table 8-3. Simulated DMSP radiances, I ($\text{mWcm}^{-2}\mu\text{m}^{-1}\text{sr}^{-1}$), assuming a uniform urban aerosol layer of depth H (km) and indicated relative humidity. In each column, τ is the total optical depth at $0.55 \mu\text{m}$ wavelength.

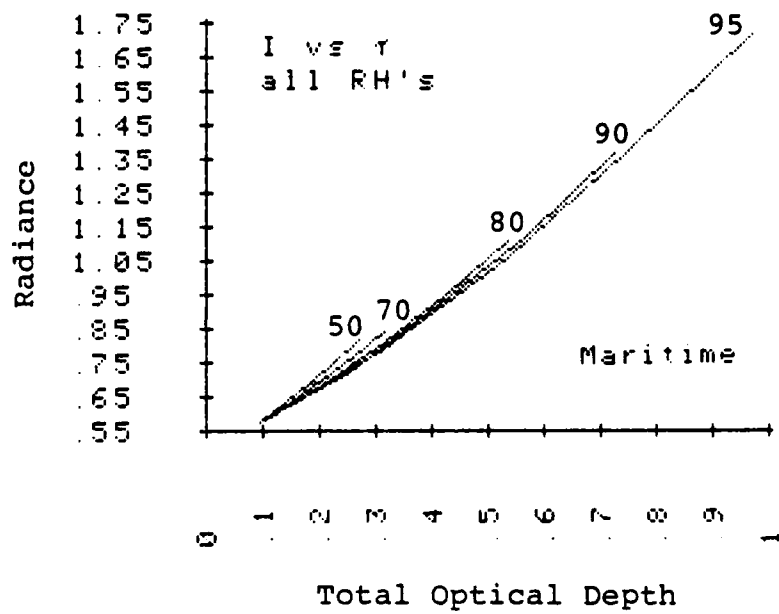


Figure 8-4. Simulated DMSP radiance ($\text{mWcm}^{-2}\mu\text{m}^{-1}\text{sr}^{-1}$) vs. total optical depth (at $0.55 \mu\text{m}$ wavelength) for indicated relative humidities (maritime aerosol).

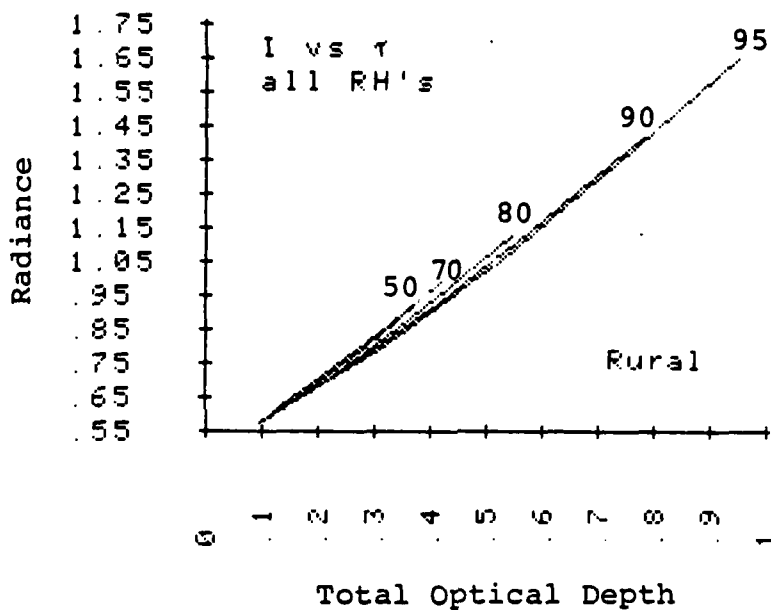


Figure 8-5. Simulated DMSP radiance ($\text{mWcm}^{-2}\mu\text{m}^{-1}\text{sr}^{-1}$) vs. total optical depth (at $0.55 \mu\text{m}$ wavelength) for indicated relative humidities (Rural aerosol).

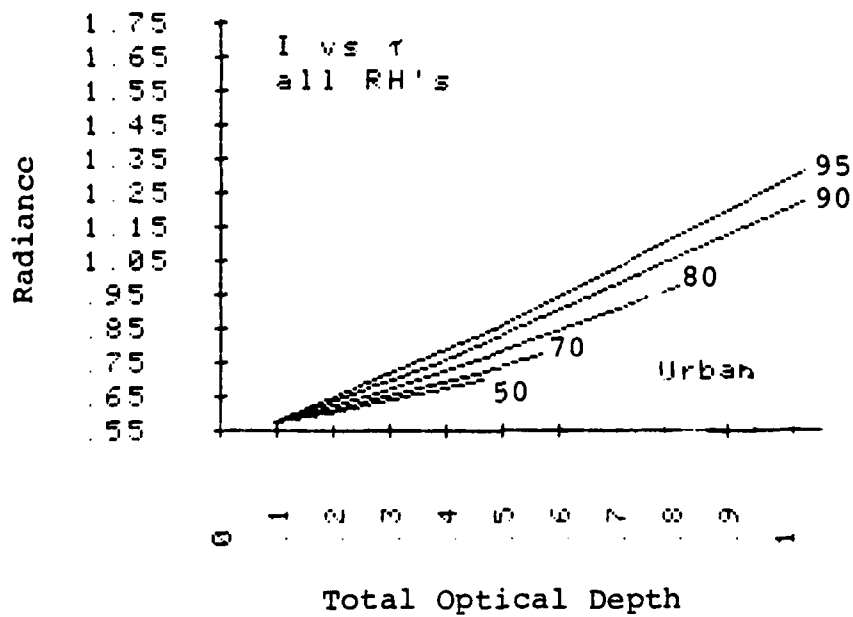


Figure 8-6. Simulated DMSP radiance ($\text{mWcm}^{-2}\mu\text{m}^{-1}\text{sr}^{-1}$) vs. total optical depth (at $0.55 \mu\text{m}$ wavelength) for indicated relative humidities (Urban aerosol).

Maritime Aerosol

RH	Linear Regression	r^2
50	$\hat{I} = 0.440 + 1.375\hat{\tau}$	0.999
70	$\hat{I} = 0.451 + 1.228\hat{\tau}$	0.998
80	$\hat{I} = 0.440 + 1.220\hat{\tau}$	0.995
90	$\hat{I} = 0.424 + 1.259\hat{\tau}$	0.994
95	$\hat{I} = 0.402 + 1.309\hat{\tau}$	0.992
all	$\hat{I} = 0.441 + 1.248\hat{\tau}$	0.992

Table 8-4. Straight line fits to radiance simulations (maritime aerosol).

Rural Aerosol

RH	Linear Regression	r^2
50	$\hat{I} = 0.444 + 1.300\hat{\tau}$	0.998
70	$\hat{I} = 0.444 + 1.274\hat{\tau}$	0.998
80	$\hat{I} = 0.441 + 1.237\hat{\tau}$	0.997
90	$\hat{I} = 0.429 + 1.244\hat{\tau}$	0.996
95	$\hat{I} = 0.417 + 1.265\hat{\tau}$	0.995
all	$\hat{I} = 0.445 + 1.232\hat{\tau}$	0.995

Table 8-5. Straight line fits to radiance simulations (rural aerosol).

Urban Aerosol

RH	Linear Regression	r^2
50	$\hat{I} = 0.540 + 0.336\hat{\tau}$	0.997
70	$\hat{I} = 0.529 + 0.419\hat{\tau}$	0.998
80	$\hat{I} = 0.511 + 0.564\hat{\tau}$	0.999
90	$\hat{I} = 0.500 + 0.695\hat{\tau}$	0.999
95	$\hat{I} = 0.478 + 0.810\hat{\tau}$	0.999
all	$\hat{I} = 0.432 + 0.789\hat{\tau}$	0.969

Table 8-6. Straight line fits to radiance simulations (urban aerosol).

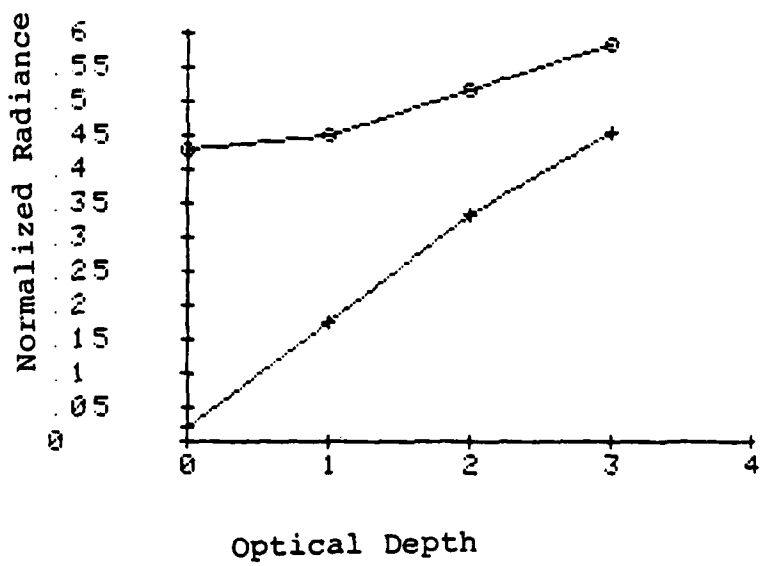


Figure 8-8. Normalized radiance ($I/\mu_0 F$) vs. optical depth for surface reflectance values of 0.02 (+) and 0.43 (o), respectively.

(normalized to an irradiance of unity) on optical depth for surface reflectance values of 0.02 and 0.43 (Kaufman and Joseph, 1982). This calculation was done using the radiative transfer solution given in Section 6 assuming a nadir viewing sensor with solar zenith angle of 60° and an aerosol model with single scatter albedo of unity (i.e. non-absorbing) and asymmetry parameter of 0.63. The aerosol optical properties represent a low relative humidity, rural aerosol and the simulation is appropriate for Landsat 2-MSS6. Note that for low surface reflectance (such as over the ocean) the radiance/optical depth behavior is very linear over a wide domain of optical depth values.

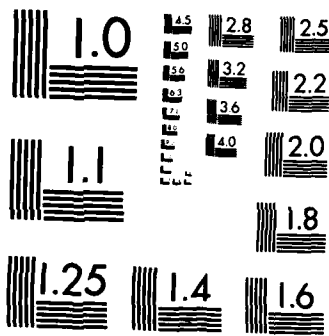
It should be noted, however, that there are discernible differences among these linear relationships dependent both on aerosol model and relative humidity. The most notable of these may be distinguished by examining the dependence of the slopes of the I vs. τ relationships for each aerosol model on relative humidity. For the maritime model, for example, radiance increase with optical depth is more rapid at low than at high relative humidities. For the rural aerosol model, this trend is noted, however, the slopes ($\Delta I/\Delta \tau$) are almost independent of relative humidity. Finally, distinctive behavior is noted for the urban model. There a separate regression line is required to characterize each relative humidity. Furthermore, the slope variation with relative humidity is opposite to that noted for the maritime and rural models, i.e. the rate of change of radiance with

increases at higher relative humidities.

These differences may be explained by recalling that the radiative transfer theory relating aerosol optical properties to simulated radiance requires a minimum of three input variables including optical depth, single scattering albedo, and scattering phase function (cf. equations 6-5 through 6-12). These optical properties are dependent on aerosol size distribution and index of refraction which may ultimately be related to chemical composition and meteorological variables such as relative humidity (see Isaacs, 1980; Sections 4 and 5). For a given chemical composition, therefore, the optical properties cited above are related in a unique manner allowing optical depth to act as a surrogate for the others. The differences observed in the radiance/optical depth relationships above are thus manifestations of the subtle differences due to differing composition dependent relative humidity growth factors and aerosol absorption properties. This may be illustrated by decoupling the three optical parameters τ , ω_0 , g in a theoretical calculation. Figure 8-9 illustrates radiance changes for a fixed optical depth of unity due to variations in single scattering albedo and asymmetry factor. For a fixed albedo of $\omega_0 = 0.95$ the crosses (+) indicate a decrease in simulated radiance with increases in asymmetry factor, e.g., there is less backscatter to the sensor. Conversely, for a fixed g factor, the circles (o) indicate an increase in radiance with increasing ω_0 (i.e., decreasing aerosol absorption). Relating these results to the radiance/

optical depth relationships illustrated in Figures 8-4, 8-5, 8-6, a slope ($\Delta I/\Delta\tau$) decrease (increase) may be associated with an increase (decrease) in asymmetry factor, g , or decrease (increase) in single scattering albedo, ω_0 .

As relative humidity increases aerosol growth is manifested in an effective size distribution change (Nilsson, 1979), increasing the number of larger particles. This is illustrated in Figure 8-10 by the decrease in calculated Junge coefficient for the maritime model with increasing relative humidity. A corresponding increase in g factor occurs. This effect is largest for the maritime aerosol which responds most drastically to relative humidity increases (cf. Figure 4-3b). Since the maritime aerosol model is essentially non-absorbing (Figure 4-1), its single scattering albedo remains fairly constant with relative humidity and the size distribution (i.e., g factor) increase effect dominates decreasing the $\Delta I/\Delta\tau$ slope at higher humidities. The behavior noted for the urban aerosol is due to its absorption component. As relative humidity increases water is added to the aerosol and its volume mixed index of refraction becomes increasingly less absorbing. The resultant single scattering albedo thus increases drastically with relative humidity (cf. Figure 4-7b). Although aerosol growth also increases the g factor (Figure 4-7c), the albedo increase effect dominates resulting in the increasing $\Delta I/\Delta\tau$ slope observed in Figure 8-6. The rural model results (Figure 8-5) are an intermediate case with slightly less increase in g



MICROCOPY RESOLUTION TEST CHART
NATIONAL BUREAU OF STANDARDS-1963-A

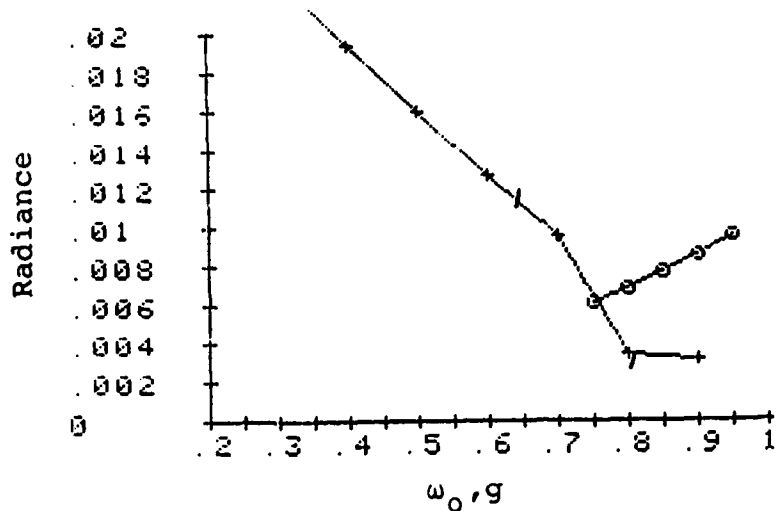


Figure 8-9. Radiance changes with single scattering albedo and asymmetry parameter for fixed optical depth of unity.

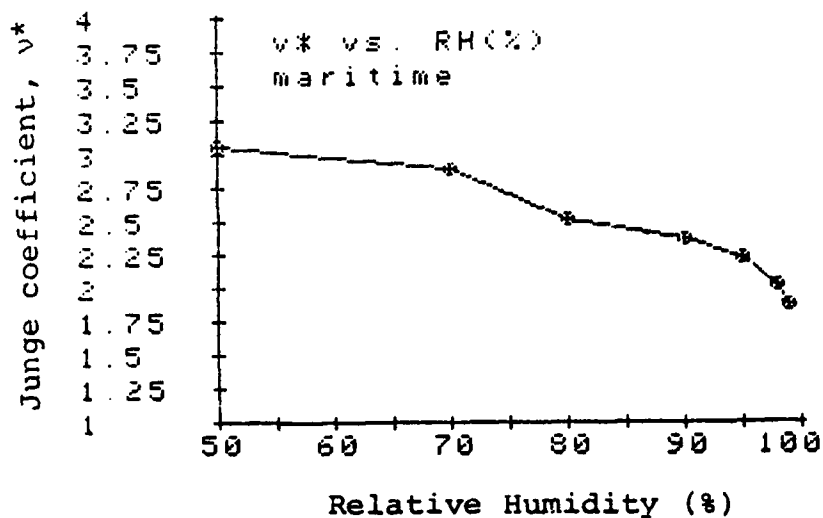


Figure 8-10. Effective size distribution change with relative humidity.

factor and greater increase in ω_0 with relative humidity compared to the maritime model.

A unique linear predictor equation relating radiance and optical depth would provide a significant practical simplification to the inference of surface range from remotely sensed radiance. The results presented here suggest that a potential ambiguity is introduced by the presence of absorbing aerosol species such as the carbonaceous component of the urban model. Figure 8-11 illustrates a composite of individual I vs. τ relationships for all relative humidities and each aerosol model. A single linear relationship may suffice for both maritime and rural models. Since less solar radiation is backscattered to the satellite sensor by an absorbing aerosol, however, a given remotely sensed radiance for the urban model corresponds to a higher optical depth and hence higher boundary layer extinction (i.e. reduced range) than predicted assuming single scattering albedos near unity. Since the presence of absorbing components is suggested even in remote regions (Rosen et al., 1981; Gerber and Hindman, 1981) and the usual definition of visual range must be modified when considering absorbing aerosols (Roessler and Faxrog, 1981), inference of visual range may not be straightforward. Additionally, since carbon is uniformly absorbing throughout the near IR and thermal IR spectral regions (Twitty and Weinman, 1971), its presence has a significant impact on multispectral range prediction. For these reasons a method of inferring both optical depth and single scattering albedo may be advisable.

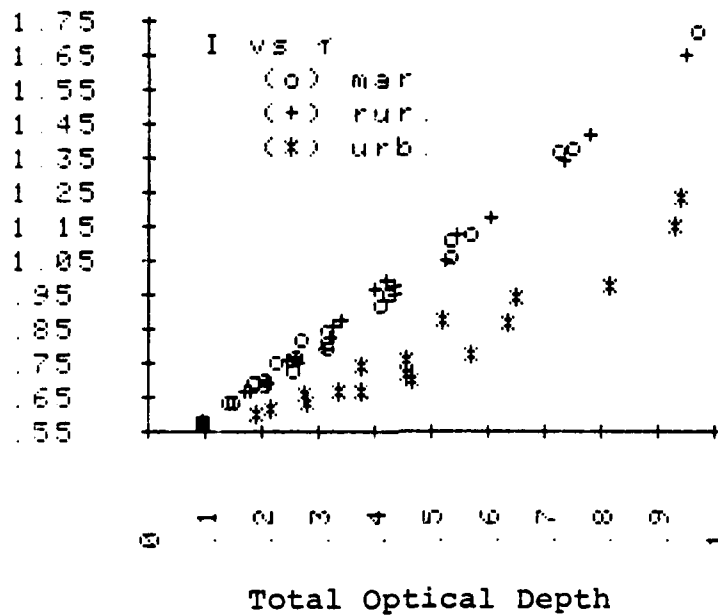


Figure 8-11. Simulated DMSP radiances ($\text{mWcm}^{-2} \mu\text{m}^{-1} \text{sr}^{-1}$) vs. total optical depth (at $0.55 \mu\text{m}$ wavelength) for maritime (o), rural (+), and urban (*) aerosol models and all relative humidities.

9. MULTISPECTRAL RANGE RETRIEVAL

9.1 Rationale

The performance of electro optical systems in the lower atmosphere is constrained by wavelength-dependent extinction due to a variety of mechanisms including aerosol scattering and absorption, molecular (line) absorption, Rayleigh scattering, and various continuum absorption features. Assuming that the extinction (in km^{-1}) at wavelength λ_i due to the summed contributions of the above phenomena is known and given by $\beta_T(\lambda_i)$, a reliable assessment of system effectiveness can be obtained by evaluating the inverse extinction length or range (km):

$$R(\lambda_i) = C_i / \beta_T(\lambda_i) \quad (9-1)$$

For example, at $0.55\mu\text{m}$, equation (9-1) is a statement of the Koschmieder (1924) equation with $C_i = 3.9$ and $R(0.55\mu\text{m})$ defining the visual range. One immediate application of the DMSP radiance/aerosol optical depth relationships derived previously (Section 8) is in the estimation of the aerosol extinction contribution to total extinction in equation (9-1) above. Utilizing this capability, a prototype range retrieval algorithm is formulated in this section to infer optical range in the near surface environment from satellite observations. By utilizing available models of molecular and continuum extinction features, the domain of wavelength applicability may be extended from the visible

region to include the 4 and 10 μ m windows.

9.2 Aerosol Contribution

The aerosol optical depth $\tau(\lambda_j)$ at wavelength λ_j inferred from the previously derived DMSP radiance/optical depth relationships is fundamentally:

$$\tau(\lambda_j) = \int_0^{\infty} [\beta_1(\lambda_j, z) + \beta_2(\lambda_j, z)] dz \quad (9-2)$$

where β_1 and β_2 are contributions to total extinction due to the accumulation and coarse modes, respectively. It is assumed that (9-2) may be approximated as:

$$\tau(\lambda_j) \simeq \beta_1(\lambda_j) H_1 + \beta_2(\lambda_j) H_2 \quad (9-3)$$

where β_1 , β_2 are modal extinctions representative of the near surface environment and H_1 , H_2 (km) are mixing heights corresponding to each mode. This supposition requires either a uniform extinction layer near the surface or a vertical distribution characterized by an exponential with scale height, H_i . Alternatively, (9-3) may be replaced by an appropriate mixed layer model of the vertical extinction profile to relate the inferred $\tau(\lambda_j)$ value with surface value of β_1 and β_2 . It is further assumed that: (1) the coarse mode contribution is calculable from the Munn-Katz oceanic wind speed/relative humidity dependent size distribution at each required wavelength, and (2) the accumulation mode size distribution is fixed by relative humidity and

requires only normalization to a number density N_1 (cm^{-3}) using the input optical depth. Thus, given input of satellite radiance inferred optical depth, $\tau(\lambda_j)$, relative humidity (RH), windspeed (WS), and the mixing heights H_1 , H_2 , the aerosol extinction contributions at any set of λ_i wavelengths may be evaluated based on the following algorithm steps:

9.2.1 Calculate extinction coefficient of oceanic mode at λ_j , $\beta_2(\lambda_j)$, from input RH, WS.

9.2.2 Calculate optical depth at λ_j of oceanic model using input oceanic scale height, H_2 :

$$\tau_2(\lambda_j) = H_2 \beta_2(\lambda_j)$$

9.2.3 Calculate non-oceanic (i.e., accumulation mode) optical depth at λ_j from input satellite-inferred optical depth $\tau_s(\lambda_j)$:

$$\tau_1(\lambda_j) = \tau_s(\lambda_j) - \tau_2(\lambda_j)$$

9.2.4 Calculate fine mode extinction at λ_j , $\beta_1(\lambda_j)$ using input fine mode scale height H_1 and equation (9-3) above:

$$\beta_1(\lambda_j) = [\tau_s(\lambda_j) - H_2 \beta_2(\lambda_j)] H_1^{-1}$$

9.2.5 Calculate number density in fine mode N_1 by ratio of inferred fine mode extinction to a model fine mode extinction per unit number density $\hat{\beta}_1^M(\lambda_j)$:

$$N_1 = \frac{\beta_1(\lambda_j)}{\hat{\beta}_1^M(\lambda_j)}$$

9.2.6 Calculate fine mode extinction at i required wavelengths using N_1 and model extinctions at i wavelengths for input relative humidities:

$$\beta_i(\lambda_i, RH) = N_1 \hat{\beta}_1^M(\lambda_i, RH)$$

9.2.7 Calculate ranges at each required λ_i using equation (9-1).

In practice, required values of the relative humidity/windspeed dependent oceanic mode extinction are obtained by interpolation between a sufficiently-dense set of stored extinction values using a modified Kasten-type (1969) relation of the form:

$$\frac{\beta_2(RH_1, WS_1)}{\beta_2(RH_2, WS_2)} = \left[\frac{(1-RH_2)}{(1-RH_1)} \right]^\alpha \left(\frac{WS_1}{WS_2} \right)^\beta \quad (9-4)$$

where the required constants, α , β are evaluated within each sub-interval ($WS_1 < WS < WS_2$; $RH_1 < RH < RH_2$).

Table 9-1 illustrates simulated retrieved surface aerosol extinction contributions using the algorithm described above and assuming input data including an aerosol optical depth of 0.5 at $0.65\mu\text{m}$ inferred from visible radiance data and supporting meteorological data including a relative humidity of 75%, surface wind speed of 7.0 ms^{-1} , and scale heights H_1 , H_2 of 1.2 and 0.8 km, respectively. Extinctions are retrieved for five wavelengths including the visual range and three corresponding to Nd (1.06), DF (3.8), and CO_2 (10.6) laser lines, respectively. For all except $0.55\mu\text{m}$ the value of C_i in equation (9-1) is set equal to unity.

λ_j (μm)	(a) Aerosol Contributions		(b) Non-aerosol contributions				(c) Range	
	β_1 (km^{-1})	β_2 (km^{-1})	$[\beta_1 + \beta_2]$ (km^{-1})	β_R (km^{-1})	β_N (km^{-1})	β_H (km^{-1})	β_G (km^{-1})	R_j (km)
0.55	4.94(-1)	2.88(-2)	5.23(-1)	1.23(-2)	--	--	--	7.3
0.65	3.99(-1)	2.72(-2)	4.26(-1)	6.21(-3)	--	--	--	2.3
1.06	1.78(-1)	2.79(-1)	2.05(-1)	8.64(-4)	--	--	--	4.9
3.80	7.05(-3)	2.08(-2)	2.78(-2)	5.18(-6)	2.3(-3)	1.06(-3)	2.76(-2)	17.0
10.60	6.90(-3)	4.08(-3)	1.10(-2)	8.55(-8)	--	1.31(-1)	3.28(-2)	5.7

Table 9-1. Sample output from VIS/IR range program. Input data: $H_1 = 1.2$ km, $H_2 = 0.8$ km,

$WS = 7 \text{ ms}^{-1}$, $RH = 75\%$, $\tau(0.65) = 0.5$, $T = 288^\circ \text{K}$. Output: (a) Aerosol contributions, (b) Non-aerosol contributions, (c) Optical range.

9.3 Non-Aerosol Contribution

In addition to the aerosol contributions β_1 , β_2 , the total extinction may include additional non-aerosol contributions due to Rayleigh scattering, β_R , molecular line absorption, β_G , and continuum absorption due to water vapor, β_H , and nitrogen, β_N , i.e.:

$$\begin{aligned} \beta_T(\lambda_i) = & \beta(\lambda_i) + \beta_2(\lambda_i) + \beta_R(\lambda_i) + \beta_G(\lambda_i) \\ & + \beta_H(\lambda_i) + \beta_N(\lambda_i) \end{aligned} \quad (9-5)$$

The relative importance of each contribution is dependent on wavelength.

9.3.1 Rayleigh scattering

The Rayleigh scattering coefficient is calculated using the LOWTRANS5 (Kneizys, et al., 1980) expression suggested by Shettle et al. (1980) based on a least square fit to the values of Penndorf (1957):

$$\beta_R(\lambda) = [926.759\lambda^4 - 10.7123\lambda^2]^{-1} \quad (9-6)$$

Calculated values appropriate for sea levels are shown in Table 9-1.

9.3.2 Molecular line absorption

The extinction contribution at each wavelength due to molecular line absorption is evaluated by summing absorption coefficients due to relevant gaseous absorbers (from among H_2O , CO_2 , O_3 , N_2O , CO , CH_4 , and O_2) using spectral line

parameters obtained from the most recent version of the AFGL compilation (McClatchey et al., 1973). For each spectral line ℓ and absorbing species i , the absorption coefficient β_{ℓ}^i is given by:

$$\beta_{\ell}^i(\nu, P, T) = n_i(P, T) S_{\ell}(T) f_{\ell}(\nu, P, T) \quad (9-7)$$

where n_i is the species i number density (molecule cm^{-3}) at pressure P and temperature T . S_{ℓ} is the line strength ($\text{cm}^{-1}/\text{molecule cm}^{-2}$), and f_{ℓ} is the line shape (cm). The total gaseous absorption coefficient is obtained by summing over all lines and species:

$$\beta_G(\nu, P, T) = \sum_i \sum_{\ell} \beta_{\ell}^i(\nu, P, T) \quad (9-8)$$

The specific methodology employed is described in Susskind and Searl (1977) who provide details of the model atmosphere and cut off criteria for the inclusion of center and wing line contributions. Conceptually the calculation is similar to that done in the LASER computer code (McClatchey and D'Agati, 1978). For the calculations described here, the model atmosphere was modified to input relative humidity to determine water vapor number density and output values were weighted with a square instrument filter function of half width 0.5 cm^{-1} . Calculated values at $3.8\mu\text{m}$ and $10.6\mu\text{m}$ of 0.0276 km^{-1} and 0.0328 km^{-1} , respectively [see Table 9-1] correspond primarily to CO_2 and H_2O contributions (some CH_4 at $3.8\mu\text{m}$).

9.3.3 Continuum absorption

Water vapor continuum absorption, β_H , at both 3.8 and 10.6 μm and the pressure induced nitrogen continuum absorption, β_N , in the 4 μm region are included in Table 9-1. The nitrogen continuum is based on the measurements of Shapiro and Gush (1966) as described in Susskind and Searl (1977). In the 8-11 μm region the water vapor self broadening is evaluated based on the values from Bignell (1970). These calculations are consistent with those using Burch (1970) and Roberts et al. (1976) as applied in LOWTRAN5. Near 4 μm , the water vapor continuum is based on the values given by Burch et al. (1971). Water vapor continuum effects are dependent on its abundance (partial pressure, mass density, etc.) and thus an additional input parameter is required. As described previously the partial pressure of water vapor was input as relative humidity for a fixed layer temperature (288.1 K at approximately standard pressure). Thus the additional parameter here is the layer temperature. Figure 9-1 illustrates the variation of the total water vapor continuum absorption coefficient β_H at 10.6 μm with relative humidity. The absolute water vapor abundance ranges from 2.0 gm^{-3} (RH \approx 15.7%) to 10.9 gm^{-3} (RH \approx 85%). Also illustrated in Figure 9-1 are the individual contributions due to self, β_H^S , and foreign broadening, β_H^f .

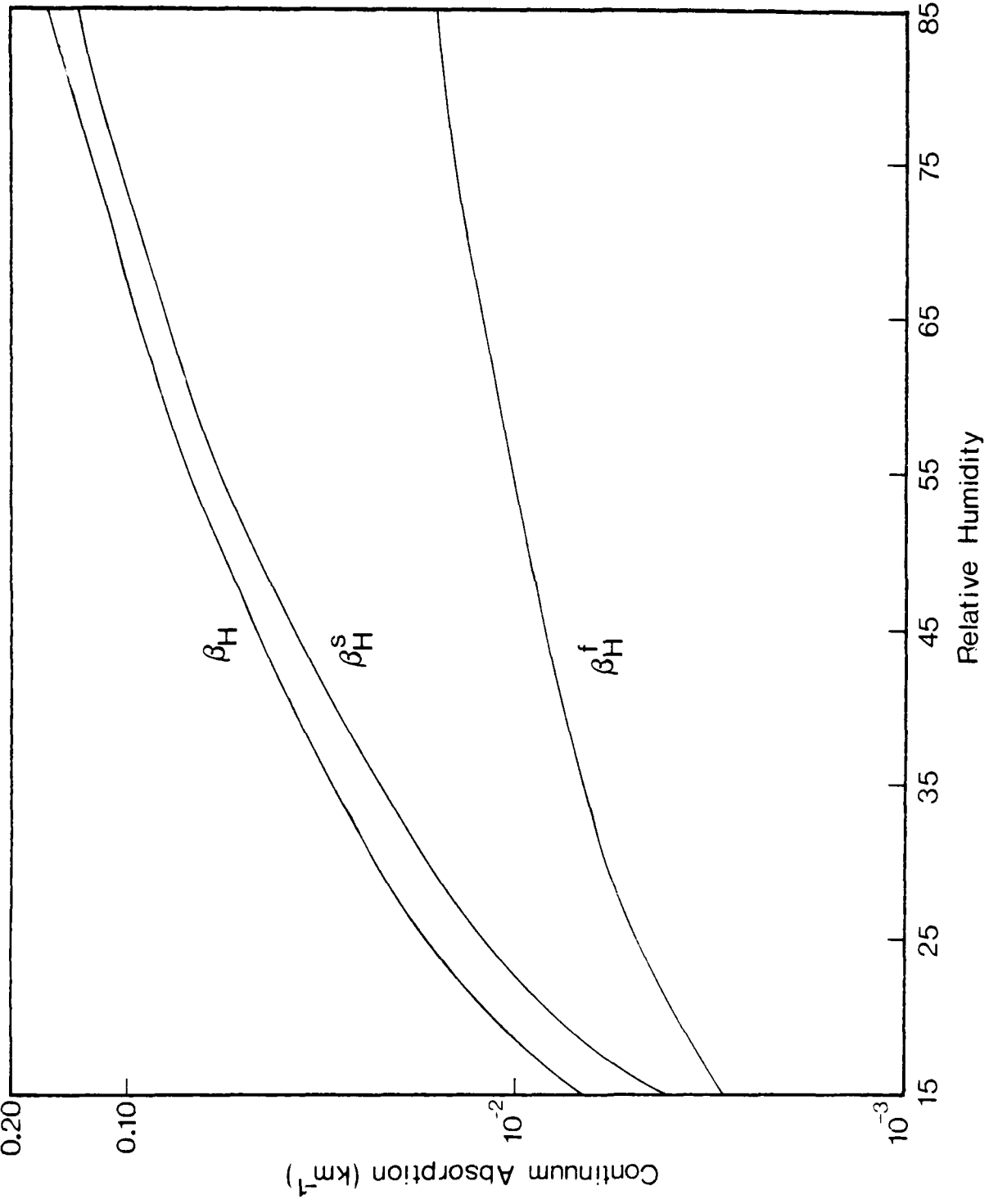


Figure 9-1. Water Vapor Continuum Absorption β_H at 10.6 μm vs. Relative Humidity (β_H^S = self broadening; β_H^f = foreign broadening) at $T = 288.1$ K and $P = 1025$ mb.

9.4 Multispectral Range Retrieval Results

By using equation (9-1) [where the total extinction is defined by (9-5)] and evaluating the aerosol contributions based on algorithm steps (9.2.1 - 9.2.7) and non-aerosol contributions as described in Section 9.3, optical ranges are retrieved for the wavelengths and conditions listed in Table 9-1. These results are presented in Table 9-1 under heading (c). Note that while range is almost exclusively determined by aerosol extinction at visible and near IR wavelengths, the significance of non-aerosol effects increases with wavelength. At $3.8\mu\text{m}$ aerosol extinction and non-aerosol effects (primarily line absorption) are about equal while at $10.6\mu\text{m}$, optical range is almost solely a function of water vapor abundance due to continuum absorption.

While this example is quite case specific, it illustrates a methodology to retrieve optical ranges at desired wavelengths using satellite based visible radiances as an aid in the inference of aerosol extinction contributions. For wavelengths in the visible region, optical range may potentially be inferred from the satellite radiances alone with some supporting meteorology (RH, WS, H). At longer wavelengths where non-aerosol contributions to extinction become significant (such as the water vapor continuum near $10\mu\text{m}$), additional input data (such as absolute humidity) is required. Such information may also be potentially available from remote sensing data. In any case, the technique

described here provides the framework to evaluate a priori, the impact of various meteorologically dependent extinction mechanisms on optical range. This capability may be exploited to provide a multispectral range retrieval algorithm when supported by the requisite satellite data source. Further discussion of data needs may be found in Goroch (1982).

10. SUMMARY, CONCLUSIONS, AND RECOMMENDATIONS

10.1 Report Summary

This report has described the results of the second stage of model development and application undertaken in the investigation of the sensitivity of remotely sensed radiances in the DMSP VHR/LF spectral region (0.4 to 1.1 μ m) to near surface meteorological parameters such as relative humidity, wind speed, and aerosol characteristics including mixing height and number density. A research grade computer code developed in an earlier study (Isaacs, 1980) to approximately simulate DMSP visible and near infrared radiances has been upgraded and augmented with additional capabilities desired in the analysis of imagery for tactical purposes including: (a) treatment of continental (i.e., urban and rural) aerosol size distribution and composition models in addition to previously implemented maritime models for application to coastal regions or open ocean areas under the influence of continental origin air masses, (b) data simulation calculations based on realistic sun/sensor geometries through the implementation of simplified satellite subtrack/sensor scan line and solar ephemeris subroutines, and (c) approximate ocean surface reflection modeling for potential sunlint regions based on both the classical Fresnel relations and the empirical wind dependent statistics of sea surface slope orientations. Additionally, the approximate, analytical radiative transfer submodel

incorporated into the code is fully described and the results of comparisons with accurate numerical treatments are provided for a variety of scattering situations. Comprehensive program documentation is included consisting of listings of the algorithm, sample output, and operating instructions for implementation on a desk top minicomputer.

A variety of simulation studies employing the algorithm are discussed illustrating the effect of relative humidity and mixing height on radiances in non sunglint situations for both rural and urban aerosol models as compared to the maritime models previously examined (i.e. in Isaacs, 1980). Radiance calculations in sunglint regions using the maritime aerosol model illustrate the effect of relative humidity, wind speed, and aerosol scale height on the intensity gradient observed along simulated sensor scan lines in the vicinity of the primary specular point. Additionally, the model is exercised to simulate a swath of DMSP imagery for illustrative purposes. Results of these simulations confirm the behavior generally observed in relevant imagery for corresponding meteorological analysis case studies as previously reported (cf. Fett and Mitchell, 1973).

Comparison of model predicted values to measured data are presented in two contexts: (a) multiwavelength aerosol extinction coefficient profiles calculated from field measured size distributions are compared to model predicted values based on measured relative humidity profiles as the required meteorological input. Predicted and measured

values are equated at one wavelength thus providing a measure of relative wavelength dependence. In general, the maritime aerosol model performs well except at high relative humidities. (b) Model calculated radiances along a simulated scan line in sunglint were compared to data points obtained from sensometry for the corresponding hardcopy imagery. The model input data included the appropriate satellite and solar specific data (AN, TN, SD, etc.) and relevant meteorological data supplied with the imagery. Due to lack of overall data calibration, the modeled results were normalized to one data point. The resulting comparison is promising, considering the assumptions invoked.

In addition to these imagery simulation exercises potentially related to meteorological analyses, application of the algorithm to the inference of surface propagation parameters was explored. Utilizing the model's capability to provide simulated radiances for specified meteorology and choice of aerosol, DMSP radiance/aerosol optical depth relationships were computed. Results provide a theoretical fit of radiance to aerosol optical depth for maritime, rural, and urban aerosols and relative humidities of 50 through 95%. These may be applied to the retrieval of aerosol optical depth (at visible wavelengths) from appropriately calibrated DMSP radiances.

Since surface propagation parameters are desired at other than visible wavelengths, a prototype algorithm was devised to infer optical range multispectrally using the

DMSP radiance/optical depth relationships described above to provide the aerosol contribution to extinction.

10.2 Conclusions

The following conclusions and observations are based on the work summarized above:

- Although limited in scope, the validation effort associated with the MAGAT data set indicates that the AFGL maritime aerosol model performs relatively well where expected.
- A variety of comparisons performed between the model adopted approximate radiative transfer scheme and accurate numerical treatments for a range of optical depths, angular scattering functions, and observer/sun orientations leads to the conclusion that simulated radiances are accurate to within 10% overall. This level of accuracy is consistent with the accuracy of input data and the intended purpose of the model, i.e. the simulation of meteorological influences in the imagery. The results of specific sensitivity tests conclude that adoption of simple analytical phase function representations and the hybrid modified δ -Eddington flux parameterization are appropriate choices.
- The wind-driven, rough ocean surface reflection model implemented within the radiance simulation

code provides a good representation of the sunglint phenomenon as compared to accurate numerical treatments, simulated radiance comparisons to hardcopy imagery, and qualitative observations.

- Model simulations in sunglint regions suggest a decrease in radiance in the vicinity of the primary specular point due to increases in aerosol optical depth (related to increased relative humidity or scale height). Away from the primary sunglint region, radiances increase with increasing optical depth as predicted in previous studies.
- A comparison of the optical properties of the maritime and recently implemented rural and urban models suggests that some care must be taken in the interpretation of meteorological influences on individual air masses. For example, the maritime aerosol coarse mode is much more hygroscopic than the others, while the carbon component of the urban aerosol is critical in determining its radiative properties.
- As a consequence of the above, each aerosol composition model and relative humidity range exhibit unique radiance/optical depth relationships. While those for maritime and rural aerosols are close enough to permit a single linear

predictor equation to be used operationally, those for the urban aerosol introduce a potential ambiguity. It appears that it may be important to know whether the air mass aerosol under investigation has any carbon component present (anthropogenic or natural). This may be important in the vicinity of inland seas, coastal regions, or open ocean in situations of long range transport. A parameter which may potentially be retrievable in this regard is the single scattering albedo (Kaufman and Joseph, 1982).

- A sample multispectral range retrieval exercise illustrates both the dominance of aerosol extinction in constraining range at visible wavelengths and the complementary significance of non-aerosol extinction contributions in the infrared. With respect to the latter, calculated aerosol extinction accounts for less than 7% of the total at $10.6\mu\text{m}$, while that for water vapor continuum absorption is 75%. While visible radiance data may be useful in predicting visible range, it must be augmented by absolute humidity data from other sources to evaluate IR range.

10.3 Recommendations

Although limited, the validation exercises described in this report associated with both the MAGAT data and

various radiance simulations give some confidence that even though simple techniques are employed, the overall simulation is capable of providing realistic depictions of the sensitivity of remotely sensed radiances to the various meteorological data inputs. Based on the simulation and validation studies reported on here, it is appropriate to recommend the computer model documented above as a potential tool to aid in the analysis of DMSP visible imagery. Exercising the code in the course of imagery analysis provides the opportunity for validation through experience. Additionally, it is probable that the data available from future experimental programs will provide additional opportunity for testing and evaluation.

In the course of the study it became clear that an analogous imagery simulation code would be potentially useful in the analysis of corresponding infrared window (i.e., DMSP T L/F) imagery. Since case study analysis is most often performed with both data sets side-by-side in an "eyeball" multispectral comparison, it is reasonable to suggest quantification of the observed phenomenon. Such a combined simulation tool may be helpful in determining the difference between low level moisture, sea surface temperature, and low level aerosol effects.

Another rationale for recommending further simulation in the IR window is the need to quantify low level water vapor effects to supplement the IR range retrieval problem discussed previously. Further development of the prototype

range retrieval algorithm proposed above is recommended including investigation of the potential use of the IR T/LF data to provide the required water vapor amounts in the near surface environment.

Finally, it should be noted that the simulation code as documented is configured for a specific purpose, that of interactive DMSP radiance simulation. With suitable modification the basic algorithm will provide a simulated wavelength dependent radiance sensed at a given location for an input data vector of site specific meteorological variables. Thus the potential exists to use the basic algorithm as a module within a larger model to simulate fields of either radiance or flux or in an inverse mode with supplementary input to infer the data fields from radiance fields. Transformation fields may also be computed to simulate one visible sensor's data from another's radiance field. These uses remain to be explored.

11. ACKNOWLEDGEMENTS

The author wishes to thank Dr. A. Goroch and Mr. R. Fett of the Naval Environmental Prediction Research Facility for helpful discussions and the various data which they kindly provided in support of this work. Communications in the course of this program with Dr. R. Fraser, Mr. W. Hering, Dr. Y. Kaufman, and Dr. E. Shettle are gratefully acknowledged. Dr. P. B. Ryan assisted in formulating portions of the HP-85 computer code presented here. The assistance of Mr. W. Martin of the Office of Naval Research is greatly appreciated.

Finally, the author is indebted to his colleagues at AER including Drs. L. D. Kaplan, N.D. Sze and M.K.W. Ko. The manuscript was capably prepared by L. Gibson and S. Piro.

12. REFERENCES

- Abhyankar, K.D., Fymat, A.L. (1971) Tables of Auxiliary Functions for Non-Conservative Rayleigh Phase Matrix in Semi-Infinite Atmospheres, Ap. J. Supplement Series, No. 195, 23, 35-192.
- Ahmad, Z. and R.S. Fraser (1982) An Iterative Radiative Transfer Code for Ocean-Atmosphere Systems. J. Atmos. Sci., 39, 656-665.
- Anderson, R.K. et al. (1974) Applications of Meteorological Satellite Data in Analysis and Forecasting. ESSA Techn. Report NESC 51 (including Supplement, Nov., 1971 and Supplement No. 2, March 1973), National Environmental Satellite Service, NOAA, Washington, D.C., 350 pp.
- Acquista, C., F. House, and J. Jafolla (1981) N-Stream Approximations to Radiative Transfer. J. Atmos. Sci., 38, 1446-1451.
- Barnes, J.C., R.G. Isaacs, C.J. Bowley and A.J. Bussey (1979) Comparative Study of Anomalous Gray Shade Patterns in DMSP and LANDSAT Imagery. NAVENVPREDRSCHFAC CR 79-05, Naval Environmental Prediction Research Facility, Monterey, CA.
- Barrick, D.E. (1972) Remote Sensing of Sea State by Radar. in Remote Sensing of the Troposphere, V.E. Derr (ed.), U.S. Department of Commerce.
- Bergstrom, R.W. (1973) Comments on the Estimation of Aerosol Absorption Coefficients in the Atmosphere. Beitr. Physik Atmos., 46, 198-202.
- Bergstrom, R.W., B.L. Babson and T.P. Ackerman (1980) Calculation of Multiple Scattered Radiation in Clean Atmospheres. Paper presented at the Symposium on Plumes and Visibility: Measurements and Model Components, November 10-14, Grand Canyon, Arizona, Atmospheric Environment, 15, 1821-1826.
- Bignell, K.J. (1970) Water-Vapour Infrared Continuum. Quart. J.R. Met Soc., 9, p. 390.
- Burch, D.E. (1970) Semiannual Technical Report: Investigation of the Absorption of Infrared Radiation by Atmospheric Gases. Aeronutronic Report-U-4784.

- Burch, D.E., D.A. Gryvnak and J.D. Pembroke (1971) Investigation of the Absorption of Infrared Radiation by Atmospheric Gases: Water, Nitrogen, Nitrous Oxide. Publication No. U-4897, Aeronutronic Division, Philco-Ford Corporation, Newport Beach, California.
- Burke, H.K. and N.D. Sze (1977) A Comparison of Variational and Discrete Ordinate Methods for Solving Radiative Transfer, J. Quant. Spectrosc. Radiat. Transfer, vol. 17, 783-793.
- Burt, W.V. (1954) Albedo Over Wind-Roughened Water. J. Meteor., 11, 283-290.
- Carlstedt, J.L., T.W. Mullikin (1966) Chandrasekhar's X and Y Functions. Astroph. J. Suppl., 12, No. 113, 449.
- Chandrasekhar, S. (1966) Radiative Transfer. Dover Publications.
- Coakley, J.A., Jr. and P. Chylek (1975) The Two-Stream Approximation in Radiative Transfer: Including the Angle of the Incident Radiation. J. Atmos. Sci., 32, 409-418.
- Coulson, K.L., J.V. Dave and Z. Sekera (1960) Tables Related to Radiation Emerging from a Planetary Atmosphere with Rayleigh Scattering, University of Calif. Press.
- Curran, R.J. (1972) Ocean Color Determination Through a Scattering Atmosphere. Appl. Opt., 11, 1857-1866.
- Cox, C. and W. Munk (1954) Statistics of the Sea Surface Derived from Sun Glitter. J. Marine Res., 13 (2), 198-227.
- Deirmendjian, D. (1969) Electromagnetic Scattering on Spherical Polydispersion, New York Elsevier Publ.
- Dave, J.V. and J. Gazdag (1970) A Modified Fourier Transform Method for Multiple Scattering Calculations in a Plane-Parallel Mie Atmosphere. Appl. Opt., 9, 1457-1466.
- Dave, J.V. (1972) Development of Programs for Computing Characteristics of Ultraviolet Radiation. Technical Report Contract NAS 5-21680 NASA Goddard Space Flight Center, Greenbelt, MD 20771.
- Duce, R.A., C.K. Unni, B.J. Ray, J.M. Prospero, J.T. Merrill (1980) Long-Range Transport of Soil Dust from Asia to the Tropical North Pacific: Temporal Variability. Science, 209, 1522-1524.

- Eaton, F.D. and I. Dirmhim (1979) Reflected Irradiance Indicatrices of Natural Surfaces and Their Effect on Albedo. Appl. Opt., 18, 7, 994-1008.
- Elterman, L. (1970) Vertical Attenuation Model with Eight Surface Meteorological Ranges 2 to 13 Kilometers. Report No. AFCRL-70-0200, March 1970, Air Force Cambridge Research Laboratories.
- Fett, R.W. and R.G. Isaacs (1979) Concerning Causes of "Anomalous Gray Shades" in DMSP Visible Imagery. J. Appl. Meteor., 18, 1340.
- Fett, R.W. and W.F. Mitchell (1977) Navy Tactical Applications Guide: Vol. 1, Technique and Applications of Image Analysis (DMSP). NEPRF Applications Report 77-03. Tactical Applications Department, Naval Environmental Prediction Research Facility, Monterey, CA.
- Fillmore, J.A. and A.H. Karp (1980) Choosing an Approximation to the Equation of Radiative Transfer. J. Atmos. Sci., 37, 1880-1883.
- Fowler, M.G., J.H. Willand, D.T. Chang and R.G. Isaacs (1977) Estimation of the Geophysical Properties of the Ocean Surface Using Aircraft Microwave Measurements. ERT P-1143F. Prepared for NASA Goddard Space Flight Center.
- Fraser, R.S. (1976) Satellite Measurement of Mass of Sahara Dust in the Atmosphere. Appl. Opt., 15, 10, 2471-2479.
- Fraser, R.W. and R.J. Curran (1976) Effects of the Atmosphere on Remote Sensing in Remote Sensing of Environment. J. Lintz, Jr. and D.S. Simonett (eds.) Addison Wesley Publishing, pp. 34-84.
- Gaut, N., M.G. Fowler, R.G. Isaacs, D.T. Chang and E.C. Reifenstein III (1975) Studies of Microwave Remote Sensing of Atmospheric Parameters. AFCRL-TR-75-0007.
- Gerber, H.E. and E.E. Hindman (1981) Report on the First International Workshop on Light Absorption by Aerosol Particles. Proceedings, Technical Symposium East 1981, SPIE, Washington, D.C.
- Goody, R.M. (1964) Atmospheric Radiation: I. Theoretical Basis. Oxford University, 436 pp.
- Goroch, A.K. (1982) Summary of Recommendations for Inference of IR Range from Satellite Observations. Draft Report NEPRF, Monterey, Calif. 93940.

- Griggs, M. (1975) Measurements of Atmospheric Aerosol Optical Thickness Over Water Using ERTS-1 Data. JAPCA, 25, 622-626.
- Griggs, M. (1978a) Determination of Aerosol Content in the Atmosphere from LANDSAT Data. NASA CR-155788.
- Griggs, M. (1978b) TIROS-N AVHRR Data for Measurement of Atmospheric Aerosols. SAI-78-973-LJ.
- Griggs, M. (1979a) Satellite Observations of Atmospheric Aerosols During the EOMET Cruise. J. Atmos. Sci., 36, 695.
- Griggs, M. (1979b) Satellite Measurements of Tropospheric Aerosols. SPIE, 195, Atmospheric Effects on Radiative Transfer, 100-104.
- Guinn, J.A. Jr., G.N. Plass and G.W. Kattawar (1979) Sunglint Glitter on a Wind-Ruffled Seas: Further Studies. Appl. Opt., 18, 6, 842-849.
- Heney, L.G. and Greenstein, J.L. (1941) Diffuse Radiation in the Galaxy, Ap. J., 93, 70-83.
- Hewlett Packard (1979) HP-85 Owner's Manual and Programming Guide. Hewlett Packard Co., Corvallis, OR.
- Hansen, J.E. and L.D. Travis (1974) Light Scattering in Planetary Atmospheres. Space Sci. Rev., 16, 527-610.
- Hering, W.S. (1981) An Operational Technique for Estimating Visible Spectrum Contrast Transmittance. University of California at San Diego, Scripps Institution of Oceanography, Visibility Laboratory, SIO Ref. 82-1 AFGL-TR-81-0198.
- Hovenier, J.W. (1971) Multiple Scattering of Polarized Light in Planetary Atmospheres. Astr. Astrophys., 13, 7-29.
- Irvine, W.M. (1965) Multiple Scattering by Large Particles. Ap. J., 142, 1563-1575.
- Irvine, W.M. (1968) Multiple Scattering by Large Particles. II. Optically Thick Layers. Ap. J., 152, 823-834.
- Isaacs, R.G. (1980) Investigation of the Effect of Low Level Maritime Haze on DMSP VHR and LF Imagery. NAVENVPRD-RSCHFAC CR-80-06, Naval Environmental Prediction Research Facility, Monterey, CA.

- Isaacs, R.G. (1981) The Role of Radiative Transfer Theory in Visibility Modeling: Efficient Approximate Techniques. Atmos. Env., 15, 10/11, 1827.
- Isaacs, R.G., J.C. Barnes, J.C. Cogan and D.T. Chang (1974) Near IR Observations of Clouds. ERT Document P-1275-2. Environmental Research & Technology, Inc., Concord, MA.
- Isaacs, R.G. and D.T. Chang (1975) Experimental Evaluation of Atmospheric Effects on Radiometric Measurements Using the EREP of Skylab. Final Report, Contract NAS 9-013343. Environmental Research & Technology, Inc., Concord, MA.
- Isaacs, R.G. and H. Özkaynak (1980) Uncertainties Associated with the Implementation of Radiative Transfer Theory Within Visibility Models. Second Joint Conference on Applications of Air Pollution Meteorology, New Orleans, LA, 24-27 March, 362-369. American Meteorology Society, Boston, MA.
- Joseph, J.H., W. Wiscombe and J. Weinman (1976) The Delta-Eddington Approximation for Radiative Flux Transfer. J. Atmos. Sci., 33, 2452-2459.
- Kasten, F. (1969) Visibility Forecast in the Phase of Pre-Condensation. Tellus, 21, 631-635.
- Kaufman, Y.J. (1979) Effect of the Earth's Atmosphere on the Contrast for Zenith Observation. J. Geophys. Res., 84, 3165.
- Kaufman, Y.J. (1981) Combined Eye-Atmospheric Visibility Model. Appl. Opt., 20, 1525.
- Kaufman, Y.J. (1982) Solution of the Equation of Transfer for Remote Sensing Over Nonuniform Surface Reflectivity. J. Geophys. Res., 87, C6, 4137-4147.
- Kaufman, Y.J. and J.H. Joseph (1982) Evaluation of Surface Albedos and Extinction Characteristics of the Atmosphere from Satellite Images. J. Geophys. Res., 87, 1287.
- Kerschgens, M., V. Pilz and E. Raschke (1978) A Modified Two-Stream Approximation for Computations of the Solar Radiation Budget in a Cloudy Atmosphere. Tellus, 30, 429-435.
- Kneizys, F.X., E.P. Shettle, W.O. Gallery, J.H. Chetwynd, Jr., L.W. Abreau, J.E.A. Selby, R.W. Fenn and R.A. McClatchey (1980) Atmospheric Transmittance/Radiance: Computer Code LOWTRAN5. AFGL-TR-80-0067. Air Force Geophysics Laboratory, Hanscom AFB, MA 01731.

- Kornfield, J.I. (1974) On the Determination of Sea Surface Wind or Stress From Sunglint Observed by an Earth Synchronous Satellite. Measurements from Satellite Systems, 1-60, Space Science and Engineering Center, University of Wisconsin.
- Koschmieder, H. (1924) Theorie der Horizontalen Sichtweite. Beitr. Phys. frei Atmos., 12, 33-53 and 171-181.
- Kraus, E.B. (1972) Atmosphere-Ocean Interaction. Oxford University Press, London, 275 pp.
- Lenoble, J. (1970) Importance de la polarisation dans le Rayonnement Diffuse par une Atmosphere Planetaire, J. Quant. Spectro. Radiat. Trans., 10, 533.
- Lenoble, J. (1977) Standard Procedures to Compute Atmospheric Radiative Transfer in a Scattering Atmosphere. IAMAP, Boulder, CO.
- Liou, K.N. (1973) A Numerical Experiment on Chandrasekhar's Discrete-Ordinate Method for Radiative Transfer: Applications to Cloudy and Hazy Atmospheres. J. Atmos. Sci., 30, 1303-1326.
- Liou, K.N. (1974) Analytic Two-Stream and Four-Stream Solutions for Radiative Transfer. J. Atmos. Sci., 31, 1473-1475.
- Liou, K.N. (1980) An Introduction to Atmospheric Radiation. Academic Press, New York, 392 pp.
- MacKay, J.H. (1959) On the Gaussian Nature of Ocean Winds. Internal Technical No. 8, Engineering Experiment Station, Georgia Institute of Technology, Atlanta, GA.
- McClain, P.E. and A.E. Strong (1969) On Anomalous Dark Patches in Satellite Viewed Sunglint Areas. Mon. Wea. Rev., 97, 875-884.
- McClatchey, R.A. and A.P. D'Agati (1978) Atmospheric Transmission of Laser Radiation: Computer Code LASER. AFGL-TR-78-0029, Air Force Geophysic Laboratory, Hanscom AFB, MA 01751.
- McClatchey, R.A., W.S. Benedict, S.A. Clough, D.E. Burch, R.F. Calfee, K. Fox, L.S. Rothman and J.S. Garing (1973). AFCRL Atmospheric Absorption Line Parameters Compilation. Environmental Research Papers, No. 434, AFCRL-TR-73-0096, Air Force Cambridge Research Laboratories, Bedford, MA.

- Meador, W.E. and W.R. Weaver (1980) Two-Stream Approximations to Radiative Transfer in Planetary Atmospheres: A Unified Description of Existing Methods and a New Improvement. J. Atmos. Sci., 37, 630-643.
- Mekler, Y. and Y.J. Kaufman (1980) The Effect of Earth's Atmosphere on Contrast Reduction for a Nonuniform Surface Albedo and 'Two Halves Field.' J. Geophys. Res., 85, C7, 4067-4083.
- Mekler, Y. and Y.J. Kaufman (1982) Contrast Reduction by the Atmosphere and Retrieval of Nonuniform Surface Reflection. Appl. Opt., 21, 310-316.
- Mullamaa, Y. (1964) Atlas of the Optical Characteristics of a Disturbed Sea Surface. Acad. Sci. Estonian SSR, 109 pp.
- Nagel, M.R., H. Quenzel, W. Kweta and R. Wendling (1978) Daylight Illumination-Color-Contrast Tables. Academic Press.
- Nilsson, B. (1979) Meteorological Influence on Aerosol Extinction in the 0.2-40.0 μ m wavelength range. Appl. Opt., 18, 3457-3473.
- Norton, C.C., F.R. Mosher, B. Hinton, D.W. Martin, D. Santek and W. Kuhlrow (1980) A Model for Calculating Atmospheric Turbidity Over Oceans from Grostationary Satellite Data. J. Appl. Meteor., 19, 633-644.
- Penndorf, R. (1957) Tables of the Refractive Index for Standard Air and the Rayleigh Scattering Coefficient for the Spectral Region between 0.2 and 20 μ m and their Application to Atmospheric Optics. J. Opt. Soc. Amer., 47, 176-182.
- Pierson, W.J. and L. Moskowitz (1964) A Proposed Spectral Form for Fully Developed Wind Seas Based on the Similarity Theory of S.A. Kitaigorodskii. J. Geophys. Res., 69, 5818-5190.
- Pierson, W.J. and R.A. Stacy (1973) The Elevation, Slope and Curvature Spectra of a Wind-Roughened Sea Surface. NASA Contractor Report CR 2247, Langley Research Center.
- Plass, G.N., G.W. Kattawar and J.A. Guinn, Jr. (1975) Radiative Transfer in the Earth's Atmosphere and Ocean: Influence of Ocean Waves. Appl. Opt., 14, 8, 1924-1936.

- Ramsey, R.C. (1968) Study of the Remote Measurement of Ocean Color. Final Report, TRW, NASW-1658.
- Raschke, E. (1972) Multiple Scattering Calculation of the Transfer of Solar Radiation in an Atmosphere-Ocean System. Beiträge zur Physik der Atmosphäre, 45, 1-19.
- Roberts, R.E., J.E.A. Selby and L.M. Biberman (1976) Infrared Continuum Absorption by Atmospheric Water Vapor in the 8-12 μ m Window. Appl. Opt., 14, 2085.
- Roessler, D.M. and F.R. Faxvog (1981) Visibility in Absorbing Aerosols. Atmos. Env., 15, 151-155.
- Rosen, H., T. Noovakov and B.A. Bodhaine (1981) Soot in the Arctic. Atmos. Environ., 15, 8, 1371-1374.
- Rothman, L.S. and R.A. McClatchey (1976) Appl. Optics, 15, 2615.
- Sekera, Z. and A.B. Kahle (1966) Scattering Functions for Rayleigh Atmospheres of Arbitrary Thickness, Memorandum R-452-PR, The Rand Corporation.
- Selby, J.E.A. and R.A. McClatchey (1972) Atmospheric Transmittance from 0.25 to 28.5 μ : Computer Code LOWTRAN2. AFCRL-TR-0745.
- Selby, S.M. (1967) Standard Mathematical Tables. The Chemical Rubber Co., Cleveland, OH, 724 pp.
- Shapiro, M.M. and H.P. Gush (1966) Canad. J. Physics, 44, 949.
- Shettle, E.P. and R.W. Fenn (1979) Models for the Aerosols of the Lower Atmosphere and the Effects of Humidity Variations on their Optical Properties. AFGL-TR-79-0214 Air Force Geophysics Laboratories, Hanscom AFB, MA.
- Shettle, E.P., F.X. Kneizys and W.O. Gallery (1980) Suggested Modification to the Total Volume Molecular Scattering Coefficient in LOWTRAN: Comment. Appl. Opt., 19, 17, 2873-2874.
- Stibbs, D.W.M. and R.E. Weir (1959) On the H-Functions for Isotropic Scattering. Month. Nat. R. Astron. Soc., 119, 512.
- Sze, N.D. (1976) Variational Methods in Radiative Transfer Problems. J. Quant. Spectrosc. Radiat. Transfer, 17, 783-793.

- Susskind, J. and J.E. Searl (1977) Atmospheric Absorption Near 2400 cm^{-1} . J. Quant. Spectrosc. Radiat. Transfer, 18, 581-587.
- Susskind, J. and J.E. Searl (1978) Synthetic Atmospheric Transmittance Spectra Near 15 and $4.3 \mu\text{m}$. J. Quant. Spectrosc. Radiat. Transfer, 19, 195-215.
- Takashima, T. and Y. Takayama (1981) Emissivity and Reflectance of the Model Sea Surface for the Use of AVHRR Data of NOAA Satellites. Papers in Meteorology and Geophysics, 32, 4, 267-274.
- Tanre, D., M. Herman, P.Y. Deschamps and A. De Leffe (1979) Atmospheric Modeling for Space Measurements of Ground Reflections, Including Bidirectional Properties. Appl. Opt., 18, 21, 2587-2694.
- Towne, D.H. (1967) Wave Phenomena. Addison-Wesley, Reading, MA, 480 pp.
- Tsui, T.L. and R.W. Fett (1980) Determination of the Primary Specular Point in the Sunglint Pattern of a Polar Orbiting Satellite Image. NAVENVPREDRSCHFAC Technical Report TR 80-03. Naval Environmental Prediction Research Facility, Monterey, CA.
- Twitty, J.T. and J.A. Weinman (1971) Radiative Properties of Carbonaceous Aerosols. J. Appl. Meteor., 10, 725-731.
- Wiscombe, W.J. and G.W. Grams (1976) The Backscattered Fraction in Two-Stream Approximations. J. Atmos. Sci., 33, 2440-2451.
- Wells, W.C., G. Gall and M.W. Munn (1977) Aerosol Distribution in Maritime Air and Predicted Scattering Coefficients in the Infrared. Appl. Opt., 16, 543.
- Wylie, D.P., B.B. Hinton and K.M. Millett (1981) A Comparison of Three Satellite-Based Methods for Estimating Surface Winds Over Oceans. J. Appl. Met., 20, 439-449.

APPENDIX A: DERIVATION OF APPROXIMATE ANALYTICAL
SOLUTION TO RADIATIVE TRANSFER EQUATION

Following Kaufman (1979), the analytical solution to the radiative transfer equation (6-1, 6-2) used in this study is derived by approximating the integral term in the source function J (6-2) by assuming that the upward ($\mu > 0$) and downward ($\mu < 0$) diffuse (i.e. scattered) intensity fields are independent of direction (μ, ϕ) and given by I^+ and I^- , respectively. Mathematically, this approach may be considered as a two-point quadrature of the angular integration over upper and lower hemispheres. Physically, the method is interpretable as an approximation of the multiply scattered contributions to the intensity field. For incident solar irradiance πF , Equation (6-2) is approximated as:

$$\begin{aligned}
 J_s(\tau, \pm \mu, \phi) \approx & \frac{F e^{-\tau/\mu_0}}{4} P(\mu, \mp \mu_0; \phi, \phi_0) \\
 & + \frac{I^+}{4\pi} \int_0^1 \int_0^{2\pi} P(\mu, \pm \mu'; \phi, \phi') d\mu' d\phi' \\
 & + \frac{I^-}{4\pi} \int_0^1 \int_0^{2\pi} P(\mu, \mp \mu'; \phi, \phi') d\mu' d\phi' \quad (A.1)
 \end{aligned}$$

Upon substitution of (A.1), the radiative transfer Equation (6-1) is written separately for each of the two streams, I^\pm as:

$$\begin{aligned}
\mu \frac{dI^+}{d\tau} &= I^+ - \frac{I^+}{4\pi} \int_0^{2\pi} \int_0^1 P(\mu, +\mu'; \phi, \phi') d\mu' d\phi' \\
&\quad - \frac{I^-}{4\pi} \int_0^{2\pi} \int_0^1 P(\mu, -\mu'; \phi, \phi') d\mu' d\phi' \\
&\quad - \frac{F}{4} P(\mu, -\mu_0; \phi, \phi_0) e^{-\tau/\mu_0} \tag{A.2a}
\end{aligned}$$

$$\begin{aligned}
-\mu \frac{dI^-}{d\tau} &= I^- - \frac{I^+}{4\pi} \int_0^{2\pi} \int_0^1 P(\mu, -\mu'; \phi, \phi') d\mu' d\phi' \\
&\quad - \frac{I^-}{4\pi} \int_0^{2\pi} \int_0^1 P(\mu, \mu'; \phi, \phi') d\mu' d\phi' \\
&\quad - \frac{F}{4} P(\mu, \mu_0; \phi, \phi_0) e^{-\tau/\mu_0} \tag{A.2b}
\end{aligned}$$

The angular integrations in (A.2a,b) are performed by noting the phase function normalization:

$$\omega_0 = \frac{1}{4\pi} \int_0^{2\pi} \int_{-1}^{+1} P(\mu, \mu'; \phi, \phi') d\mu' d\phi' \tag{A.3}$$

and defining the azimuthally symmetric function, P^0 ; the backscatter fraction for monodirectional radiation, β ; and the backscatter fraction for isotropic radiation, β' as:

$$P^0(\mu, \mu') = \frac{1}{2\pi} \int_0^{2\pi} P(\mu, \mu'; \phi, \phi') d\phi' \quad (\text{A.4})$$

$$\beta(\mu) = \frac{1}{2\omega_c} \int_0^1 P^0(\mu, \mu') d\mu' \quad (\text{A.5})$$

$$\beta' = \int_0^1 \beta(\mu') d\mu' \quad (\text{A.6})$$

Applying these definitions, the intensity Equations (A.2) become:

$$\begin{aligned} \mu \frac{dI^+}{d\tau} &= I^+ - I^+ \omega_0 [1 - \beta(\mu)] - I^- \omega_0 \beta(\mu) \\ &\quad - \frac{F}{4} P(\mu, -\mu_0; \phi, \phi_0) e^{-\tau/\mu_0} \end{aligned} \quad (\text{A.7a})$$

$$\begin{aligned} -\mu \frac{dI^-}{d\tau} &= I^- - I^+ \omega_0 \beta(\mu) - I^- \omega_0 [1 - \beta'(\mu)] \\ &\quad - \frac{F}{4} P(\mu, \mu_0; \phi, \phi_0) e^{-\tau/\mu_0} \end{aligned} \quad (\text{A.7b})$$

Assuming that the scattered diffuse intensities are given by the fluxes $F^\pm(\tau)$ such that:

$$I^\pm(\tau, \mu, \phi) = F^\pm(\tau)/\pi \quad (\text{A.8})$$

Equation (A.7) may be written as:

$$\mu \frac{dI^+}{d\tau} - I^+ = - \frac{\omega_0}{\pi} \left\{ F^+ [1-\beta(\mu)] + F^- \beta(\mu) \right\} - \frac{F}{4} P(\mu, -\mu_0; \phi, \phi_0) e^{-\tau/\mu_0} \quad (\text{A.9a})$$

$$- \mu \frac{dI^-}{d\tau} - I^- = - \frac{\omega_0}{\pi} \left\{ F^+ \beta(\mu) + F^- [1-\beta(\mu)] \right\} - \frac{F}{4} P(\mu, \mu_0; \phi, \phi_0) e^{-\tau/\mu_0} \quad (\text{A.9b})$$

Integration of equations (A.9) over the angle yields coupled equations for the fluxes:

$$\frac{dF^+}{d\tau} = 2F^+ [1-\omega_0(1-\beta')] - 2F^- \omega_0 \beta' - \pi F \omega_0 \beta(\mu_0) e^{-\tau/\mu_0} \quad (\text{A.10a})$$

$$\frac{dF^-}{d\tau} = -2F^- [1-\omega_0(1-\beta')] + 2F^+ \omega_0 \beta' + \pi F \omega_0 [1-\beta(\mu_0)] e^{-\tau/\mu_0} \quad (\text{A.10b})$$

Applying the boundary conditions [(6-4) in the text]:

$$\left. \begin{aligned}
 F^-(\tau=0) &= 0 \\
 F^+(\tau=\tau^*) &= A_L [\pi \mu_0 e^{-\tau^*/\mu_0} + F^-(\tau=\tau^*)]
 \end{aligned} \right\} \quad (38)$$

the solutions for F^\pm are

$$F^+(\tau) = Ae^{k\tau} + Be^{-k\tau} + Ce^{-\tau/\mu_0} \quad (A.11a)$$

$$F^-(\tau) = \frac{1}{\gamma_2} \left\{ A(\gamma_1 - k)e^{k\tau} + B(\gamma_1 + k)e^{-k\tau} + \gamma e^{-\tau/\mu_0} \right\} \quad (A.11b)$$

where the appropriate constants are given by:

$$\gamma_1 = 2 [1 - \omega_0(1 - \beta')] \quad (A.12)$$

$$\gamma_2 = 2 \omega_0 \beta' \quad (A.13)$$

$$k = (\gamma_1^2 - \gamma_2^2)^{\frac{1}{2}} \quad (A.14)$$

$$A = [B(\gamma_1 + k) + Y]/(k - \gamma_1) \quad (A.15)$$

$$B = (E_1 e^{k\tau^*} + E_2 e^{-\tau^*/\mu_0}) / (E_3 e^{k\tau^*} + E_4 e^{-k\tau^*}) \quad (A.16)$$

$$C = \pi \omega_0 \left\{ \frac{\beta(\mu_0)}{\mu_0} - \gamma_1 \beta(\mu_0) - \gamma_2 [1 - \beta(\mu_0)] \right\} \\
 \times \left(\frac{\mu_0^2}{1 - k^2 \mu_0^2} \right) \quad (A.17)$$

$$Y = C \left(\gamma_1 + \frac{1}{\mu_0} \right) - \pi F \omega_0 \beta(\mu_0) \quad (\text{A.18})$$

$$E_1 = Y \left[1/(\gamma_1 - k) - A_2/\gamma_2 \right] \quad (\text{A.19})$$

$$E_2 = \left[-C + \pi F \mu_0 A_L + \frac{A_L Y}{\gamma_2} \right] \quad (\text{A.20})$$

$$E_3 = (\gamma_1 + k) \left[1/(k - \gamma_1) + A_L/\gamma_2 \right] \quad (\text{A.21})$$

$$E_4 = \left[1 - A_L (\gamma_1 + k)/\gamma_2 \right] \quad (\text{A.22})$$

The solution for the upward (i.e. emergent) intensity, $I^+(\tau, \mu, \phi)$, is obtained by integrating equation (A.9) subject to the boundary conditions:

$$I^-(\tau=0, \mu, \phi) = 0 \quad (43)$$

$$I^+(\tau=\tau^*, \mu, \phi) = F^+(\tau=\tau^*)/\pi \quad (44)$$

to obtain [compare to text (6-5)]:

$$I^+(\tau, \mu, \phi) = D_1 e^{\tau/\mu} + \frac{U_1 e^{k\tau}}{1-\mu k} + \frac{U_2 e^{-k\tau}}{1+\mu k} + \frac{U_3 e^{-\tau/\mu_0}}{1+\mu/\mu_0} \quad (\text{A.23})$$

where:

$$D_1 = \left[\frac{F^+(\tau^*)}{\pi} - \frac{U_1 e^{k\tau^*}}{1-\mu k} - \frac{U_2 e^{-k\tau^*}}{1+\mu k} - \frac{U_3 e^{-\tau^*/\mu_0}}{1+\mu/\mu_0} \right] e^{-\tau^*/\mu} \quad (\text{A.24})$$

$$U_1 = \frac{A\omega_0}{\pi} \left[1 - \beta(\mu) + \frac{\beta(\mu)}{\gamma_2} (\gamma_1 - k) \right] \quad (\text{A.25})$$

$$U_2 = \frac{B\omega_0}{\pi} \left[1 - \beta(\mu) + \frac{\beta(\mu)}{\gamma_2} (\gamma_1 + k) \right] \quad (\text{A.26})$$

$$U_3 = \frac{C\omega_0}{\pi} [1 - \beta(\mu)] + \frac{\omega_0}{\pi} \frac{\beta(\mu)}{\gamma_2} Y + \frac{F}{4} P(\mu, -\mu_0; \phi, \phi_0) \quad (\text{A.27})$$

The required value of $F^+(\tau^*)$ in D_1 (A.24) is available from equation (A.11a). The values of β' , $\beta(\mu)$, and $\beta(\mu_0)$ in the above expressions are obtained from Figure 6-3 after calculating the appropriate asymmetry parameter, g , using equation (6-13). Values of τ^* and ω_0 are obtained using the modeled optical data for gases and aerosols as described in Sections 3 and 5 of Isaacs (1980).
and 5, respectively.

APPENDIX B: PROGRAM DESCRIPTION

B.1 Technical Approach

A major goal of this research program has been the development of an analysis tool relating in situ meteorological variables and remotely sensed radiances. This section describes and documents the research grade computer algorithm developed during the course of this work and subsequently applied to the simulations of DMSP VHR and LF imagery presented in previous sections. The general technical approach adopted in formulating the simulation model code is summarized in Figure B-1 reproduced from Isaacs (1980).

Requisite input parameters include the meteorological variables characterizing the lower atmosphere: relative humidity (RH), wind speed (WS), number density (N), or visual range (V_r), and aerosol scale heights for both fine and course aerosol size ranges (H_1 , H_2 , respectively). The input required for specification of the sun/atmosphere-ocean/sensor geometric configuration consists of spacecraft and solar ephemeris data including: the longitude of the ascending node (AN), the time of the ascending node (TN), the solar declination angle (SD) for the desired date, and the time of the scan line desired (T). The sensor zenith angle, solar zenith angle, and azimuth angle difference which were previously input data are now computed based on the above input using the approach described earlier in

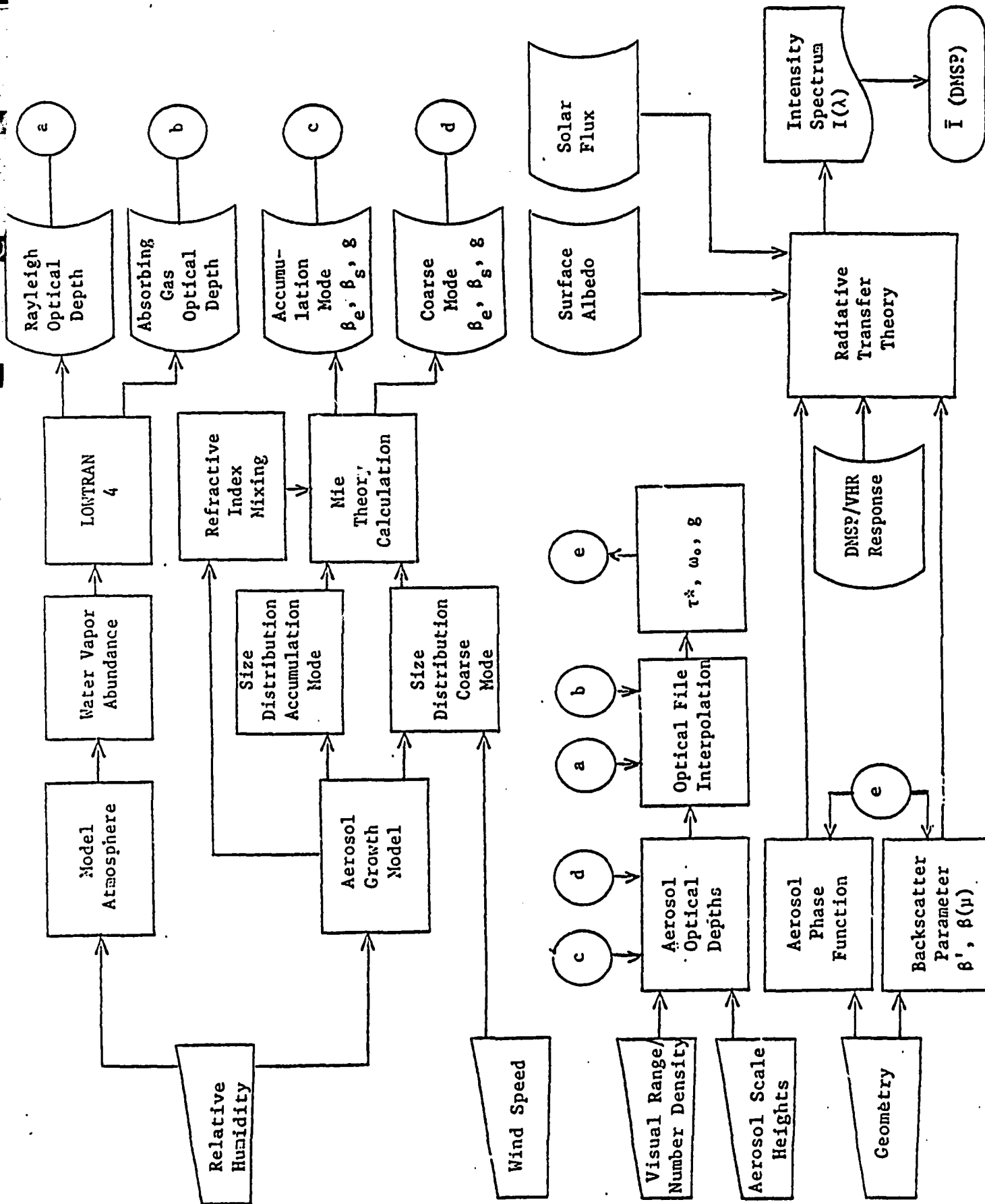


Figure B-1 Technical approach (from Isaacs, 1980).

Section 5. The results obtained for each set of input parameters are an intensity (or radiance) spectrum for wavelengths between 0.4 and 1.1 μm , $I(\lambda)$, and a DMSP VHR response function weighted radiance, $\bar{I}(\text{DMS})$, in units of $\text{mW}/\text{cm}^2\text{-}\mu\text{m}\text{-sr}$.

The process linking input parameters and desired output as illustrated in Figure B-1 may be divided into four basic modeling efforts: (a) atmospheric transmission (i.e., exclusive of aerosols), (b) physical modeling of aerosol properties including relative humidity and wind speed dependence of aerosol size distribution and index of refraction, (c) determination of wavelength-dependent aerosol optical properties, and finally, (d) radiative transfer theory. A description of the approaches to incorporate these processes within the simulation model algorithm is described in Isaacs (1980). The present version of the code contains several additions and changes subsequently implemented and described in previous sections of this document. These include: (a) incorporation of rural and urban aerosol models (Section 4), (b) calculation of sun/sensor geometry directly from spacecraft and solar ephemeris data (Section 5), and treatment of surface reflection in potential sunlint regions (Section 7).

B.2 Program Attributes

These programs simulate the radiances potentially available from DMSP VHR and LF sensors. Input and output are formulated to support meteorological analyses of hard copy imagery. Calculations include the following features: (1) evaluation of solar subpoint, satellite subpoint, and scan

line surface element pixel location (i.e., latitude/longitude) based on ascending node time and location, desired scan line time, and solar declination angle, calculation of solar zenith angle, sensor zenith angle, azimuth angle difference, and azimuth relative to prevailing wind direction, (3) effective ocean surface reflectivity defined using sun/sensor geometry, input wind speed and direction based on the Fresnel relations and Cox-Munk sea slope statistics, and (4) radiative transfer calculations based on the above to simulate sensor incident radiances.

As currently configured (Version 81/3), the program is coded in the extended BASIC language (Hewlett-Packard, 1979) and is implemented on a desk top (HP-85) computer system. Conversions to higher order languages should be relatively easy if desired. The version documented here is in a user-oriented, interactive format suited for individual case analyses and thus requires realtime operator intervention to supply input data. The software is organized into a main program, three subprograms, and twelve supporting data files. These are identified and described by function or contents in Table B-1. The relationship between these program elements is grossly summarized by the program logic flow chart pictured in Figure B-2.

In order to optimize computational efficiency the primary iteration loop is within the RADTRA subprogram and performs the radiative transfer calculations necessary to simulate the radiances for each pixel in the chosen scan line.

Name	Program (P) or Data (D)	Bytes	Description
SLGP	P	256	Scan line generator (sun/ pixel/sensor geometry)
RUFF3	P	256	Specular surface reflectivity
RADTRA	P	256	Optical properties and radiative transfer
FLUX	D	288	Solar flux
FADAT1	D	6912	Tropospheric aerosol model
FADAT2	D	6912	Maritime aerosol model
URBDAT	D	6912	Urban aerosol model
RURDAT	D	6912	Rural aerosol model
CA-0WS	D	4320	M-K coarse mode (0 ms^{-1})
CA-5WS	D	4320	M-K coarse mode (5 ms^{-1})
CA-7WS	D	4320	M-K coarse mode (7 ms^{-1})
CA-10WS	D	4320	M-K coarse mode (10 ms^{-1})
LTRAN4	D	2880	Clear atmosphere optical depths
PHI	D	288	DMSP VHR response function
ALBEDO	D	288	Lambert sea surface albedo

Table B-1. Simulation Model Software
File Attributes and Purpose

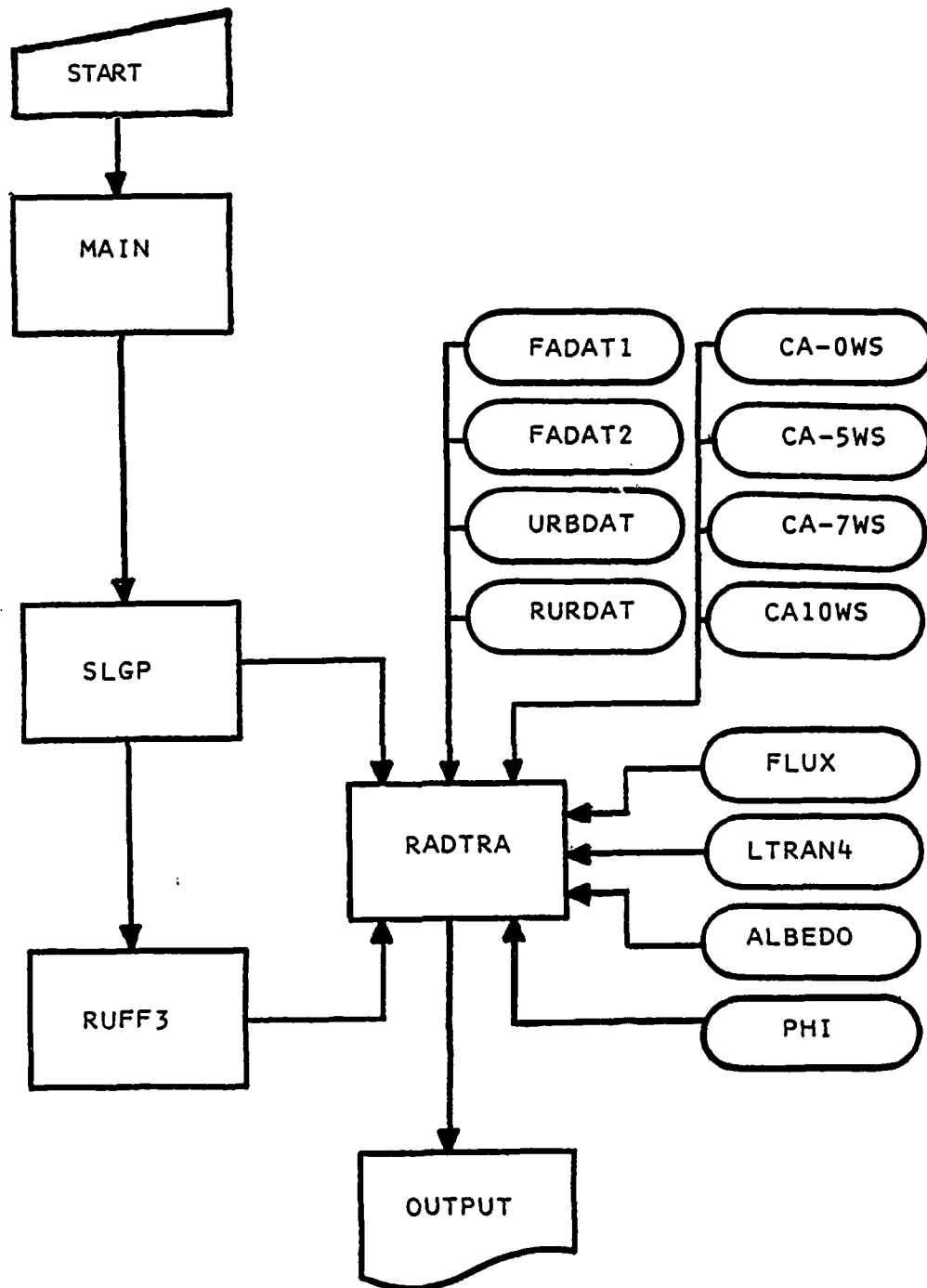


FIGURE B-2: SIMULATION MODEL FLOW CHART

Before entering this loop, sun/sensor geometry is evaluated (in SLGP) for the entire scan line supporting both the determination of effective reflectivity (in RUFF3) for each pixel and the transfer calculation. Optical data files are read once before the main iteration loop. As a consequence of this configuration, input variables may not change along a scan line.[†]

B.3 Program Listings

Current listings of the simulation model computer code are given in Tables B-2 through B-5. Included are the main calling driver (MAIN, Table B-2a,b) and the three subroutine programs identified above in Table B-1. These are: the scan line generator program (SLGP, Table B-3a,b), the wind-driven, ocean surface model (RUFF3, Table B-4a,b,c,d), and the radiative transfer program (RADTRA, Table B-5a,b,c,d,e).

B.4 Sample Calculation

As a guide to program operation, this section presents a sample calculation from the user's vantage point. For illustrative purposes, it is assumed that the program code (as listed in Section B.4) and the associated data files (see Table B-1) are stored in the cartridge format and the program is run on an HP-85 computer. The case analyzed in this example is identical to that discussed in Section 7.7

[†] This restriction is easily removed by reprogramming.

```

1 ! *****NEPRF/ONR-MAIN*****
  Main Prog.-Satellite Imagery
  **R. Isaacs/AER, Inc./1981**
2 ! *****
3 ! *****Version 81/3*****
4 ! These programs simulate the
  imagery potentially available
  from the DMSP VHR and LF
  sensors.
5 ! Calculations include the
  following features:
6 ! (1) evaluation of solar sub
  point, satellite subpoint,
  and scan line pixel location
  (lat/lon)
7 ! based on ascending node time
  and location, desired scan
  line time and solar declination
  angle
8 ! (2) calculate solar zenith
  angle, sensor zenith angle,
  relative azimuth, and azimuth
  difference
9 ! with respect to prevailing
  wind direction.
10 ! (3) based on sun/sensor geometry
  , input wind speed and
  wind direction, an effective
  ocean
11 ! surface reflectivity is
  computed using Cox-Munk sea
  slope statistics and Fresnel
  relations.
12 ! (4) computed geometry and
  surface reflectance are
  input to radiative transfer
  calculations.
13 ! The radiative transfer
  scheme is described in Isaacs,
  1980 (NAVENVPREDRSCHFAC CR 80-
  06)
14 ! Due to the approx nature of
  the calculation, results must
  be carefully interpreted(
  see text)
15 ! Required are meteorological
  data to characterize the
  optical properties of the
  atmosphere
16 ! including relative humidity,
  aerosol scale heights(fine/
  coarse), and choice of one
  of four
17 ! aerosol models:(tropospheric,
  maritime, rural, urban)
18 ! (5) Results include radiances
  (mW/cm**2-um-sr) in (0.4-
  1.1um)range and DMSP weighted
  values
19 ! for each selected scan line
  pixel.

```

Table B-2a. Listing-MAIN Program

```

20 ! *****
31 ! Software is organized into
    three(3) subprograms(P)and t
    welve(12)data files(D) liste
    d below:
32 ! SLGP   P   scan line genera
33 !       P   tion program
34 ! RUFF3  P   specular surface
35 !       P   reflectivity
36 ! RADTRA D   optical proper
37 !       D   ties and radia
38 !       D   tive transfer
39 ! FLUX   D   solar flux
40 ! FADAT1 D   trop aer. mod.
41 ! FADAT2 D   marit. aer. mod.
42 ! URBDAT D   urban aer. mod.
43 ! RURDAT D   rural aer. mod.
44 ! CA-0WS D   coarsemode(0m/s)
45 ! CA-5WS D   coarsemode(5m/s)
46 ! CA-7WS D   coarsemode(7m/s)
47 ! CA10WS D  coarsemode(10m/s

48 ! LTRAN4 D   clear atm. model
49 ! PHI    D   DMSP response
50 ! ALBEDO D   sea surf. albedo
51 !       D   (Lambert reflect
    )
52 ! *****
79 PRINT "*****
    *****"
80 PRINT "*DMSP VHR/LF Imagery
    Simulation*"
81 PRINT "*   R.G.ISHACS/AER,I
    nc./1981   *"
82 PRINT "*           Version 81/
    3           *"
83 PRINT "*****
    *****"
90 PRINT " RADIANCES FOR SCAN L
    INE AT:   "
110 OPTION BASE 1
120 COM U(11),U0(11),D8(11)
130 COM W9
140 COM F2(11),Y9
150 Y9=0
160 CHAIN "SLGP"
170 END

```

Table B-2b. Listing-MAIN Program (continued)

```

1 ! *****NEPRF/OHR-SLGP*****
  *Scan Line Generator Prog **
  **R. Isaacs/AER, Inc. /1981**

2 DISP "Scan Line Geometry Pro
  gram: Assumes sun sync orbit
  w/ alt.=833km, per.=101.35m
  "

3 DEG
4 OPTION BASE 1
5 DISP "LONG(AN)=Des";
6 INPUT L0
7 COM U(11),U0(11),D0(11)
8 COM W9
9 COM F2(11),Y9
10 DISP "AN(GMT)=HH,MM,SS";
11 INPUT H0,M0,S0
12 Y9=1
15 DISP "Desired T(GMT)=HH,MM,S
  S";
16 INPUT H1,M1,S1
20 P0=101.35
25 DISP "Solar Decl Ang = ";
26 INPUT D9
27 DISP "Scan Line Print? (1)Ye
  s/(0)No"
28 INPUT P7
30 PRINT "LONG(AN)=",L0
31 PRINT "AN(GMT) =",H0,M0,S0
32 PRINT "Scan(GMT)=",H1,M1,S1
40 ! U = ARRAY OF SAT ZEN ANG C
  OS
41 ! U0= ARRAY OF SUN ZEN ANG C
  OS
42 ! D0= ARRAY OF AZI ANG DIFF
90 ! GENERATE Sat.Sub Point Tra
  ck
100 T0=H0+M0/60+S0/3600
110 T1=H1+M1/60+S1/3600
115 L9=(T1-T0)*15
116 L8=(T1-12)*15
118 PRINT "Sol Decl. =",D9
119 PRINT "Sol Long. =",L8
120 P=P0/60
130 C=(T1-T0)*360/P
140 B=90
150 A1=8.7
160 T1=COS(.5*(B-C))*SEC(.5*(B+C
  ))*COT(.5*A1)
170 T2=SIN(.5*(B-C))*CSC(.5*(B+C
  ))*COT(.5*A1)
180 B1=ATN(T1)+ATN(T2)
190 C1=ATN(T1)-ATN(T2)
200 T3=TAN(.5*(B-C))*SIN(.5*(B1+
  C1))*CSC(.5*(B1-C1))
210 A=2*ATN(T3)
220 L1=90-A
230 L2=L0+C1+L9
235 PRINT "Sub. Pt. Lat/Long =",
  L1,"/",L2

```

Table B-3a. Listing-SLGP Subprogram

```

500 ! SCAN LINE GENERATOR
510 E=90-L1
520 D1=81.3
530 FOR N=1 TO 11
540 F=(N-1)*13.303/10
550 T5=COS(.5*(E-F))*SEC(.5*(E+F
)))*COT(.5*D1)
560 T6=SIN(.5*(E-F))*CSC(.5*(E+F
)))*COT(.5*D1)
570 E1=ATN(T5)+ATN(T6)
580 F1=ATN(T5)-ATN(T6)
590 D=2*ATN(TAN(.5*(E-F))*SIN(.5
*(E1+F1))*CSC(.5*(E1-F1)))
600 L3=90-D
610 L4=L2-F1
615 IF P7=0 THEN 630
620 PRINT "Scan Line Pixel =",N
621 PRINT "Pixel Lat/Long =",L3,
"/",L4
630 X=(N-1)*1479/10
631 Z=ATN(X/833)
750 ! SOLAR POSITION DATA FOR SC
AN
751 ! D9=DECLINATION ANGLE
752 ! H9=SUNS HOUR ANGLE
753 ! Z9=SOLAR ZENITH ANGLE
754 ! A9=SOLAR AZIMUTH ANGLE
762 H9=L4-L8
770 Z9=90-ASN(SIN(L3)*SIN(D9)+CO
S(L3)*COS(D9)*COS(H9))
780 Q1=90-L3
782 Q2=Z9
784 Q3=90-D9
786 Q4=.5*(Q1+Q2+Q3)
788 Q5=SIN(Q4-Q2)*SIN(Q4-Q1)/(SI
N(Q2)*SIN(Q1))
790 A9=ACS(1-2*Q5)
795 IF H9<0 THEN A9=360-A9
800 IF P7=0 THEN 900
801 PRINT "Sat. Zen Ang =",Z
802 PRINT "Hour Ang. =",H9
803 PRINT "Sol Zen Ang =",Z9
804 PRINT " Sol Azm Ang =",A9
900 U(N)=COS(Z)
901 U0(N)=COS(Z9)
902 D8(N)=261.3-A9
1000 NEXT N
2000 PRINT "*****OCEAN SURFA
CE*****"
2001 PRINT " REFLECTAN
CE"
3000 CHAIN "RUFF3"
9999 END

```

Table B-3b. Listing-SLGP Subprogram (continued)

```

10 ! ****NEPRF/ONR-RUFF3****
   **Wind-driven ocean surf. **
   ** R.Isaacs/AER,Inc./1982 **
20 ! ****
   **
30 OPTION BASE 1
40 COM U(11),U0(11),D0(11),W9,F
   2(11),Y9
50 DISP "WIND SPEED(M/S):1(0.0)
   ,2(5.0),3(7.0),4(10.0)";
60 INPUT W9
70 PRINT "Wind Speed = ",W9
80 ON W9 GOTO 90,110,130,150
90 W=.005
100 GOTO 160
110 W=5
120 GOTO 160
130 W=7
140 GOTO 160
150 W=10
160 DISP "WIND AZ.(ie N=000,E=09
   0,S=180,W=270)";
170 INPUT W1
180 PRINT "Wind Dir.(deg)=",W1
190 FOR Q=1 TO 11
200 DEG
210 T0=ACS(U0(Q))
220 T2=ACS(U(Q))
230 D=D0(Q)
240 RAD
250 B=W1+98.7
260 ! **** DEFINE ****
270 ! Z1 = UPWIND SLOPE COMP(ZU)
280 ! Z2 = CROSSWIND SLOPE COMP(
   ZC)
290 ! U0 = SOLAR ZENITH ANG COS
300 ! T0 = SOLAR ZENITH ANG
310 ! D = SOLAR AZIMUTH DIFFER
   ENCE
320 ! B = AZIMUTH DIFF. BETW.
   SUN AND WIND
330 ! T2 = OBSERVER ZENITH ANGLE
340 ! VEC(n)=SURF. NORM.
350 ! VEC(s)=SOLAR DIR.
360 ! VEC(o)=OBSERV. DIR
370 ! W = WIND SPEED (M/S)
380 U0=COS(DTR(T0))
390 U=COS(DTR(T2))
400 PRINT U0,U
410 ! CARTESIAN COORDS. OF S0
420 S1=SQR(1-U0^2)*COS(DTR(180+B
   ))
430 S2=SQR(1-U0^2)*SIN(DTR(180+B
   ))
440 S3=U0
450 ! SPHERICAL COORDS. OF N0
460 D0=180+B
470 ! CARTESIAN COORDINATES OF O
   BSERVER DIRECTION
480 O1=SIN(DTR(T2))*COS(DTR(180+
   B+D))

```

Table B-4a. Listing-RUFF3 Subprogram

```

490 O2=SIN(DTR(T2))*SIN(DTR(180+
    B+D))
500 O3=U
510 D2=180+B+D
520 ! ***** ROTATE AXES *****
530 ! EVALUATE z^'=(s x o )
540 C1=S2*O3-O2*S3
550 C2=O1*S3-S1*O3
560 C3=S1*O2-S2*O1
570 ! COMPONENTS OF x^'=(S1,S2,S
    3)
580 A1=S1
590 A2=S2
600 A3=S3
610 ! COMPONENTS OF y^'=(z^')x(x
    ^')
620 B1=A3*C2-A2*C3
630 B2=A1*C3-A3*C1
640 B3=A2*C1-A1*C2
650 ! ***** DOT PROD. CHK.*****
660 A=A1*B1+A2*B2+A3*B3
670 B=B1*C1+B2*C2+B3*C3
680 C=A1*C1+A2*C2+A3*C3
690 ! ***** MAG. CHK.*****
700 E=SQR(A1^2+A2^2+A3^2)
710 F=SQR(B1^2+B2^2+B3^2)
720 G=SQR(C1^2+C2^2+C3^2)
730 ! ***** NORMALIZE *****
740 A1=A1/E
750 A2=A2/E
760 A3=A3/E
770 B1=B1/F
780 B2=B2/F
790 B3=B3/F
800 C1=C1/G
810 C2=C2/G
820 C3=C3/G
830 H=SQR(A1^2+A2^2+A3^2)
840 I=SQR(B1^2+B2^2+B3^2)
850 J=SQR(C1^2+C2^2+C3^2)
860 ! ***COMPUTE < BETW. s^ and
    o^ = A0 *****
870 A0=RTD(ACS(O1*S1+O2*S2+O3*S3
    ))
880 ! *****COMPS. OF n^'*****
890 N1=COS(DTR(A0/2))
900 N2=SIN(DTR(A0/2))
910 N3=0
920 ! *****ROTATE BACK *****

930 M1=A1*N1+B1*N2
940 M2=A2*N1+B2*N2
950 M3=A3*N1+B3*N2
960 ! ***** SPHERICAL REP.*****
970 T3=RTD(ACS(M3/SQR(M1^2+M2^2+
    M3^2)))
980 D3=RTD(ATN(M2/M1))
990 ! *****FIND SLOPES,Z1,Z2****
    *
1000 Z1=-M1/M3

```

Table B-4b. Listing-RUFF3 Subprogram (continued)

```

1010 Z2=-M2/M3
1020 IF ABS(Z1)<.001 THEN 1030 E
      LSE 1040
1030 Z1=0
1040 IF ABS(Z2)<.001 THEN 1050 E
      LSE 1060
1050 Z2=0
1060 ! CONTINUE
1070 ! **** FRESNEL REFL. ****
1080 Q1=1
1090 Q2=1.338
1100 A4=DTR(A0/2)
1110 A5=ASN(Q1*SIN(A4)/Q2)
1120 U1=(TAN(A4-A5)/TAN(A4+A5))^2
1130 U2=(-SIN(A4-A5)/SIN(A4+A5))^2
1140 R9=.5*(U1+U2)
1150 A6=A0/2
1160 ! ****COX-MUNK STATS. ****
1170 G1=SQR(.00316*W)
1180 G2=SQR(.003+.00192*W)
1190 P9=EXP(-.5*((Z1/G1)^2+(Z2/G2)^2))/(2*PI*G1*G2)
1200 P5=(U2-U1)/(U2+U1)
1210 ! ****DEFINE EFFECTIVE****
1220 ! **SPECULAR REFLECTION **
1230 !   F2 = Effective Fresnel
           Reflectivity
1240 !   F2 =(Fresnel Ref)*(Prob
           of Zu,Zc from
           C-M)
1250 F2(Q)=R9*P9/(4*M3^4*U(Q))
1260 PRINT "PIXEL #=",Q,"Rf(effe
ctive)=",F2(Q),"POL. =",P5
1270 NEXT Q
1280 CHAIN "RADTRA"
1290 END

```

Table B-4c. Listing-RUFF3 Subprogram (continued)

```

1 ! *****NEPRF/ONR-RADTRA****
  **Radiative Transfer Prog****
  **R. Isaacs/AER, Inc./1982****
2 PRINT "*****RADIANCES****
  *****"
91 OPTION BASE 1
92 COM U(11),U0(11),D8(11),W9,F
  2(11),Y9
97 DIM U9(2),A9(10,5),U8(9),B7(
  2)
98 DIM T1(36),T2(36),T3(36),T4(
  36),T5(36),T6(36),G3(36),G4(
  36)
99 DIM I1(36),F9(36),A2(36),P9(
  36)
100 DIM L9(36)
103 DISP "REL. HUMIDITY,RH(%)=1(
  0%),2(50%),3(70%),4(80%),5(9
  0%),6(95%),7(98%),8(99%)";
104 INPUT R9
107 DISP "AEROSOL SCALE HTS.(KM)
  : FINE, COARSE"
108 INPUT H1,H2
110 DISP "AEROSOL MODEL:(1)TROPO
  SPHERIC,(2)MARITIME,(3)RURAL
  ,(4)URBAN";
111 INPUT Q9
123 PRINT "REL. HUM.[RH(%)]=",R9
125 PRINT "AEROSOL SCALE HTS(KM)
  - FINE:",H1,"COAR
  SE:",H2
126 ON Q9 GOTO 127,129,131,133
127 PRINT "TROPOSPHERIC AEROSOL"
128 GOTO 134
129 PRINT "MARITIME AEROSOL"
130 GOTO 134
131 PRINT "RURAL AEROSOL"
132 GOTO 134
133 PRINT "URBAN AEROSOL"
134 !
140 ! READ DATA FILES FROM TAPE
      3
141 ! SOLAR IRRADIANCE -F9
142 ASSIGN# 1 TO "FLUX"
143 FOR I=1 TO 36
144 READ# 1 ; F9(I)
145 NEXT I
146 ASSIGN# 1 TO *
147 ! RESPONSE FUNC. - P9
148 ASSIGN# 2 TO "PHI"
149 FOR I=1 TO 36
150 READ# 2 ; P9(I)
151 NEXT I
152 ASSIGN# 2 TO *
153 ! FINE AEROSOL DATA-T2,T5,G3
154 ON Q9 GOTO 155,157,159,161
155 ASSIGN# 3 TO "FADAT1"
156 GOTO 165
157 ASSIGN# 3 TO "FADAT2"
158 GOTO 165

```

Table B-5a. Listing-RADTRA Subprogram

```

159 ASSIGN# 3 TO "RURDAT"
160 GOTO 165
161 ASSIGN# 3 TO "URBDAT"
165 FOR I=1 TO 8
166 FOR J=1 TO 36
167 READ# 3 ; A,B,C
168 IF I<>R9 THEN 172
169 T2(J)=A*H1
170 T5(J)=B*H1
171 G3(J)=C
172 NEXT J
173 NEXT I
174 ASSIGN# 3 TO *
175 ! SURFACE ALBEDO - A2
176 ASSIGN# 4 TO "ALBEDO"
177 FOR I=1 TO 36
178 READ# 4 ; A2(I)
179 NEXT I
180 ASSIGN# 4 TO *
181 ! LOWTRAN DATA -T1,T4
182 ASSIGN# 5 TO "LTRAN4"
183 FOR I=2 TO 6
184 FOR J=1 TO 36
185 READ# 5 ; A,B
186 IF I<>R9 THEN 190
187 T1(J)=A
188 T4(J)=B
189 NEXT J
190 NEXT I
191 NEXT I
192 ASSIGN# 5 TO *
200 ! COARSE MODE AEROSOL-T3,T6,
    G4 - TROPOSPHERIC ONLY
201 IF Q9#1 THEN 300
202 ON W9 GOTO 203,205,207,209
203 ASSIGN# 6 TO "CA-0WS"
204 GOTO 210
205 ASSIGN# 6 TO "CA-5WS"
206 GOTO 210
207 ASSIGN# 6 TO "CA-7WS"
208 GOTO 210
209 ASSIGN# 6 TO "CA10WS"
210 FOR I=2 TO 6
211 FOR J=1 TO 36
212 READ# 6 ; A,B,C
213 IF I<>R9 THEN 217
214 T3(J)=A*H2
215 T6(J)=B*H2
216 G4(J)=C
217 NEXT J
218 NEXT I
219 ASSIGN# 6 TO *
299 GOTO 315
300 REM DUMMY ARRAY VALUES
301 FOR J=1 TO 36
304 T3(J)=0
307 T6(J)=0
309 G4(J)=0
313 NEXT J
315 DISP "ALL FILES READ"
320 FOR Z=1 TO 11

```

Table B-5b. Listing-RADTRA Subprogram (continued)

```

330 A8=F2(Z)
340 U0=U0(Z)
341 U=U(Z)
342 D=D0(Z)-180
345 PRINT "PIXEL # =",Z
346 PRINT "OBS. ZENITH( $\nu$ ) =",U
347 PRINT "SUN ZENITH( $\nu_0$ ) =",U0
348 PRINT "AZIMUTH ANG. ( $\phi$ ) =",D
349 PRINT "Rf(eff.) =",A8
350 FOR L=1 TO 36
360 IF L>=16 THEN 370 ELSE 390
370 A8=0
390 T0=T1(L)+T2(L)+T3(L)
391 W0=(T5(L)+T6(L))/(T2(L)+T3(L))
392 G=(T5(L)*G3(L)+T6(L)*G4(L))/(T5(L)+T6(L))
393 A1=A2(L)
399 F=F9(L)/PI
414 D=OTR(D)
416 C1=-U*U0+SQR(1-U^2)*SQR(1-U0^2)*COS(D)
418 C2=U*U0+SQR(1-U^2)*SQR(1-U0^2)*COS(D)
420 S=ACS(-C2)
425 S1=RTD(S)
435 P1=W0*(1-G^2)/(1+G^2-2*G*C1)^1.5
440 P2=W0*(1-G^2)/(1+G^2-2*G*C2)^1.5
442 P1=(T4(L)*.75*(1+C1^2)+(T5(L)+T6(L))*P1)/T0
443 P2=(T4(L)*.75*(1+C2^2)+(T5(L)+T6(L))*P2)/T0
444 W0=(T4(L)+T5(L)+T6(L))/T0
445 G=(T5(L)*G3(L)+T6(L)*G4(L))/(T4(L)+T5(L)+T6(L))
446 ! H-G PHASE FUNCTION
447 GOSUB 2000
448 GOSUB 2300
500 Q=4*(1-G^2*(1-U0))
501 G1=(7-3*G^2-W0*(4+3*G)+W0*G^2*(4*B0+3*G))/Q
502 G2=-((1-G^2-W0*(4-3*G)-W0*G^2*(4*B0+3*G-4))/Q
503 K=SQR(G1^2-G2^2)
504 C=PI*F*W0*(B0/U0-G2*(1-B0)-G1*B0)*U0^2/(1-K^2*U0^2)
505 E1=(C*(G1+1/U0)-PI*F*W0*B0)*(1/(G1-K)-A1/G2)
506 E2=-C+PI*F*U0*A1+A1/G2*(C*(G1+1/U0)-PI*F*W0*B0)
507 E3=(G1+K)*(-1/(G1-K)+A1/G2)
508 E4=1-A1/G2*(G1+K)
509 B=(E1*EXP(K*T0)+E2*EXP(-T0/U0))/(E3*EXP(K*T0)+E4*EXP(-K*T0))
510 A=(B*(G1+K)+(C*(G1+1/U0)-PI*F*W0*B0))/(K-G1)
699 I2=A8*PI*F*EXP(-T0/U0)*EXP(-T0/II)

```

Table B-5c. Listing-RADTRA Subprogram (continued)

```

701 REM UPWARD INTENSITY
710 U1=A*(W0/PI)*(1-B2+B2/G2*(G1
-K))
711 U2=B*(W0/PI)*(1-B2+B2/G2*(G1
+K))
712 U3=C*(W0/PI)*(1-B2)+W0*B2/(P
I*G2)*(C*(G1+1/U0)-PI*F*W0*B
0)+F/4*P1
713 F5=A*EXP(K*T0)+B*EXP(-K*T0)+
C*EXP(-T0/U0)
714 D2=F5/PI-U1*EXP(K*T0)/(1-U*K
)
715 D3=-U2*EXP(-K*T0)/(1+U*K)-U3
*EXP(-T0/U0)/(1+U/U0)
716 D1=EXP(-T0/U)*(D2+D3)
719 T=0
720 I1(L)=D1*EXP(T/U)+U1*EXP(K*T
)/(1-U*K)+U2*EXP(-K*T)/(1+U*
K)+U3*EXP(-T/U0)/(1+U/U0)+I2
721 L9(L)=.4+(L-1)*.02
722 PRINT L9(L),I1(L),I2
749 RESTORE
750 NEXT L
800 ! COMPUTE DMSP WEIGHTED INTE
NSITIES
801 S1=0
802 S2=0
803 FOR I=1 TO 36
804 S1=S1+P9(I)*I1(I)
805 S2=S2+P9(I)
806 NEXT I
807 I9=S1/S2
810 PRINT "BANDPASS-WEIGHTED INT
ENSITY =",I9
901 NEXT Z
1999 GOTO 9996
2000 REM DATA FOR H-G B0,B1,B2
2030 FOR Q=1 TO 10
2040 FOR S=1 TO 5
2050 READ A9(Q,S)
2060 NEXT S
2070 NEXT Q
2080 DATA .5,0,0,0,0,.5,.1397929
2889,-1.5989873995,3.518411
6963,-2.5592172257,.5,-.120
19000482
2090 DATA -.2724219928,.63859601
23,-.7459840146,.5,-.460171
23188,1.18747390274,-2.0812
230849
2100 DATA .85392041407,.5,-.4068
28796532,.49409050834,-1.01
44699491,.4272082373,.5,-.3
001541656
2110 DATA -.35928947292,.1589475
781,.00049606046,.5,-.55347
4414782,.37397957743,-.7476
1782865
2120 DATA .42711266606,.5,-.6267
94663911,.18057740986,-.374
16958202,.32038683614,.5,-.
84678101

```

Table B-5d. Listing-RADTRA Subprogram (continued)

```

2130 DATA .50718036245, -.3740740
      109, .2136746594, .5, -.406823
      676662, .01406832224, .105560
      7702
2140 DATA -.2128054157
2150 FOR I=1 TO 9
2160 READ U8(I)
2170 NEXT I
2180 DATA 0, .1, .2, .3, .4, .5, .6, .8
      , 1
2200 RETURN
2300 REM BACKSCATTER INTERP
2310 U9(1)=U
2311 U9(2)=U0
2320 FOR R=1 TO 2
2330 IF U9(R)<.1 THEN 2500
2340 IF U9(R)<.2 THEN 2502
2350 IF U9(R)<.3 THEN 2504
2360 IF U9(R)<.4 THEN 2506
2370 IF U9(R)<.5 THEN 2508
2380 IF U9(R)<.6 THEN 2510
2390 IF U9(R)<.8 THEN 2512
2400 IF U9(R)<=1 THEN 2514
2500 Q=1
2501 GOTO 2515
2502 Q=2
2503 GOTO 2515
2504 Q=3
2505 GOTO 2515
2506 Q=4
2507 GOTO 2515
2508 Q=5
2509 GOTO 2515
2510 Q=6
2511 GOTO 2515
2512 Q=7
2513 GOTO 2515
2514 Q=8
2515 Y5=0
2516 Y6=0
2517 Y7=0
2518 Q1=Q+1
2525 FOR S=1 TO 5
2526 Y9=A9(Q,S)*G^(S-1)
2527 Y8=A9(Q1,S)*G^(S-1)
2528 Y3=A9(10,S)*G^(S-1)
2529 Y7=Y7+Y9
2530 Y6=Y6+Y8
2531 Y5=Y5+Y3
2532 NEXT S
2540 B7(R)=Y7+(Y6-Y7)*(U9(R)-U8(
      Q))/(U8(Q1)-U8(Q))
2541 NEXT R
2550 B1=Y5
2551 B2=B7(1)
2552 B0=B7(2)
2560 RETURN
9996 PRINT USING 9997
9997 IMAGE 4/
9998 CHAIN "MAIN"
9999 END

```

Table B-5e. Listing-RADTRA Subprogram (continued)

with the exception of the input wind speed of 7.0 ms^{-1} (radi-
ances in §7.7 are simulated using 5.0 ms^{-1}).

Running the program from tape commences by loading the main program (LOAD "MAIN") followed by a run command (RUN key). As the printer prints the heading illustrated in Figure B-4, the SLGP subprogram is loaded. Figure B-3 illustrates the CRT display during the running of the program. Items preceded by an asterisk and in parentheses indicate operations during which the CRT is blanked out. Displays followed by question marks (i.e., "?") require operator input. Data entered in response by the user (followed by an END LINE key) are indicated on subsequent lines.

After SLGP is loaded, the display commencing in Figure B-3a asks for satellite and solar ephemeris data to accomplish the scan line geometry calculation. Data required are: (1) the longitude (in degrees W) of the ascending node (AN), (2) the GMT time of the ascending node (TN) in hours, minutes and seconds (not input format), (3) the GMT time of the desired scan line (in same input format), and (4) the solar declination angle (SD) for the desired date. The user has the option of selecting a scan line print giving the latitude and longitude (in decimal degrees) and other information pertaining to each of the eleven available pixels. Figure B-4 illustrates the subsequent printer output from SLGP for the input data shown in Figure B-3a and selecting a scan line print. (If a scan line print is not selected, output is not given for each pixel, but the calculations are done and stored for later use.)

* (loading SLGP)

(a) Scan Line Geometry Program: Assu
mes sun sync orbit w/ alt.=833k
m, per.=101.35m
LONG(AN)=Deg?
94.0
AN(GMT)=HH,MM,SS?
15,00,08
Desired T(GMT)=HH,MM,SS?
15,06,10
Solar Decl Ang = ?
19.2
Scan Line Print? (1)Yes/(0)No
?
1

* (loading RUFF3)

(b) WIND SPEED(M/S):1(0.0),2(5.0),3(
7.0),4(10.0)?
3
WIND AZ.(ie N=000,E=090,S=180,W=
270)?
000

* (loading RADTRA)

(c) REL. HUMIDITY,RH(%):1(0%),2(50%)
,3(70%),4(80%),5(90%),6(95%),7(
8%),8(99%)?
6
AEROSOL SCALE HTS.(KM):FINE,COAR
SE
?
.08,0
AEROSOL MODEL:(1)TROPOSPHERIC,(2
)MARITIME,(3)RURAL,(4)URBAN?
2

* (loading required data files)

(d) ALL FILES READ

Figure B-3. Display during simulation run.

```

*****
*DMSP VHR/LF Imagery Simulation*
*   R.G.ISARCS/AER, Inc./1981   *
*         Version 81/3         *
*****
  RADIANCES FOR SCAN LINE AT:
LONG(AN)=          94
AN(GMT) =          15
  0                8
Scan(GMT)=         15
  6                10
Sol Decl. =        19.2
Sol Long. =
  46.541666667
Sub. Pt. Lat/Long =
  21.172148517 /
  98.9061061921
Scan Line Pixel = 1
Pixel Lat/Long =
  21.172148517 /
  98.9061061921
Sat. Zen Ang = 0
Hour Ang. =
  52.3644395251
Sol Zen Ang =
  48.9648006036
Sol Azm Ang =
  82.5050391655
Scan Line Pixel = 2
Pixel Lat/Long =
  21.3675008272 /
  97.4940357987
Sat. Zen Ang =
  10.0680032943
Hour Ang. =
  50.9523691317
Sol Zen Ang =
  47.6348009984
Sol Azm Ang =
  83.0424938691
Scan Line Pixel = 3
Pixel Lat/Long =
  21.5510145928 /
  96.0783079082
Sat. Zen Ang =
  19.550054325
Hour Ang. =
  49.5366412412
Sol Zen Ang =
  46.3048143283
Sol Azm Ang =
  83.5874018942
Scan Line Pixel = 4
Pixel Lat/Long =
  21.7225478104 /
  94.6591113539
Sat. Zen Ang =
  28.0421331669

```

Figure B-4. SLGP output.

After printing the heading at the top of Figure B-5, subprogram RUFF3 is loaded. When this operation is over, the display asks for wind speed and wind direction information (Figure B-3b). After the wind azimuth is entered, the ocean surface model calculations are performed for each pixel. (The display screen will flash with various intermediate results.) Final pixel-by-pixel effective reflectivities are printed as demonstrated in Figure B-5. Completion of this operation results in the heading in Figure B-6 being printed followed by loading of the radiative transfer program (RADTRA). This portion of the code requests (see Figure B-3c) relative humidity (only options 2 through 6 will work), fine and coarse aerosol scale heights, and one of the four available aerosol optical properties models. Subsequent to specifying these input parameters, required relevant data files are read. When completed, the display notes "ALL FILES READ" and the radiative transfer calculation for each pixel commences.

As illustrated in Figure B-6, the output consists of zenith angle cosines for sensor (observer) and sun, azimuth angle difference, and effective reflectivity for each pixel, followed by a radiance spectrum within the DMSP bandpass from 0.4 to 1.1 μm (each 0.02 μm) consisting of first, the total radiance, and, second, the surface contribution only for comparison purposes. Following the wavelength dependent radiances the DMSP response weighted radiance (total only) is given.

Radiances are calculated for each numbered pixel corresponding to the location given in the scan line print

*****OCEAN SURFACE*****
 REFLECTANCE

Wind Speed =	3	
Wind Dir.(deg)=	0	
.656522556696	1	
PIXEL #=	1	
Rf(effective)=		POL. =
1.22914923601E-4		
.290272498678		
.673853731358		
.984600959627		
PIXEL #=	2	
Rf(effective)=		POL. =
1.74398210756E-3		
.407491354815		
.690821660688		
.942349513481		
PIXEL #=	3	
Rf(effective)=		POL. =
1.00910703736E-2		
.531580891445		
.707417198008		
.882602122384		
PIXEL #=	4	
Rf(effective)=		POL. =
2.97354893974E-2		
.647079252209		
.72363139738		
.8153044345		
PIXEL #=	5	
Rf(effective)=		POL. =
5.43412865455E-2		
.743166854252		
.739455518437		
.747830184897		
PIXEL #=	6	
Rf(effective)=		POL. =
7.15977009487E-2		
.816479854642		
.754801031085		
.684405604278		
PIXEL #=	7	
Rf(effective)=		POL. =
7.55542157374E-2		
.869162695817		
.76989962009		
.626876843527		
PIXEL #=	8	
Rf(effective)=		POL. =
6.84923138666E-2		
.905609943523		
.784503189581		
.575668001212		

Figure B-5. RUFF3 output.

```

*****RADIANCES*****
REL. HUM. ERH(%)J=      6
AEROSOL SCALE HTS(KM)-
  FINE:                .08
  COARSE:              0
MARITIME AEROSOL
PIXEL # =             1
OBS. ZENITH(μ) =      1
SUN ZENITH(μo) =
.656522556697
AZIMUTH ANG.(φ)=
-1.205039165
Rf(εff.)=
1.22914923601E-4
.4
5.62023339111
6.59214596227E-3
.42
6.11269169159
9.4228298862E-3
.44
5.16401864033
1.10159262563E-2
.46
4.92361403792
1.39160356865E-2
.48
3.99839627317
1.46528288137E-2
.5
3.15216336054
1.49552162204E-2
.52
2.4483416146
1.47966128413E-2
.54
1.96670604235
1.47568724604E-2
.56
1.6391982723
.014454008219
.58
1.38375212138
1.47455989775E-2
.6
1.12580610198
1.46729097147E-2
.62
.968356891441
1.45658123949E-2
.64
.824724520471
1.45226991842E-2
.66
.697253079743
1.44003175387E-2
.68
.584552465139
1.41825712095E-2
.7
.444821611869
.72
.359214328192
.74
.334542917271
.76
.297924222246
.78
.259153684984
.8
.224477329539
.82
.14158028171
.84
.158181618455
.86
.15594041316
.88
.137305041092
.9
.100996069207
.92
4.33918657656E-2
.94
2.66866606121E-2
.96
3.14809637237E-2
.98
.057094337495
1
7.33573788027E-2
1.02
.066103012938
1.04
5.94410921661E-2
1.06
5.36809643037E-2
1.08
4.87745057828E-2
1.1
.027649917209
BANDPASS-WEIGHTED INTENSITY =
.618357806254

```

Figure B-6. RADTRA output (pixel #1 only).

(Figure B-4). When all eleven pixels have been treated, the program terminates with a "BEEP."

4-
DT